

# REPORT DOCUMENTATION PAGE

Form Approved  
OMB No. 0704-0188

Public reporting burden for this collection of information is estimated to average 1 hour per response, including the time for reviewing instructions, searching existing data sources, gathering and maintaining the data needed, and completing and reviewing the collection of information. Send comments regarding this burden estimate or any other aspect of this collection of information, including suggestions for reducing this burden, to Washington Headquarters Services, Directorate for Information Operations and Reports, 1215 Jefferson Davis Highway, Suite 1204, Arlington, VA 22202-4302, and to the Office of Management and Budget, Paperwork Reduction Project (0704-0188), Washington, DC 20503.

1. AGENCY USE ONLY (Leave blank)

2. REPORT DATE

25 Oct 95

3. REPORT TYPE AND DATES COVERED

4. TITLE AND SUBTITLE

Using The Quasigeostrophic Potential  
Vorticity Height Tendency Equation To Diagnose  
the Development of Mesospheric Mobile Troughs

5. FUNDING NUMBERS

6. AUTHOR(S)

Randy Joseph LeFevre

7. PERFORMING ORGANIZATION NAME(S) AND ADDRESS(ES)

AFIT Students Attending:

Texas A & M University

8. PERFORMING ORGANIZATION  
REPORT NUMBER

95-023D

9. SPONSORING/MONITORING AGENCY NAME(S) AND ADDRESS(ES)

DEPARTMENT OF THE AIR FORCE

AFIT/CI

2950 P STREET, BLDG 125

WRIGHT-PATTERSON AFB OH 45433-7765

10. SPONSORING/MONITORING  
AGENCY REPORT NUMBER

11. SUPPLEMENTARY NOTES

12a. DISTRIBUTION/AVAILABILITY STATEMENT

Approved for Public Release IAW AFR 190-1

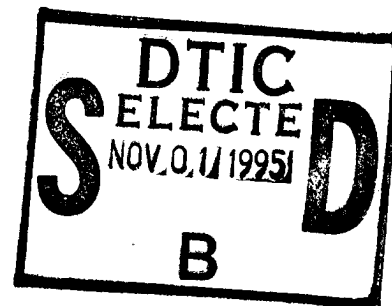
Distribution Unlimited

BRIAN D. Gauthier, MSgt, USAF

Chief Administration

12b. DISTRIBUTION CODE

13. ABSTRACT (Maximum 200 words)



19951031 110

DTIC QUALITY INSPECTED 5

14. SUBJECT TERMS

15. NUMBER OF PAGES

220

16. PRICE CODE

17. SECURITY CLASSIFICATION  
OF REPORT

18. SECURITY CLASSIFICATION  
OF THIS PAGE

19. SECURITY CLASSIFICATION  
OF ABSTRACT

20. LIMITATION OF ABSTRACT

**USING THE QUASIGEOSTROPHIC POTENTIAL VORTICITY  
HEIGHT TENDENCY EQUATION TO DIAGNOSE THE  
DEVELOPMENT OF MDTROPOSPHERIC MOBILE TROUGHS**

A Dissertation

by

**RANDY JOSEPH LEFEVRE**

Submitted to the Office of Graduate Studies of  
Texas A&M University  
in partial fulfillment of the requirements for the degree of

**DOCTOR OF PHILOSOPHY**

May 1995

Major Subject: Meteorology

**USING THE QUASIGEOSTROPHIC POTENTIAL VORTICITY  
HEIGHT TENDENCY EQUATION TO DIAGNOSE THE  
DEVELOPMENT OF MIDTROPOSPHERIC MOBILE TROUGHS**

A Dissertation

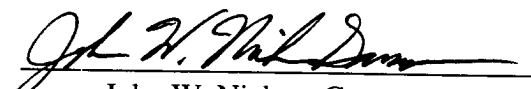
by

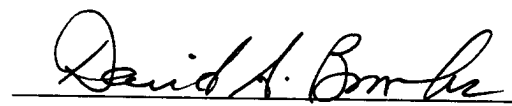
**RANDY JOSEPH LEFEVRE**

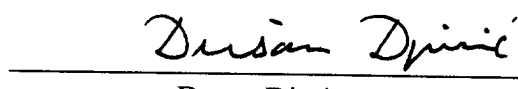
Submitted to Texas A&M University  
in partial fulfillment of the requirements  
for the degree of

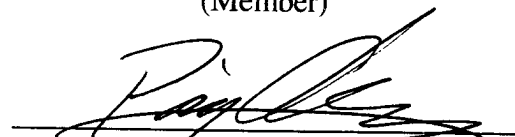
**DOCTOR OF PHILOSOPHY**

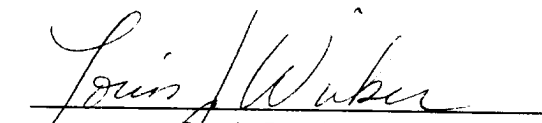
Approved as to style and content by:

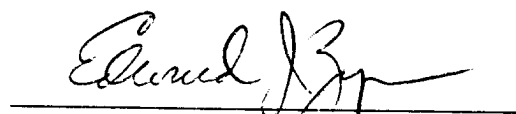
  
John W. Nielsen-Gammon  
(Chairman of Committee)

  
David A. Brooks  
(Member)

  
Dusan Djuric  
(Member)

  
Ping Chang  
(Member)

  
Louis J. Wicker  
(Member)

  
Edward J. Zipser  
(Head of Department)

May 1995

Major Subject: Meteorology

<b>Accession For</b>	
NTIS GRA&I	<input checked="checked" type="checkbox"/>
DTIC TAB	<input type="checkbox"/>
Unannounced	<input type="checkbox"/>
Justification	
By	
Distribution/	
Availability Codes	
Dist	Avail and/or Special
A-1	

## ABSTRACT

Using the Quasigeostrophic Potential Vorticity Height Tendency Equation to Diagnose the Development of Midtropospheric Mobile Troughs. (May 1995)

Randy Joseph Lefevre, B. A., Sonoma State University;

M. S., Naval Postgraduate School

Chair of Advisory Committee: Dr. John W. Nielsen-Gammon

The purpose of this research was to develop a technique to quantify the intensification mechanisms present in the development of midtropospheric mobile troughs. Mobile troughs are generally considered precursors to midlatitude cyclogenesis. The midlatitude cyclones are the primary sources of synoptic scale weather patterns. The overall project was separated into three tasks: a description of trough development characteristics, the construction of the diagnostic framework, and the demonstration of the diagnostic technique using a mobile trough.

The description of mobile trough development characteristics was accomplished by compiling a 20-year climatology of the frequency of mobile trough genesis and termination over the northern hemisphere. The climatology used an objective trough tracking technique based on the relationship between midtropospheric mobile troughs and the maximum transport of geostrophic curvature vorticity. The geographical shape of trough genesis and termination regions are associated with orography.

The quantitative technique used to diagnose the dynamical mechanisms responsible for mobile troughs was based on the quasigeostrophic potential vorticity (QGPV) geopotential height tendency equation. The piecewise inversion of QGPV advection was used to recover the associated height tendency (intensification).

The trough initially developed due to the transport of kinetic energy from upstream disturbances (downstream development). Baroclinic processes were not present during the genesis, but participated later in the development. The deformation of QGPV also contributed to the intensification, but was mainly a factor in the decay.



## ACKNOWLEDGMENTS

I owe every aspect of my life to my Lord, Jesus Christ. His ultimate sacrifice, along with His grace and mercy, gave me the strength to persevere the challenges of completing this research. Second, I owe my family countless hours of quality time that I robbed from them during the preparation of this document. Third, I acknowledge my advisory committee and their commitment to my original research goals.

My chairman, Dr. John Nielsen-Gammon, consistently gave me ideas and focused my efforts. Dr. Lou Wicker helped me solve my numerous numerical inconsistencies. Dr. Dusan Djuric was always available to discuss the application of my ideas to meteorology. Drs. David Brooks and Ping Chang kept me on track and often raised warning flags of poor science. Dr. Lonnie Jones, my Graduate Council Representative, gave me perspective.

Dr. Ken Bowman was instrumental in helping me overcome my difficulties with spherical harmonic analysis. Dr. Michael Morgan often helped me “hash-out” the details of the QGPV diagnostic technique. Dr. James P. McGuirk provided wise and timely counsel related to university matters.

The United States Air Force (USAF) Institute of Technology supported me financially, and gave me the opportunity to complete this degree. This research was partially funded by the National Science Foundation under grant ATM-9218306.

## TABLE OF CONTENTS

	Page
ABSTRACT .....	iii
ACKNOWLEDGMENTS .....	iv
TABLE OF CONTENTS .....	v
LIST OF TABLES .....	vii
LIST OF FIGURES .....	viii
 CHAPTER	
I INTRODUCTION .....	1
II MOBILE TROUGH CLIMATOLOGY .....	6
1. Introduction .....	6
2. Data .....	8
3. Method .....	8
a. Objective trough identification .....	8
b. Trough tracking .....	10
c. Advection region .....	14
d. Final search for trough connection .....	17
4. Trough lifespans .....	17
5. Comparison with Sanders' hero .....	19
6. Inhomogeneities in the tracking statistics .....	24
7. Trough genesis and termination .....	29
8. Summary and discussion .....	36
III QGPV THINKING .....	41
1. Definition of potential vorticity .....	41
2. Traditional diagnostics .....	44
3. QGPV height tendency equation .....	47
4. Theoretical considerations .....	49
5. Thought behind QGPV thinking .....	62
6. Expected error in quasigeostrophic dynamics .....	64
7. Summary .....	68
IV DATA AND METHOD .....	70
1. Data .....	70
2. Basic state possibilities .....	70
3. Low-pass basic state .....	74
a. Overview of spherical harmonic method .....	74
b. Choosing the large-scale .....	79

CHAPTER	Page
4. QGPV inversion method.....	85
5. Verification of the linear QGPV inversion.....	94
6. Interpretation of the QGPV equation.....	96
7. Interpretation of the QGPV height tendency equation.....	114
8. Summary.....	119
V CASE STUDY OF MOBILE TROUGH DEVELOPMENT .....	120
1. Selecting the mobile trough .....	120
2. Life history of the trough at 500 mb.....	121
3. Diagnosing the trough development mechanisms .....	131
a. Baroclinic process.....	146
b. Deformation process.....	158
c. Downstream development process .....	166
d. Trough-merger process.....	178
e. Combination of processes .....	178
4. Sensitivity to the selection of the large-scale .....	184
5. Summary.....	185
VI CONCLUSION .....	186
REFERENCES .....	189
APPENDIX	
1 TELLUS RELEASE LETTER .....	194
2 QGPV DERIVATION.....	195
3 UNPUBLISHED MANUSCRIPT BY NIELSEN-GAMMON (1994).....	202
VITA .....	220

## LIST OF TABLES

	Page
Table 5.1. The definition of the acronyms used to describe the intensification processes. ....	132
Table 5.2. Intensity and distance comparison for flanking ridges. ....	172

## LIST OF FIGURES

	Page
Fig. 2.1. A 500 mb geopotential height and ECA analysis for 0000 UTC 22 February 1986.....	11
Fig. 2.2. A polar-coordinate schematic showing the shape of the 12-hour advection region.....	16
Fig. 2.3. Histogram of trough lifespan.....	18
Fig. 2.4. Comparison of S88's longest-lived trough with objectively-tracked mobile troughs, 1200 UTC 22 October 1985 through 0000 UTC 25 October 1985.....	21
Fig. 2.5. Comparison of S88's longest-lived trough with objectively-tracked mobile troughs, 0000 UTC 7 October 1985 through 1200 UTC 8 October 1985.....	23
Fig. 2.6. A graph of mean lifespan of unscreened troughs versus time.....	25
Fig. 2.7. Frequency of trough appearance on 12-hourly 500 mb analyses for the period January 1969 through May 1980. ....	27
Fig. 2.8. Frequency of trough appearance on 12-hourly 500 mb analyses for the period June 1980 through December 1988. ....	28
Fig. 2.9. Frequency of trough genesis during all months throughout the twenty year dataset.....	30
Fig. 2.10. Frequency of trough termination during all months throughout the twenty year dataset. ....	31
Fig. 2.11. Frequency of trough genesis minus trough termination for all months throughout the dataset. ....	33
Fig. 2.12. Frequency of trough genesis during winter throughout the twenty year dataset. ....	34
Fig. 2.13. Frequency of trough termination during winter throughout the twenty year dataset.....	35
Fig. 2.14. Frequency of trough genesis during summer throughout the twenty year dataset.....	37
Fig. 2.15. Frequency of trough termination during summer throughout the twenty year dataset.....	38
Fig. 3.1. A time-mean meridional-vertical cross section of the zonally averaged meridional gradient of QGPV from 25°N through 75°N from 0000 UTC 1 December through 5 December 1980.....	51

	Page
Fig. 3.2. The distribution of total QGPV on the 372 mb pressure surface from 0000 UTC 3 December 1980. ....	53
Fig. 3.3. The distribution of geopotential height on the 372 mb pressure surface from 0000 UTC 3 December 1980. ....	54
Fig. 3.4. Vertical cross sections through the resulting geopotential height fields associated with interior QGPV anomalies and surface temperature anomalies. ....	57
Fig. 3.5. Vertical cross sections through the resulting geopotential height fields associated with a single interior QGPV anomaly and multiple interior QGPV anomalies. ....	59
Fig. 3.6. A schematic diagram showing the effect of horizontal scale as applied to a Rossby wave. ....	61
Fig. 3.7. A schematic model through a developing baroclinic system. ....	67
Fig. 4.1. A schematic diagram of the spherical harmonic process used to get the large-scale QGPV field. ....	76
Fig. 4.2. A schematic diagram of triangular and rhomboidal truncation. ....	78
Fig. 4.3. A log-plot showing the normalized power of each zonal wavenumber for geopotential height, relative vorticity, and QGPV. ....	81
Fig. 4.4. The full geopotential height field at 472 mb for 0000 UTC 3 December 1980. ....	82
Fig. 4.5. The low-pass geopotential height field using only wavenumbers 0 through 7 at 472 mb for 0000 UTC 3 December 1980. ....	83
Fig. 4.6. The low-pass geopotential height field using only wavenumbers 0 through 6 at 472 mb for 0000 UTC 3 December 1980. ....	84
Fig. 4.7. The large-scale geopotential height field using zonal wavenumbers 0 through 6 and total wavenumbers 0 through 6 at 472 mb for 0000 UTC 3 December 1980. ....	86
Fig. 4.8. A schematic diagram showing the main and intermediate pressure levels, and the boundary pressure levels. ....	88
Fig. 4.9. Vertical profile of the influence of QGPV anomalies from the eight main levels and the boundaries on the 472 mb pressure level. ....	95
Fig. 4.10. The perturbation height field at 472 mb for 0000 UTC 3 December 1980 after adding the effect from the eight levels and the top and bottom boundaries. ....	97
Fig. 4.11. The original perturbation height field at 472 mb for 0000 UTC 3 December 1980. ....	98

	Page
Fig. 4.12. The full QGPV field for 0000 UTC 3 December 1980 at 372 mb.....	100
Fig. 4.13. The large-scale QGPV field for 0000 UTC 3 December 1980 at 372 mb. ....	101
Fig. 4.14. The small-scale QGPV field for 0000 UTC 3 December 1980 at 372 mb. ....	102
Fig. 4.15. The full geopotential height field for 0000 UTC 3 December 1980 at 372 mb.....	103
Fig. 4.16. The large-scale geopotential height field for 0000 UTC 3 December 1980 at 372 mb. ....	104
Fig. 4.17. The small-scale geopotential height field for 0000 UTC 3 December 1980 at 372 mb. ....	105
Fig. 4.18. Term 1 valid at 0000 UTC 3 December 1980 at 372 mb.....	107
Fig. 4.19. Term 3 valid at 0000 UTC 3 December 1980 at 372 mb.....	108
Fig. 4.20. Term 2 valid at 0000 UTC 3 December 1980 at 372 mb.....	110
Fig. 4.21. Term 4 valid at 0000 UTC 3 December 1980 at 372 mb.....	111
Fig. 4.22. Term 5 valid at 0000 UTC 3 December 1980 at 372 mb.....	112
Fig. 4.23. Term 6 valid at 0000 UTC 3 December 1980 at 372 mb.....	113
Fig. 4.24. The 12-hour temporal finite difference at 372 mb using the 0000 UTC and 1200 UTC 3 December 1980 geopotential height fields.....	116
Fig. 4.25. The 24-hour temporal finite difference at 372 mb using the 1200 UTC 2 December and 1200 UTC 3 December 1980 geopotential height fields. ....	117
Fig. 4.26. The 372 mb geopotential height tendency field using the linear inversion of the 0000 UTC 3 December 1980 QGPV advection field. ....	118
Fig. 5.1. A 500 mb geopotential height analysis for 0000 UTC 1 December 1980. ....	122
Fig. 5.2. A 500 mb geopotential height analysis for 0000 UTC 3 December 1980. ....	124
Fig. 5.3. A 500 mb geopotential height analysis for 0000 UTC 10 December 1980. ....	125
Fig. 5.4. A 922 mb geopotential height analysis on 0000 UTC 1 December 1980. ....	127
Fig. 5.5. A 922 mb geopotential height analysis on 0000 UTC 5 December 1980. ....	128

	Page
Fig. 5.6. A 372 mb analysis of the geopotential height field for 0000 UTC 3 December 1980.....	130
Fig. 5.7. Time series of geopotential height and geopotential height tendency at 372 mb.....	133
Fig. 5.8. Time series of geopotential height and geopotential height tendency at 872 mb.....	135
Fig. 5.9. The large-scale geopotential height field at 372 mb on 0000 UTC 3 December 1980.....	137
Fig. 5.10. The small-scale geopotential height field at 372 mb on 0000 UTC 3 December 1980.....	138
Fig. 5.11. The large-scale QGPV field at 372 mb on 0000 UTC 3 December 1980. ....	139
Fig. 5.12. The small-scale QGPV field at 372 mb on 0000 UTC 3 December 1980. ....	140
Fig. 5.13. The large-scale geopotential height field at 922 mb on 0000 UTC 3 December 1980.....	141
Fig. 5.14. The small-scale geopotential height field at 922 mb on 0000 UTC 3 December 1980.....	142
Fig. 5.15. The large-scale vertical gradient geopotential height at 922 mb on 0000 UTC 3 December 1980. ....	143
Fig. 5.16. The small-scale vertical gradient geopotential height at 922 mb on 0000 UTC 3 December 1980. ....	144
Fig. 5.17. A schematic diagram of the baroclinic process.....	148
Fig. 5.18. Time series of geopotential height tendency describing the baroclinic process. ....	149
Fig. 5.19. The 372 mb baroclinic component analysis at 1200 UTC 1 December 1980. ....	151
Fig. 5.20. The 372 mb baroclinic component analysis at 0000 UTC 2 December 1980. ....	152
Fig. 5.21. The 372 mb baroclinic component analysis at 0000 UTC 3 December 1980. ....	153
Fig. 5.22. The 372 mb baroclinic component analysis at 0000 UTC 4 December 1980. ....	154
Fig. 5.23. The 922 mb baroclinic component analysis at 1200 UTC 1 December 1980. ....	156



	Page
Fig. 5.24. The 922 mb baroclinic component analysis at 0000 UTC 3 December 1980. ....	157
Fig. 5.25. A schematic diagram of the horizontal deformation process.....	160
Fig. 5.26. Time series of geopotential height tendency describing the deformation process. ....	161
Fig. 5.27. The 372 mb horizontal deformation component analysis at 1200 UTC 1 December 1980.....	163
Fig. 5.28. The 372 mb horizontal deformation component analysis at 1200 UTC 2 December 1980.....	164
Fig. 5.29. The 372 mb horizontal deformation component analysis at 0000 UTC 4 December 1980.....	165
Fig. 5.30. Time series of vertical shear deformation process. ....	167
Fig. 5.31. A schematic diagram of the downstream development process. ....	169
Fig. 5.32. Time series of geopotential height tendency describing the downstream development process.....	170
Fig. 5.33. The 372 mb downstream development component analysis at 0000 UTC 1 December 1980. ....	174
Fig. 5.34. A 372 mb hemispheric geopotential height analysis valid at 0000 UTC 1 December 1980.....	175
Fig. 5.35. The 372 mb downstream development component analysis at 1200 UTC 1 December 1980. ....	176
Fig. 5.36. The 372 mb downstream development component analysis at 0000 UTC 3 December 1980. ....	177
Fig. 5.37. Time series of geopotential height tendency due to the combination of the baroclinic, deformation and downstream development processes.....	179
Fig. 5.38. Time series of geopotential height tendency due to the residual process.....	180
Fig. 5.39. Time series of geopotential height tendency due to the non-deformation advection. ....	182
Fig. 5.40. Times series of geopotential height tendency due to the combination of the three one-way processes.....	183

## CHAPTER I

### INTRODUCTION

The purpose of this research is to develop and apply a quantitative method to describe the dynamics of middle-to-upper tropospheric mobile troughs, or “short-waves”. This purpose implies a detailed definition or description of midtropospheric mobile troughs exists. A review of recent and past literature reveals a general lack of information directly related to midtropospheric mobile troughs. There are numerous references, both observational and theoretical, to Rossby waves, baroclinic waves, quasi-persistent long-waves and the relationship of these waves to cyclogenesis. The interest in cyclogenesis and cyclone life cycles is justified because the day-to-day “weather” near the surface is often directly related to the development or decay of cyclones. However, the description of the midtropospheric troughs in these studies, if there is a description, usually focuses on how the trough affects the surface or lower troposphere.

Why has there been a lack of interest in mobile troughs? Is it because we understand, completely, the kinematic and dynamic intricacies of mobile troughs? Hardly. Is it because the mobile troughs are self-sustaining and isolated from the surface weather phenomena? Not so. In fact, it is now generally accepted knowledge that most, if not all, cases of surface cyclogenesis are somehow related to a precursor midtropospheric trough (Petterssen 1955, Petterssen and Smebye 1971). What dynamical processes initiate and maintain the troughs long enough for them to interact with, or generate, the surface cyclone?

Baroclinic instability and baroclinic processes have often been attributed as the “cause” of midtropospheric waves due to the relationship between the simple, normal mode baroclinic models and the observed atmospheric waves (Eady 1949 as referenced in Hoskins et al. 1985, Charney 1947). Is this always true? Do mobile troughs always form in areas considered baroclinically active? What other mechanisms, if any, play in the formation and maintenance of mobile troughs?

---

The journal model for this dissertation is the *Journal of Atmospheric Science*.

These questions related to mobile troughs are difficult to answer given the traditional diagnostic tools, such as energy conversion (Plumb 1983, Dole and Black 1990, Black and Dole 1993). Recent work by Orlanski and Sheldon (1993) and Nielsen-Gammon (1995), using nontraditional techniques, suggest other mechanisms besides baroclinic processes could be important to trough development. The diagnostic tool developed in this research is based on the quasigeostrophic approximation. The technique includes numerous simplifications to the actual atmosphere, and therefore can only identify gross processes participating in the life cycle of mobile troughs. However, the nature of the quasigeostrophic simplifications allows quantitative assessment of the development processes.

The body of this dissertation focuses on diagnosing midtropospheric mobile trough development from a potential vorticity perspective. The application of traditional diagnostic approaches, such as calculating energy conversion between the basic state and eddies upon the basic state, is not included here. The energetic analyses are useful in examining the consistency between the observed evolution of a tropospheric-deep event and the predicted evolution based on a physical model of the conversions. However, the energetic analyses may not be useful in discriminating between the specific mechanisms responsible for the conversion of energy.

For example, baroclinic instability has been described as an exchange of energy from the available potential energy of the basic state to the potential energy of the eddies and then to the kinetic energy of the eddies. If the flow of energy follows the baroclinic path and the midtropospheric mobile trough is amplifying, then one might conclude baroclinic instability was occurring. However, there may be additional mechanisms present that contribute to the conversion of energy to the eddies; for example, the vertical superposition of two separate eddies would likely contribute to this energy conversion. In a pure sense, baroclinic instability requires the intensification of both upper and lower disturbances. The information required to delineate the baroclinic and superposition processes is not available by energy conversion calculations alone.

The potential vorticity diagnostics introduced in this research provide a more fundamental basis for interpreting the dynamics specific to mobile troughs. The individual components responsible for each mechanism can be diagnosed separately. Instead of being the “black-box” approach to diagnosing mobile trough development by energy conversion, the potential vorticity approach allows a simple means to determine the “building blocks” of trough development.

Before delving into the mobile trough development processes, a clear understanding of the characteristics of mobile troughs is required. Chapter II of this dissertation presents an objective method to identify and track mobile troughs throughout the northern hemisphere. The trough climatology presented in this chapter is one of three known studies focused on the climatological behavior of mobile troughs. Sanders (1988) compiled a history of trough life cycles as they propagated along one contour on 500 mb geopotential height analyses over a nine year period. He found the wavelength of the midtropospheric waves varied from 1500 km to 3500 km (wavenumber 19 to wavenumber 8 at 45° N). The average phase speed was  $12 \text{ m s}^{-1}$ . The troughs observed by Sanders are slightly faster than the  $8 \text{ m s}^{-1}$  “short-wave” phase speed calculated using the barotropic Rossby dispersion relationship described in Petterssen (1956) and Palmen and Newton (1969). Sanders also indicated areas of frequent trough genesis and termination. Sanders’ results are comprehensive, but are based on subjective techniques which may be unreliable and difficult to reproduce.

Dean (1993) used an objective trough tracking technique to study the behavior of two or more mobile troughs merging or separating. He focused on the interaction of the troughs, not on the life cycle of the individual troughs.

The objective trough identification and tracking technique described in Chapter II is based on the transport of curvature vorticity. Included in this chapter is a discussion of the theoretical work related to mobile trough dynamics. The climatological results presented in this chapter suggest additional mechanisms beyond baroclinic instability participate in mobile trough development, since trough formation is common in geographical areas not considered baroclinically active.

Chapter III describes the theoretical basis for using a quasigeostrophic (QG), specifically QG potential vorticity (QGPV), diagnostic technique. This chapter provides a detailed argument for using the QGPV form of the geopotential height tendency equation as the primary diagnostic tool used to determine mobile trough development. Included in the discussion is the advantage of the QGPV technique over traditional diagnostic techniques such as the omega equation and the traditional height tendency equation. A discussion of the expected error using QG analyses is presented as it relates to mobile trough diagnostics. The term “QGPV thinking” is introduced to describe the relationship between QGPV and its associated three dimensional geopotential height field.

Chapter IV outlines the method used to calculate the QGPV, and the method used to invert the QGPV and the advection of QGPV to recover the associated geopotential height and geopotential height tendency, respectively. The dynamical reason for using piecewise inversion of QGPV is discussed as it relates to mobile trough development. This chapter includes a definition of the large-scale background flow and the small-scale perturbations superimposed upon this background flow. The small-scale negative anomalies of geopotential height are considered the midtropospheric mobile troughs for this part of the study. Chapter IV forms the foundation for the detailed analysis of a mobile trough to follow in Chapter V.

Chapter V demonstrates the QGPV geopotential height tendency diagnostic technique on one specific case of mobile trough development. The purpose of this chapter is two-fold. First, it will show the practicality of using QGPV thinking as a diagnostic tool for trough intensification. Second, it will quantify three main intensification processes evident in the mobile trough’s life cycle. The results presented in this chapter are consistent with theory, and show unequivocally that baroclinic processes only played a secondary role in the trough’s initial intensification. The primary trough initiation mechanism was due to the transport of kinetic energy through the wave group velocity. This energy transport is referred to as downstream development (Orlanski and Sheldon 1993).

Chapter VI will summarize the major results and conclusions of this research. Included in this chapter is the author’s assessment of using the QGPV technique as a

means to diagnose mobile trough development. The application of the techniques developed here, both the objective trough tracking and QGPV diagnostic, enhance our understanding of mobile troughs. However, many questions remain unanswered. This chapter will suggest areas for additional research using the techniques presented in this dissertation.

## CHAPTER II

### MOBILE TROUGH CLIMATOLOGY

The entire text and figures in this chapter are reproduced from a manuscript accepted by *Tellus* for publication (Lefevre and Nielsen-Gammon, 1995). *Tellus* has copyright privileges to this manuscript, but approved its reproduction for this dissertation only (Appendix 1). The text and figure captions were reformatted and moved into the body of this chapter to meet the requirements of Texas A&M University. The two appendices, originally attached to the manuscript, were also moved into the body of this chapter. The references and acknowledgment were included with the dissertation references and acknowledgment.

#### 1. Introduction

When one examines midlatitude height or pressure fields, one finds a tendency for closed contours at the surface and open, wavy contours near the jet stream level. Synoptic meteorologists use the terms "short wave" and "long wave" to categorize the wave properties. Petterssen (1956, p. 138) stated: "In typical cases one finds about four to five major waves around the hemisphere and these are called the long waves, or Rossby waves, after Rossby who first investigated their principal properties. Superimposed upon these long waves one finds shorter waves (often of quite small amplitudes) traveling through the slowly moving train of long waves." Long waves are quasi-stationary, while short waves are mobile.

The study of mobile troughs is motivated by their abundance in the atmosphere and their relationship to cyclogenesis. Petterssen (1955) noted that cyclogenesis occurs when an area of upper-level positive (cyclonic) vorticity advection associated with a pre-existing trough becomes superimposed over a low-level baroclinic zone. Petterssen and Smebye (1971) called this form of cyclogenesis "Type B" to distinguish it from the traditional description of an instability growing simultaneously from small amplitude at upper and lower levels (Type A). Sanders (1986) and others have found that Type B cyclogenesis is predominant, and even the existence of Type A cyclogenesis is questioned by some.

Despite the crucial role played by upper-level mobile troughs in cyclogenesis, few have studied the observed development and maintenance of mobile troughs. The only published synoptic climatology of upper-level mobile troughs in the northern hemisphere was by Sanders (1988, hereafter S88), who subjectively tracked bends in the 500 mb 552 dam geopotential height contour. He found that the median life span of mobile troughs was 12 days, with one "hero" lasting for 57 days and traveling twice around the northern hemisphere. The average phase speed of the troughs was estimated at  $14.3^\circ$  longitude per day, which corresponds to  $12 \text{ m s}^{-1}$  at  $40^\circ \text{ N}$ . Trough genesis occurred more often over land, usually over and downstream of major mountain barriers, and most troughs terminated over oceans.

The S88 study has helped spawn theoretical interest in upper-level mobile troughs. Recent studies include Staley (1988), Snyder and Lindzen (1988), Whitaker and Barcilon (1992a), Whitaker and Barcilon (1992b), Rivest et al. (1992), and Rivest and Farrell (1992). Ideas range from localized baroclinic instability to quasi-neutral modes triggered by favorably-configured initial disturbances. Also relevant to the problem of mobile trough generation is recent work by Orlanski and Katzfey (1991), Chang (1993), Orlanski and Chang (1993), and Orlanski and Sheldon (1993) showing that upper-level mobile troughs can be generated by the transfer of energy from upstream baroclinically-growing cyclones.

The S88 study suffers from two serious shortcomings. First, because the tracking algorithm is based on subjective, qualitative criteria, the results are sensitive to the person doing the tracking. It is possible that troughs may be sustained by a subjective bias toward continuity. Second, because troughs were required to exist on the 552 dam contour, the climatology is strongly weighted toward midlatitude mobile troughs and cannot distinguish between a trough which forms on the 552 dam contour and a trough which moves toward the 552 dam contour from higher or lower latitudes.

The purpose of the present study is to produce a synoptic climatology of upper-level mobile troughs over the northern hemisphere using an objective trough tracking algorithm.



Results will be compared to S88 and to the characteristics of cyclones and bandpass wave activity.

## 2. Data

The 500 mb data used in this study consisted of National Meteorological Center (NMC) 12-hourly gridded analyses for the period 1969 through 1988. The data, taken from CD-ROM (Mass et al. 1987), is on the NMC Octagonal Grid, a polar stereographic projection centered at the North Pole. The grid spacing varies from approximately 450 km at the pole to approximately 200 km at the equator. We focus on 500 mb to allow direct comparison with S88, and because the 500 mb level has been demonstrated to be an ideal single level for identifying upper-tropospheric mobile troughs that affect the lower troposphere.

## 3. Method

### *a. Objective trough identification*

The tracking of specific surface-based disturbances is typically performed by following specific pressure minima. The pressure extremum must attain a specific threshold amplitude, measured by the number of closed contours surrounding the minimum, and the tracking may be performed either subjectively (e.g., Petterssen, 1956; Zishka and Smith, 1980) or objectively (e.g., Alpert et al., 1990, Sinclair, 1994).

At 500 mb, vorticity would seem to be a natural choice, since synopticians often use vorticity to subjectively track troughs. Dean (1993) has tracked vorticity maxima to study trough mergers and fractures. However, this technique fails for the simple dynamical case of a one-dimensional barotropic Rossby wave propagating along a shear zone on an  $f$ -plane. No maxima or minima of vorticity can exist, despite the possibility of high-amplitude troughs with large positive vorticity advection (PVA) downstream.

Relative vorticity may be subdivided in natural coordinates into shear vorticity and curvature vorticity:

$$\zeta_g = -\frac{\partial V_g}{\partial n} + \frac{V_g}{R_s} \quad (2.1)$$

In the (2.1)  $\zeta_g$  is geostrophic relative vorticity,  $V_g$  is the magnitude of the geostrophic wind,  $n$  is a distance measured in the direction normal to the flow, and  $R_s$  is the radius of curvature of the geostrophic flow. The use of curvature vorticity to identify troughs would potentially circumvent the problem discussed above. However, it was found that curvature maxima often corresponded to closed, stationary circulation centers, or were located well poleward of the jet core where the strongest PVA would be occurring.

Both difficulties are avoided if the geostrophic curvature vorticity is multiplied by the magnitude of the geostrophic wind. This produces a quantity which may be called Eulerian Centripetal Acceleration, or ECA:

$$ECA \equiv \frac{V_g^2}{R_s} \quad (2.2)$$

One interpretation of ECA is as the centripetal acceleration experienced by an air parcel following the instantaneous geostrophic streamlines. It can also be interpreted as the transport of curvature vorticity by the geostrophic wind, which would be located just upstream of regions of PVA. However, a dynamical interpretation is unnecessary; the purpose of (2.2) is to define a quantity whose maxima at 500 mb correspond one-to-one with those features a synoptician would subjectively identify as mobile troughs.

The use of a quasi-conserved quantity, such as Ertel's potential vorticity (PV) or quasigeostrophic potential vorticity, for tracking troughs was considered and rejected. Since Rossby waves propagate along PV gradients, a given wavelike mobile trough cannot be tracked by following a particular air parcel with anomalously high PV. Also, a given trough may be associated with a PV anomaly at one level or several levels. However, the use of ECA provides a measure of trough significance, since a given PV anomaly must be sufficiently strong to affect the geostrophic wind field at 500 mb to be identified as a trough.

In Fig. 2.1, ECA maxima are compared to the 500 mb geopotential height field and to troughs on the 552 dam contour as identified and reported by S88. It is readily seen that troughs are rarely of maximum intensity along the 552 dam contour, based upon either ECA maxima or subjective interpretation. However, there is a one-to-one

correspondence between 552 dam contour curvature maxima and nearby ECA maxima with magnitudes of  $3.5 \times 10^{-4} \text{ m s}^{-2}$  or greater. For example, trough "K" over the central Atlantic Ocean is associated with a mobile trough whose maximum intensity is marked by ECA as being near the 540 dam contour. Thus, ECA can serve as a marker for the same troughs which S88 tracked as curvature maxima on the 552 dam contour. A critical advantage of ECA, though, is that it allows troughs to be followed even when they move north or south away from the 552 dam contour. Numerous intense troughs, such as the one over the British Isles or the southwestern United States, are captured by ECA but were missed by the S88 method.

*b. Trough tracking*

The mobile trough tracking portion of this technique evolved from an algorithm developed by Dean (1993) and was based on the premise that 500 mb mobile troughs can loosely be regarded as being steered by the 500 mb flow. The motion of a progressive Rossby wave, for example, would be due to the combination of the advective velocity and a smaller propagation velocity. Therefore, one would expect to find a given trough some distance downstream twelve hours later.

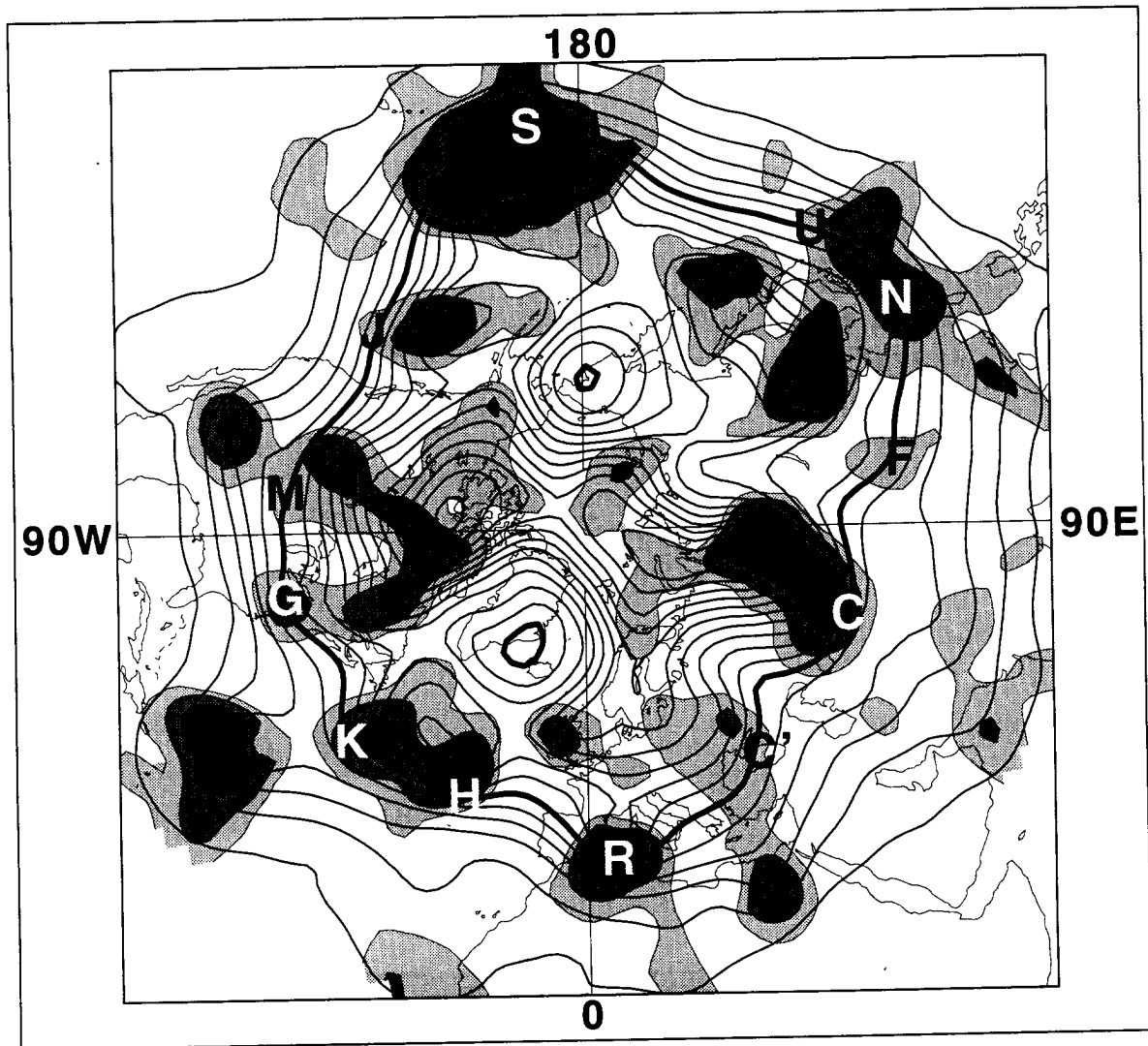


Fig. 2.1. A 500 mb geopotential height (contours every 6 dam) and ECA (in units of  $10^{-4} \text{ m s}^{-2}$ ) analysis for 0000 UTC 22 February 1986. The trough labels correspond to Sanders (1988). The thick contour is the 552 dam contour. The regions with ECA greater than or equal to  $1 \times 10^{-4} \text{ m s}^{-2}$  are shaded. The shading corresponds to contours of 1, 4, 10 and  $30 \times 10^{-4} \text{ m s}^{-2}$ , respectively.

The tracking algorithm proceeds through a sequence of twelve-hourly 500 mb height analyses in chronological order, computing the geostrophic wind and ECA. At each analysis time, the gridded ECA data is searched for the occurrence of positive maxima of ECA, defined as a grid point whose ECA is larger than any of the eight surrounding grid points. Each potential maximum is then passed through a second check, which compares the ECA magnitude at the grid point to the magnitude of ECA in a circle surrounding the grid point at a radius equal to the grid spacing. The magnitude of the ECA along the circle was determined using bilinear interpolation. To be retained as a maximum the central value must be  $1.0 \times 10^{-4} \text{ m s}^{-2}$  greater than the ECA on at least 65 percent of the circumference of the circle. In essence, a significant trough is one whose ECA is greater than  $1.0 \times 10^{-4} \text{ m s}^{-2}$ , and is at least  $1.0 \times 10^{-4} \text{ m s}^{-2}$  greater than the immediately adjacent area.

The threshold used in this study was based on a comparison between the objective method and subjectively analyzed 500 mb geopotential height charts. A lower threshold would include random, disorganized vorticity variations within areas of very weak flow, and a higher threshold would unnecessarily delay genesis events and speed termination events.

For each new maximum, the algorithm loops through all troughs present at the previous analysis time, using a method adapted from Dean (1993). A mean vector geostrophic wind is computed from the geostrophic wind at the location of the new maximum and the geostrophic wind at each previous trough location. This wind is used to compute a hypothetical motion for each previous trough. If the location of the new maximum agrees with the "expected" location of any previous trough, a "hit" is recorded. After performing this calculation for all preexisting troughs, the following possibilities exist:

- 1) No hits were recorded. The maximum is designated a new trough, and its position is recorded as a genesis event.
- 2) One hit was recorded. The maximum is deemed to be the current position of the trough which recorded the hit. The track information for that trough is updated.

- 3) One hit was recorded, but with a trough which had already been tracked onto the current analysis. This event is considered a splitting (fracture) trough. The maximum is designated a new trough, its genesis location is assigned to be the previous position of the trough which recorded the hit, and the current position of the new trough is the current position of the maximum.
- 4) Two or more hits were recorded, but all were with troughs which had already been tracked onto the current analysis. The trough for which the first hit was found is deemed to have been the splitting trough, and the tracks are handled as in case 3.
- 5) Two or more hits were recorded, with at least one of the troughs not yet tracked onto the current analysis. The maximum is deemed to be the current position of the as-yet-untracked trough with the longest lifespan of all such troughs recording a hit. The track information for that trough is updated.

After all maxima have been compared with the previous positions of trough tracks, there are typically one or more trough tracks which failed to be connected with a maximum in the current analysis. Similarly, there may be one or more trough tracks originating in the current analysis, according to case 1. A final search is performed to see if any trough genesis events took place near the expected position of a trough which has terminated. This search covers a larger area than that used in the initial search. Any trough whose termination was followed by a birth twelve hours later sufficiently near its expected position is deemed to have continued its existence; the genesis is negated and the genesis position becomes the trough's current position. In the case of conflict, the trough whose expected position is closest to the genesis event is preferred.

All completed trough tracks are subject to the following additional screening to eliminate weak troughs, short-lived troughs, and subtropical troughs: (1) Any troughs which fail to attain a magnitude of  $4.0 \times 10^{-4} \text{ m s}^{-2}$ , which roughly correspond to the minimum magnitude of an S88 trough, are discarded. (2) Any troughs which fail to travel as far north as  $30^\circ\text{N}$  for at least one day (two 12-hourly maps) are discarded. (3) Any troughs which fail to survive for at least two days (four 12-hourly maps) are discarded.

The term "unscreened trough" will be used to identify all troughs which pass test (3), without regard to tests (1) and (2).

When one or two analyses were missing, the expected advection distance was increased by the appropriate factor, and troughs were tracked across the data gap. However, within the data set were several gaps of three or more consecutive map times, across which it was deemed imprudent to attempt to objectively track mobile troughs. To avoid bias and to ensure that essentially all troughs stored prior to a data gap have a sufficient opportunity to live a full lifespan, any troughs which are generated within fifteen days of such a gap were discarded. Also, since their times and places of births were unrecorded, any troughs which existed on the first analysis following a gap of three or more consecutive analysis times were discarded. As a result of the gaps and the measures taken because of them, troughs which formed on 4.7% of the days within the 20-year period are missing from this climatology. All event frequencies presented below have been corrected for this shortfall.

The authors validated the ECA trough tracking technique by comparing the ECA results over two weeks to subjective tracks constructed by several volunteer analysts. The ECA results compared favorably with the subjective results. The ECA method typically initiated and terminated mobile troughs with one 12-hour time period of the subjective analyses. There did not seem to be an overall bias toward truncating or overextending the life span of the troughs. However, four troughs identified by the subjective analyses lasted for the entire two-week period (none of the subjective analyses agreed on all four troughs), whereas only one trough tracked by the objective technique lasted that long. Each segment of the longest ECA track was successfully tracked by the subjective analyses, but the subjective analyses typically split and merged three different troughs to complete the longest ECA track.

### *c. Advection region*

To empirically determine the most probable area within which the trough would be expected to be found, a polar coordinate system is centered on the current location of a

given trough exceeding the mobile trough threshold. For each trough found twelve hours later, the mean geostrophic velocity is computed from the velocity of the new trough and the velocity of the original trough. The position of each new trough is then plotted on the polar diagram relative to the position each trough would have if it had been advected by the mean geostrophic velocity for twelve hours. If this process is repeated for all troughs in the 20-year data set, the result should consist of two contributions: a background trough count which represents the likelihood of finding a trough at any given point at any given time, and a non-random area of higher trough counts which represents the location to which each trough moves in twelve hours.

The resulting plot is shown in Fig. 2.2 with the circular ring at the twelve-hour advective distance and the downstream axis oriented toward the right. It is not surprising to find the highest frequency of mobile troughs at distances less than or equal to the 12-hour advective distance and approximately along the downstream direction. The winter season advection pattern (not shown) was similar to Fig. 2.2, but the summer season pattern (not shown) had more axial variation. The region of enhanced frequency is roughly elliptical, which was the shape of the advection region Alpert et al. (1990) used to objectively track surface cyclones.

To incorporate the advection region in the ECA tracking algorithm, radials extending from the center (origin) were constructed every 15 degrees. A prescribed distance along each radial was used to determine if a point was inside or outside of the advective region.



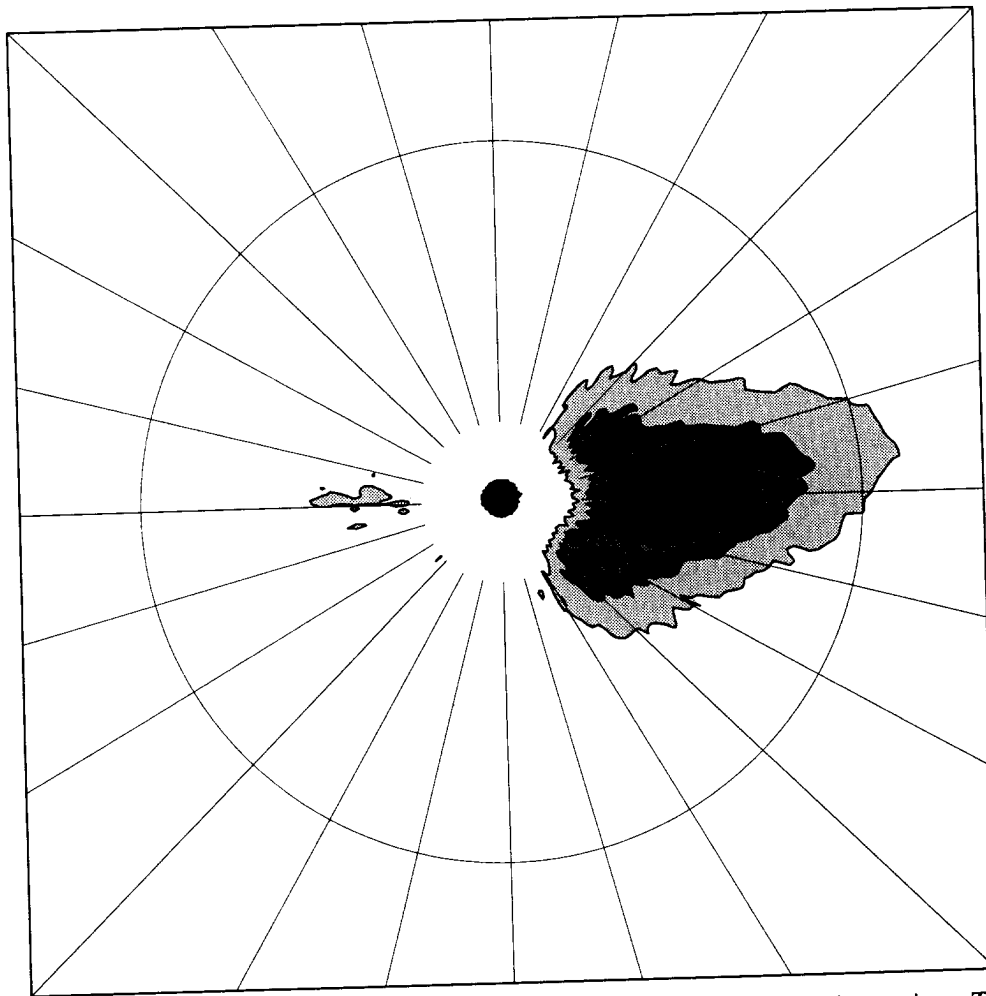


Fig. 2.2. A polar-coordinate schematic showing the shape of the 12-hour advection region. The shaded area depicts the location of the highest 12-hour advection frequency (normalized to  $49,000 \text{ km}^2$ ). The contours represent 350, 600, 800 and 1000 troughs, respectively. The circle identifies the 12-hour advection distance.

*d. Final search for trough connection*

Occasionally, the objective tracking method would terminate one trough and begin another trough twelve hours later in a close proximity of the first trough's termination. Since the objective method did not find the second trough within the 12-hour advection region, it thought the two troughs were separate. We investigated numerous occurrences of these termination-genesis couplets and found it reasonable to connect the new point to the old track. An additional search routine was developed to avoid this type of error, by broadening the search area when a trough terminates.

The final search algorithm searches the area around two key points. The first point is the location of the first trough's termination. The second point is near the center of the advective region downstream of the first trough's termination. To be considered for linkage the genesis must be within 500 km of the first key point or within one 12-hour advective distance of the second point. The trough genesis nearest one of these points is connected to the first trough and the genesis is negated.

#### **4. Trough lifespans**

The lifespan distribution of the 27,469 mobile troughs satisfying the criteria listed in Section 3 is shown in Fig. 2.3. Here, lifespan (in days) is half the number of consecutive twelve-hourly analyses on which a given trough was identified, and, in the case of a one or two analysis data gap, the number of analyses on which the trough was presumed to have existed. The average lifespan of a mobile trough was 5.3 days, and the median lifespan was 4 days. The seasonal variation of mean trough lifespan was insignificant. The winter and summer mean lifespans were 5.2 days. The spring mean lifespan was 5.3 days, and the fall was 5.4 days.

The distribution in Fig. 2.3 closely approximates a geometric distribution. The probability that a particular trough will cease to exist on the next analysis is 0.13 and is independent of how long that trough has existed so far. It therefore appears that upper-level mobile troughs are not subject to a life cycle of growth and decay of some typical length.

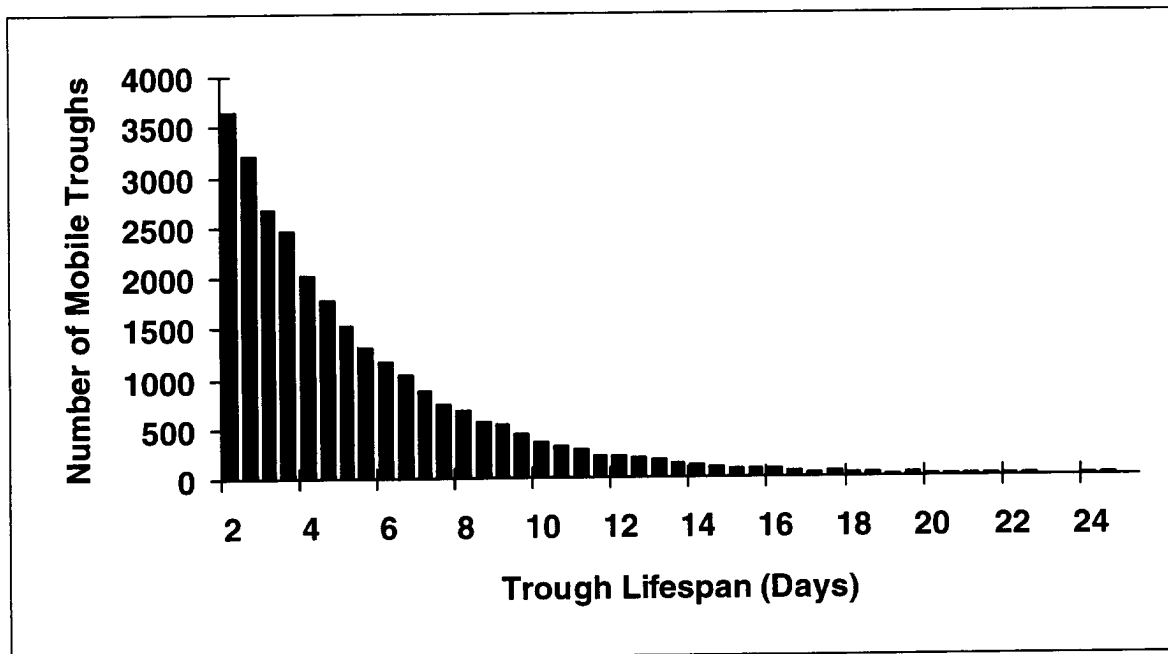


Fig. 2.3. Histogram of trough lifespan. The mean lifespan was 5.3 days, and the median was 4 days.

The lifespan of mobile troughs does depend on the place of birth of mobile troughs. For example, there is a strong dependence on latitude. Troughs forming near the pole exist for an average of four days, while troughs forming near  $40^{\circ}\text{N}$  exist for an average of six days. It is not known whether this effect is real or a consequence of the polar stereographic grid, which has a finer grid spacing at the equator. The smaller-scale troughs that form and remain closer to the equator can be resolved better than the smaller-scale troughs near the pole.

## 5. Comparison with Sanders' hero

Fig. 2.3 is in conflict with the S88 climatology. The S88 troughs had a median duration of twelve days. In his six-month sample, Sanders identified five troughs which lasted 45 days or longer. In contrast, the longest-lived trough tracked by the objective method through twenty years of analyses lasted just 44 days. Although the objective method has been shown to identify features which are closely related to the S88 troughs, the difference between single-contour subjective tracking and objective tracking by ECA yields vastly different trough histories and lifespans.

To better understand the difference between objective and subjective tracking, the life history of the longest-lived trough in the S88 climatology (his trough "M") was examined with respect to the objective tracking of features associated with it. It was found that, although an objectively-tracked mobile trough could almost always be identified with the S88 trough, fourteen different objectively-identified mobile troughs participated in its lifespan. In our opinion, of the thirteen discrepancies, the ECA objective tracking was superior in ten instances, the S88 subjective method was superior in one instance, and neither method was satisfactory in the remaining two. Two examples are presented below to illustrate the nature of the problem of trough tracking and to allow the reader to develop his or her own interpretation of the performance of each method.

Fig. 2.4 is a series of maps of 500 mb geopotential height and absolute geostrophic vorticity for a period one month into the lifespan of the S88 hero trough (which we denote with the letter "S"). In the first map, at 1200 UTC 22 October 1985, trough S is

approaching central Asia. Sanders used only 0000 UTC analyses for this and other tracks; 1200 UTC analyses were not available to him for central Asia. The 1200 UTC plotted positions of the S88 trough have been interpolated from the 0000 UTC positions.

The ECA method identifies two mobile troughs in the map domain at 1200 UTC 22 October 1985. One, trough A, has been associated with trough S for about two days. The other, trough B, is exiting the domain to the east. Both troughs are associated with along-stream maxima of geostrophic vorticity, with positive vorticity advection (PVA) ahead and negative vorticity advection (NVA) behind.

Twelve hours later, the region of PVA associated with trough A has become more elongated, and according to the objective method, trough A has split. The southern ECA maximum continues the track; the northern maximum, near 60°N, 95°E, is not assigned a letter because it failed to persist for two days and therefore never became an official trough. The square brackets indicate that trough A terminates on this map and could not be identified twelve hours later. Upstream, the parentheses indicate the location of birth of trough C. Trough C's birth appears to be of a common type: a closed vorticity center becomes elongated, with the original trough moving off to the northeast and a new trough forming in northwesterly flow behind it. While trough C is barely detectable at first, it eventually intensifies and satisfies the ECA strength criterion by 0000 UTC 24 October 1985. At that time, trough S is consistent with the position of trough C.

On the final map, at 0000 UTC 25 October 1985, trough S is collocated with a brand-new objectively-tracked trough, trough E. Trough C appears to have maintained good continuity as it moved off to the northeast, away from the 552 dam contour.

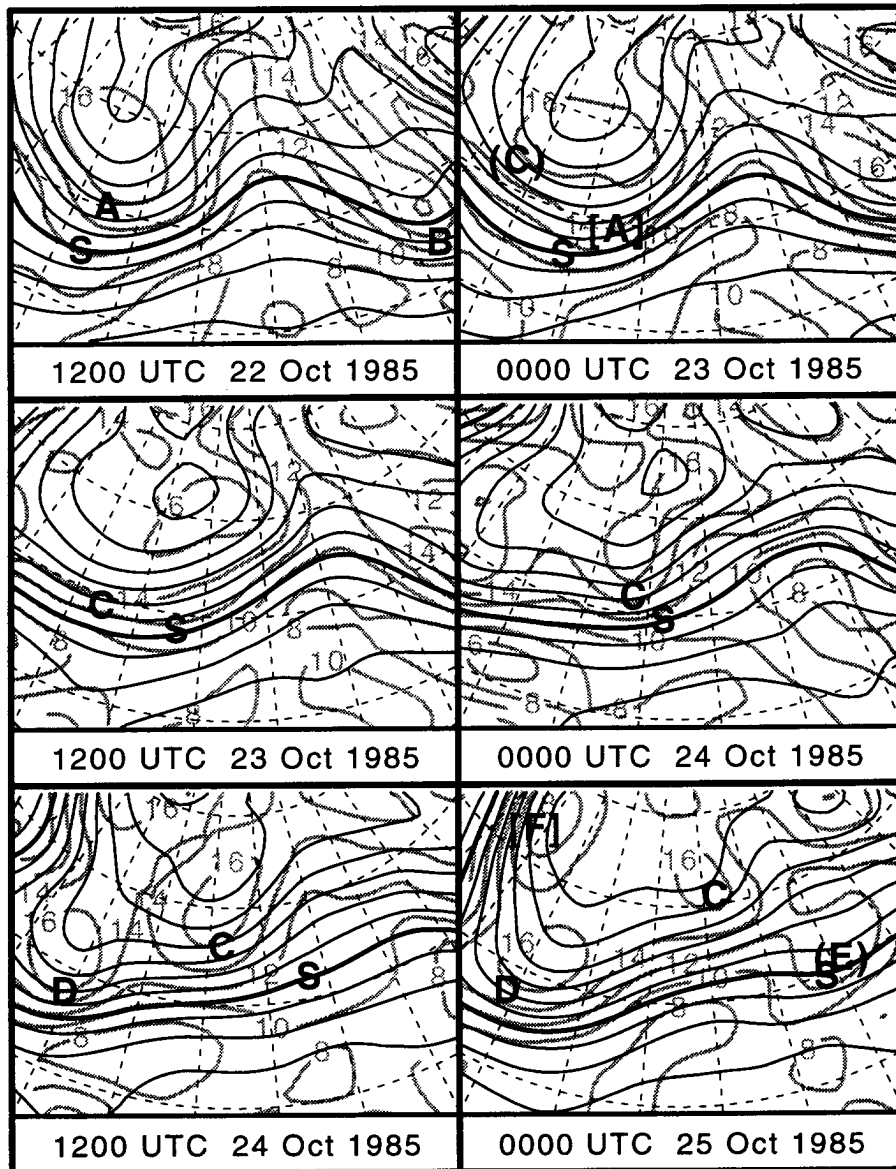


Fig. 2.4. Comparison of S88's longest-lived trough ("S") with objectively-tracked mobile troughs ("A" through "F"), 1200 UTC 22 October 1985 through 0000 UTC 25 October 1985. Height is contoured in black with an increment of 6 dam and absolute geostrophic vorticity is contoured in gray with an increment of  $2.0 \times 10^{-5} \text{ s}^{-1}$ . The thick black contour identifies 552 dam geopotential height. The square brackets, [ ], indicate the trough terminated at this map time. The parentheses, ( ), indicate the trough formed at this map time. Latitude and longitude lines (dashed) are at  $10^\circ$  increments; the center bottom latitude and longitude are  $40^\circ\text{N}$  and  $85^\circ\text{E}$ , respectively.

It appears that the objective ECA method has correctly identified the split and death of one trough and the birth of two others, events which were undetected by the S88 method. This process, in which one trough moves to the north or weakens while a new trough forms to its west, seems to have been a common source of error in the subjective method. In this instance, it is possible that the original trough A weakened as it approached the central Asian highlands and redeveloped as trough E on the lee slopes. However, as no continuous vorticity feature is detectable by eye during this hypothesized transit, it would be difficult to justify the statement that the 500 mb trough remained in existence during the transit.

The second example (Fig. 2.5) is taken from early in trough S's lifespan, as it first crossed the dateline. At 0000 UTC 7 October 1985, trough S is associated with the very intense trough I, which has just wrapped up and is undergoing north-south elongation. The objective method again splits the trough, with the southern lobe terminating at 0000 UTC 8 October 1985 near trough S and the northern lobe (unmarked, because it was short-lived) terminating twelve hours later. Meanwhile, a second region of strong PVA develops upstream, near 172°W at 1200 UTC 8 October 1985.

The objective method identifies this second region with the continuation of trough G. An alternative interpretation is that trough J, which supposedly split from trough G, is legitimately the continuation of trough G, and that the second region of PVA is actually a new trough. However, this PVA is not associated with the original trough I; that trough, and the PVA ahead of it, can be tracked from 180° at 1200 UTC 7 October 1985 to 170°W at 0000 UTC 8 October 1985 and to 160°W at 1200 UTC 8 October 1985. We conclude from this example that the S88 tracking was in error, and that the objective method selected one of the two available interpretations consistent with the data.

These two examples are representative of situations in which the objective method can have difficulty: a trough passing over high orography, a trough approaching a stationary region of anticyclonic curvature (not shown), and a trough splitting. We believe that the objective method tended to arrive at a defensible solution in most cases, while the S88 method clearly failed to track mobile troughs properly.

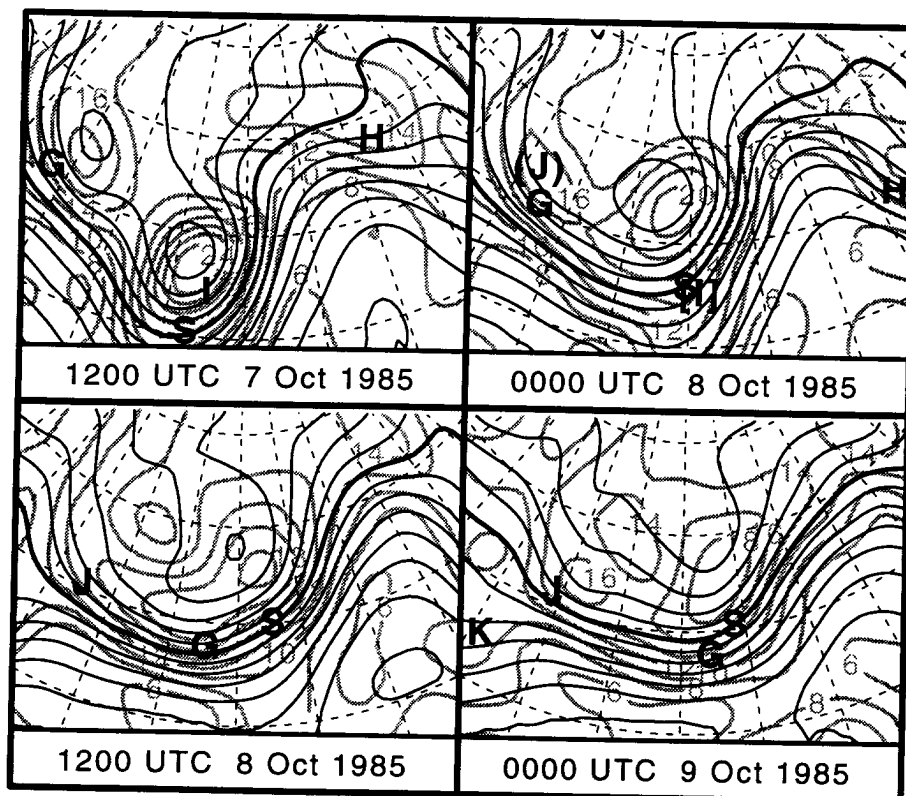


Fig. 2.5. Comparison of S88's longest-lived trough ("S") with objectively-tracked mobile troughs ("G" through "K"), 0000 UTC 7 October 1985 through 1200 UTC 8 October 1985. Heights, absolute vorticity, and trough labels are as in Fig. 3. Latitude and longitude lines (dashed) are at 10° increments; the center bottom latitude and longitude are 40°N and 170°W, respectively.



Notice that, in Fig. 2.5, a succession of troughs with an average wavelength of 1500-2000 km are tracked by the ECA method through a long-wave stationary trough. The use of the NMC Octagonal Grid analyses forces an effective short-wavelength cutoff for mobile troughs, since features with wavelengths shorter than about 1000 km cannot be represented in the analyses. Conversely, the use of a vorticity-based identification tool effectively eliminates long-wavelength features such as the stationary trough.

The life history of the longest-lived objectively-tracked trough was also closely examined. It was found that the objective technique appeared to switch from one trough to another three times during the 44-day track. During 30 consecutive days of tracking, the objective and subjective tracks agreed, so it seems likely that mobile troughs can survive as entities for a month or longer.

## 6. Inhomogeneities in the tracking statistics

Fig. 2.6 is a graph of mean unscreened trough lifespan as a function of time. In this figure, all troughs tracked for at least two days are included, whether or not they achieved minimum intensity or existed north of 30°N. While one might expect, or hope, that the trough statistics would remain stable from year to year, there is a strong tendency for longer-lived mobile troughs during the latter years of the 20-year dataset. At several points, there appear to be large, abrupt shifts in the mean lifespans.

The three largest discontinuities correspond to three of the seven changes made in the final analysis procedures at NMC during this period (Dey, 1989; Shuman, 1989). In September 1974, NMC switched from a Cressman analysis scheme to a Hough analysis. At that time, mean lifespans increased from 4.0 days to 4.3 days, and an apparent annual cycle in mean lifespan was eliminated. In September 1978, the Hough analysis was dropped in favor of optimal interpolation, and mean lifespans dropped back down to 4.0 days. Finally, in May 1980, the assimilation model was changed from a nine-layer finite-difference model to a twelve-layer spectral model, and mean lifespans increased to 4.7 days.

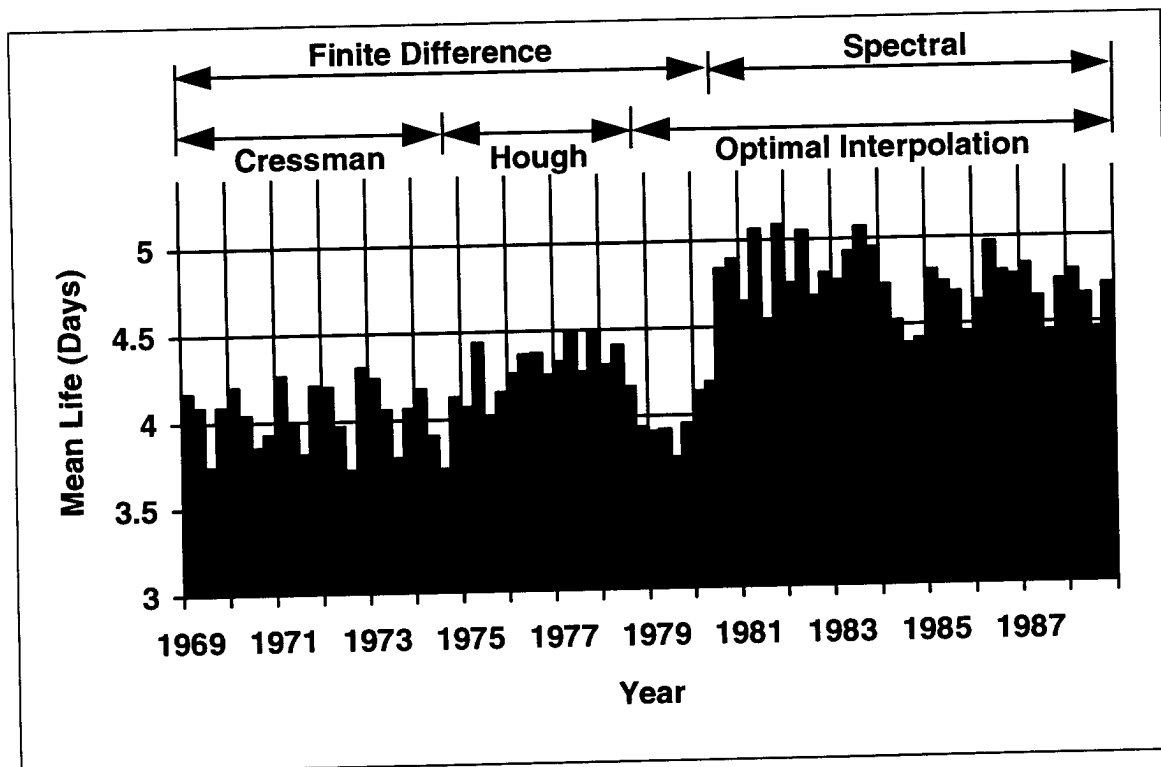


Fig. 2.6. A graph of mean lifespan of unscreened troughs (in days) versus time. Each column represents three months. The labels at the top identify the different procedures used by the National Meteorological Center (NMC) for the analyses. Note the seasonal variation within each year and the obvious differences in mean trough lifespan as the numerical analysis scheme changed.

Despite the inhomogeneities in the characteristics of the data set, the geographical distribution of mobile troughs and their genesis and termination locations remained remarkably stable in middle and high latitudes. Figs. 2.7 and 2.8 compare the frequency of occurrence of objectively-tracked unscreened mobile troughs on twelve-hourly analyses for the periods before and after the switch from a finite-difference model to a spectral model. Note that Figs. 2.7 and 2.8 are not a climatology of trough tracks, and will be biased against regions where the mean flow is stronger and troughs tend to be farther apart, such as the North Pacific. Figures 2.7 and 2.8 may be compared directly to cyclone frequencies such as those shown by Petterssen (1956).

Both maps share regions of high trough frequency over the North Pacific, North America, and North Atlantic. The consistency over the oceans is reassuring, and suggests that the presumed poorer quality of the early oceanic analyses has not seriously biased the statistics. Areas of low trough frequency correspond very closely to areas with the highest orography: the Tibetan Plateau, Greenland, and the Rocky Mountain Cordillera. These low-frequency areas will also appear as unlikely locations for trough genesis or termination.

Lower latitudes are dominated by regions of localized frequency maxima, which generally are much more prominent in the earlier portion of the dataset. These areas include the Mediterranean, northern India, and southeastern Asia. These are plausible areas for the existence of mobile troughs, but the relative frequency of mobile troughs there is sensitive to the analysis technique and therefore cannot be established in this study. We presume that the more recent analyses are more reliable.

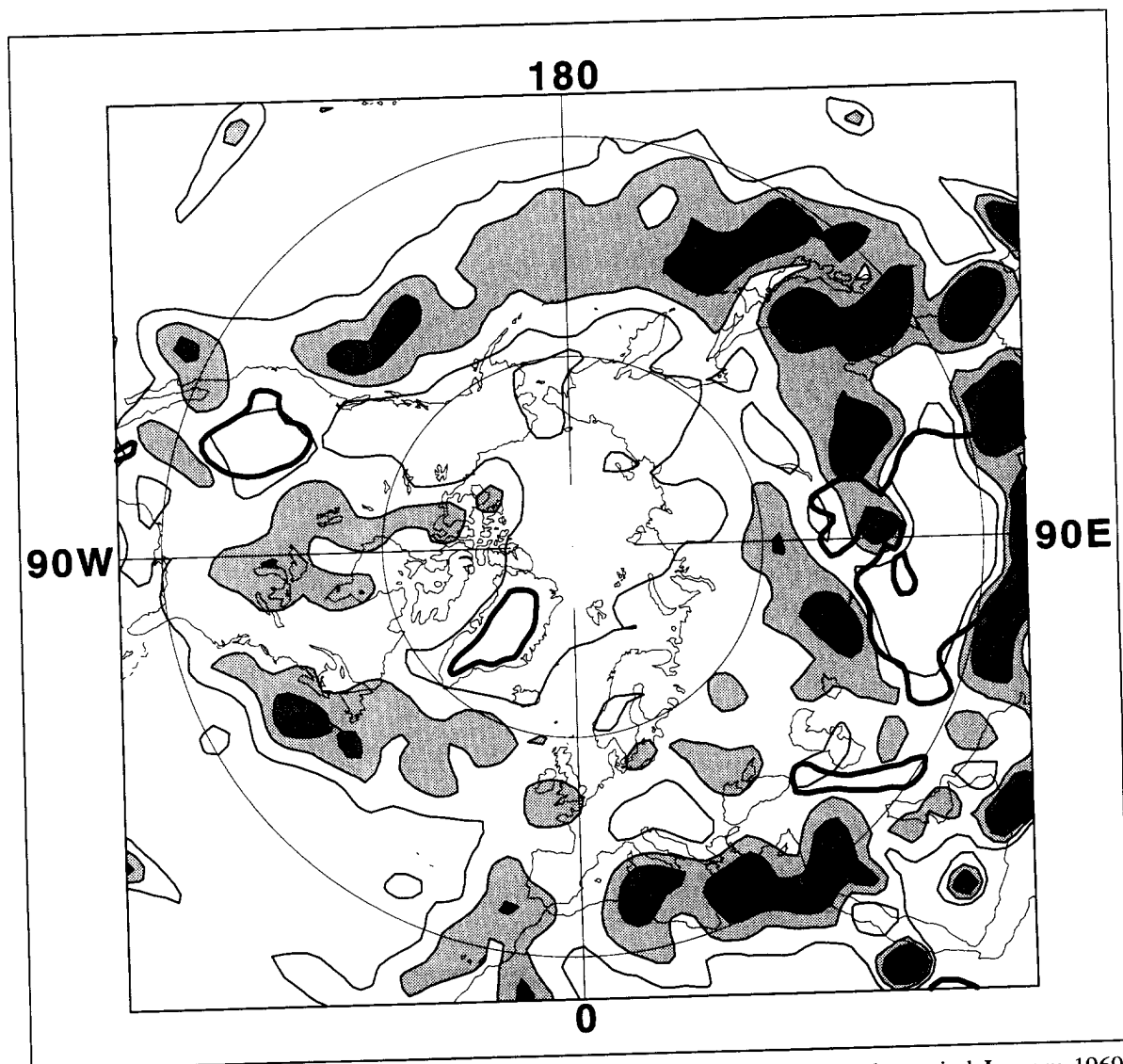


Fig. 2.7. Frequency of trough appearance on 12-hourly 500 mb analyses for the period January 1969 through May 1980. The single, unshaded contour is at 100 troughs per  $10^6 \text{ km}^2$  per year. The contour shading represents 140, 180, 220 and 260 troughs per  $10^6 \text{ km}^2$  per year, respectively. The thick contours encircle elevated terrain higher than 2000 meters. The terrain data was taken from the National Meteorological Center's  $2.5^\circ$  resolution data set.

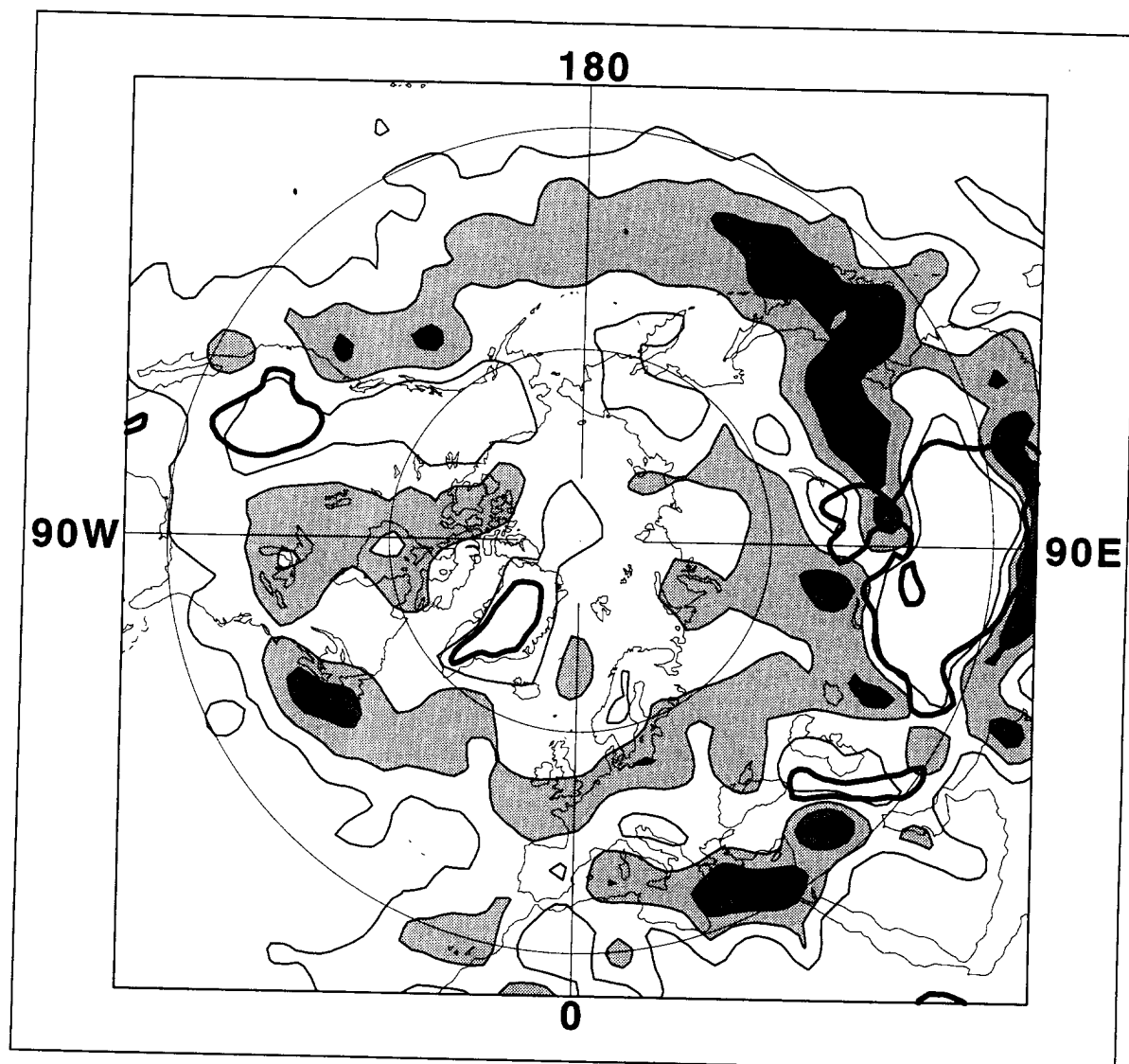


Fig. 2.8. Frequency of trough appearance on 12-hourly 500 mb analyses for the period June 1980 through December 1988. The single, unshaded contour is at 100 troughs per  $10^6$  km<sup>2</sup> per year. The contour shading represents 140, 180, 220 and 260 troughs per  $10^6$  km<sup>2</sup> per year, respectively. The thick contours encircle elevated terrain higher than 2000 meters. The terrain data was taken from the National Meteorological Center's 2.5° resolution data set.

## 7. Trough genesis and termination

The rates of trough genesis and termination over the northern hemisphere throughout the twenty-year data set are shown in Figs. 2.9 and 2.10. The three most favored regions of mobile trough genesis (Fig. 2.9) are over eastern Asia (Mongolia and northeastern China), north-central North America, and the Mediterranean Sea. Genesis events are unlikely over eastern Russia and over major mountain ranges. Two of the preferred regions are upstream of the major oceanic storm tracks (Wallace et al., 1988).

S88 also identified the prominent genesis regions over Asia and North America. However, S88's Asian genesis area does not extend as far east and S88's North American genesis events are farther south. The favored region over the Mediterranean is not captured by S88 because the 552 dam contour rarely extends so far south. We hypothesize that S88's genesis maximum over eastern Europe is a consequence of troughs forming over the Mediterranean and northern Europe and subsequently affecting the 552 dam contour.

Mobile trough termination events (Fig. 2.10) are very rare in the preferred genesis regions over North America and Asia. The region with the most frequent trough termination is over the eastern Pacific Ocean, upstream from a major mountain barrier. A second prominent termination region traces the western outline of the western Asian massif, composed of the Tien Shan, the Hindu Kush, the Himalayas, and the Tibetan Plateau. The eastern edges of the two termination regions almost exactly coincide with the western edges of the mountain barriers. Both of these termination regions are directly upstream of major genesis regions on the lee sides of these mountains. As seen in Figs. 2.7 and 2.8, relatively few troughs are tracked over these mountainous area. Either the objective method fails to track troughs as they pass over mountain barriers, or a large fraction of troughs which encounter mountain barriers are weakened and destroyed by them. The latter explanation is favored by the localized termination regions on the windward side of mountain ranges and the much broader generation regions beyond the lee.

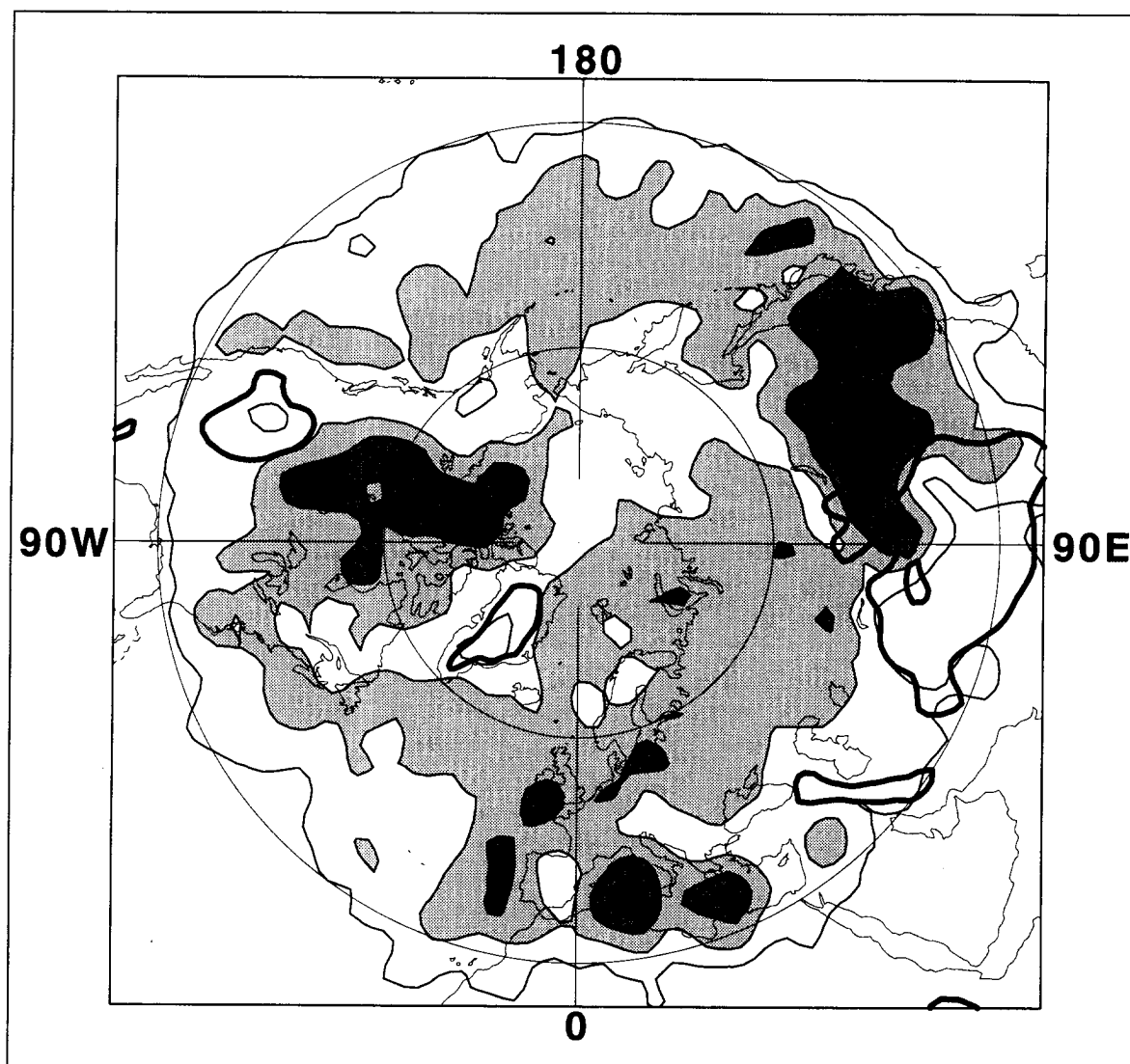


Fig. 2.9. Frequency of trough genesis during all months throughout the twenty year dataset. The solid contour shading represents 10, 15, 20 and 25 events per  $10^6 \text{ km}^2$  per year, respectively. The thick contours encircle elevated terrain higher than 2000 meters.

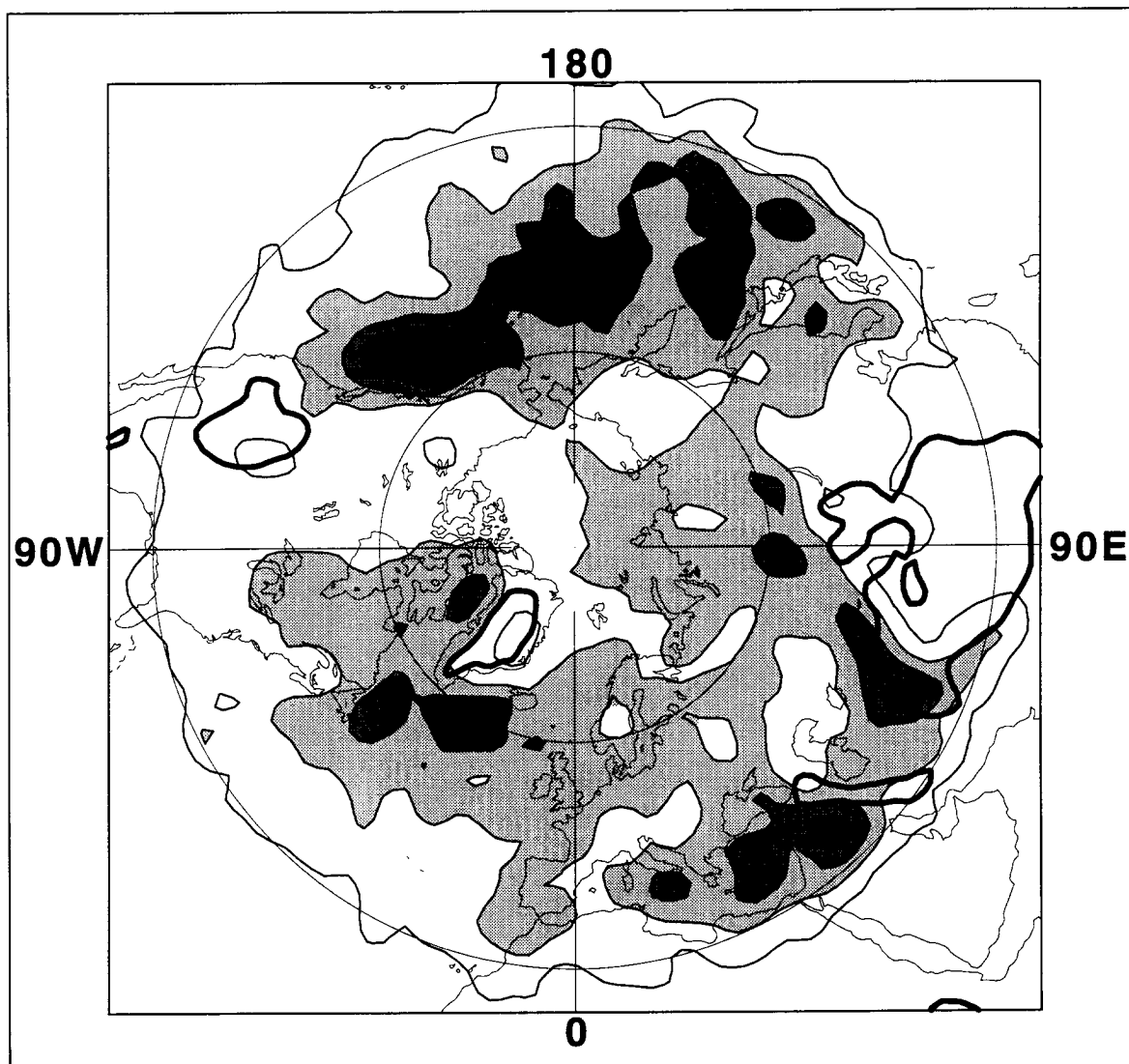


Fig. 2.10. Frequency of trough termination during all months throughout the twenty year dataset. The solid contour shading represents 10, 15, 20 and 25 events per  $10^6$  km<sup>2</sup> per year, respectively. The thick contours encircle elevated terrain higher than 2000 meters.



Undoubtedly, as mentioned in Section 5, some troughs are inappropriately lost as they pass over stationary long-wave ridges, where the large-scale flow is curved anticyclonically. This would contribute to the termination region in the eastern Pacific, as troughs approach the climatological ridge in the geopotential height field along the west coast of North America. Except for an underestimate of termination events at low and high latitudes, the distribution of trough terminations in S88 agrees with the major termination features found here.

Fig. 2.11 shows the excess of genesis events over termination events per year. In general, as found by S88, genesis events are favored over land and termination events are favored over oceans. Trough genesis is preferred upstream of oceanic storm tracks, while trough termination is favored within and downstream of oceanic storm tracks. In addition, an area of preferred termination over western Asia is downstream of an area of preferred genesis over the Mediterranean Sea. Also, genesis events are favored over the extreme eastern Atlantic Ocean and off the southwestern coast of the United States. The eastern Atlantic generation region conflicts with S88, which found that the eastern Atlantic was dominated by a preferred termination region over and west of Europe. A similar pattern was also found by Dean (1993), who performed an objective climatology of 500 mb absolute vorticity centers.

The overall seasonal trough genesis patterns are similar to each other, and with the 20-year genesis patterns. In winter the same prominent areas of genesis (Fig. 2.12) and termination (Fig. 2.13) are found as in the charts including all months (Figs. 2.9 and 2.10). One difference is over the Pacific, where during winter, troughs tend to be generated in a narrow band between 30°N and 45°N. Termination events continue to be broadly distributed over the Pacific, but tend to be farther north than generation events. Also, both genesis and termination activity is enhanced over the south-central United States. The southward migration of trough activity is consistent with the seasonal migration of the strongest westerly winds.

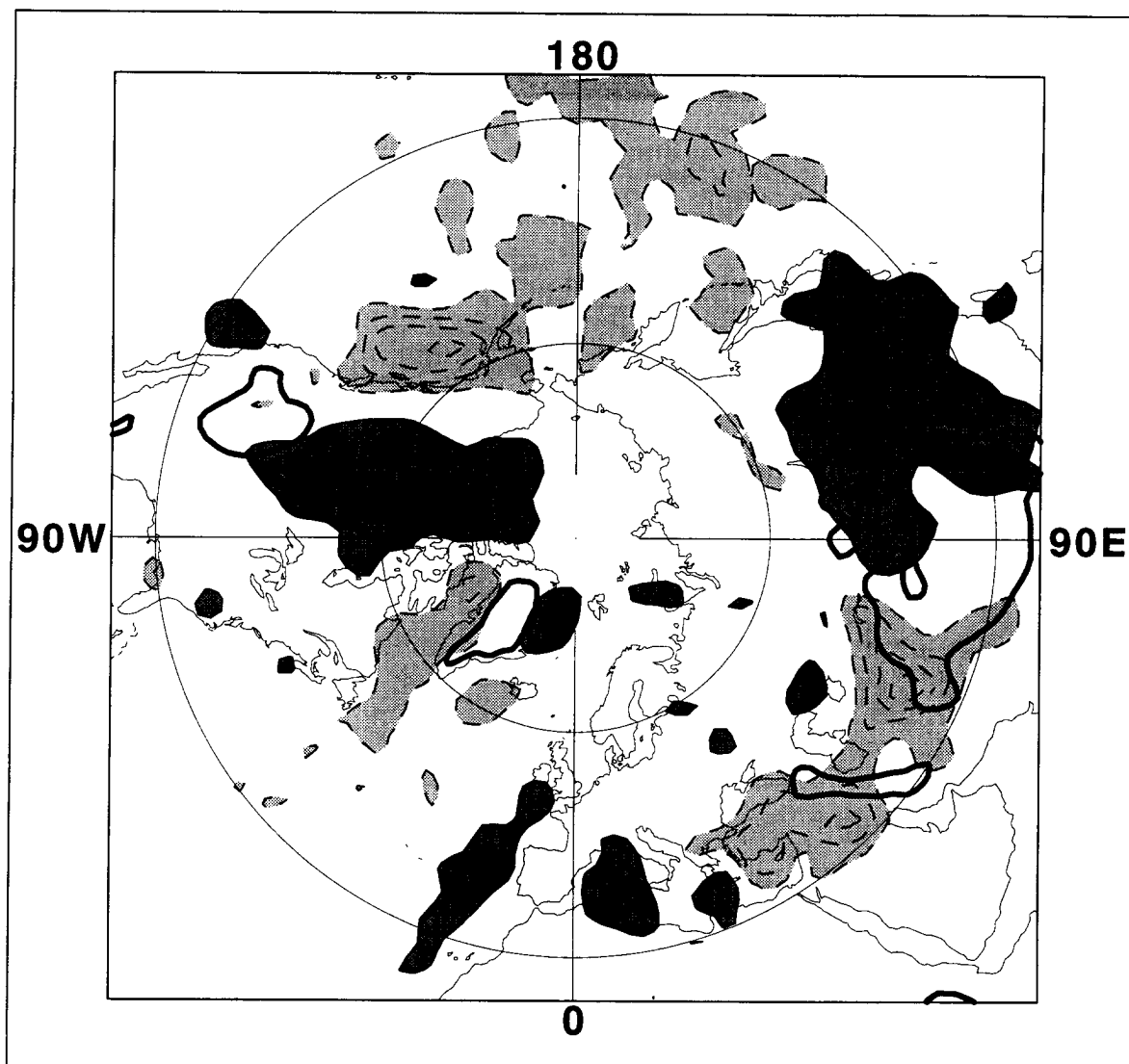


Fig. 2.11. Frequency of trough genesis minus trough termination for all months throughout the dataset. The darker shading and solid contours are areas where genesis exceeds termination. The solid contours represent values of 4, 8, 12 and 16 events per  $10^6 \text{ km}^2$  per year, respectively. The lighter shaded areas and dashed contours are areas where trough termination exceeds genesis. The dashed contours represent values of -4, -8, -12 and -16 events per  $10^6 \text{ km}^2$  per year, respectively. The zero contour is not plotted. The thick contours encircle elevated terrain higher than 2000 meters.

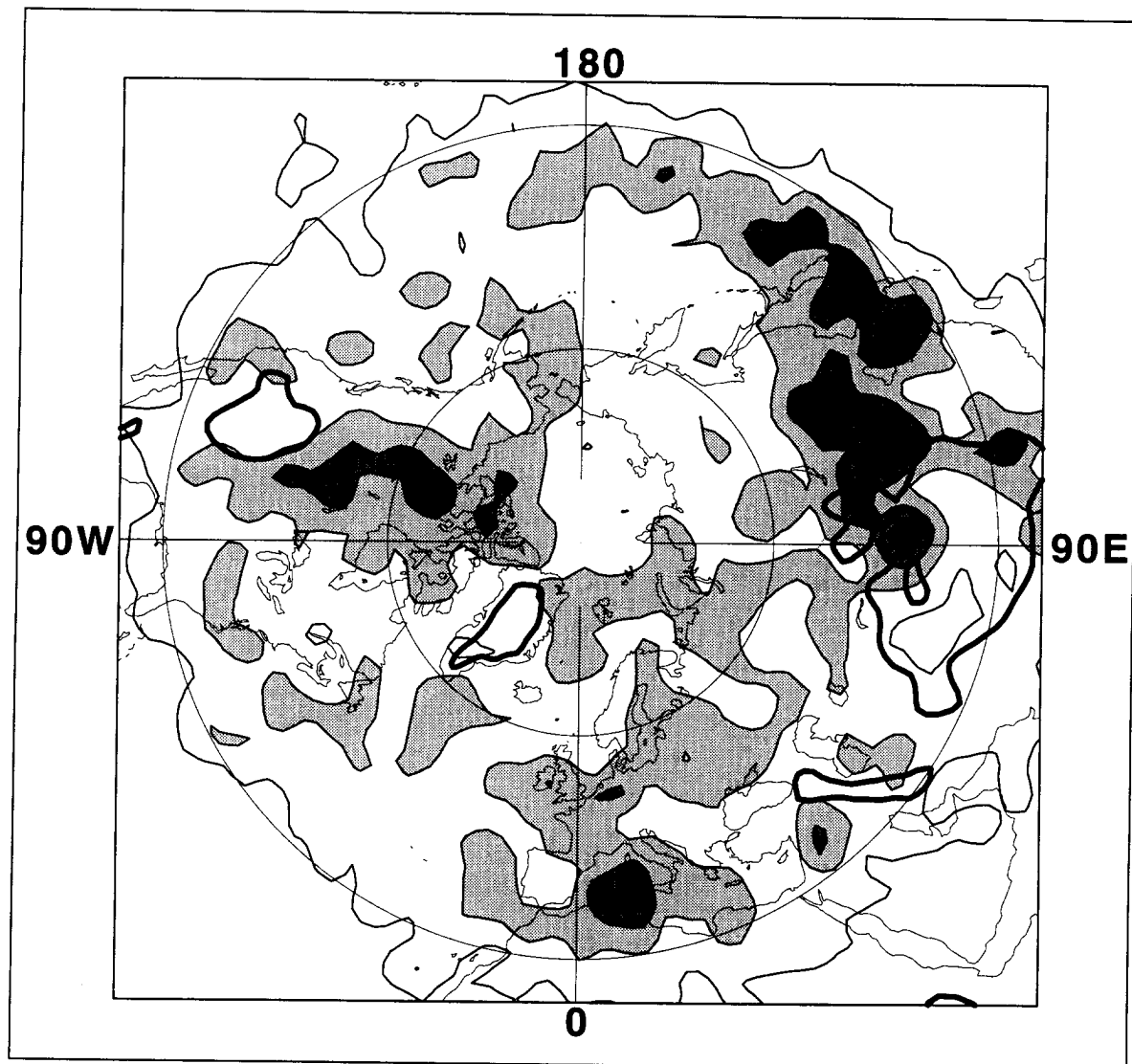


Fig. 2.12. Frequency of trough genesis during winter (DJF) throughout the twenty year dataset. The solid contours represent 3, 5, 7 and 9 events per  $10^6$  km<sup>2</sup> per season, respectively. The thick contours encircle elevated terrain higher than 2000 meters.

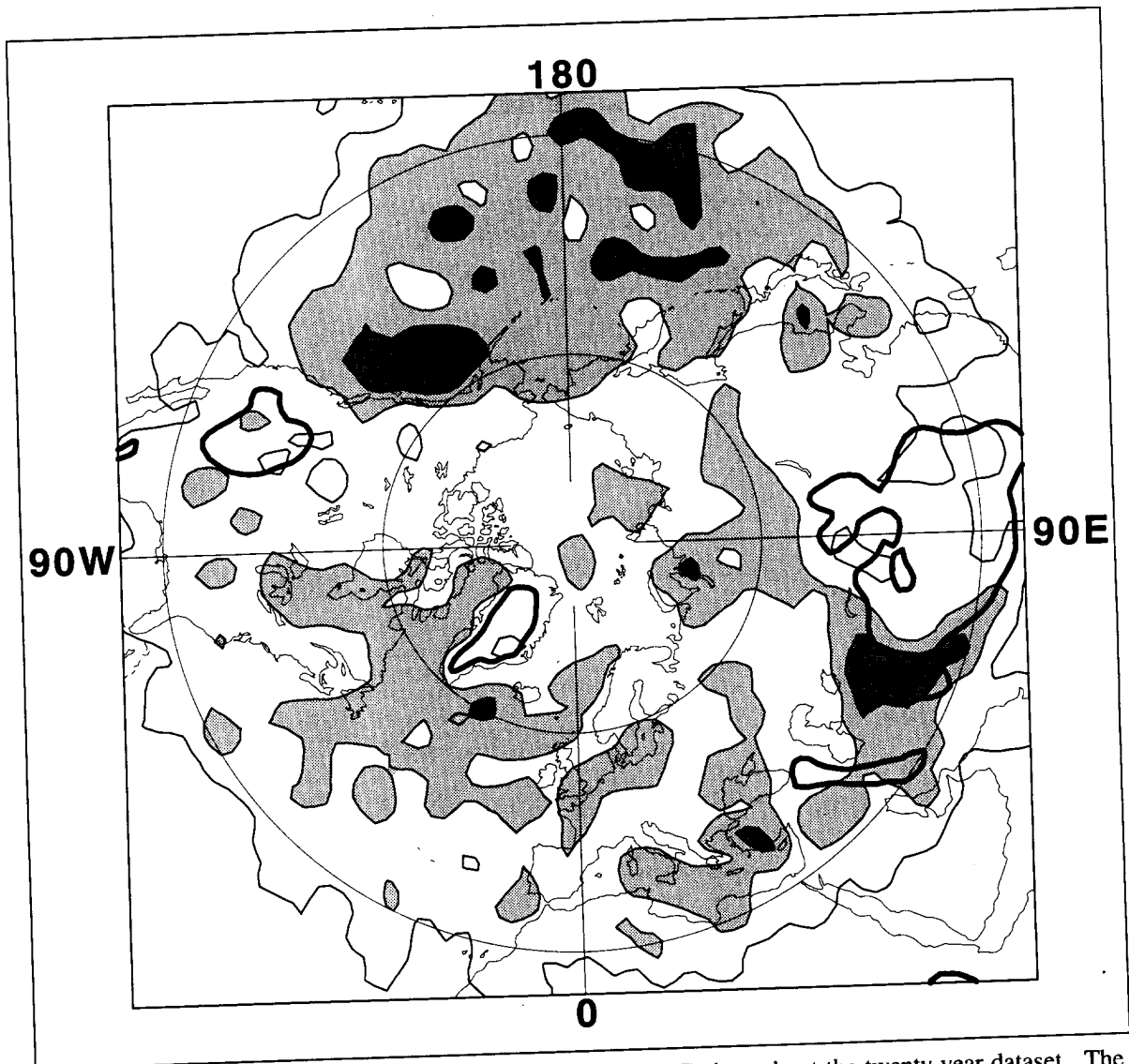


Fig. 2.13. Frequency of trough termination during winter (DJF) throughout the twenty year dataset. The solid contours represent 3, 5, 7 and 9 events per  $10^6 \text{ km}^2$  per season, respectively. The thick contours encircle elevated terrain higher than 2000 meters.

In summer both genesis (Fig. 2.14) and termination (Fig. 2.15) events are more rare. Since trough lifespans are similar in the two seasons, troughs themselves must be rarer during summer. While the eastern Asian and Mediterranean genesis regions remain, the North American genesis region is weaker and displaced farther east. Two new prominent genesis regions appear, one over the central North Pacific and the other over the eastern Atlantic. There is little overlap with the area of wintertime genesis over the Pacific, suggesting that the broadness of the genesis pattern in the overall statistics is a consequence of averaging over a variety of jet positions. The termination region upstream of the western Asia massif is lost in summer, most likely as a consequence of the jet stream being farther north.

## 8. Summary and discussion

A method of objectively identifying midtropospheric mobile troughs has been developed and applied to twenty years of 500 mb analyses. The technique uses the product of the geostrophic curvature vorticity and the geostrophic wind speed, here called the Eulerian Centripetal Acceleration (ECA), to identify troughs, and estimates the motion of troughs from the 500 mb steering flow. This method was shown to be superior to the subjective curvature-of-contour technique of S88 in tracking features in the 500 mb vorticity field.

Mobile trough lifespans were found to obey a geometric distribution: the probability of a trough surviving to the next analysis was independent of the age of the trough. Lifespans were in general much shorter than S88 reported, with the longest-lived trough objectively tracked for 44 days. The median lifespan of "significant" mobile troughs was 4 days.

Mobile troughs appeared to follow preferred tracks, more frequently appearing over the storm track areas of the oceans and over the northern continents and the Mediterranean. Mobile troughs were rarely found over areas of high orography. The most likely area to find a trough north of 30°N was over the Yellow Sea, upstream of the major surface cyclone intensification region over the Pacific.

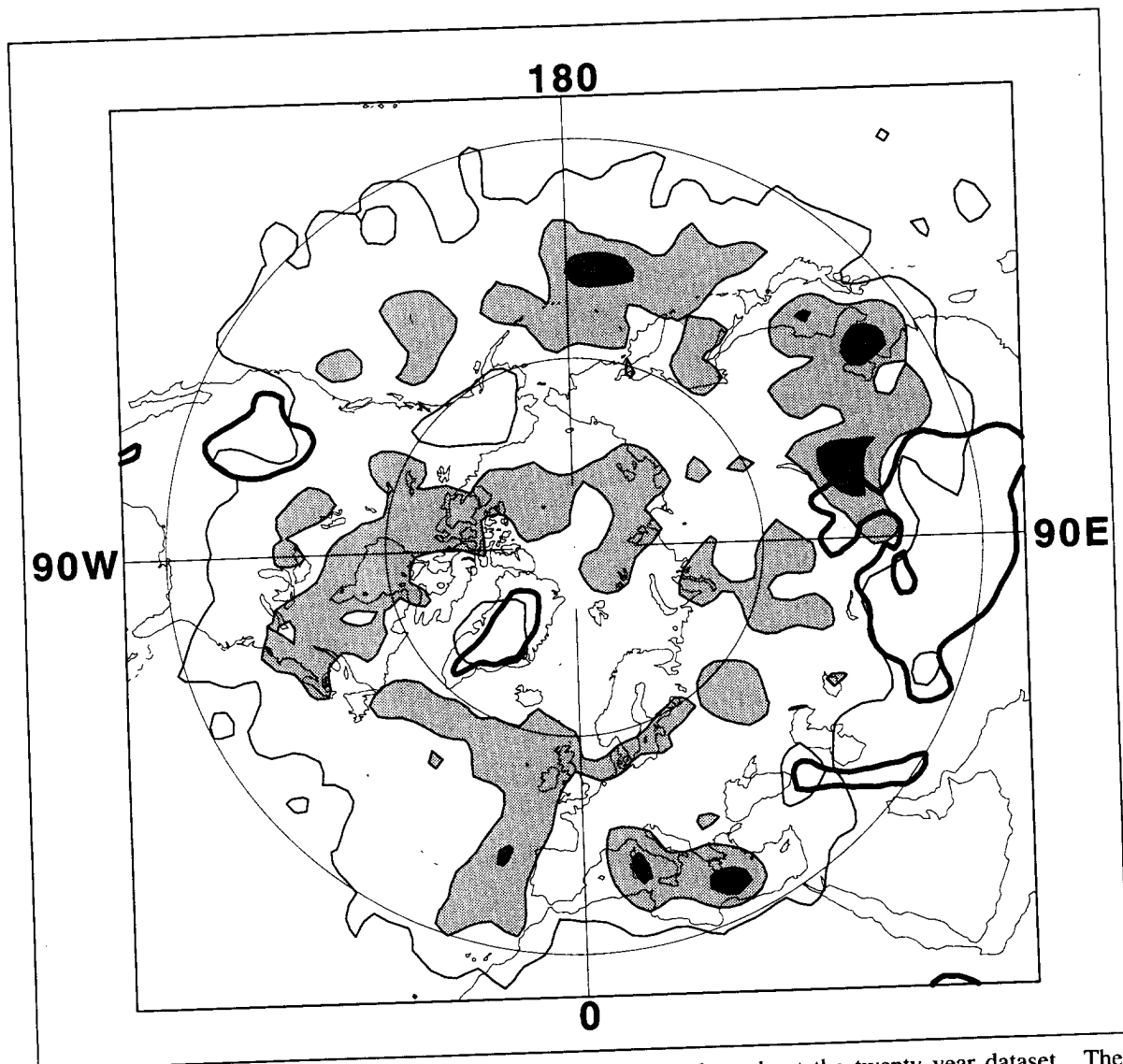


Fig. 2.14. Frequency of trough genesis during summer (JJA) throughout the twenty year dataset. The contours represent 3, 5, 7 and 9 events per  $10^6$  km<sup>2</sup> per year. The thick contours encircle elevated terrain higher than 2000 meters.

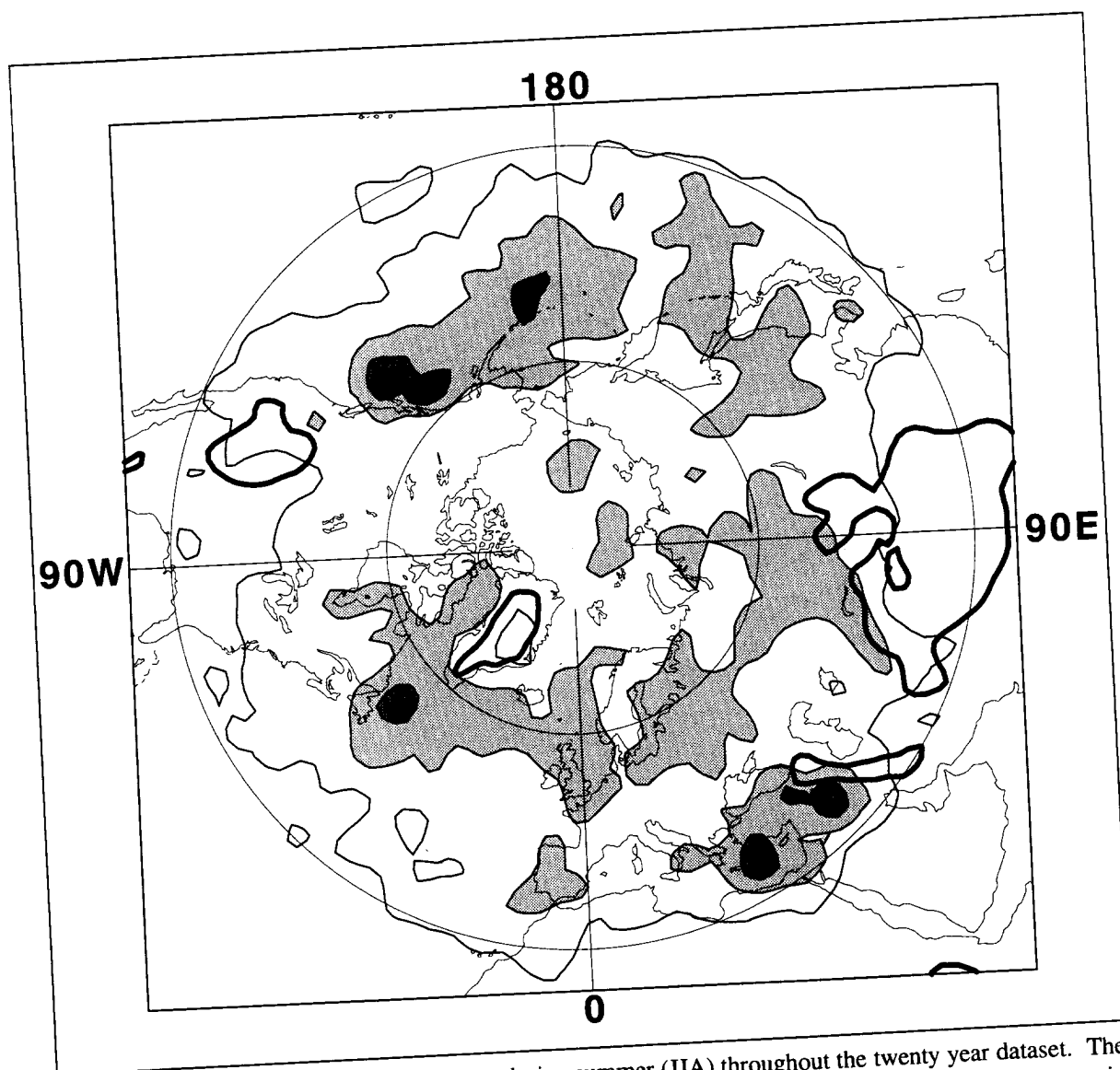


Fig. 2.15. Frequency of trough termination during summer (JJA) throughout the twenty year dataset. The contours represent 3, 5, 7 and 9 events per  $10^6$  km<sup>2</sup> per year. The thick contours encircle elevated terrain higher than 2000 meters.

These frequency maps cannot be directly compared to counts of cyclone tracks passing through grid boxes, but they are comparable to the earlier climatologies of surface cyclone frequencies reported by Petterssen (1956) and Klein (1957). Over both the Atlantic and the Pacific, the axis of maximum trough frequency is displaced south of the axis of maximum cyclone frequency, probably because the cyclone frequency counts include mature, stationary cyclones which tend to lie north of the main band of westerlies. Across low latitudes from the Mediterranean to southeast Asia, preferred locations of mobile troughs and surface cyclones coincide. Over North America, the trough frequency maps lack an area of maximum frequency along the axis of high frequency of surface (lee) cyclones.

The major difference between preferred areas of surface cyclogenesis and upper-tropospheric mobile trough genesis is over the western oceans. While these are preferred regions for surface cyclone formation and intensification, these areas are much less active at upper levels than the major centers for mobile trough formation over central Asia and central North America. This is consistent with observations that typical rapidly-deepening surface cyclones over western oceans are triggered by preexisting upper-level short waves of significant amplitude (Sanders, 1986; Wash et al., 1988). Indeed, as found by S88, there is a robust tendency for mobile troughs to form over land and dissipate over water, with the notable exception of troughs which terminate on the upwind side of the Tibetan Plateau.

The eastern Asia trough genesis region is active year-round. Except for the relative lack of trough genesis south of Japan, the genesis pattern closely corresponds to the preferred locations of surface cyclogenesis found by Chen et al. (1991). However, the year-round activity over Mongolia contrasts with the behavior of surface cyclogenesis in that area, which is suppressed in winter (Whitaker and Horn, 1984, Chen et al., 1991). Over North America, cyclogenesis events form a narrow band in the lee of the mountains, while mobile trough genesis events are more broadly distributed downwind.

The above results are complementary to recent studies of bandpass variance and storm tracks. Both Blackmon et al. (1977) and Wallace et al. (1988) show the areas of high



bandpass variance originating over eastern Asia at 500 mb and over Japan at 1000 mb. The bandpass variance maps show much less dependence on orography than the mobile trough frequency maps, doubtless due to mountains helping to amplify ridges even as they weaken troughs. The two prominent areas of genesis over the central continents are adjacent to and directly upstream of areas of 500 mb mobile disturbance amplification (Wallace et al., 1988). While we believe that dynamic processes in the genesis regions favor trough formation there, it is also possible that troughs that form there have a better chance of surviving at least two days because they quickly move into a region favoring intensification.

These results also complement the objective climatology of 500 mb cutoff cyclones and anticyclones performed by Bell and Bosart (1989). Not surprisingly, 500 mb closed low centers are most often found north of areas of high frequency of 500 mb mobile troughs. In middle and high latitudes, 500 mb closed low centers tend to form downstream of the major trough genesis areas, consistent with the model of troughs forming or intensifying within the storm track areas, and eventually becoming closed centers. In contrast, the areas of enhanced mobile trough formation south of 40°N in spring (not shown) neatly coincide with areas of cutoff low formation, implying that both processes occur simultaneously.

The ECA method does not explicitly screen out stationary troughs. Some of the troughs in the climatology actually became stationary for more than 24 hours. Most of these troughs were found in the northeastern Pacific and the Gulf of Alaska (not shown), in an area with strong time-mean curvature of the 500 mb flow.

## CHAPTER III

### QGPV THINKING

The seminal review paper covering potential vorticity is by Hoskins et al. (1985). Hoskins et al. expanded the concept of “vorticity thinking”, used by fluid dynamists, to describe the dynamics of geophysical fluids in terms of potential vorticity--“potential vorticity thinking.”. The purpose of this chapter is to introduce the potential vorticity quantity, and more specifically the quasigeostrophic variant, and to describe the qualitative and quantitative fluid flow diagnostics available with its use. This chapter includes a review of some of the previous work associated with potential vorticity, and the advantage of quasi-geostrophic potential vorticity (QGPV) over classical diagnostics. The “real” atmosphere is not quasigeostrophic. This chapter will describe the expected sources of error between QGPV analyses and the full nonlinear atmosphere, including friction and diabatic heating. The ideas presented in this chapter are not necessarily new. They are, however, organized into one location and summarized as related to the case studies to follow in Chapter V.

#### 1. Definition of potential vorticity

In the late 1930s Rossby developed the concept of the conservation of absolute vorticity and fluid column thickness in a barotropic atmospheric model; he coined the term potential vorticity (see Hoskins et al., 1985, for a complete history of potential vorticity). As the systematic use of isentropic charts for displaying atmospheric motion became popular, Rossby extended the barotropic potential vorticity ideas to the layered isentropic analysis. He defined the isentropic potential vorticity ( $P_R$ ) as

$$P_R = \frac{(f + \zeta_\theta)}{\Delta} \quad (3.1)$$

where

$$\zeta_\theta = \mathbf{k} \cdot \nabla_\theta \times \mathbf{V} \quad (3.2)$$

is the isentropic relative vorticity, defined as the component of the relative vorticity vector normal to an isentropic surface. The quantity,  $f$ , is the Coriolis parameter or planetary vorticity, and  $\Delta$  is the thickness between adjacent isentropic surfaces. The vector,  $\mathbf{V}$ , is the three-dimensional wind vector. The isentropic potential vorticity is a scalar quantity.

Ertel (1942) independently derived a three-dimensional continuously stratified version of the potential vorticity ( $P$ ) for any compressible and inviscid fluid,

$$P = \frac{\zeta_a \cdot \nabla_3 \theta}{\rho} \quad (3.3)$$

where  $\rho$  is density,  $\zeta_a$  is an absolute vorticity vector (sometimes simplified to the sum of the vertical component of the relative vorticity,  $\zeta$ , and the planetary vorticity,  $f$ ),  $\theta$  is any conserved property that depends on the pressure ( $p$ ) and density ( $\rho$ ), and  $\nabla_3$  is the three-dimensional gradient operator. Meteorologists usually use potential temperature for  $\theta$ . If the atmosphere is assumed to be hydrostatic, then two alternate versions of Ertel's potential vorticity (3.3) are

$$P = -g(f\mathbf{k} + \nabla_p \times \mathbf{V}) \cdot \nabla_p \theta \quad (3.4)$$

for isobaric vertical coordinates, and

$$P = \frac{-g(f + \mathbf{k} \cdot \nabla_\theta \times \mathbf{V})}{\frac{\partial p}{\partial \theta}} \quad (3.5)$$

for isentropic vertical coordinates.

In the above equations  $\mathbf{k}$  is the unit vector in the vertical direction,  $\nabla_p$  is the three-dimensional gradient operator in the  $(x, y, p)$  coordinate system,  $\nabla_\theta$  is the three-dimensional gradient operator in the  $(x, y, \theta)$  coordinate system,  $g$  is gravity,  $f$  is the Coriolis parameter,  $\mathbf{V}$  is the three-dimensional wind vector, and  $p$  is pressure.

The two most appealing aspects of potential vorticity ( $P$ ) are: 1) its conservation following fluid motion, and 2) its functional relationship with the atmospheric wind, temperature and height or pressure. The complete kinematic structure of the atmosphere can be determined by inverting (solving) the potential vorticity equation, (3.4) or (3.5)

(Egger 1990, Hoskins et al. 1985). Together, the Lagrangian tracer and invertibility principle of potential vorticity allow the diagnosis of the complete balanced kinematic and dynamical characteristics of the atmosphere.

Three considerations are required to perform the inversion (Hoskins et al. 1985):

- 1) Some kind of atmospheric balance condition (geostrophic, quasigeostrophic, semigeostrophic, gradient wind, Charney-balance, etc.) must be assumed. The applicability of the result depends on the level of balance used to invert the three-dimensional field of potential vorticity. It is the balance condition that relates the three-dimensional scalar potential vorticity to the processes present in the “real” atmosphere.
- 2) The potential vorticity inversion has to be associated with a reference state of the atmosphere. Over the globe, for example, the mean potential vorticity within any isentropic layer is zero. To describe the complete balanced state of the atmosphere the total amount of mass within the layer must be specified, in addition to the potential vorticity distribution.
- 3) Boundary conditions must be specified, which adds complexity to the solutions.

The background material presented thus far describes the nature of the potential vorticity analyses. Hoskins et al. (1985) is the best source of information dealing with the details of isentropic potential vorticity and a fairly complicated balance condition. However, the focus of the potential vorticity diagnostics used in this research will be from the quasigeostrophic (QG) point of view. The advantage of QG diagnostics is its simplicity; the linear inversion operator allows unambiguous interpretations. Quasigeostrophic diagnostics capture the essence of the synoptic and large-scale dynamics of the atmosphere inherent in the full nonlinear primitive equations.

The form of the QGPV equation used throughout this research is

$$\frac{d_g q}{dt} = 0 \quad (3.6)$$

where

$$q \equiv \frac{g}{f_0} \nabla^2 z + f + g f_0 \frac{\partial}{\partial p} \left( \frac{1}{\sigma} \frac{\partial z}{\partial p} \right) \quad (3.7)$$

The reader is encouraged to review Appendix 2 for a complete derivation of QGPV and the definition of variables and constants in (3.6) and (3.7).

## 2. Traditional diagnostics

Before plowing into QGPV diagnostics it is appropriate to review traditional atmospheric flow diagnostic techniques. The reader can find the following equations in any introductory atmospheric dynamics textbook (Holton 1992, Bluestein 1992, Bluestein 1993, Haltiner and Williams 1980, to name a few). To be consistent with the QGPV discussion to follow later, friction and diabatic heating are neglected from the discussion of traditional diagnostics. The discussion in this section assumes the static stability is not a function of pressure. In the QGPV diagnostics presented in this research the static stability is a function of pressure.

Synoptic meteorologists often focus on vertical motion as a means of identifying the locations of initiation and development of surface cyclones and anticyclones. Vertical motion ( $\omega$ ) is related, through the continuity equation, to divergence. The  $\omega$ -equation, written in coordinates consistent with this paper, is

$$\left( \nabla^2 + \frac{f_0^2}{\sigma} \frac{\partial^2}{\partial p^2} \right) \omega = -\frac{f_0}{\sigma} \frac{\partial}{\partial p} \left( -\mathbf{V}_g \cdot \nabla (\zeta_g + f) \right) + \frac{g}{\sigma} \nabla^2 \left( -\mathbf{V}_g \cdot \nabla \frac{\partial z}{\partial p} \right) \quad (3.8)$$

The left hand side of (3.8) is equivalent to a three-dimensional Laplacian of vertical motion ( $\omega$ ) with a scaled vertical coordinate. The first term on the right hand side is the differential vertical variation of absolute vorticity advection by the geostrophic wind ( $\mathbf{V}_g$ ). It is not vorticity advection itself but the vertical change in vorticity advection that is important for vertical motion.

The magnitude of the surface (or let's assume 1000 mb) geostrophic wind is typically less than at higher altitudes in the atmosphere. In addition, the surface vorticity pattern is usually made of cells of closed low and high vorticity contours which are nearly parallel to the low-level height contours. Therefore, the magnitude of low-level vorticity advection

is typically less than the magnitude of vorticity advection in the middle and upper troposphere. Synopticians will often focus on the 500 mb vorticity advection pattern to diagnose areas of upward and downward vertical motion. Areas of positive vorticity advection, typically between an upper-level geopotential height trough and ridge, have negative differential vorticity advection with respect to pressure. The minus sign on the right hand side makes the vorticity term on the right hand side positive. A characteristic of the Laplacian operator (or inverse Laplacian operator) is that the result of the operation tends to be opposite in sign from the quantity being operated on. Therefore, a positive forcing term on the right hand side produces a negative  $\omega$ , which means upward vertical motion. The vorticity advection term contributes to upward vertical motion between the trough and ridge. Similar reasoning implies downward motion between the ridge and trough.

The second term on the right hand side of (3.8) is the Laplacian of thickness advection. The thickness between two adjacent pressure surfaces is proportional, via the hydrostatic approximation, (A2.13), to the negative of temperature. The quantity within the parentheses of the Laplacian operator in the second term on the right hand side of (3.8) is the negative of temperature advection. The Laplacian operator, in addition to changing the sign of the operand, emphasizes maxima and minima. Therefore, centers of warm air advection will make the second term on the right hand side of (3.8) positive. A positive value on the right hand side corresponds to upward vertical motion above the layer in question. Likewise, cold air advection corresponds to downward vertical motion.

The height tendency equation,

$$\left( \nabla^2 + \frac{f_0^2}{\sigma} \frac{\partial^2}{\partial p^2} \right) \left( \frac{\partial z}{\partial t} \right) = \frac{f_0}{g} \left( -\mathbf{V}_g \cdot \nabla (\zeta_g + f) \right) + \frac{f_0^2}{\sigma} \frac{\partial}{\partial p} \left( -\mathbf{V}_g \cdot \nabla \frac{\partial z}{\partial p} \right) \quad (3.9)$$

relates the advection of absolute vorticity and temperature to the local change in geopotential height of a given pressure surface. It is interesting to note that the three-dimensional Laplacian operator on the left hand side of (3.9) is the same operator as in (3.8). Even though the right hand side of (3.9) contains similar forcing terms, the vertical

gradient operator is now on the thermal advection term (the second term on the right hand side) and the Laplacian operator is not present in either forcing term.

The first forcing term on the right hand side of (3.9) simply contributes to negative (decreasing) height tendencies in areas of positive vorticity advection, and positive (rising) height tendencies in areas of negative vorticity advection. The second term on the right hand side is the differential of the negative of temperature advection. Negative height tendencies occur in areas of cold advection decreasing in the vertical direction. Positive height tendencies are associated with warm advection decreasing in the vertical direction.

Sutcliffe (1947) and Petterssen (1956) developed equations for diagnosing surface and midtropospheric development based on forcing occurring at discrete levels (the 1000 mb and 500 mb levels) and the geopotential thickness between the 1000 mb and 500 mb levels (see Carlson 1991 for a discussion of these equations). To relate the vorticity and thermal dynamic forcing, both equations use advection by the thermal wind and vorticity calculated from the thermal wind (called thermal vorticity,  $\zeta_T$ ). Sutcliffe's equation focuses on the 1000 mb divergence as an indicator of development, whereas Petterssen's equation focuses on the tendency of 500 mb geostrophic relative vorticity. The disadvantage of Sutcliffe's equation is the neglect of spatial and temporal static stability changes. Petterssen included stability in his diagnostic equation. Both equations work fine in a qualitative sense, but due to their simplifications they are not practical for quantitative work at each level of the troposphere.

Trenberth (1978) developed a diagnostic  $\omega$ -equation with forcing by a single term formed by the combination of the vorticity and temperature advection terms. The Trenberth equation is an extension of the Sutcliffe and Petterssen ideas to the continuous quasigeostrophic atmosphere. Bluestein (1992, section 5.7.3) provides a nice discussion of the Trenberth equation. The Trenberth equation,

$$\left( \nabla^2 + \frac{f_0^2}{\sigma} \frac{\partial^2}{\partial p^2} \right) \omega = \frac{2f_0}{\sigma} \left( \frac{\partial \mathbf{V}_g}{\partial p} \bullet \nabla \zeta_g \right) \quad (3.10)$$

includes the advection of geostrophic relative vorticity by the thermal wind. It includes the effects of static stability, but neglects a portion of the geostrophic flow--two deformation terms.

The traditional approaches to cyclone or midtropospheric wave development focus on the geostrophic vorticity advection and temperature (or thickness) advection, which can be combined together to produce a single forcing based on the advection by the thermal wind. Hoskins et al. (1978) developed another form of the  $\omega$ -equation called the Q-vector  $\omega$ -equation,

$$\left( \nabla^2 + \frac{f_0^2}{\sigma} \frac{\partial^2}{\partial p^2} \right) \omega = -2 \nabla \cdot \mathbf{Q} \quad (3.11)$$

where

$$\mathbf{Q} = -\frac{R}{\sigma p} \begin{pmatrix} \frac{\partial \mathbf{V}_g}{\partial x} \cdot \nabla T \\ \frac{\partial \mathbf{V}_g}{\partial y} \cdot \nabla T \end{pmatrix} \quad (3.12)$$

Bluestein (1992) and Holton (1992) provide excellent discussions of Q-vector diagnostics. The advantages of the Q-vector form of the  $\omega$ -equation are that the forcing term on the right hand side of (3.11) combines the thermal and vorticity advection terms into one term. Second, no additional assumptions beyond quasigeostrophic theory were used--no terms were neglected. Therefore, the forcing of vertical motion is complete (exact). Third, the Q-vector diagnostics are simple to interpret. The Q-vector is an elegant parameter for diagnosing quasigeostrophic atmospheric flow, but it is not conserved following geostrophic motion. The nonconservation of Q-vectors means each analysis is independent from the previous one.

### 3. QGPV height tendency equation

Synopticians use the vertical motion or geopotential height tendency to diagnose the three-dimensional development of atmospheric cyclones. The quasigeostrophic height tendency equation, (3.9), expresses the Laplacian of the height tendency as being forced



by terms involving the advection of vorticity and temperature. While this partitioning allows the forcing to be easily evaluated on conventional weather maps, it does not distinguish between distinct dynamical intensification processes and suffers from the near cancellation of the forcing terms.

Quasigeostrophic potential vorticity diagnostics, on the other hand, allow one to determine the three-dimensional nature of cyclone development from the magnitude and sign of one term, the advection of QGPV. Using piecewise potential vorticity inversion, to be discussed later, it is possible to determine the intensification of a system by the amplification and redistribution of QGPV. Such partitioning allows one to identify the specific dynamical processes present in the developing or decaying midtropospheric mobile trough.

If the total derivative in (3.6) is expanded and the local derivative in time is applied to the definition of  $q$ , the resulting equation is

$$\frac{g}{f_0} \nabla^2 \left( \frac{\partial z}{\partial t} \right) + g f_0 \frac{\partial}{\partial p} \left( \frac{1}{\sigma} \frac{\partial}{\partial p} \left( \frac{\partial z}{\partial t} \right) \right) = -\mathbf{V}_g \cdot \nabla q \quad (3.13)$$

because the Coriolis parameter,  $f$ , doesn't change with time. Assuming the static stability ( $\sigma$ ) does not vary in the vertical direction, (3.9) becomes

$$\left( \nabla^2 + \frac{f_0^2}{\sigma} \frac{\partial^2}{\partial p^2} \right) \left( \frac{\partial \phi}{\partial t} \right) = f_0 (-\mathbf{V}_g \cdot \nabla q) \quad (3.14)$$

using  $\phi = gz$ . For a complete description of the QGPV height tendency equation and its traditional application to meteorological analyses of midtropospheric cutoff cyclones see Bell and Bosart (1993a and 1993b).

The operator on the left hand side of (3.14) is the same operator as in the traditional omega and geopotential height tendency equations. The forcing on the right hand side of (3.14) contains the effects of both the absolute vorticity and stratification or temperature advection. However, like the Q-vector, the QGPV forcing is an exact formulation of the quasigeostrophic forcing. Unlike the Q-vector, the QGPV contained within the forcing is

conserved following geostrophic flow and can be used to diagnose dynamical changes of the system.

The traditional geopotential height tendency equation written from within a QGPV framework, (3.14), except with static stability being a function of pressure, will be used in a nontraditional way to describe the formation and amplification of midtropospheric mobile troughs. Chapters IV and V will describe the piecewise inversion of the QGPV geopotential height tendency equation and how to interpret the results of the inversion.

#### **4. Theoretical considerations**

The purpose of this section is to introduce the reader to the theoretical considerations of “QGPV thinking.” The discussion will primarily follow discussions by Hoskins et al. (1985) and Chapter 1 of Bluestein (1993), but will be tailored to QGPV diagnostics and midtropospheric applications. The two references mentioned above focus on potential vorticity in isentropic coordinates, use a fairly complex balance condition, and emphasize surface development. The focus of this research, however, is on the middle and upper troposphere.

This section will discuss the two distinguishing properties of potential vorticity: 1) the QGPV is conserved following quasigeostrophic motion (3.6), and 2) the definition of QGPV can be inverted (solved) to retrieve the three-dimensional geopotential height field corresponding to the QGPV field. These two properties summarize the advantages of QGPV thinking over traditional quasigeostrophic diagnostics and Ertel’s PV thinking using a nonlinear balance condition. First, conservation allows the comparison of QGPV from one time to another. Second, the QGPV inversion is linear so the resulting geopotential height field is an exact replica of the height field used to compute it (Davis and Emanuel 1991, Davis 1992a).

At this point the reader must be thinking QGPV inversion is ludicrous. Why is it necessary to invert the QGPV field to get the height field when the height field was used to calculate the QGPV field in the first place? The answer is the piecewise inversion technique allows the diagnosis of the atmospheric response to QGPV forcing from

different levels (Davis and Emanuel 1991, Davis 1992a, Holopainen and Kaurola 1991). Since the QGPV inversion is linear, the sum of the individual levels (pieces in piecewise) will equal the total effect of QGPV. Therefore, understanding the effect of one level upon another is simply a matter of applying the appropriate partitioning scheme.

Quasigeostrophic potential vorticity thinking and QGPV inversion are actually based on QGPV anomalies from a basic state,  $q = \bar{q} + q'$ , where  $q$  is the total QGPV,  $\bar{q}$  is the basic state QGPV, and  $q'$  is the QGPV anomaly. The choice of  $\bar{q}$  is arbitrary, and is based on the physical reasoning one hopes to extract from the QGPV system. The  $\bar{q}$  field used in this research is unique. It is based on the long-wave pattern present in the middle troposphere at a specific time. The discussion of  $\bar{q}$  will be postponed until Chapter IV. For the purpose of this discussion, assume  $\bar{q}$  is the Coriolis parameter which can be written,

$$\bar{q}(y) = f(y) \quad (3.15)$$

This  $\bar{q}$  reference state is used by Hoskins et al. (1985) in their discussion of QGPV diagnostics. Charney and Stern (1962) used the zonal mean geopotential height field to define  $\bar{q}$ . The QGPV discussion to follow is based on the definition of  $q$ , (3.7), as applied to the QGPV anomaly, written

$$q' = q - f = \frac{g}{f_0} \nabla^2 z + g f_0 \frac{\partial}{\partial p} \left( \frac{1}{\sigma} \frac{\partial z}{\partial p} \right) \quad (3.16)$$

To get a “feel” for the application of QGPV thinking to tropospheric analysis, it is important to understand how QGPV is distributed throughout the atmosphere. The study of QGPV in this research is focused on the northern hemisphere, so the following discussion and figures are from a northern hemisphere perspective.

The horizontal gradient of QGPV (total  $q$ ) is typically concentrated along the equator and in the midlatitudes. It is most noticeable in the lower and upper troposphere (Fig. 3.1). The middle troposphere is generally void of significant north-south QGPV gradients.

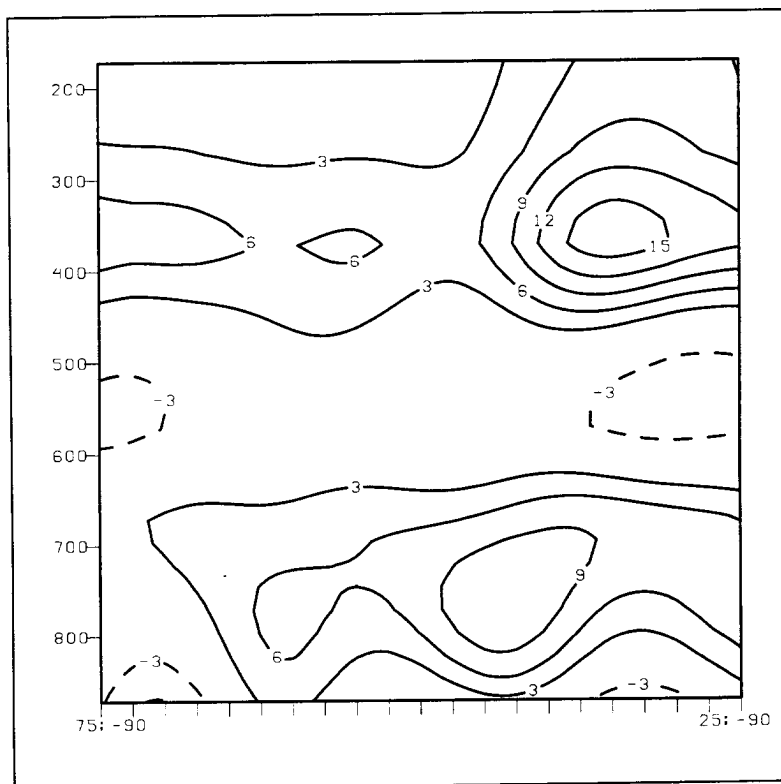


Fig. 3.1. A time-mean meridional-vertical cross section of the zonally averaged meridional gradient of QGPV from 25°N through 75°N from 0000 UTC 1 December through 5 December 1980. The contour interval is  $3 \times 10^{-11} \text{ m}^{-1} \text{ s}^{-1}$ . The vertical axis is pressure (mb).

A northern hemisphere isobaric QGPV analysis at 372 mb and the corresponding geopotential height analysis for the same level are given in Figs. 3.2 and 3.3. The largest values of QGPV are typically found near the North Pole because the 372 mb level occurs well into the stratosphere there. Because the magnitude of positive QGPV is much greater in the stratosphere, and the stratosphere dominates the middle and upper pressure levels near the North Pole, the QGPV contours covering the higher latitudes on constant pressure maps are referred to as the “stratospheric reservoir” of QGPV.

The sharp trough in the geopotential height field over the Great Lakes region in Fig. 3.3 corresponds to a sharp undulation from the stratospheric reservoir of QGPV in Fig. 3.2. When discussing undulations in the QGPV field it is customary to refer troughs and ridges. However, a trough is actually an area of large positive QGPV values. The reason for the trough terminology is that large positive QGPV anomalies, like vorticity maxima, are usually associated with a trough in the geopotential height field. Likewise, a ridge in the geopotential height field is typically projected as an area of small QGPV values. It is more meaningful to refer an area of locally large positive QGPV as a positive QGPV anomaly, and an area of locally small positive (or negative) QGPV as a negative QGPV anomaly. The local anomaly terminology is used even though the QGPV field in Fig. 3.2. is not necessarily a  $q'$  field. This QGPV terminology, however, falls short when referring to the southern hemisphere. Arguably, the most meaningful terminology would be to speak of “cyclonic PV anomalies” and be hemispheric independent (John W. Nielsen-Gammon, personal communication).

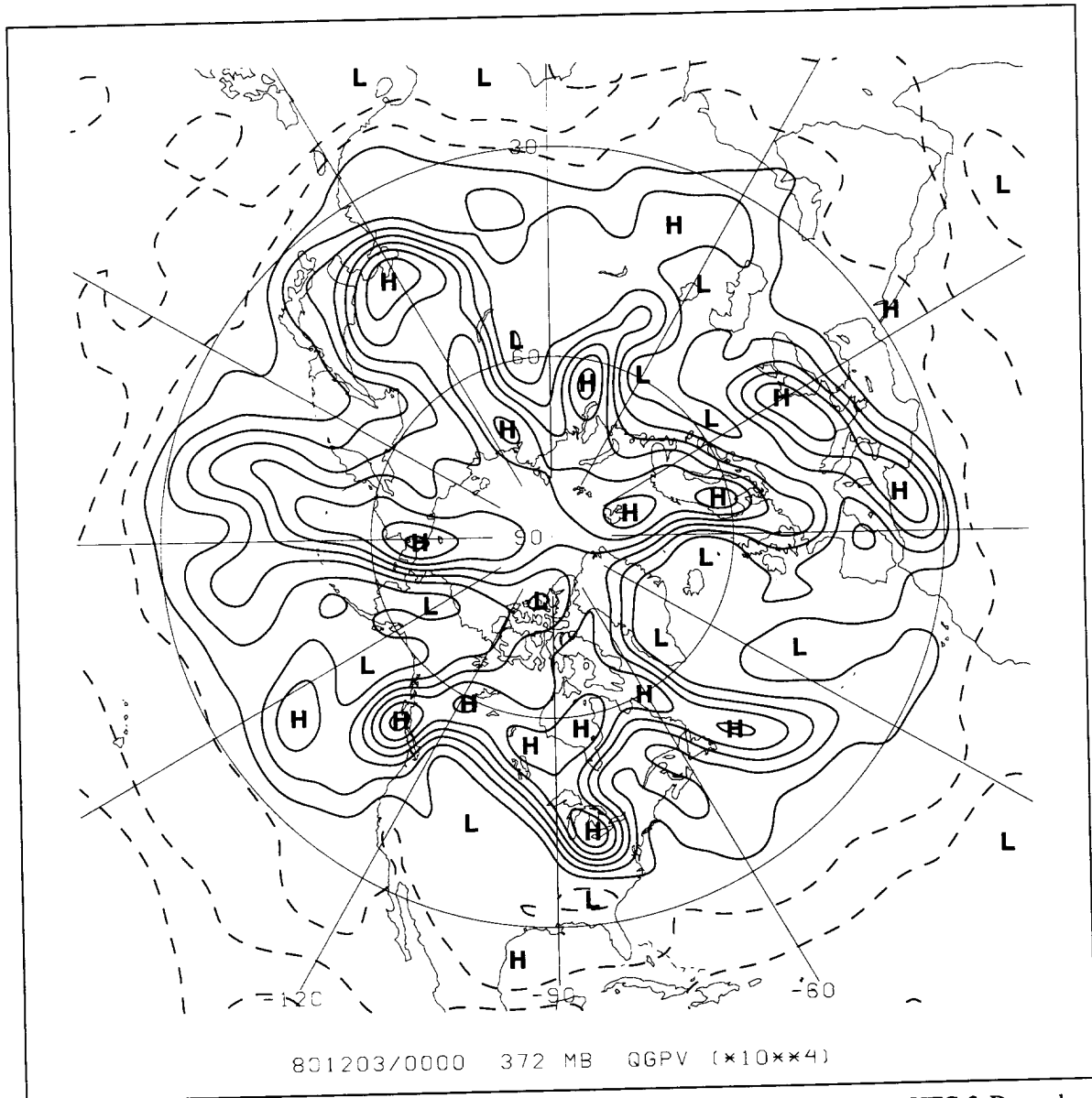


Fig. 3.2. The distribution of total QGPV on the 372 mb pressure surface from 0000 UTC 3 December 1980. The contour interval is  $1 \times 10^{-4} \text{ s}^{-1}$ . Negative contours are dashed. The first solid contour is equal to zero.

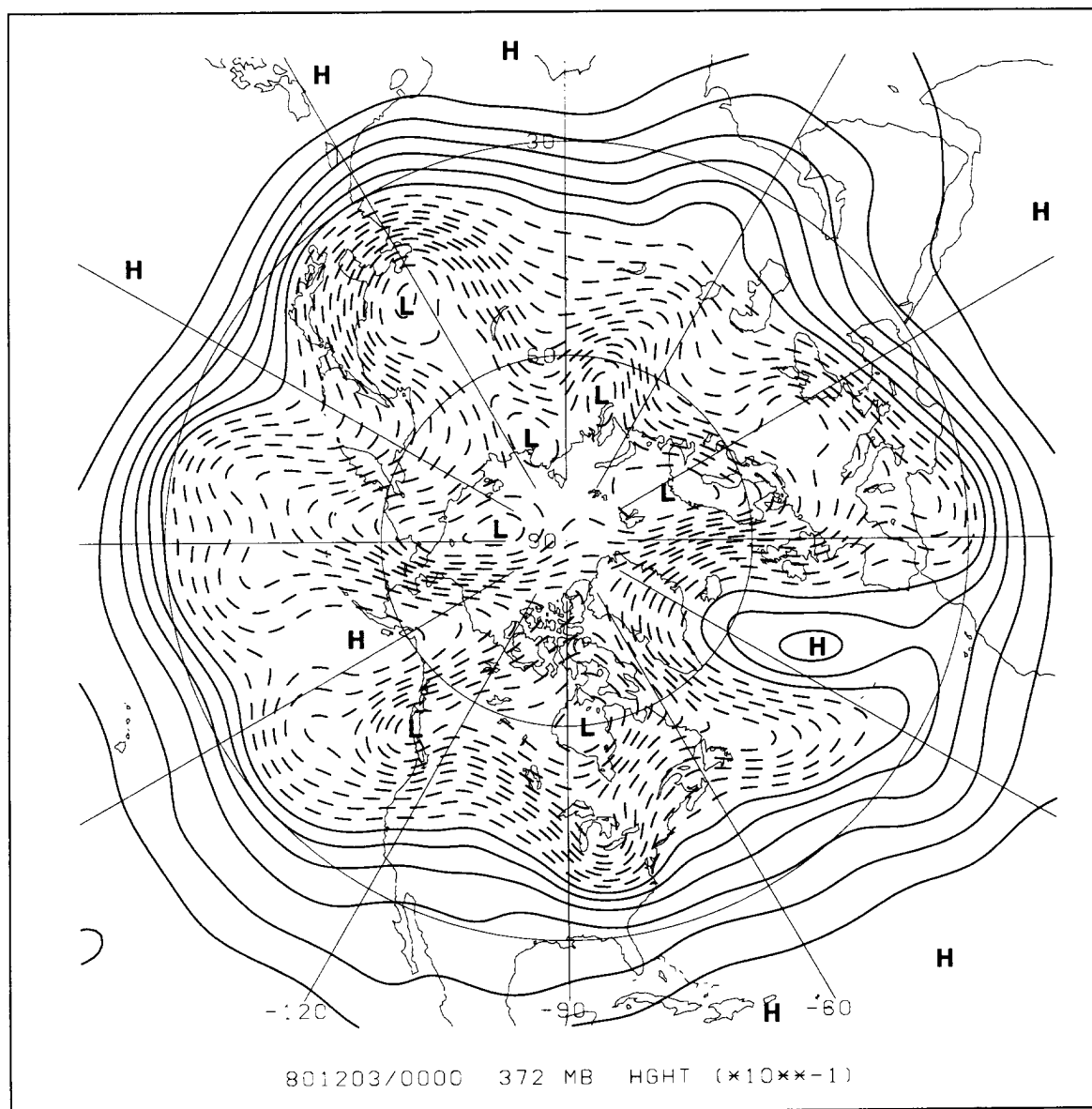


Fig. 3.3. The distribution of geopotential height on the 372 mb pressure surface from 0000 UTC 3 December 1980. The mean northern hemisphere geopotential height has been removed. The contour interval is 6 dam. Negative contours are dashed. The first solid contour is equal to zero.

Since QGPV is conserved following quasigeostrophic flow, the QGPV field gets translated, rotated and deformed during its evolution. The shape of the QGPV field and the local production of QGPV “protruding from” and “absorbing into” the stratospheric reservoir form the basis of QGPV thinking. According to (3.16) a positive QGPV anomaly is associated with positive relative vorticity (the first term on the right hand side), or positive stratification (the second term on the right hand side), or both. Positive (negative) relative vorticity corresponds with a local geopotential height minimum (maximum) in the horizontal, consistent with Figs. 3.2 and 3.3. Since the large-scale reference atmosphere is statically stable ( $\sigma$  is positive), a positive (negative) stratification term corresponds with a vertical geopotential height minimum (maximum).

Thorpe (1985) and Thorpe (1986) illustrate, using isentropic potential vorticity (IPV) and a gradient wind balance condition, that a warm surface temperature anomaly is associated with cyclonic circulation, and a cold surface temperature anomaly is associated with an anticyclonic circulation. The correspondence between surface potential temperature anomalies and interior potential vorticity anomalies was also discussed by Bretherton (1966).

If the reference state static stability is considered to be constant, the computation of geopotential from  $q'$  is simply a matter of inverting a scaled three-dimensional Laplacian operator. The resultant of the Laplacian operator is typically of opposite sign from its operand, and amplifies the small scale patterns of the flow. Therefore, the inverse Laplacian of  $q'$  will produce a smoother height field, consistent with Figs. 3.2 and 3.3. To help visualize the results of QGPV inversions consider (3.14) with constant stability,

$$\frac{f_0}{g} q' = \nabla^2 z' + \frac{f_0^2}{\sigma} \frac{\partial^2 z'}{\partial p^2} \quad (3.17)$$

If the vertical coordinate ( $p$ ) is scaled by

$$d\tilde{p} = \frac{f_0}{\sigma^{1/2}} dp \quad (3.18)$$

then



$$\frac{f_0}{g}q = \nabla_3^2 z \quad (3.19)$$

where the Laplacian operator on the right hand side is three-dimensional and the vertical coordinate is  $\tilde{p}$ . The result, (3.19), is a basic Poisson's equation.

The schematics presented in Fig. 3.4 were generated by solving (3.19) using a  $xy\tilde{p}$  Cartesian domain with 101 points on each side. The basic state was a pure zonal height ( $z$ ) field increasing linearly in the vertical. The upper-level QGPV anomaly (forcing) was spherical and of constant magnitude within the sphere. The surface anomalies in Fig. 3.4 simulated surface temperature anomalies, unless they were equal to zero. The imposed boundary conditions for all simulations were von Neumann (derivative-type).

The boundary conditions in Fig. 3.4 were such that in the upper-level cases there was no temperature perturbation at any boundary. In the surface temperature cases there was no  $q'$  anomaly within the interior, and the top was homogeneous. Like Hoskins et al. (1985), the midtropospheric positive (negative)  $q'$  is associated with cyclonic (anticyclonic) winds and negative (positive) height anomalies within and away from the perturbations. At the surface the positive (negative) temperature anomalies and increased (decreased) thickness were associated with cyclonic (anticyclonic) winds and negative(positive) height perturbations within the anomaly and away from it.

The tropopause is not present in these schematics because the static stability was constant in the vertical. However, it is worth noting that the tropopause undulation shown by Hoskins et al. (1985) would not be present within the QG system. Rivest and Farrell (1992) show a flat tropopause in their vertical cross sections through the QG simulations. In the QG system the static stability is only a function of the vertical coordinate. The tropopause, and high QGPV air in the stratosphere, can not vary significantly from the basic state in the horizontal plane or the QG assumption is violated, unless the tropopause is treated explicitly within the quasigeostrophic framework.

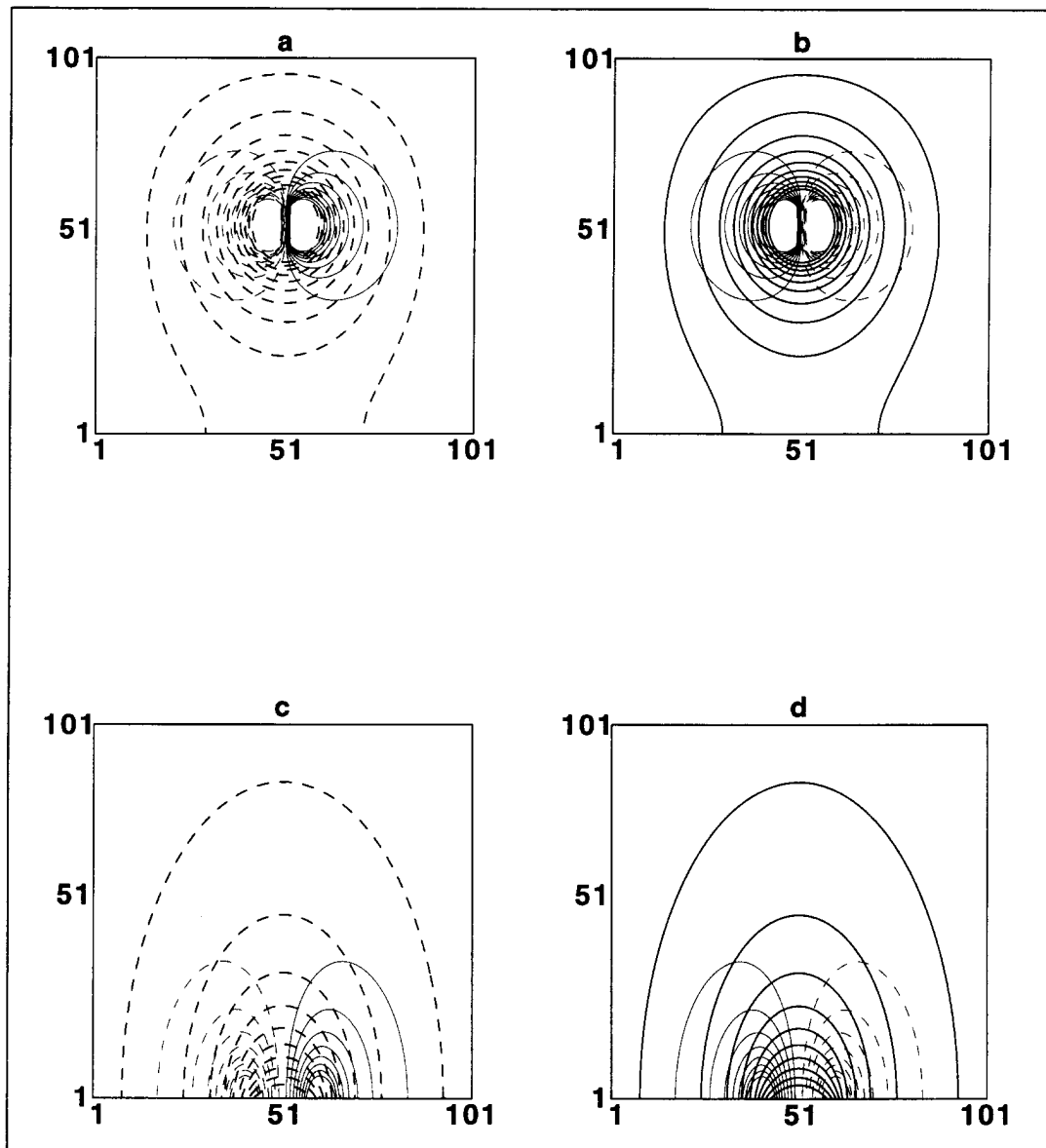


Fig. 3.4. Vertical cross sections through the resulting geopotential height fields associated with interior QGPV anomalies and surface temperature anomalies. The horizontal axis is in the  $x$  direction. The vertical axis is the scaled pressure coordinate described in the text. In a) a positive QGPV anomaly was put in the center of the domain. In b) a negative QGPV anomaly was put in the center of the domain. In c) a positive temperature anomaly was put at the surface in the center of the  $x$  axis. In d) a negative temperature anomaly was put at the surface in the middle of the  $x$  axis. In all cases the anomaly had a radius of 10. The thick contours are nondimensional height (contour interval is 4). The thin contours are nondimensional geostrophic wind (contour interval is 0.5). Negative values are dashed. The zero contour is not drawn.

The schematics in Fig. 3.4 imply the effect of the QGPV anomaly extends horizontally and vertically away from the anomaly. From (3.18) we see the effective vertical scale of the QGPV anomaly is inversely proportional to the square root of the static stability. If the static stability is sufficiently low, the effect of an isolated QGPV anomaly can extend throughout the troposphere. However, if opposite-signed QGPV anomalies are present, the vertical influence depends on the horizontal scale of the anomalies.

The conceptualization of a QGPV anomaly representing an electromagnetic charge within the three-dimensional environment can be extended to the interaction between multiple charges (Bishop and Thorpe 1994). The process of multiple QGPV anomalies influencing one specific location is called superposition. Superposition can be considered a trough intensification mechanism and therefore will be discussed in detail later in this chapter.

The basic concepts of superposition can be visualized by considering two independent positive QGPV anomalies (Fig. 3.5). Individually, each anomaly affects the three-dimensional geopotential height environment like in Fig. 3.4. The anomalies are not symmetric in these figures because of proximity of the lateral boundaries. The geopotential height anomaly at the "X" in Figs. 3.5a and 3.5b due to each individual anomaly is  $-13.7$ . However, if the QGPV anomalies are allowed to interact (become superposed), the geopotential height anomaly at the "X" in Fig. 3.5c is  $-27.5$ . If the QGPV anomalies are brought closer together (the superposition process) the geopotential height anomaly is  $-68.7$  (Fig. 3.5d).

Intensification can be inferred by examining the change in the maximum height perturbation, located near the center of each anomaly. When only a single anomaly is present, the minimum values of  $z'$  is  $-116$ . When both anomalies are present, as in Fig. 3.5c, the minimum  $z'$  is  $-120$ . Finally, when the anomalies are touching, Fig. 3.5d, the minimum  $z'$  is  $-131$ . The  $z'$  decreased by 15 through superposition.

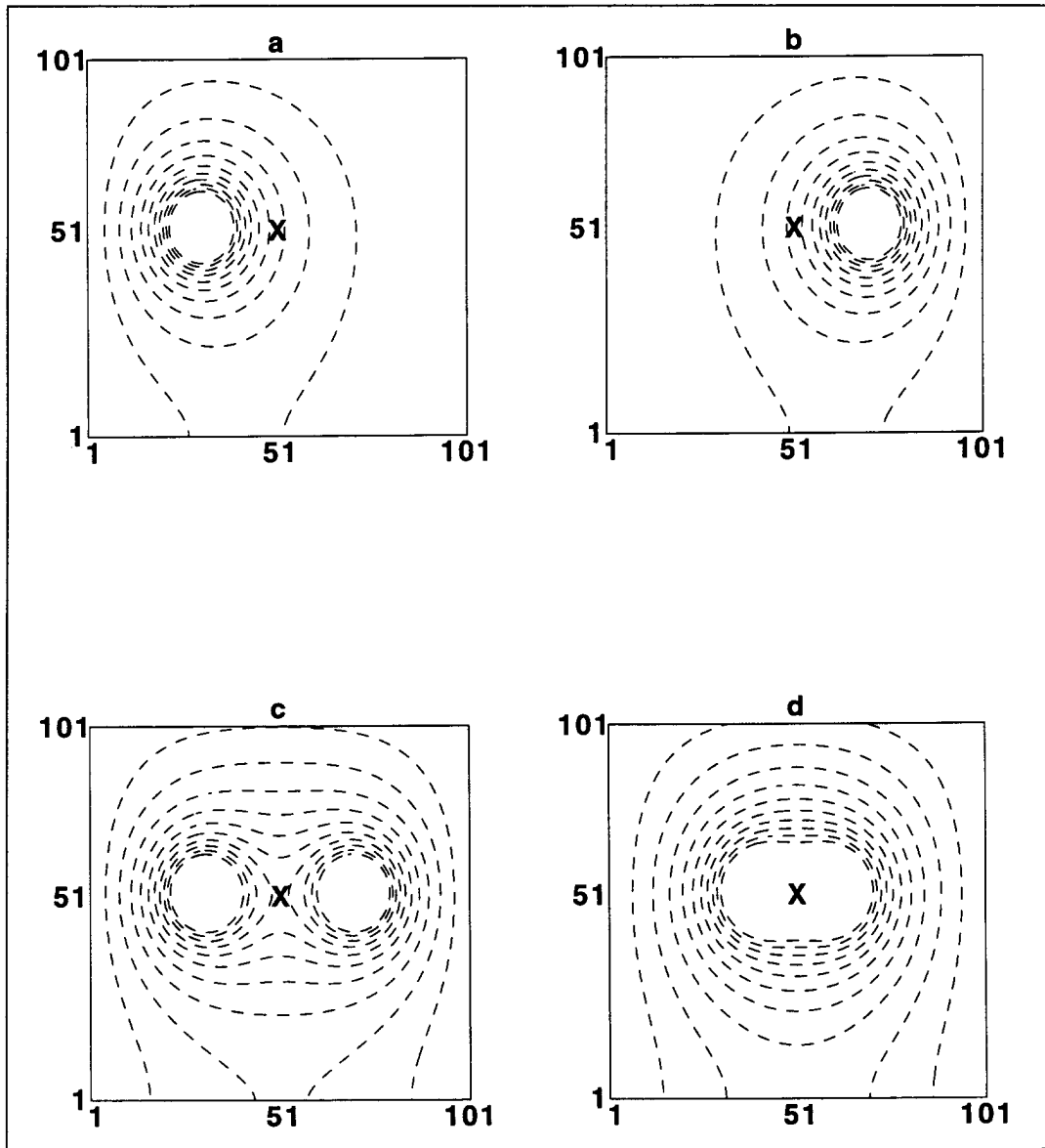


Fig. 3.5. Vertical cross sections through the resulting geopotential height fields associated with a single interior QGPV anomaly and multiple interior QGPV anomalies. The horizontal axis is in the  $x$  direction. The vertical axis is the scaled pressure coordinate described in the text. In a) a positive QGPV anomaly was put at  $x = 31$  and in the middle of the  $p$  axis. In b) a positive QGPV anomaly was put at  $x = 71$  and in the middle of the  $p$  axis. In c) the two anomalies of (a) and (b) were combined. In d) the two anomalies were brought closer together ( $x = 41$  and  $61$ ). In all cases the anomaly had a radius of 10. The thick contours are nondimensional height (contour interval 4). All the contours are negative.

Another way to quantify the intensification of the geopotential field is by the (nondimensional) integrated kinetic energy throughout the entire domain. The integrated kinetic energy for the two charges separated by a greater distance, and the two charges located close together, after being scaled in relation to the single charge, are 2.0 and 2.2, respectively. The superposition of the two charges increased the integrated kinetic energy of the domain.

Using the concept of superposition, it is possible to describe the effect of differing horizontal scale between positive and negative anomalies associated with a given Rossby wave (Robinson 1989). For example, a Rossby wave of a given horizontal scale may have equal QGPV anomalies that look like the “+” and “-” on the left half of Fig. 3.6. The positive anomaly will have a certain response on “A”. The negative anomaly will have less effect on “A” since it is farther away (by distance “1” measured from the arc to the negative anomaly). The configuration on the right side of Fig. 3.6 has the same “+” and “-” anomalies, but they are separated by a greater distance. The effect of the negative anomaly on “A” will be less than in the previous case because the negative anomaly is farther away from “A” (e.g. “2” is greater than “1”). Thus, in the second example, the penetration depth of the positive anomaly is greater because, at a given distance, there is less cancellation (destructive interference) with neighboring anomalies.

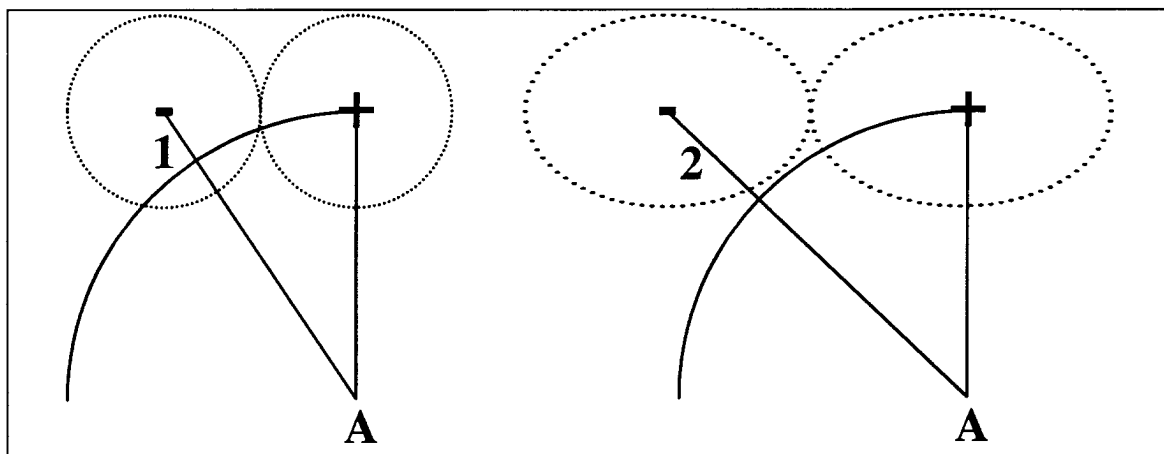


Fig. 3.6. A schematic diagram showing the effect of horizontal scale as applied to a Rossby wave. On the left, the “+” and “-” QGPV anomalies affect the geopotential height anomaly at point “A”. The “-” has less affect on “A” because it is farther away. On the right, the same “+” and “-” are separated by a greater distance due to a larger scale Rossby wave. The “-” has less of an affect on “A” than in the left hand diagram because it is farther away from “A”.

## 5. Thought behind QGPV thinking

Nielsen-Gammon, in an unpublished manuscript (Appendix 3), conceptualized many of the current theories of upper level mobile trough formation using schematic diagrams of potential vorticity. He presented a general overview of the distribution of potential vorticity for the following mechanisms:

1. baroclinic instability
2. barotropic instability
3. Riest-Farrell
4. trough-merger
5. group velocity (including downstream development)
6. deformation
7. digging-trough

The seven mechanisms listed above are based on Rossby-wave dynamics of large and small-scale geophysical flow (Rossby 1945, Petterssen 1956, Holton 1992). Since a constant pressure slice at any midtropospheric level will generally yield two distinct regions of QGPV separated by a narrow QGPV gradient, Nielsen-Gammon's schematics using a single potential vorticity contour are a conceptual simplification of the atmosphere. The wave motions along the potential vorticity contour will produce local areas of anomalously low and high potential vorticity. The QGPV anomalies are associated with locally cyclonic and anticyclonic circulation extending away from the location of the anomalies. The three-dimensional advection of the contour by the associated flow will further modify the contour and the resulting flow field--this is the essence of QGPV thinking.

The seven mechanisms presented in Appendix 3 are the result of two fundamental intensification processes: 1) one-way amplification, and 2) superposition. In one-way amplification the advective flow induced by the QGPV anomalies "blows" across the basic state QGPV gradient, carrying higher QGPV with it, and amplifies the perturbation. In superposition the QGPV anomalies are not amplified, but the geopotential height field is changed due to the reconfiguration of the QGPV anomalies.

For example, the baroclinic intensification mechanism occurs when there is mutual intensification on both waves along the upper and lower QGPV gradients (or surface temperature gradient). The baroclinic process is the combination of two one-way amplification mechanisms. Barotropic instability can be explained likewise, but the two processes occur at the same level. If the phase of the wave between the two QGPV gradients is constant, a normal mode baroclinic (barotropic) intensification process is occurring (Hoskins et al. 1985). Otherwise, if the phase is changing, but the waves continue to amplify each other a non-modal baroclinic (barotropic) process is occurring (Nielsen-Gammon 1995, Farrell 1982, Farrell 1989). The mobile trough development diagnostic used in this research uses the overall geopotential height as the measurement of trough intensification. If the trough intensifies (deepens), and the baroclinic process is present, the trough intensified due to baroclinic instability. If the trough does not intensify, but the baroclinic process was present, the process will be referred to as baroclinic amplification.

The superposition processes can involve multiple anomalies (point sources), the reconfiguration of a volume of QGPV, or both. The reconfiguration could be due to horizontal shearing deformation, horizontal stretching deformation or vertical shearing deformation. The superposition process contributes to the intensification whenever the multiple anomalies are brought closer together or the QGPV volume obtains a more spherical shape.

The group velocity mechanism, including the downstream development mechanisms described by Orlanski and colleagues (Orlanski and Sheldon 1993, Chang 1993, Chang and Orlanski 1993, Orlanski and Chang 1993, Orlanski and Katzfey 1991), can be summarized by a one-way intensification on a single potential vorticity contour. The energy dispersion into or away from the trough is evident by the intensification or decay of the flanking ridges near the trough. The intensification is classified downstream baroclinic development (DBD) or downstream development (DD) depending on mutual intensification is contributing to the wave energy. If the downstream intensification is



occurring in a baroclinically active region, DBD is occurring, otherwise only DD is occurring.

The Riest-Farrell, trough-merger and digging-trough mechanisms can be thought of as a combination of one-way amplification and vertical or horizontal superposition. These mechanisms may include an isolated vortex interacting with the basic state QGPV gradient. Thorncroft et al. (1993) provide two paradigms of a baroclinic wave life cycle resulting in cutoff vortices. The isolated vortices can be re-engulfed into the stratospheric reservoir, producing a mobile trough in the process.

## 6. Expected error in quasigeostrophic dynamics

The quasigeostrophic (QG) approximation is not a perfect representation of the atmospheric processes (Kuo et al. 1991). One of the main assumptions in the QG approximation is that the Rossby number ( $R_o = U/f_0L$ ) is small. If the Rossby number is small the magnitude of the ageostrophic motion is much smaller than the magnitude of the geostrophic motion. Also, the geostrophic wind is quasi-nondivergent; the vertical motion is almost exactly compensated by the ageostrophic divergence. Since the atmosphere remains in QUASIGEOSTROPHIC balance, the only vertical and horizontal ageostrophic motion allowed in the system is used to maintain thermal wind (geostrophic) balance (Eliassen 1984). It is helpful to partition the total wind into physically meaningful parts to determine where the QG system falls short.

Two common partition schemes are given by,

$$\mathbf{V} = \mathbf{V}_g + \mathbf{V}_{ag} \quad (3.20)$$

and

$$\mathbf{V} = \mathbf{V}_{IR} + \mathbf{V}_{ND} \quad (3.21)$$

where  $\mathbf{V}$  is the total wind,  $\mathbf{V}_g$  is the geostrophic wind,  $\mathbf{V}_{ag}$  is the ageostrophic wind,  $\mathbf{V}_{IR}$  is the irrotational (divergent) wind, and  $\mathbf{V}_{ND}$  is the nondivergent (rotational) wind. If (3.20) and (3.21) are combined (schematically) the result is

$$\mathbf{V} = \mathbf{V}_{g,IR} + \mathbf{V}_{g,ND} + \mathbf{V}_{ag,IR} + \mathbf{V}_{ag,ND} \quad (3.22)$$

where the combined subscripts have the same meaning as the individual parts in (3.20) and (3.21).

The first term on the right hand side of (3.22) is often assumed to equal zero, but the geostrophic wind is only quasi-nondivergent--it has an irrotational part. If the divergence of the geostrophic wind is written

$$\nabla \bullet \mathbf{V}_g = \frac{\partial u_g}{\partial x} + \frac{\partial v_g}{\partial y} \quad (3.23)$$

where  $u_g$  and  $v_g$  are the west-to-east and south-to-north components of the geostrophic wind ( $\mathbf{V}_g$ ), and  $\nabla$  is the two-dimensional gradient operator. By definition,  $u_g$  and  $v_g$  are

$$u_g = -\frac{1}{f} \frac{\partial \phi}{\partial y} \quad (3.24)$$

$$v_g = \frac{1}{f} \frac{\partial \phi}{\partial x} \quad (3.25)$$

If (3.24) and (3.25) are substituted in (3.23), then

$$\nabla \bullet \mathbf{V}_g = \frac{\partial}{\partial y} \left( \frac{1}{f} \frac{\partial \phi}{\partial x} \right) - \frac{\partial}{\partial x} \left( \frac{1}{f} \frac{\partial \phi}{\partial y} \right) \quad (3.26)$$

and after simplification the right hand side of (3.26) becomes

$$\frac{1}{f_0} \left( \frac{\partial^2 \phi}{\partial x \partial y} - \frac{\partial^2 \phi}{\partial x \partial y} \right) - \frac{1}{f_0^2} \frac{\partial \phi}{\partial x} \frac{\partial f}{\partial y} = \frac{v_g}{f_0} \frac{\partial f}{\partial y} \quad (3.27)$$

where  $f_0$  replaces  $f$ , except in the south-to-north derivative.

Therefore, the irrotational part of the geostrophic wind is equal to the right hand side of (3.27). The magnitude of  $\mathbf{V}_{g,IR}$  is small in the midlatitudes, and any advection of QGPV by this component of the geostrophic wind is neglected. The neglect of this advection will not produce any significant error. The last two terms on the right hand side of (3.22), however, can contribute to significant error.

The last term on the right hand side of (3.22) is the nondivergent, or rotational, part of the ageostrophic wind. According to gradient wind balance (see Chapter 3 of Holton 1992) the “real” wind (gradient wind) is subgeostrophic in the base of troughs and

supergeostrophic in the apex of ridges. Therefore, the geostrophic wind is stronger than the actual wind in troughs and weaker in ridges. Consequently, the magnitude of the relative vorticity and QGPV is greater than the “real” atmosphere in troughs and less than the “real” atmosphere in ridges. The advection of the erroneous QGPV in troughs and ridges will be a source of error.

The third term on the right hand side of (3.22) is the irrotational, or divergent, part of the ageostrophic wind. To help visualize the effect of this term on the error, the schematic model of a developing baroclinic cyclone will be used (Fig. 3.7 as adapted from Fig. 8.4 of Holton 1992). The low-level low pressure center (L in Fig. 3.7) is associated with convergence and upward vertical motion. The low-level high pressure center (H in Fig. 3.7) is associated with divergence and downward vertical motion. The upper-level region above the surface “low” is associated with divergence, and convergence occurs above the surface “high”. The trough tilts upshear, consistent with the baroclinic instability model presented earlier in this chapter.

The area on, or near, the mid-to-upper trough is in an area of downward vertical motion. If the irrotational part of the ageostrophic wind is large (the Rossby number is not small) it may advect high QGPV air from the stratospheric reservoir into the trough. The QGPV diagnostics neglect this advection of high QGPV air, and therefore, underestimate the QGPV generation in the trough. Thus, the irrotational part of the ageostrophic wind will contribute to the error.

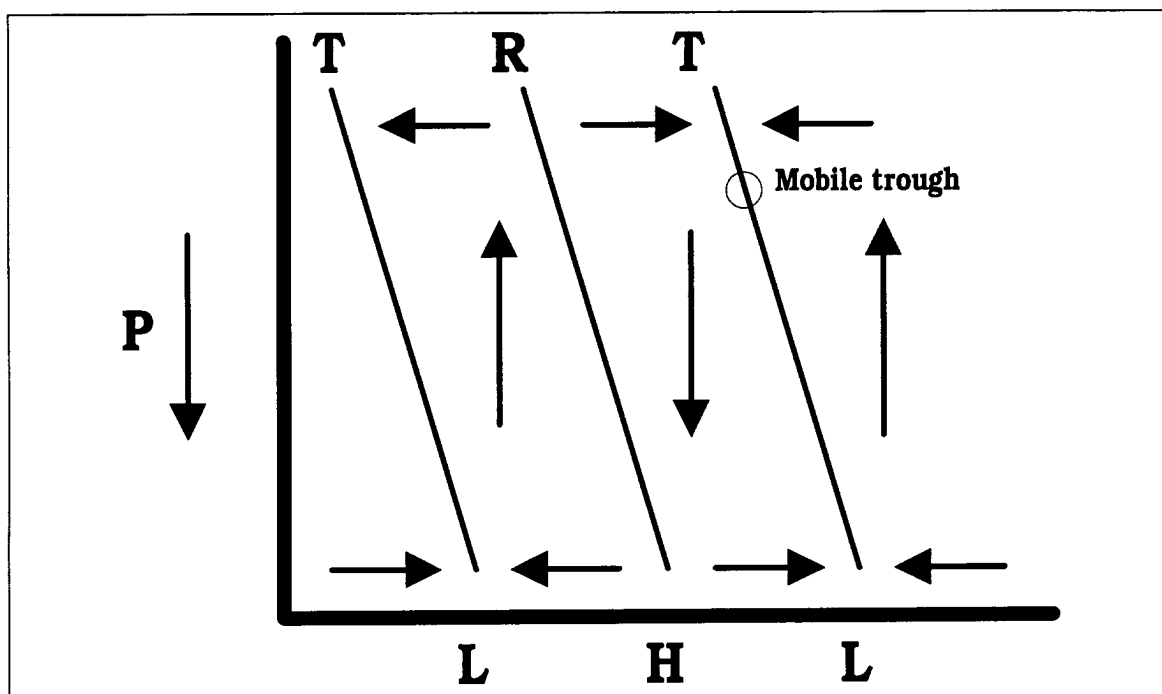


Fig. 3.7. A schematic model through a developing baroclinic system. The arrows indicate the ageostrophic flow. The vertical axis is pressure. The troughs (T) and ridge (R) tilt upshear.

The diabatic heating is neglected when developing the QG system of equations. For midtropospheric systems, the main source of diabatic heating is latent heat release associated with convection and upward vertical motion ahead of the midtropospheric trough, above the surface low pressure center (Fig. 3.7). The diabatic heating will increase the static stability and QGPV below the level of latent heat release, and decrease the QGPV above the level of latent heat release. The intensification of both the lower-level cyclone and upper-level ridge will be larger in the “real” atmosphere, but the QGPV diagnostics will not detect these differences (Davis and Emanuel 1991, Davis 1992b, Hoskins 1991). The diabatic contribution to the error is maximized downstream from the midtropospheric trough. It will not impact the diagnosis of mobile trough intensification as presented in this research.

Finally, surface friction was neglected in the derivation of QGPV. The neglect of boundary layer friction will not affect the instantaneous representation of QGPV in the middle and upper troposphere because it is sufficiently diminished away from the boundary layer. Furthermore, the lowest level used in the QGPV analyses presented here is 922 mb, not the surface. (See Chapter IV for a complete description of the vertical levels used in this research.)

## 7. Summary

QGPV thinking is a viable alternative to the traditional diagnostic tools. The advantage of QGPV diagnostics is that the complete three-dimensional nature of quasigeostrophic motion is embedded within one easy-to-manipulate quantity. The beauty of QGPV thinking is that the QGPV is conserved following geostrophic flow, and the QGPV can be inverted to recover the exact atmospheric structure associated with the QGPV. Together, the conservation and invertibility of QGPV allow one to compute the complete kinematic and dynamic character of the quasigeostrophic atmosphere. However, the QGPV assumption is not a perfect representation of the real atmosphere. Some error is inevitable due to the ageostrophic motions not present in the QG system. Diabatic heating and friction will not affect the diagnostics of mobile trough intensification.

This chapter discussed two foundational midtropospheric mobile trough initiation and maintenance mechanisms, one-way intensification and superposition. Nielsen-Gammon (Appendix 3) outlined seven specific intensification mechanisms based on this foundation:

1. Baroclinic instability
2. Barotropic instability
3. Riest-Farrell
4. Trough-merger
5. Group velocity
6. Deformation
7. Digging

Nielsen-Gammon (1995) qualitatively analyzed a case of mobile trough formation and suggested the group velocity and deformation mechanisms may have been the key players in the trough's development. The focus of this research will be to develop a method to quantitatively diagnose the mechanisms discussed in this chapter from the framework of QGPV.

## CHAPTER IV

### DATA AND METHOD

The purpose of this chapter is to describe the data used in the quasigeostrophic potential vorticity (QGPV) analyses, the choice of a basic state within which the QGPV anomalies are assumed to be embedded, and the explicit method used to invert (solve) the QGPV equation (3.7). The theoretical discussion of QGPV thinking covered in the last chapter provided the background for using the QGPV approach. However, the details of the basic state were omitted. The theory behind selecting a basic state will be included here, along with a discussion of alternate basic states.

#### 1. Data

The data used in this study (Data Set Number DS082.0) was prepared and maintained by the Data Support Section, Scientific Computing Division, National Center for Atmospheric Research (NCAR). NCAR is operated by the University Corporation for Atmospheric Research and is sponsored by the National Science Foundation.

The twice daily (0000 UTC and 1200 UTC) geopotential height data was extracted from the National Meteorological Center (NMC) final analyses for November and December 1980 (Dey 1989, Kanamitsu 1989, Kanamitsu et al. 1991). The final analyses were prepared using a 12-layer rhomboidal spherical harmonic truncation (R24). The NMC global data at each of ten pressure levels (1000 mb, 850 mb, 700 mb, 500 mb, 400 mb, 300 mb, 250 mb, 200 mb, 150 mb, and 100 mb) was archived on a  $2.5^\circ$  by  $2.5^\circ$  rectangular longitude-latitude grid. The complete global data set was available, but only the northern hemisphere was used in this study. Therefore, each time of the data set consists of three-dimensional geopotential height values in a 145 by 37 by 10 matrix.

#### 2. Basic state possibilities

The choice of a basic state,  $\bar{q}$ , upon which the QGPV anomalies,  $q'$ , propagate is somewhat arbitrary, but will dictate the interpretation of the results. The basic state should be quasistationary and represent the mean conditions of the background flow. In

addition, the signal, which are the mobile troughs in this case, should not be combined with the basic state. Various possible basic state configurations will be described, beginning with the trivial and ending with the more complex.

Recall the definition of QGPV from (3.7) given by,

$$q \equiv \frac{g}{f_0} \nabla^2 z + f + g f_0 \frac{\partial}{\partial p} \left( \frac{1}{\sigma} \frac{\partial z}{\partial p} \right) \quad (4.1)$$

where

$$\sigma = -\frac{R}{p_0} \left( \frac{p_0}{p} \right)^{c_p} \frac{d\theta_s}{dp} \quad (4.2)$$

The trivial basic state QGPV configuration is where the mean global QGPV equals zero ( $\bar{q}^G = 0$ ). The perturbation QGPV ( $q'^G = q - \bar{q}^G$ ) is the total QGPV in this case. This trivial basic state does not offer much help, because the mobile troughs are combined with the basic state waves.

Hoskins et al. (1985) chose the distribution of planetary vorticity,  $f$ , as their basic state when they discussed QGPV inversion, namely

$$\bar{q}^f = f \quad (4.3)$$

leaving

$$q'^f = \frac{g}{f_0} \nabla^2 z'^f + g f_0 \frac{\partial}{\partial p} \left( \frac{1}{\sigma} \frac{\partial z'^f}{\partial p} \right) \quad (4.4)$$

as the perturbation. Since the Coriolis parameter only varies in the meridional direction, this basic state is like having the same zonal mean for all levels. The advantage of this basic state is its simplicity. The disadvantage is that it assumes the perturbations propagate on a basic state that is identical at all levels.

Charney and Stern (1962) used the zonal mean geopotential height as their basic state,

$$\bar{q}^\lambda = f + \frac{g}{f_0} \nabla^2 \bar{z}^\lambda + g f_0 \frac{\partial}{\partial p} \left( \frac{1}{\sigma} \frac{\partial \bar{z}^\lambda}{\partial p} \right) \quad (4.5)$$

with the remaining perturbation being



$$q'^{\lambda} = \frac{g}{f_0} \nabla^2 z'^{\lambda} + g f_0 \frac{\partial}{\partial p} \left( \frac{1}{\sigma} \frac{\partial z'^{\lambda}}{\partial p} \right) \quad (4.6)$$

The advantage of the Charney and Stern basic state is also simplicity. The zonal mean geopotential height is not a poor choice because the mean atmosphere averaged over all seasons is fairly zonal, especially in the middle and upper troposphere. However, the zonal mean neglects all the inhomogeneities associated with the land-ocean contrast and topography. It also combines the long waves into the short wave or mobile trough partition.

The time mean is another obvious choice for a basic state, resulting in a QGPV field defined by

$$\bar{q}' = f + \frac{g}{f_0} \nabla^2 \bar{z}' + g f_0 \frac{\partial}{\partial p} \left( \frac{1}{\sigma} \frac{\partial \bar{z}'}{\partial p} \right) \quad (4.7)$$

and a perturbation QGPV by

$$q'' = \frac{g}{f_0} \nabla^2 z'' + g f_0 \frac{\partial}{\partial p} \left( \frac{1}{\sigma} \frac{\partial z''}{\partial p} \right) \quad (4.8)$$

The advantage of a time-mean basic state is that it includes the stationary waves forced by the land-ocean differences and topography (Davis and Emanuel 1991, Davis 1992a). Only the mobile waves will be included in the perturbation, but many of the mobile waves will be large-scale and not truly short-wave mobile troughs. The purpose of this research is the study of mobile troughs, and implicitly short-waves. According to the Rossby wave dynamics discussed in Chapter III, the eastward moving mobile troughs are typically of shorter wavelengths.

Another possible choice of basic state, the choice used in this research, is the low-pass filtered data given by,

$$\bar{q}^{LP} = f + \frac{g}{f_0} \nabla^2 \bar{z}^{LP} + g f_0 \frac{\partial}{\partial p} \left( \frac{1}{\sigma} \frac{\partial \bar{z}^{LP}}{\partial p} \right) \quad (4.9)$$

with the resulting perturbation QGPV (high-pass) given by,

$$q' = q^{HP} = \frac{g}{f_0} \nabla^2 z^{HP} + g f_0 \frac{\partial}{\partial p} \left( \frac{1}{\sigma} \frac{\partial z^{HP}}{\partial p} \right) \quad (4.10)$$

The advantage of the low-pass basic state is the perturbation QGPV is truly a perturbation from the given long-wave pattern at any given time. The desired range of scales associated with mobile troughs can be preferentially selected and partitioned into the component of perturbation QGPV. Therefore, the inversion of the perturbation QGPV field will truly be due to the short-wave mobile troughs. The disadvantage of the low-pass basic state is the subjectivity of the break between large-scale and small-scale. If the break is not clean or natural, then some of the perturbation QGPV will be partitioned with the basic state and some will be with the perturbation if scales fluctuate during the life cycle of the wave. Another disadvantage of the low-pass basic state is that the basic state is a function of time.

Two additional choices for a basic state are a time-zonal-mean as given by,

$$\bar{q}^{TZ} = f + \frac{g}{f_0} \nabla^2 \bar{z}^{TZ} + g f_0 \frac{\partial}{\partial p} \left( \frac{1}{\sigma} \frac{\partial \bar{z}^{TZ}}{\partial p} \right) \quad (4.11)$$

and the long-wave-time-mean is given by,

$$\bar{q}^{LT} = f + \frac{g}{f_0} \nabla^2 \bar{z}^{LT} + g f_0 \frac{\partial}{\partial p} \left( \frac{1}{\sigma} \frac{\partial \bar{z}^{LT}}{\partial p} \right) \quad (4.12)$$

The advantage of the time-zonal-mean (4.11) is that the stationary effects on the amplitude are captured while assuming a zonal flow. The disadvantages of this basic state are similar to both the time-mean and the zonal mean basic states. This basic state was not used because of the desire to preferentially select the short-wave mobile troughs.

The most difficult basic state considered was the long-wave-time-mean (4.12) because the time-filtered data would have to be calculated for the entire trough life span beforehand. The perturbation QGPV would have to be calculated during a second pass through the data. The advantage of this method would be to truly separate the quasistationary, large-scale waves from the mobile, small-scale waves. There is a subtle difference between (4.7) and (4.12). In the time-mean basic state, (4.7), all moving waves would be included in the perturbation partition. In the long-wave-time-mean (4.12) only

those waves of sufficiently short wavelength and moving would be partitioned in the perturbation. The slow moving long waves would be partitioned with the basic state. The low-pass basic state proved to be sufficiently robust while also being economical. The long-wave-time-mean basic state would be an obvious next step in future research.

### 3. Low-pass basic state

The low-pass basic state QGPV,  $\bar{q}$ , hereafter called the large-scale, is given by (4.9), and the resulting perturbation QGPV,  $q'$ , hereafter called the small-scale, is given by (4.10). The purpose of this section is to quantify the method used to partition the large-scale from the small-scale. This section will provide an overview of the spherical harmonic filtering method, and document the trials used to select the appropriate break between large- and small-scale.

#### *a. Overview of spherical harmonic method*

The spherical harmonic analysis tool (SPHEREPACK Version 1.1) was written by John Adams and Paul Swarztrauber of the National Center for Atmospheric Research (NCAR). SPHEREPACK can be obtained by anonymous File Transfer Protocol (ftp) to the Distributed Software Libraries at NCAR (the ftp site is ftp.ucar.edu). SPHEREPACK is a package of Fortran subroutines for computing spherical harmonic analyses (the transformation into harmonic space) and synthesis (the inverse transform back to grid point space).

Spherical harmonic analysis is used for problem solving in spherical coordinates in the same way Fourier analysis is used in Cartesian coordinates. Interpolation and smoothing on the sphere is significantly facilitated by harmonic analysis. In addition, harmonic analysis is used to eliminate the computational difficulties unique to a sphere, including the accuracy problems created by computing differential expressions at the poles (SPHEREPACK Documentation, 1992).

The basic premise behind using spherical harmonics (tailored to QGPV calculations) is to expand the geopotential height field ( $z$ ) using the appropriate associated Legendre polynomials basic set as follows,

$$z = a^2 \sum_m^M \sum_{n-m}^N (z_n^m P_n^m(\mu) e^{im\lambda}) = a^2 \sum_m^M \sum_{n-m}^N (z_n^m Y_n^m(\mu, \lambda)) \quad (4.13)$$

where

$a = 6.37 \times 10^6$  m, the radius of the earth

$m$  is the index for wave numbers around a latitude circle

$M = 72$ , the maximum wavenumber allowed for 145 grid points in SPHEREPACK

$n-m$  is the number of zero crossings (nodes) between the South and North Poles

$N = 72$ , the maximum value of  $n$  allowed for 37 grid points in the latitudinal direction

$z_n^m$  are complex coefficients such that  $(z_n^m)^* = (-1)^m z_n^{-m}$  where the  $*$  means the complex conjugate

$\lambda$  is the longitude

$\mu = \sin(\varphi) = \cos(1-\varphi)$ , where  $\varphi$  is the latitude and  $(1-\varphi)$  is the colatitude

$$P_n^m(\mu) = \left[ \frac{(2n+1)(n-m)!}{2(n+m)!} \right]^{\frac{1}{2}} \left[ \frac{(1-\mu^2)^{\frac{m}{2}}}{2^n n!} \right] \left[ \frac{d^{(m+n)}}{d\mu^{(m+n)}} (\mu^2 - 1)^n \right] \quad \text{are the normalized}$$

associated Legendre polynomials

$Y_n^m(\mu, \lambda) = P_n^m(\mu) e^{im\lambda}$  are the spherical harmonic basis functions.

The spherical harmonic expansion simplifies the representation of the Laplacian operator in computing the relative vorticity part of QGPV. The Laplacian operator becomes,

$$\nabla^2 z = -\frac{n(n+1)}{a^2} z_n^m \quad (4.14)$$

The computation of QGPV is simply a matter of transforming the relative vorticity, Coriolis parameter ( $f$ ), and stratification terms into spherical harmonic space and adding (matrix addition) their complex coefficients. Once the QGPV is transformed into spherical harmonic space it is available for low-pass filtering and an inverse transformation (synthesis) back into grid point space. A schematic of the processes using SPHEREPACK may help in visualizing the process (Fig. 4.1).

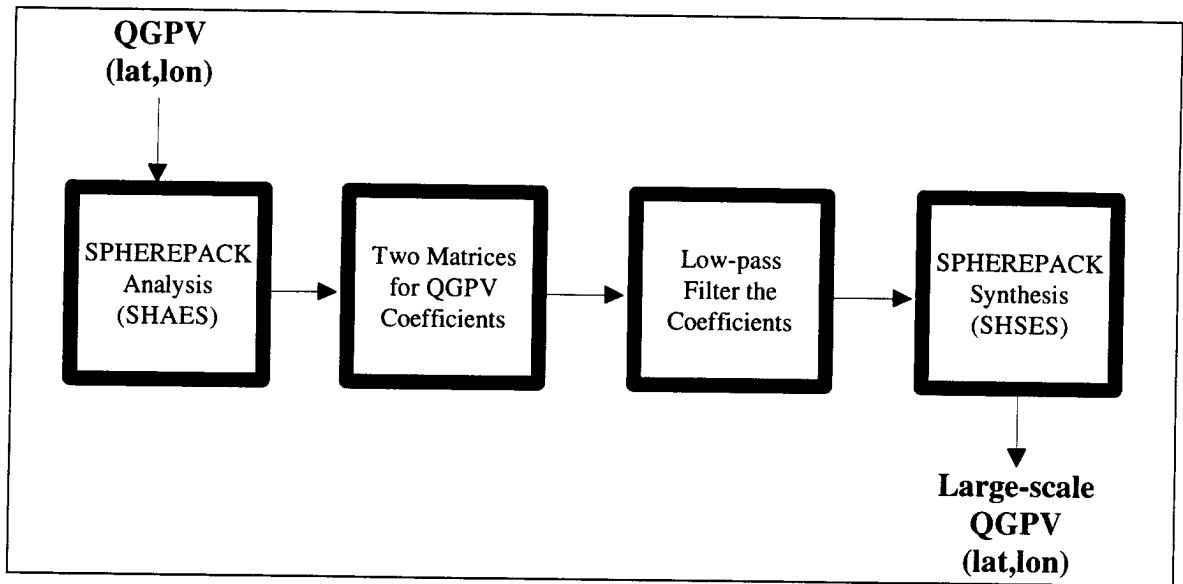


Fig. 4.1. A schematic diagram of the spherical harmonic process used to get the large-scale QGPV field.

Since only the northern hemisphere is used, the user has an option in SPHEREPACK of assuming a symmetric or antisymmetric distribution of geopotential height across the Equator. Since the geopotential height is symmetric, the symmetric option was chosen. The antisymmetric option was tested and produced similar results. The largest discrepancy occurred at the Equator.

Chapter IV of Washington and Parkinson (1986) gives a detailed description of spherical harmonic analyses, and their Appendix B gives a detailed description of associated Legendre polynomials. Alternate descriptions of spherical harmonic application to geopotential height data can be found in Haltiner and Williams (1980), Blackmon (1976), Eliassen and Machenhauer (1965), Eliassen and Machenhauer (1969), and Pratt (1976).

When low-pass filtering the complex coefficients, the shape of the truncation is important. There are two truncation configurations (Fig. 4.2) possible: 1) triangular, and 2) rhomboidal. The advantage of the rhomboidal truncation is the increased structure in the south-to-north direction due to including more of the large total wavenumbers ( $n-m$ ) in the large-scale partition. Both truncations were tested, and the rhomboidal truncation produced a more realistic large-scale pattern without sacrificing much short-wave energy in the perturbation partition.

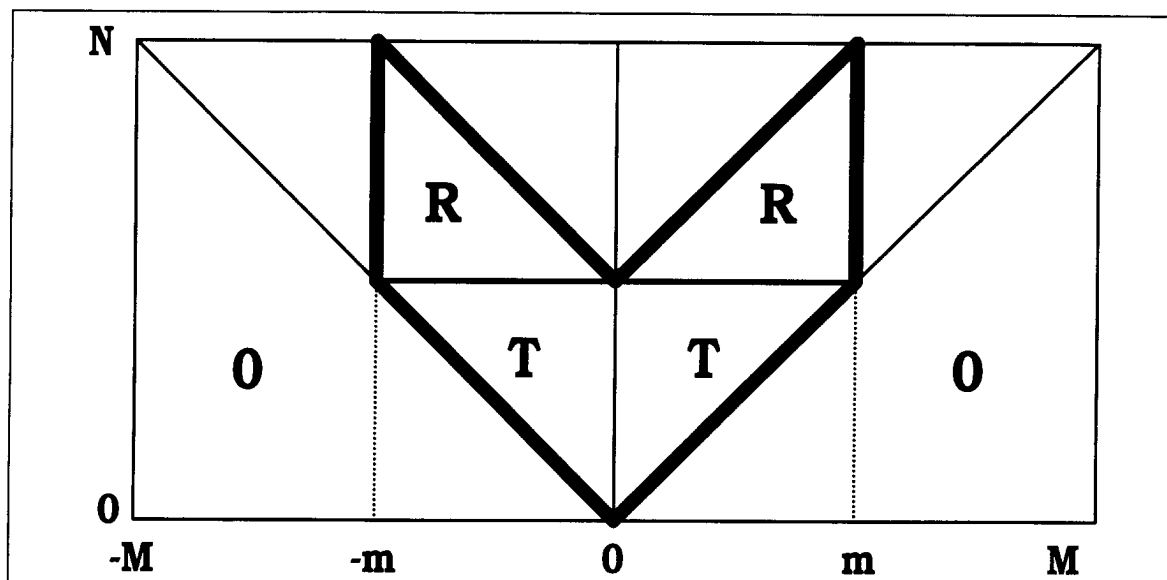


Fig. 4.2. A schematic diagram of triangular (T) and rhomboidal (R) truncation. The  $M$  and  $N$  are the dimensions of the spherical harmonic arrays.  $M$  is the number of zonal wavenumbers, and  $m$  is the large-to-small-scale cutoff. The meridional scale using triangular truncation is bounded by the triangles marked with a T. The meridional scale using rhomboidal truncation includes both the T and R areas. The coefficients below the diagonal lines extending from 0 are all equal to zero (0).

*b. Choosing the large-scale*

Blackmon (1976) analyzed 10 years of 500 mb northern hemisphere geopotential height data using spherical harmonics and time filters. He defined three categories of waves in the spatial domain:

Large-scale	Zonal wavenumbers 0 through 6
Medium-scale	Zonal wavenumbers 7 through 12
Small-scale	Zonal wavenumbers 13 through 18

Using the time filter analyses, he found the low frequency oscillations (period greater than or equal to 15 days) typically occurred with wavenumbers 0 through 7. The high frequency oscillations (period less than or equal to 5 days) had the most power in wavenumbers 10 through 12. He also found the large-scale waves generally propagate toward the west, while the medium and small-scale waves propagate toward the east.

Eliassen and Machenhauer (1965) used spherical harmonics to analyze the spectral distribution of kinetic energy for 500 mb flow during January 1957. They estimated the kinetic energy by,

$$KE = \begin{cases} \frac{1}{2}n(n+1)(A_n^0)^2 & \text{for } m = 0 \\ \frac{1}{4}n(n+1)[(A_n^m)^2 + (B_n^m)^2] & \text{for } m \neq 0 \end{cases} \quad (4.15)$$

where  $A$  and  $B$  are the complex conjugate pairs (coefficients) associated with the 500 mb streamfunction field. Their results did not show a clean break between large and small-scale flow in the kinetic energy distribution.

Gall (1976) studied the structural changes of growing baroclinic waves within a primitive equation model. He was primarily interested in the interactions between the zonal mean basic state and the small-scale perturbations. He showed that short-waves (wavenumber 15) have larger growth rates than longer waves (wavenumber seven), but the maximum eddy kinetic energy of the system occurred at wavenumber seven. This result indicates there may be a natural break in scale around wavenumber seven.



The choice of the low-pass cutoff to delineate the large-scale flow was somewhat arbitrary. In order to decrease the subjectivity of the large-to-small-scale cutoff, the power (amplitude) of each spherical harmonic was computed by using,

$$\text{Power} = \left| (z_n^m)(z_n^m)^* \right| \text{ for each } m \text{ and } n,$$

where the \* means using the complex conjugate. A log-plot of each zonal wavenumber ( $m$ ) for geopotential height, relative vorticity and QGPV (Fig. 4.3) did not reveal a clean break between large-scale and small-scale processes. Except for the dip in power at wavenumber five, one could argue for a break near wavenumber six or seven. The difference between the geopotential height line in Fig. 4.3 and the relative vorticity line is due to the Laplacian operator accentuating the small-scale features.

The method used to break the large-scale from the small-scale in this research is more practical and straight-forward for mobile trough analysis. The large-scale flow was determined by screening several examples of mobile troughs, as identified and tracked using the objective method of Chapter II. The low-pass filter was “tuned” to include the mobile troughs on the small-scale side of the break. The small-scale features of QGPV were trackable for multiple days. An example of the geopotential height analyses showing the zonal wavenumber break is provided in Figs. 4.4 through 4.6. The total geopotential height field at 472 mb (Fig. 4.4) shows a mobile trough, identified by the objective method, extending south from the Great Lakes. When the spherical coefficients were truncated at wavenumber seven (Fig. 4.5) the mobile trough appeared in the large-scale analysis. When the spherical coefficients were truncated at wavenumber six (Fig. 4.6) the mobile trough was omitted from the large-scale flow. Since the appearance of the mobile trough in the large-scale flow is undesirable, the large-scale was chosen to be zonal wavenumbers zero through six. This result is consistent with the large-scale flow identified by Blackmon (1976).

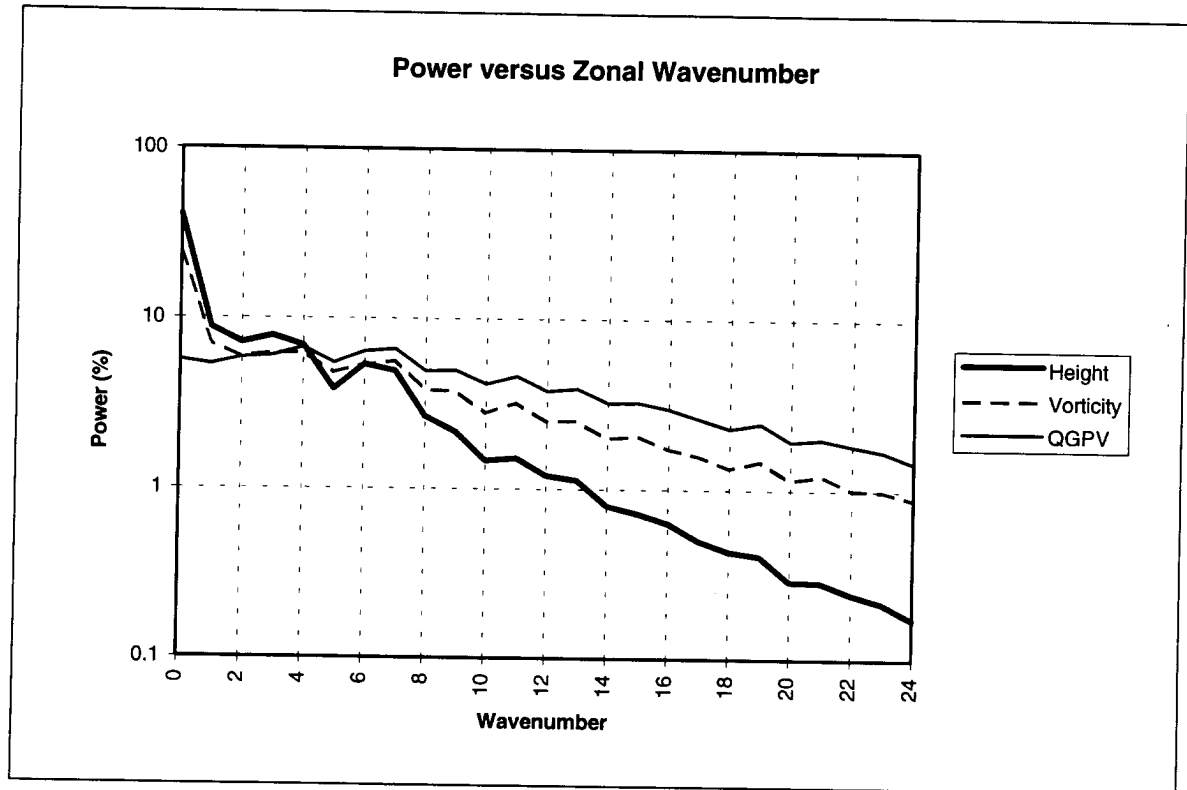


Fig. 4.3. A log-plot showing the normalized power of each zonal wavenumber ( $m$ ) for geopotential height, relative vorticity, and QGPV.

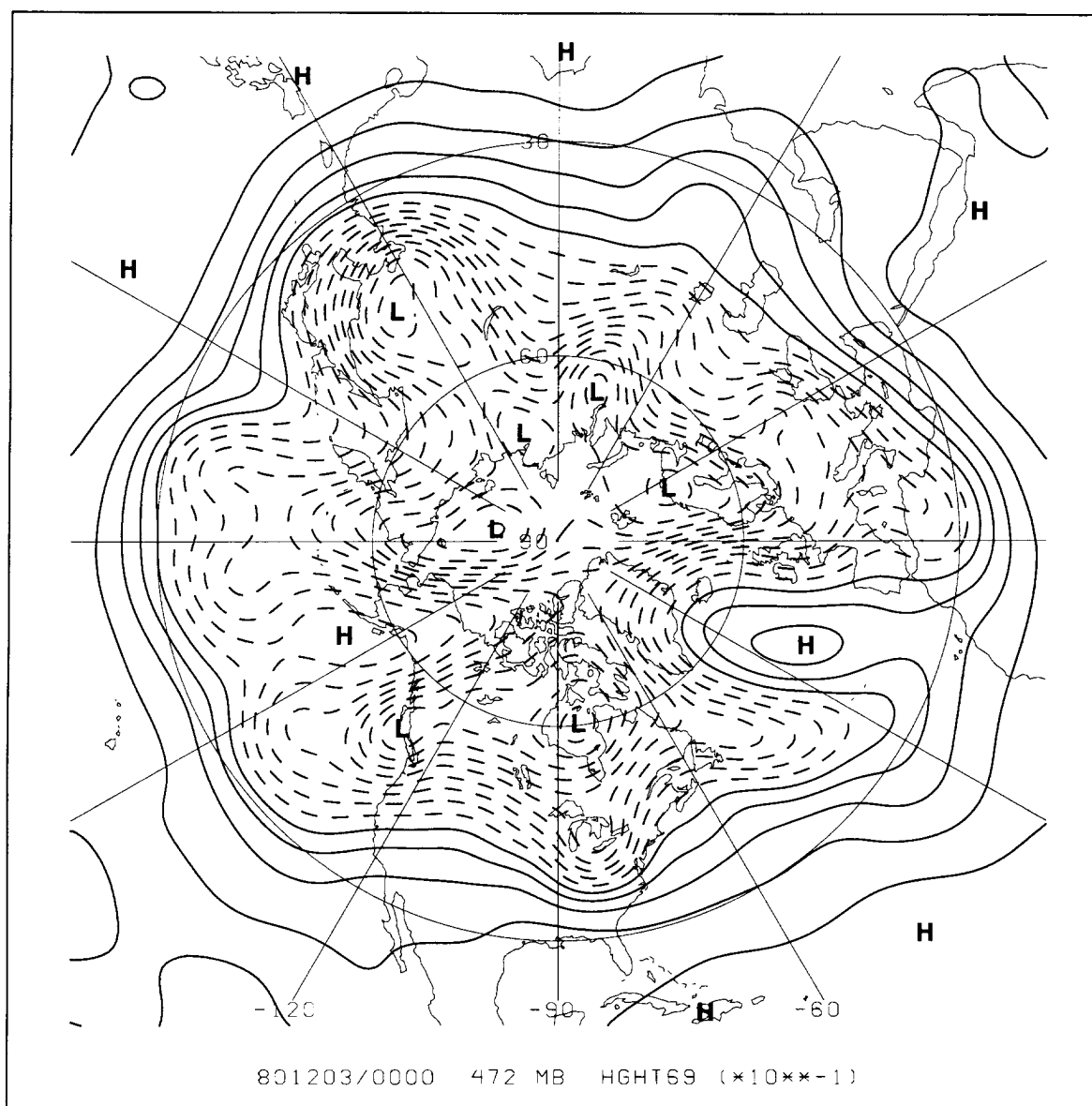


Fig. 4.4. The full geopotential height field at 472 mb for 0000 UTC 3 December 1980. The contour interval is 6 dam, and negative contours are dashed. The first solid contour is equal to zero.

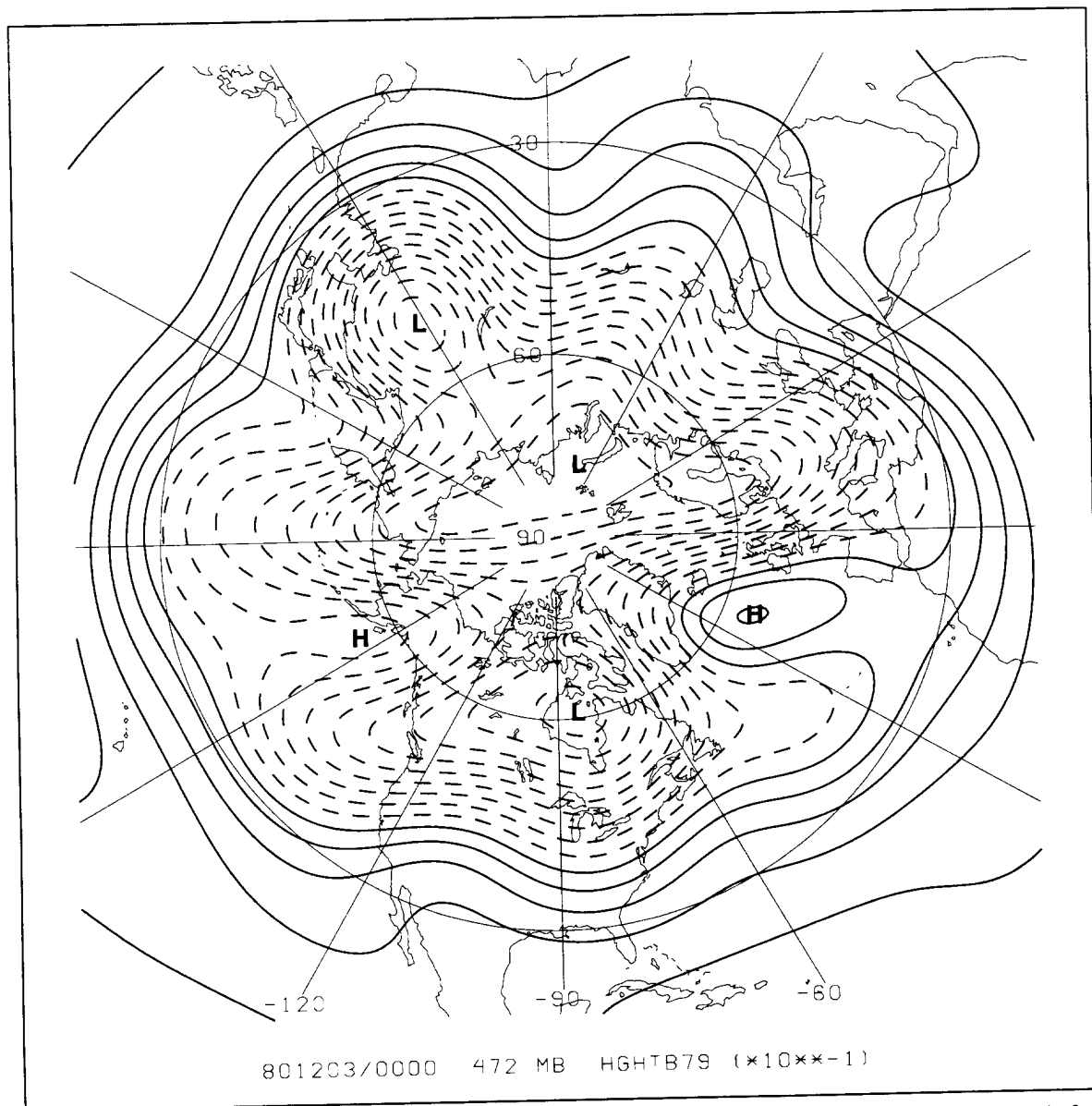


Fig. 4.5. The low-pass geopotential height field using only wavenumbers 0 through 7 at 472 mb for 0000 UTC 3 December 1980. The contour interval is 6 dam, and negative contours are dashed. The first solid contour is equal to zero.

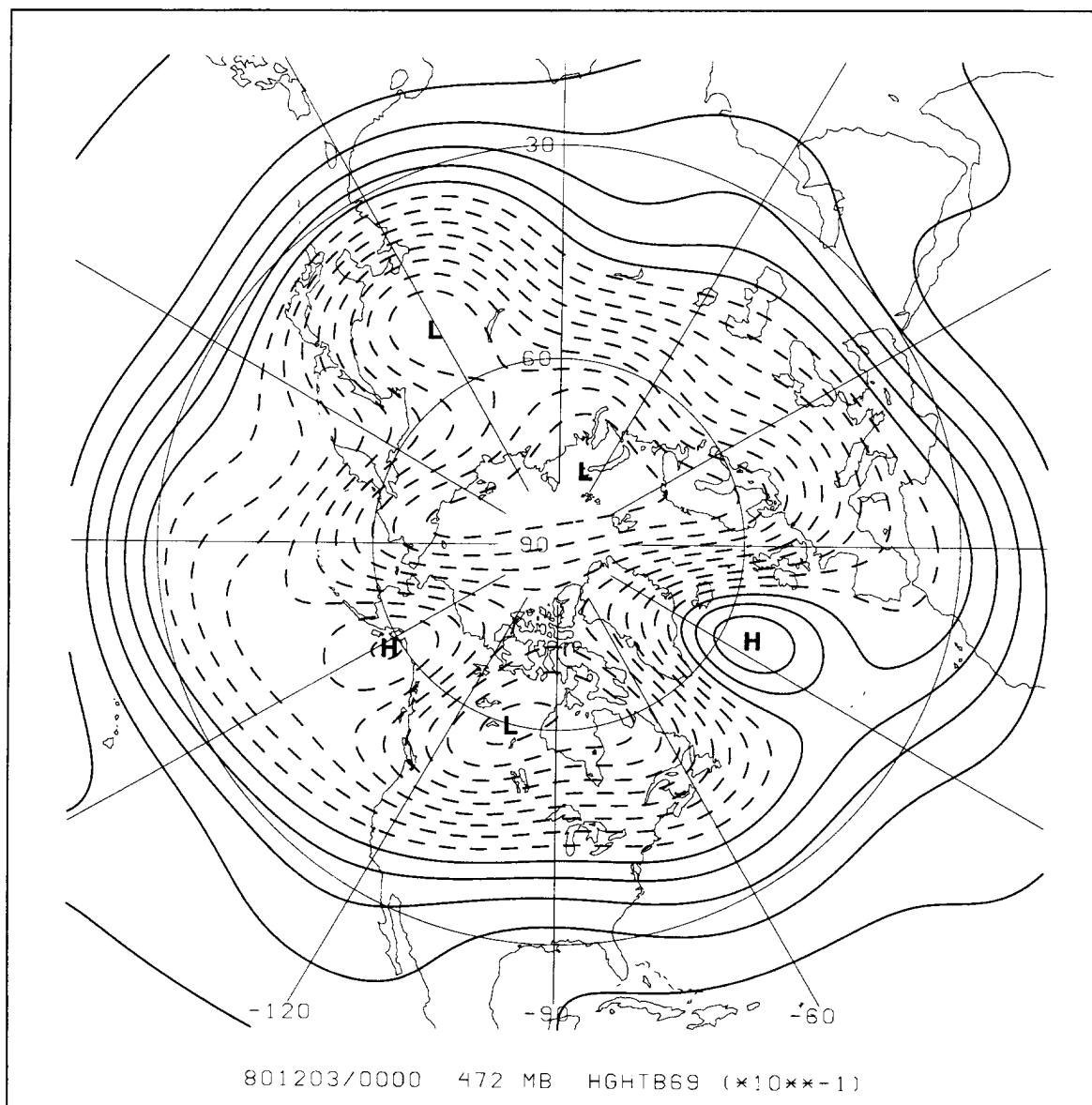


Fig. 4.6. The low-pass geopotential height field using only wavenumbers 0 through 6 at 472 mb for 0000 UTC 3 December 1980. The contour interval is 6 dam, and negative contours are dashed. The first solid contour is equal to zero.

The meridional or total wavenumber cutoff ( $n-m$ ) was determined by the appearance of the large-scale pattern. The full geopotential height field at 472 mb (Fig. 4.4) reveals locations where multiple tight gradients of geopotential height (jet streams) occur in the meridional direction. It was desirable to keep as much of this meridional structure as possible. When the total wavenumber cutoff ( $n-m$ ) was decreased below nine (for example,  $n-m = 6$  in Fig. 4.7) the north-south jet structure was smeared out. In Fig. 4.6 the total wavenumber cutoff ( $n-m$ ) was nine and the meridional structure remained in the large-scale.

#### 4. QGPV inversion method

The purpose of this section is to describe, in detail, the quasigeostrophic potential vorticity (QGPV) inversion algorithm used in this research. The QGPV equation from Chapter III is repeated here for reference purposes,

$$q = \frac{g}{f_0} \nabla^2 z + f + g f_0 \frac{\partial}{\partial p} \left( \frac{1}{\sigma} \frac{\partial z}{\partial p} \right) \quad (4.16)$$

where  $z$  is the deviation of geopotential height from the northern hemisphere mean geopotential height ( $z_s$ ) at each of the ten model levels. The  $z$  in the Laplacian of the relative vorticity term does not need to be a deviation, but doing so does not change the Laplacian. The reference static stability ( $\sigma$ ) is given by,

$$\sigma(p) = -\frac{R}{p_0} \left( \frac{p_0}{p} \right)^{\frac{c_v}{c_p}} \frac{d\theta_s}{dp} \quad (4.17)$$

where  $\theta_s$  is based on the northern hemisphere average potential temperature from January through December 1980 at the eight interior levels (not including 1000 mb and 100 mb). It was constructed by summing the potential temperature at each gridpoint at each level at each time and dividing by the total number of time steps.

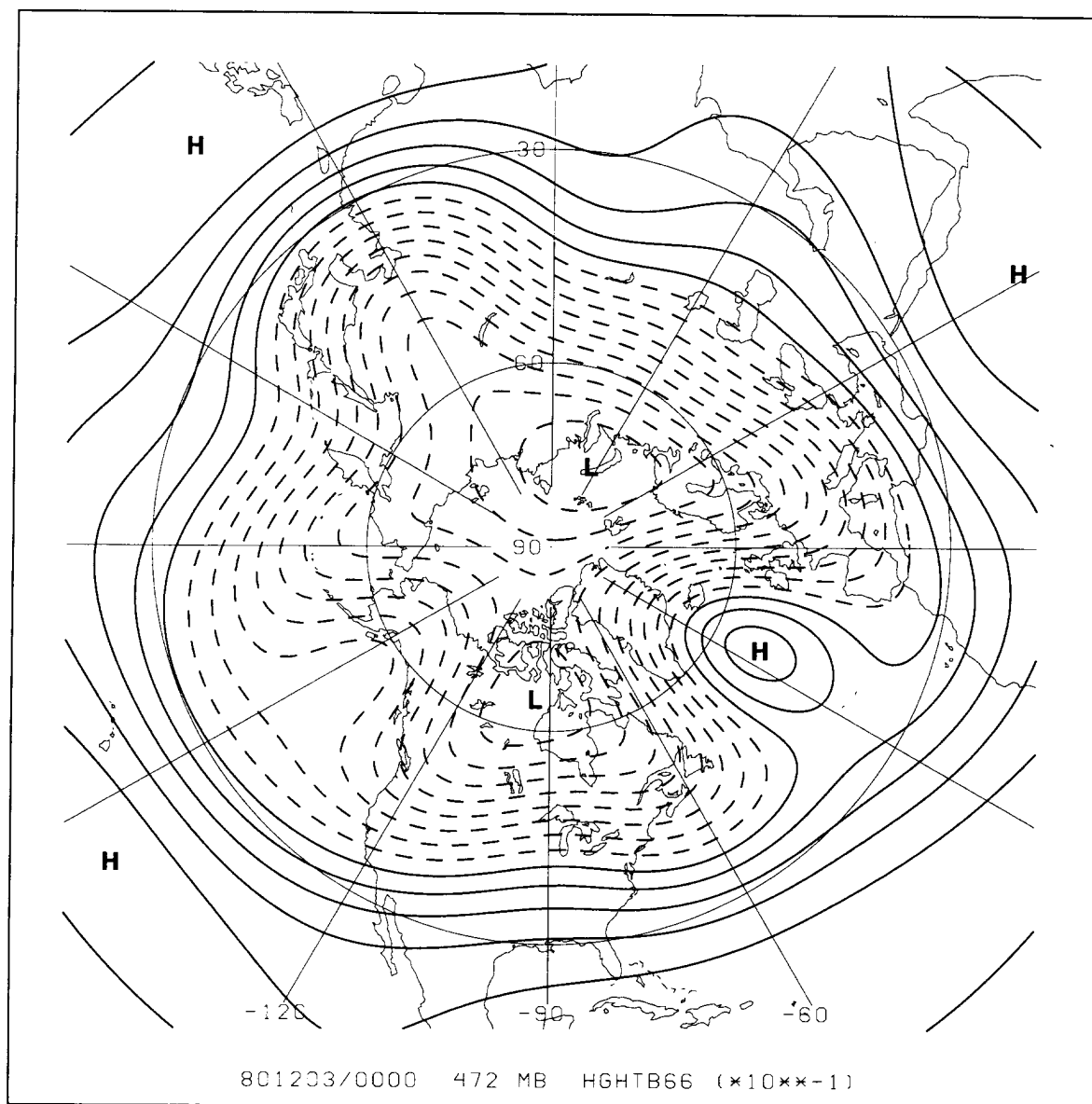


Fig. 4.7. The large-scale geopotential height field using zonal wavenumbers 0 through 6 and total wavenumbers ( $n-m$ ) 0 through 6 at 472 mb for 0000 UTC 3 December 1980. The contour interval is 6 dam, and negative contours are dashed. The first solid contour is equal to zero.

The use of the National Meteorological Center (NMC) 1000 mb temperature for boundary conditions in the inversion yielded erroneous results. This error was determined by comparing the 1000 mb potential temperature field with the potential temperature field calculated using the hydrostatic equation for several days. The analyses were comparable, except over high terrain. It appears the NMC extrapolation of tropospheric temperatures to 1000 mb temperatures over high terrain during 1980 (the year used for testing) is questionable (Chris Davis, personal communication). Instead of using the 1000 mb temperature data, the vertically averaged basic state temperature at 922 mb was calculated by the combination of the hydrostatic equation, and the ideal gas law as follows,

$$T = -\frac{g}{R} \frac{\partial z}{\partial(\ln p)} \quad (4.18)$$

In (4.18)  $z$  is the total geopotential height, not the deviation height used in the QGPV calculations, and  $T$  is the total temperature based on the mean northern hemisphere 1000 mb and 850 mb geopotential height data. The same procedure is used to calculate the mean temperature for the 122 mb level. Therefore, the actual pressure levels used as input for the static stability ( $\sigma$ ) calculations were 922 mb, 850 mb, 700 mb, 500 mb, 400 mb, 300 mb, 250 mb, 200 mb, 150 mb, and 122 mb.

The geopotential height and temperature data at the ten pressure levels were interpolated to eight interior pressure levels (Fig. 4.8) by cubic splines. The cubic spline subroutines (SPLINE and SPLINT) were modified versions of those found in Press et al. (1992). The modifications allowed the first and second derivatives to be passed in and out of the subroutines. Fig. 4.8 shows the pressure levels upon which the QGPV and the stratification were defined, the intermediate pressure levels for the stability ( $\sigma$ ) calculations, and the pressure levels for the boundary conditions.



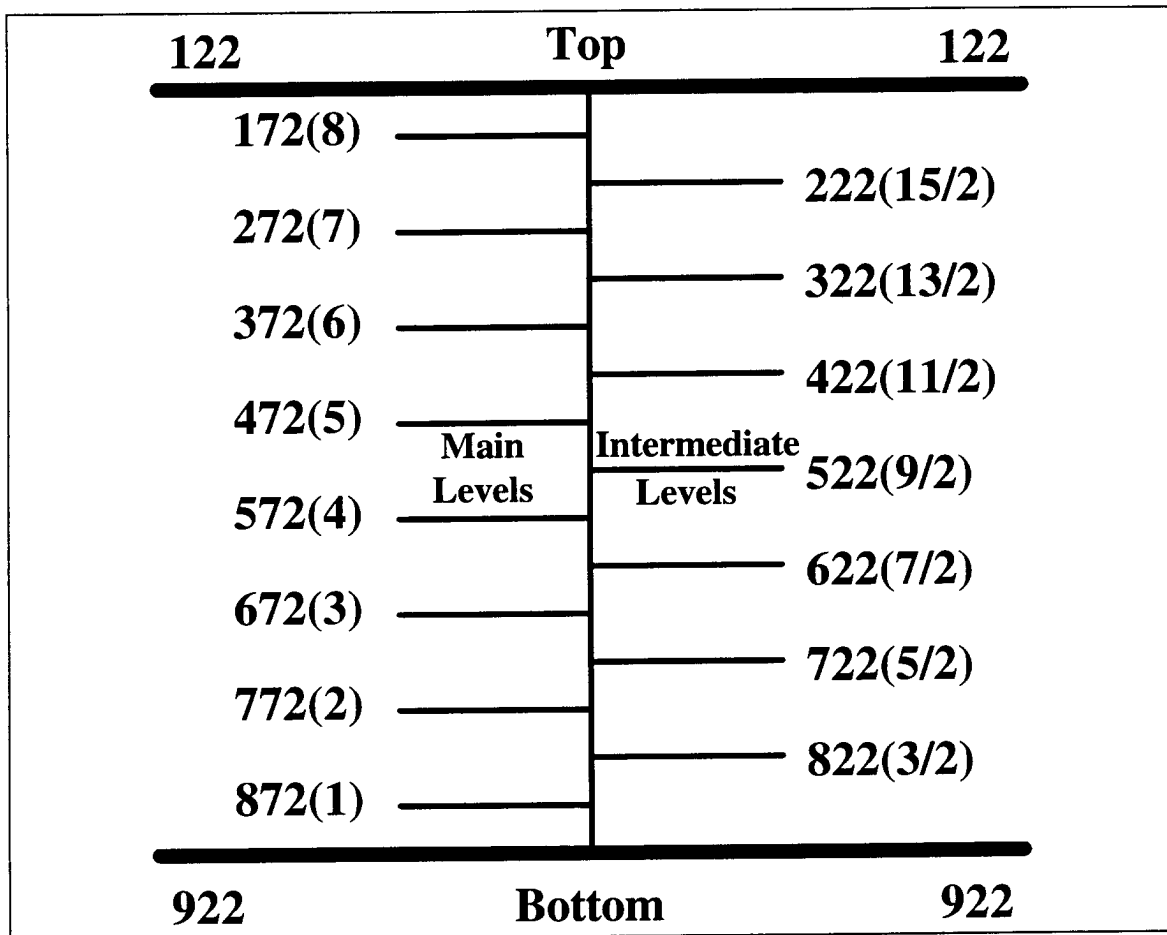


Fig. 4.8. A schematic diagram showing the main and intermediate pressure levels, and the boundary pressure levels. The ( ) refer to the k-index level used in the text.

After computing the reference static stability ( $\theta_s$ ) at the intermediate pressure levels (Fig. 4.8), the next step is to calculate the stratification term, the third term on the right hand side of (4.16), at the eight main levels. The stratification was calculated using a centered finite difference approximation to the vertical pressure derivatives. The three-dimensional stratification data was transformed into spherical harmonics using SPHEREPACK. The relative vorticity (first term on the right hand side of (4.16)) was calculated in harmonic space by,

$$\zeta_n^m = -\frac{g}{f_0} \frac{n(n+1)}{a^2} z_n^m \quad (4.19)$$

where  $z_n^m$  are the complex coefficients as discussed with (4.13). The  $\zeta_n^m$  are the complex coefficients of relative vorticity. Likewise, the Coriolis parameter,  $f$ , was transformed into spherical harmonic coefficients,  $C_n^m$ , using SPHEREPACK. The vertical gradient of the geopotential height at the two boundaries were also transformed into spherical harmonic space using SPHEREPACK.

The QGPV in spherical harmonic space,  $q_n^m$ , was computed by summing the three principal constituents at each of the eight main levels. The synthesis (retransformation) of  $q_n^m$  yields the total three-dimensional QGPV field in grid point space.

To find the large-scale QGPV field,  $\bar{q}$ , the total  $q_n^m$  were subject to a low-pass filter at each main pressure level. The top and bottom boundary condition coefficients were also subject to the same low-pass filter. The filter, as discussed in Section 3b, kept all coefficients where the zonal wavenumber ( $m$ ) was 0 through 6, and the total wavenumber ( $n-m$ ) was 0 through 9. The magnitude of all  $q_n^m$  outside of these ranges were set equal to zero. The small-scale QGPV field ( $q'$ ) was simply a matter of subtracting  $\bar{q}_n^m$  from  $q_n^m$  at each of the main levels. The boundary conditions were treated likewise. The small-scale QGPV equation is

$$q' = \frac{g}{f_0} \nabla^2 z' + g f_0 \frac{\partial}{\partial p} \left( \frac{1}{\sigma} \frac{\partial z'}{\partial p} \right) \quad (4.20)$$

where the primes denote the small-scale field. The von Neumann boundary conditions were applied using the vertical gradient of geopotential height. Eqn. (4.20) in partial finite difference form using the spherical harmonic coefficients and dropping the primes is given by,

$$q_k^* = \frac{g}{f_0} \left[ \frac{-n(n+1)}{a^2} \right] z_k^* + \frac{gf_0}{\Delta p} \frac{1}{\sigma_{k+\frac{1}{2}}} \left( \frac{\partial z^*}{\partial p} \right)_{k+\frac{1}{2}} - \frac{gf_0}{\Delta p} \frac{1}{\sigma_{k-\frac{1}{2}}} \left( \frac{\partial z^*}{\partial p} \right)_{k-\frac{1}{2}} \quad (4.21)$$

where the \* quantities refer to the complex spherical harmonic coefficients and the vertical index ( $k$ ) ranges from one to eight.

The purpose of writing (4.21) was to explain the finite difference method for the  $k \pm 1/2$  indices in the second and third terms on the right hand side. The half indices refer to the intermediate levels. The finite difference indices for the  $+1/2$  terms are the  $k+1$  and  $k$  main levels, and for the  $-1/2$  terms they are the  $k$  and  $k-1$  main levels, since these intermediate pressure level terms are involved in a vertical derivative. The full finite difference form of (4.21) is given by,

$$q_k^* = \frac{g}{f_0} \left[ \frac{-n(n+1)}{a^2} \right] z_k^* + \frac{gf_0}{(\Delta p)^2} \frac{1}{\sigma_{k+\frac{1}{2}}} (z_{k+1}^* - z_k^*) - \frac{gf_0}{(\Delta p)^2} \frac{1}{\sigma_{k-\frac{1}{2}}} (z_k^* - z_{k-1}^*) \quad (4.22)$$

and after regrouping like terms (4.22) becomes,

$$q_k^* = \left[ \frac{gf_0}{(\Delta p)^2} \right] z_{k-1}^* + \left[ \frac{g}{f_0} \left( \frac{-n(n+1)}{a^2} \right) + \frac{gf_0}{(\Delta p)^2} \left( \frac{-1}{\sigma_{k+\frac{1}{2}}} - \frac{1}{\sigma_{k-\frac{1}{2}}} \right) \right] z_k^* + \left[ \frac{gf_0}{(\Delta p)^2} \frac{1}{\sigma_{k+\frac{1}{2}}} \right] z_{k+1}^* \quad (4.23)$$

For convenience, (4.23) is rewritten

$$A_k z_{k-1}^* + B_k z_k^* + C_k z_{k+1}^* = q_k^* \quad (4.24)$$

where  $A$ ,  $B$  and  $C$  are the coefficients within the brackets of (4.23).

Eqn. (4.24) is adequate for the interior pressure levels (main levels 2 through 7 in Fig. 4.8), but will not work at the first and last pressure levels because the vertical derivatives of  $z^*$  require information below and above the main levels. However, the von Neumann top and bottom boundary conditions specify the vertical geopotential height gradients

below and above the main levels. The von Neumann boundary conditions are equivalent to specifying the bottom and top temperature anomalies at the boundaries.

If (4.21) is rewritten for the lowest main pressure level using the bottom boundary condition the result is given by,

$$q_1^* = \frac{g}{f_0} \left( \frac{-n(n+1)}{a^2} \right) z_1^* + \frac{gf_0}{(\Delta p)^2} \frac{1}{\sigma_{\frac{3}{2}}} (z_2^* - z_1^*) - \frac{gf_0}{\Delta p} \frac{1}{\sigma_{bottom}} \left( \frac{\partial z^*}{\partial p} \right)_{bottom} \quad (4.25)$$

If the like terms are grouped together, (4.25) becomes

$$B_1 z_1^* + C_1 z_2^* = q_1^{**} \quad (4.26)$$

where

$$B_1 = \frac{g}{f_0} \left( \frac{-n(n+1)}{a^2} \right) - \frac{gf_0}{(\Delta p)^2} \frac{1}{\sigma_{\frac{3}{2}}} \quad (4.27)$$

$$C_1 = \frac{gf_0}{(\Delta p)^2} \frac{1}{\sigma_{\frac{3}{2}}} \quad (4.28)$$

$$q_1^{**} = q_1^* + \frac{gf_0}{\Delta p} \frac{1}{\sigma_{bottom}} \left( \frac{\partial z^*}{\partial p} \right)_{bottom} \quad (4.29)$$

If (4.21) is rewritten for the highest main pressure level using the top boundary condition the result is given by,

$$q_8^* = \frac{g}{f_0} \left( \frac{-n(n+1)}{a^2} \right) z_8^* + \frac{gf_0}{\Delta p} \frac{1}{\sigma_{top}} \left( \frac{\partial z^*}{\partial p} \right)_{top} - \frac{gf_0}{(\Delta p)^2} \frac{1}{\sigma_{\frac{15}{2}}} (z_8^* - z_7^*) \quad (4.30)$$

If the like terms are grouped together, (4.30) becomes

$$A_8 z_7^* + B_8 z_8^* = q_8^{**} \quad (4.31)$$

where

$$A_8 = \frac{gf_0}{(\Delta p)^2} \frac{1}{\sigma_{\frac{15}{2}}} \quad (4.32)$$

$$B_8 = \frac{g}{f_0} \left( \frac{-n(n+1)}{a^2} \right) - \frac{gf_0}{(\Delta p)^2} \frac{1}{\sigma_{\frac{15}{2}}} \quad (4.33)$$

$$q_8^{**} = q_8^* + \frac{gf_0}{\Delta p} \frac{1}{\sigma_{top}} \left( \frac{\partial z^*}{\partial p} \right)_{top} \quad (4.34)$$

If the system of equations in (4.24), (4.26), (4.27), (4.28), (4.29), (4.31), (4.32), (4.33), and (4.34) are written in matrix form without the \* notation, the result is

$$\begin{pmatrix} B_1 & C_1 & 0 & 0 & 0 & 0 & 0 & 0 \\ A_2 & B_2 & C_2 & 0 & 0 & 0 & 0 & 0 \\ 0 & A_3 & B_3 & C_3 & 0 & 0 & 0 & 0 \\ 0 & 0 & A_4 & B_4 & C_4 & 0 & 0 & 0 \\ 0 & 0 & 0 & A_5 & B_5 & C_5 & 0 & 0 \\ 0 & 0 & 0 & 0 & A_6 & B_6 & C_6 & 0 \\ 0 & 0 & 0 & 0 & 0 & A_7 & B_7 & C_7 \\ 0 & 0 & 0 & 0 & 0 & 0 & A_8 & B_8 \end{pmatrix} \begin{pmatrix} z_1 \\ z_2 \\ z_3 \\ z_4 \\ z_5 \\ z_6 \\ z_7 \\ z_8 \end{pmatrix} = \begin{pmatrix} q_1 \\ q_2 \\ q_3 \\ q_4 \\ q_5 \\ q_6 \\ q_7 \\ q_8 \end{pmatrix} \quad (4.35)$$

The 8 by 8 matrix on the left hand side of (4.35) is a tridiagonal matrix. The solution to a system of equations in tridiagonal form is straight-forward and can be solved quite efficiently using a tridiagonal solver routine such as the subroutine “TRIDIAG” found in Press et al. (1992). The z-vector on the left hand side consists of the magnitudes of the complex spherical harmonic coefficients that invert (solve) the QGPV system of equations, including the temperature (vertical gradient of geopotential height) boundary conditions. The final step in the process is to synthesize (retransform) the geopotential height harmonics back into grid point space using SPHEREPACK.

The QGPV inversion method described above is similar to Holopainen and Kaurola (1991). They used the spherical harmonic method with  $M=20$  and  $N=30$ , and cubic splines to interpolate the standard pressure levels into 99 equal layers ( $\Delta p = 10$  mb) from 1000 mb to 10 mb. They used the 1000 mb temperature for a lower boundary condition and a homogeneous boundary condition at the top. Instead of solving a tridiagonal matrix, they solved a band matrix (a diagonal matrix with seven bands instead of three). The basic state (large-scale) was  $\bar{q} = f$ .

Holopainen and Kaurola performed their study to investigate the effects of three QGPV partitioning schemes. Their first experiment separated the contributions of interior QGPV anomalies from temperature anomalies at the lower boundary. Their second experiment separated the contributions of the vorticity and stratification anomalies. Their third experiment investigated the effect of upper tropospheric and lower tropospheric QGPV anomalies upon the upper and lower troposphere. The third experiment is known as piecewise QGPV inversion (Davis and Emanuel 1991, Davis 1992a).

The piecewise QGPV inversion performed by Holopainen and Kaurola proved to be the most beneficial method for diagnosing atmospheric dynamics. The piecewise inversion technique similar to Holopainen and Kaurola is used in this study of midtropospheric mobile troughs. The methodology behind the piecewise inversion is similar to the low-pass filtering, except the “zeroing” of  $q_n^m$  coefficients occurs in the vertical. All the  $q_n^m$  coefficients at every level except the level of interest are set equal to zero. The remaining QGPV inversion algorithm is the same. Holopainen and Kaurola, however, did not actually “zero-out” the QGPV away from the levels of interest in their piecewise inversion. Instead, they set the vorticity component and the potential temperature (equivalent to the vertical gradient of geopotential height) equal to zero. The algorithm they used is not consistent with the conservation of QGPV, and introduces spurious geopotential height anomalies throughout the domain (Davis 1993, Holopainen and Kaurola 1993).

The theory behind piecewise inversion is to isolate the influence of a QGPV anomaly at one level, numerous levels, or the boundaries, upon the full three-dimensional atmospheric flow. Since the focus of this study is on midtropospheric waves, typically identified on 500 mb geopotential height analyses, the 472 mb pressure level was chosen as a representative level for determining the effect of QGPV anomalies at different levels.

The vertical profile shown in Fig. 4.9 is the resulting geopotential height anomaly at 472 mb as induced by positive QGPV anomalies at each of the eight main levels and the boundaries. The positive QGPV anomaly was selected because it was associated with a typical mobile trough over the United States on 0000 UTC 3 December 1980. The

magnitude of the geopotential anomaly is  $-75$  m at 472 mb. This means the positive QGPV anomaly associated with only the 472 mb level induced a  $-75$  m height decrease at the 472 mb level. The QGPV anomaly associated with the lower boundary (922 mb) induced a  $-3$  m height decrease at the 472 mb pressure level. There is an obvious break at the 572 mb pressure level. Therefore, the levels at and above the 472 mb level, along with the upper boundary condition, are grouped together. The levels at 572 mb and below, including the lower boundary condition, are grouped together. The 372 mb level in this and other examples dominated the QGPV forcing. For this reason, the 372 mb level was chosen as the level to diagnose midtropospheric mobile troughs.

## 5. Verification of the linear QGPV inversion

Since the QGPV equation is a linear operator on the geopotential height anomaly, the superposition of QGPV anomalies (i.e. the sum of all the piecewise partitions) should reproduce the original geopotential height field. The verification of the inversion method also included a verification of the spherical harmonic transformations.

The first verification test was to simply transform the geopotential height data into and out of spherical harmonic space. The result of this transformation and inverse transformation was almost exact. The error was at the level of machine precision. However, because the assumption of the meridional symmetry between the northern and southern hemispheres, the inverse transformation of geopotential height coefficients produced a constant value along the Equator. This discrepancy should not pose a problem since the quasigeostrophic approximation is not valid at the Equator.

The next test was to compute the QGPV and compare the inverted QGPV geopotential height field (without filtering) to the original geopotential height field. Again, the inversion was almost exact.

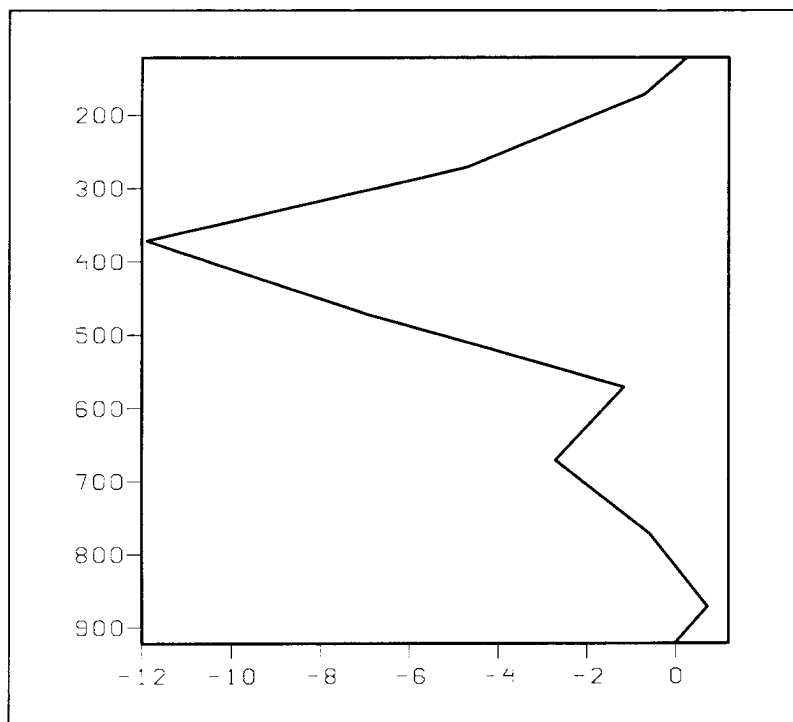


Fig. 4.9. Vertical profile of the influence of QGPV anomalies from the eight main levels and the boundaries on the 472 mb pressure level. The location of the profile was near the center of the midtropospheric mobile trough over the Great Lakes on 0000 UTC 3 December 1980. The vertical axis is pressure (mb). The horizontal axis is perturbation geopotential height (dam). Most of the profile is negative because this location was within a well-developed trough.



Finally, the piecewise inversion was tested. The small-scale QGPV field at each main pressure level was inverted separately. The sum of the eight layers and the boundary conditions (Fig. 4.10) was compared to the original small-scale geopotential height field (Fig. 4.11). The difference between the original perturbation height field and the sum of all the pieces is at the level of round-off error.

## 6. Interpretation of the QGPV equation

The QGPV equation was presented in (3.6) and (3.7). When the large and small-scale partitioning is combined with (3.6) it becomes

$$\frac{d_g q}{dt} = \frac{d_g \bar{q}}{dt} + \frac{d_g q'}{dt} \cong 0 \quad (4.36)$$

where the total geostrophic derivative is defined as,

$$\frac{d_g}{dt} \equiv \frac{\partial}{\partial t} + \mathbf{V}_g \cdot \nabla \quad (4.37)$$

The  $\cong$  sign in (4.36) is used to remind the reader about the expected error between the QG approximation and the “real” atmosphere. The total geostrophic wind,  $\mathbf{V}_g$ , can be partitioned likewise into the large-scale geostrophic wind,  $\bar{\mathbf{V}}_g$ , and the small-scale geostrophic wind,  $\mathbf{V}'_g$ , where

$$\mathbf{V}_g = \bar{\mathbf{V}}_g + \mathbf{V}'_g \quad (4.38)$$

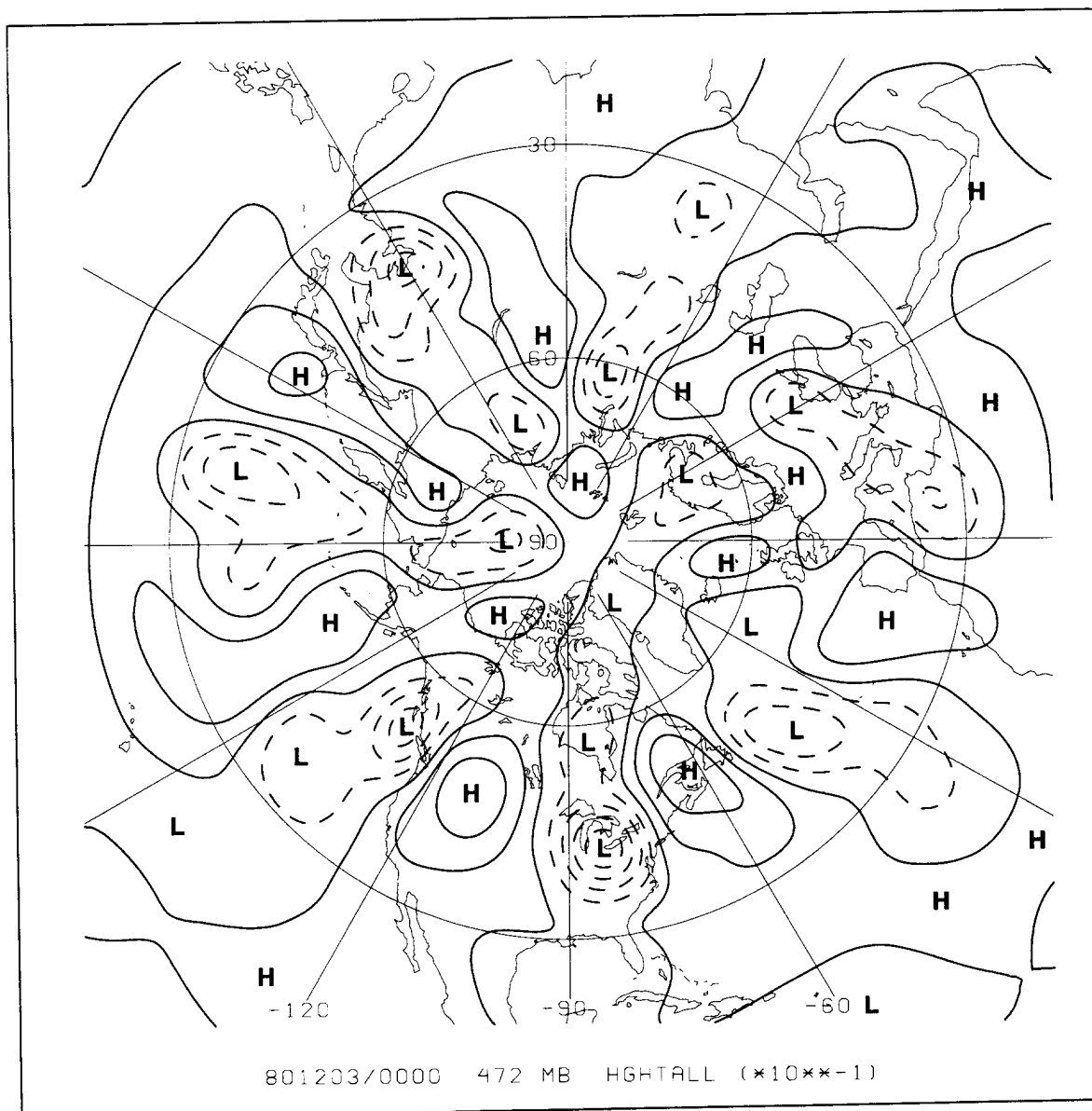


Fig. 4.10. The perturbation height field at 472 mb for 0000 UTC 3 December 1980 after adding the effect from the eight levels and the top and bottom boundaries. The contour interval is 6 dam, and the negative contours are dashed. The first solid contour is equal to zero.

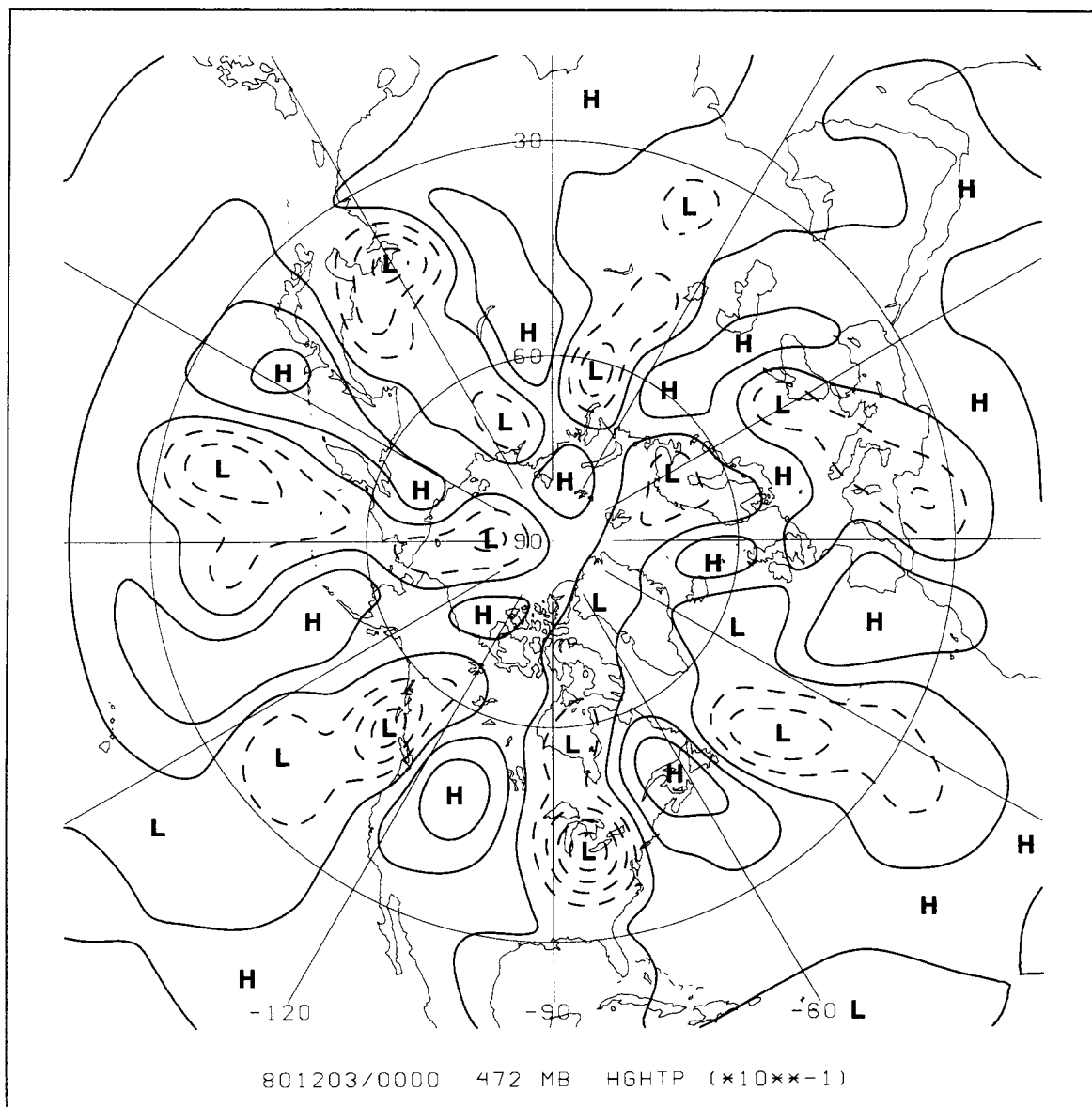


Fig. 4.11. The original perturbation height field at 472 mb for 0000 UTC 3 December 1980. The contour interval is 6 dam, and the negative contours are dashed. The first solid contour is equal to zero.

When the total derivatives in (4.36) are expanded using (4.37), and the geostrophic wind partition, (4.38), is introduced, (4.36) becomes

$$\underbrace{\frac{\partial \bar{q}}{\partial t}}_1 + \underbrace{\frac{\partial q'}{\partial t}}_2 + \underbrace{\bar{\mathbf{V}}_g \cdot \nabla \bar{q}}_3 + \underbrace{\bar{\mathbf{V}}_g \cdot \nabla q'}_4 + \underbrace{\mathbf{V}'_g \cdot \nabla \bar{q}}_5 + \underbrace{\mathbf{V}'_g \cdot \nabla q'}_6 = \varepsilon \cong 0 \quad (4.39)$$

where  $\varepsilon$  is the amount of error between the “real” atmospheric flow and the QG assumption (Black and Dole 1993). The magnitude of  $\varepsilon$  describes the magnitude of the nonconservative effects on the dynamics of the QGPV system, and also includes the difference between the instantaneous calculations of Terms 3 through 6 and the 24-hour finite difference of Terms 1 and 2.

Before discussing the advection terms in (4.39), it will be helpful to present the components of Terms 3, 4, 5 and 6. Figs. 4.12 through 4.17 show the full QGPV field, the large-scale and small-scale QGPV fields, and the corresponding geopotential height fields for 0000 UTC 3 December 1980 at 372 mb. In every instance the geopotential height field in Figs. 4.12, 4.13 and 4.14 resembles the QGPV forcing fields in Figs. 4.15, 4.16, and 4.17, respectively. The mobile trough over the Great Lakes region at this time will be used to discuss the terms in (4.39).

The first term (Term 1) on the left hand side of (4.39) is the local rate of change of the large-scale QGPV field. The second term (Term 2) is the local rate of change of the small-scale QGPV field. The third term (Term 3) is the negative of the large-scale geostrophic advection of the large-scale QGPV field. The fourth term (Term 4) is the negative of the large-scale geostrophic advection of the small-scale QGPV field. The fifth term (Term 5) is the negative of the small-scale geostrophic advection of the large-scale QGPV field. The last term (Term 6) is the negative of the small-scale geostrophic advection of the small-scale QGPV field.

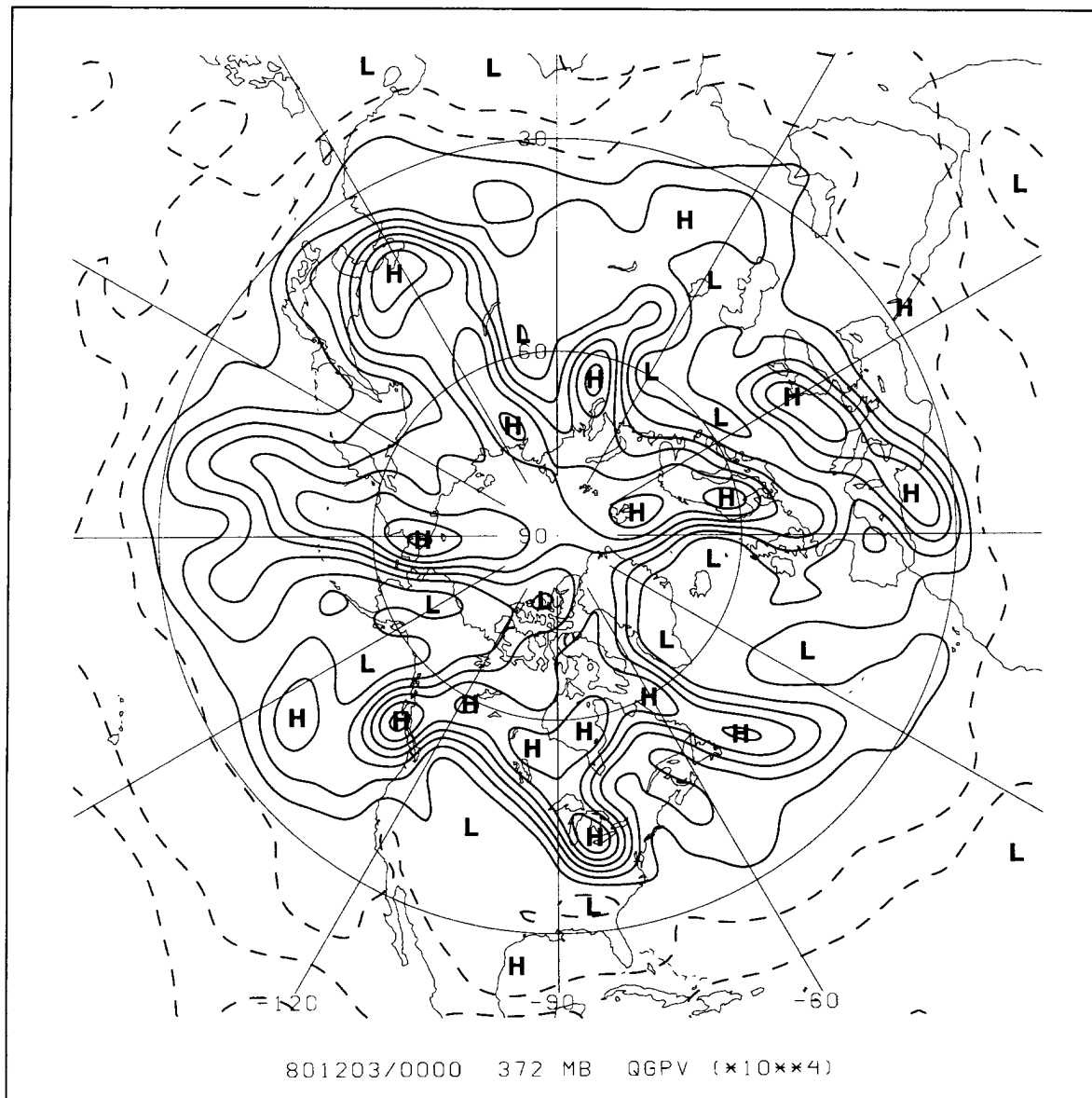


Fig. 4.12. The full QGPV field for 0000 UTC 3 December 1980 at 372 mb. The contour interval is equal to  $1 \times 10^{-4} \text{ s}^{-1}$ . Negative contours are dashed. The first solid contour is equal to zero.

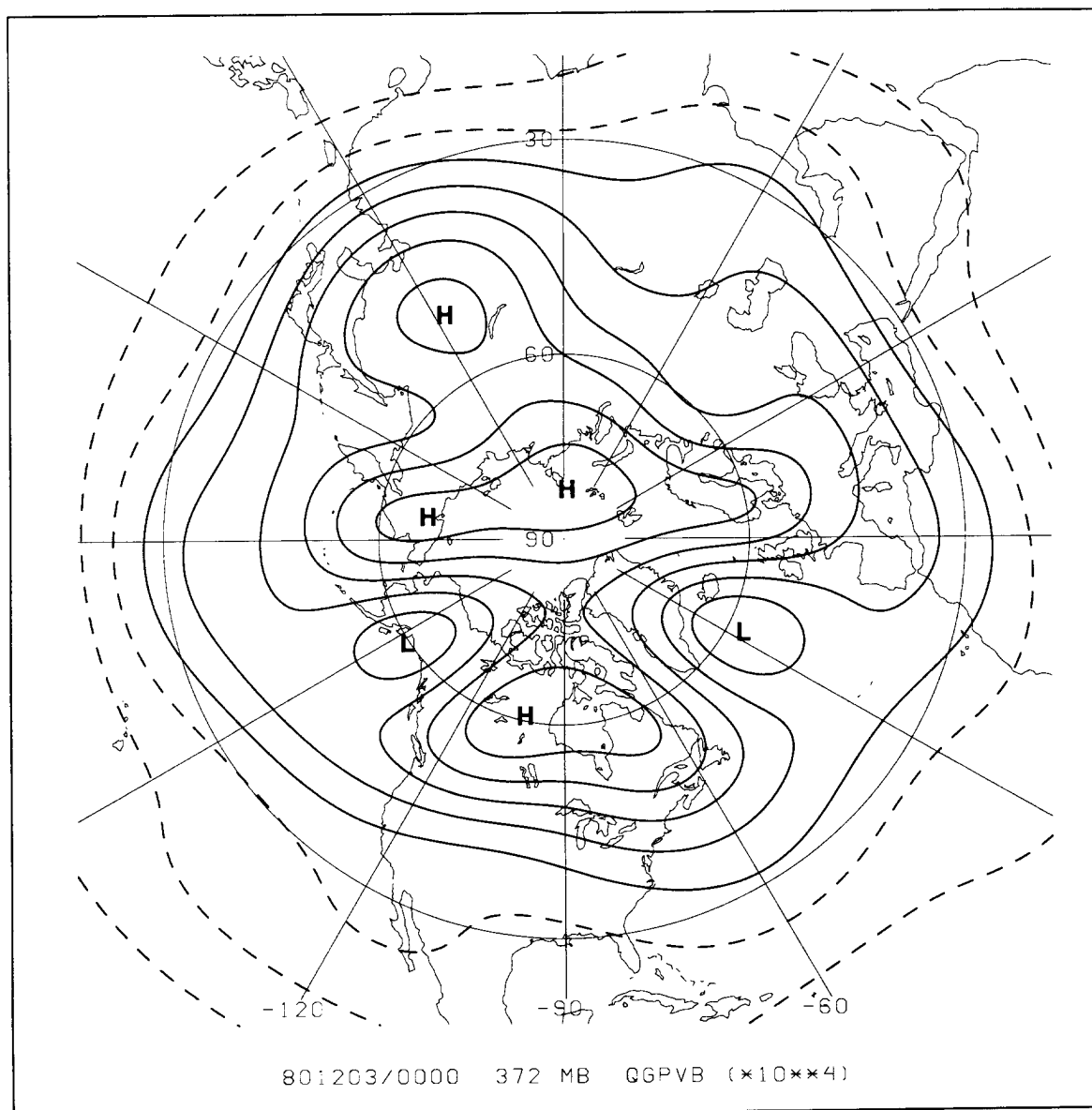


Fig. 4.13. The large-scale QGPV field for 0000 UTC 3 December 1980 at 372 mb. The contour interval is equal to  $1 \times 10^{-4} \text{ s}^{-1}$ . Negative contours are dashed. The first solid contour is equal to zero.

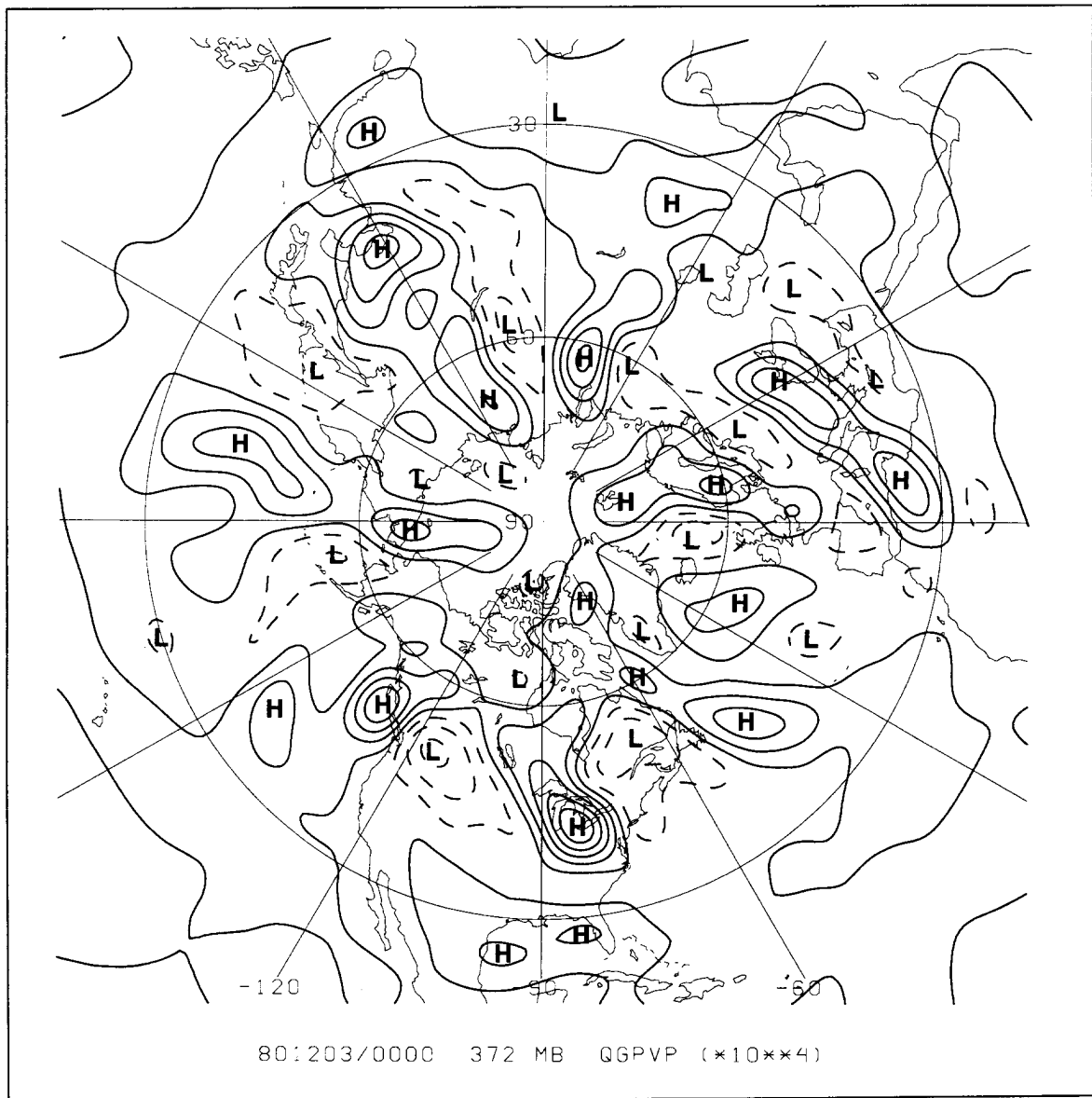


Fig. 4.14. The small-scale QGPV field for 0000 UTC 3 December 1980 at 372 mb. The contour interval is equal to  $1 \times 10^{-4} \text{ s}^{-1}$ . Negative contours are dashed. The first solid contour is equal to zero.

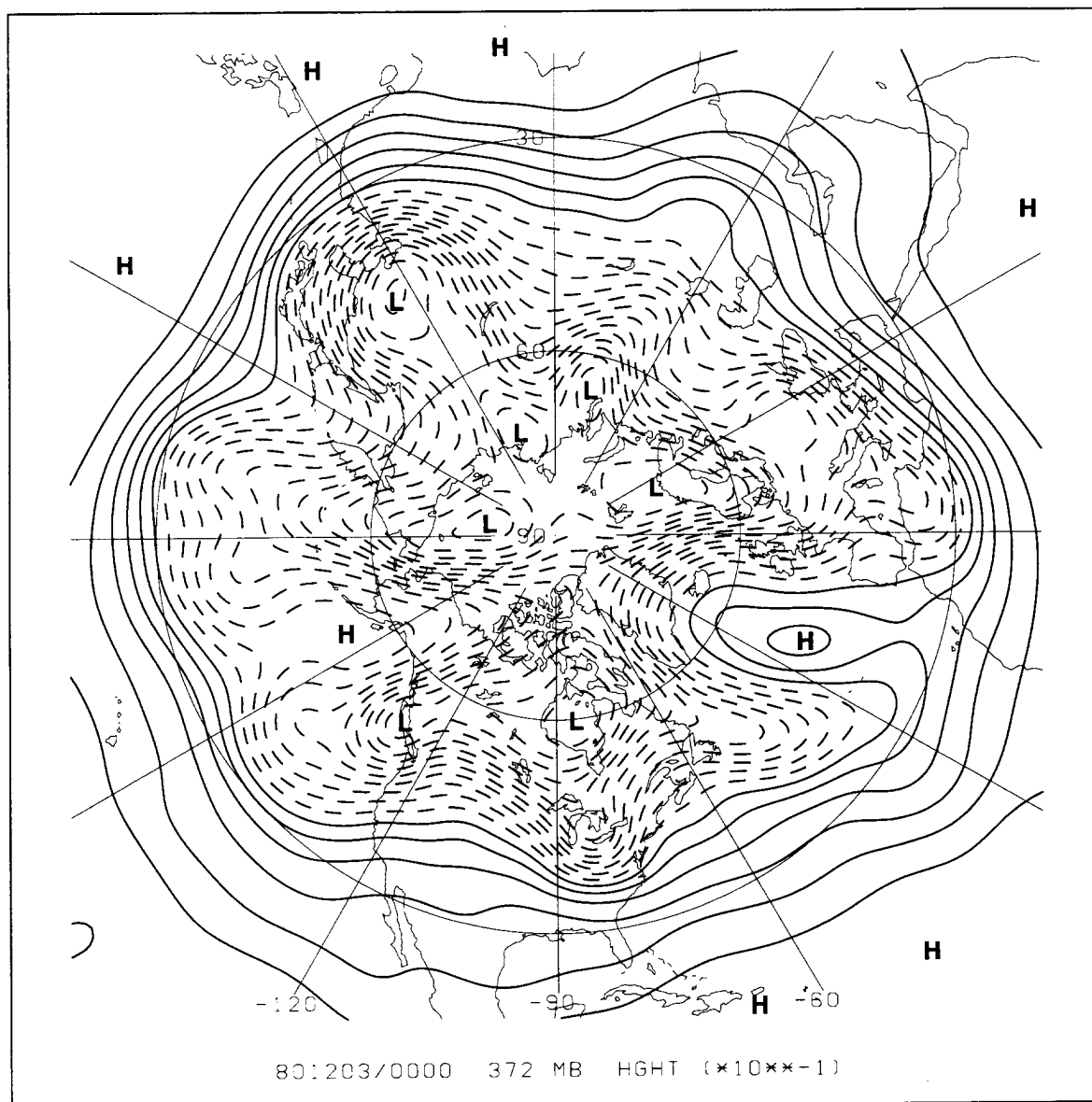


Fig. 4.15. The full geopotential height field for 0000 UTC 3 December 1980 at 372 mb. The contour interval is 6 dam. Negative contours are dashed. The first solid contour is equal to zero.



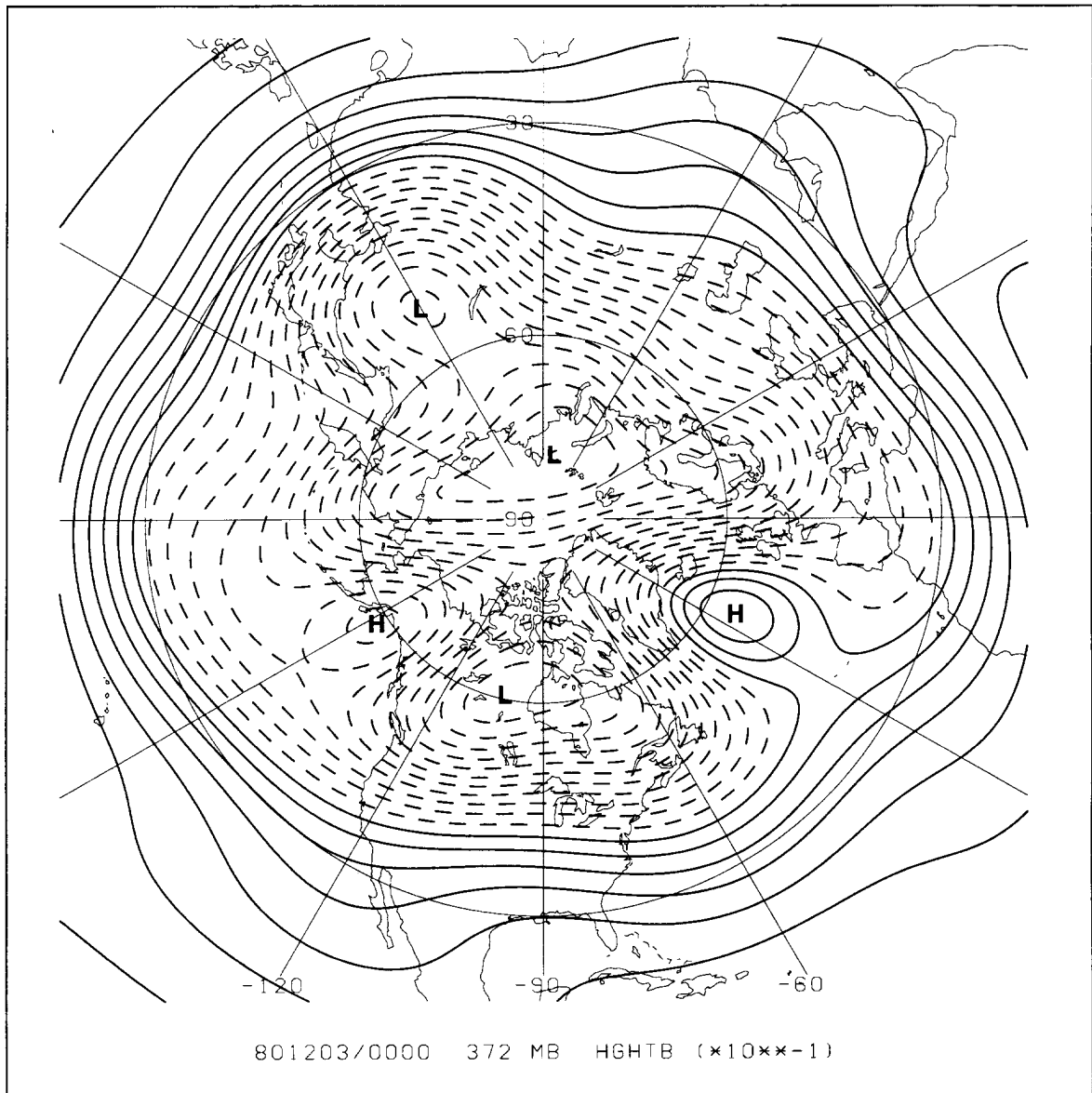


Fig. 4.16. The large-scale geopotential height field for 0000 UTC 3 December 1980 at 372 mb. The contour interval is 6 dam. Negative contours are dashed. The first solid contour is equal to zero.

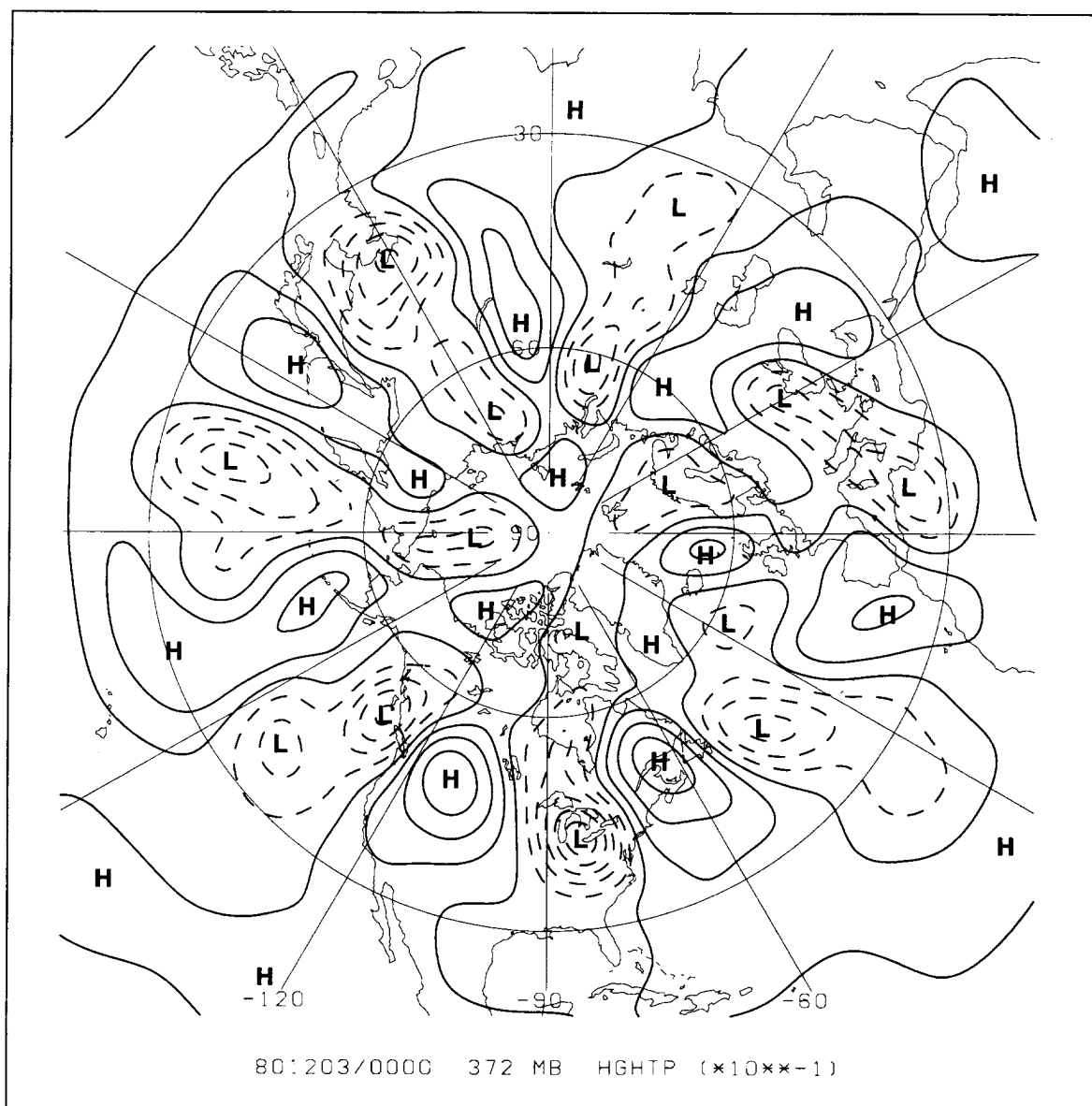


Fig. 4.17. The small-scale geopotential height field for 0000 UTC 3 December 1980 at 372 mb. The contour interval is 6 dam. Negative contours are dashed. The first solid contour is equal to zero.

If the large-scale flow is assumed to be dominated by long Rossby waves, and long Rossby waves are quasi-stationary, then the large-scale flow pattern should be quasi-stationary relative to the small-scale fields. Terms 1 and 3 should be zero or at least smaller than the other terms. The large-scale partition used in this research is similar to the large-scale category of waves in Blackmon (1976). Blackmon found his large-scale waves were in fact slowly-varying or stationary. If the large-scale pattern was defined by a pure zonal flow, then Term 3 would be exactly zero by definition of the gradient operator and dot product.

The large-scale environment in this study varies slowly in time as evident by the temporal derivative of  $\bar{q}$  in Fig. 4.18. The choice of the contour interval in Fig. 4.18 is consistent with the other figures presented later in this chapter. The lack of contours shows the small magnitude of this term.

Since the focus of this research is on mobile troughs or small-scale waves, and the nonlinear interactions due to the advections of QGPV in (4.39) produce some large-scale patterns, (4.39) will be filtered again using the high-pass filter described earlier in this chapter. After applying this filter to Terms 1 and 3 (Figs. 4.18 and 4.19), the contours are reduced to insignificant levels. For this reason, Terms 1 and 3 will be neglected from the discussion of mobile trough dynamics.

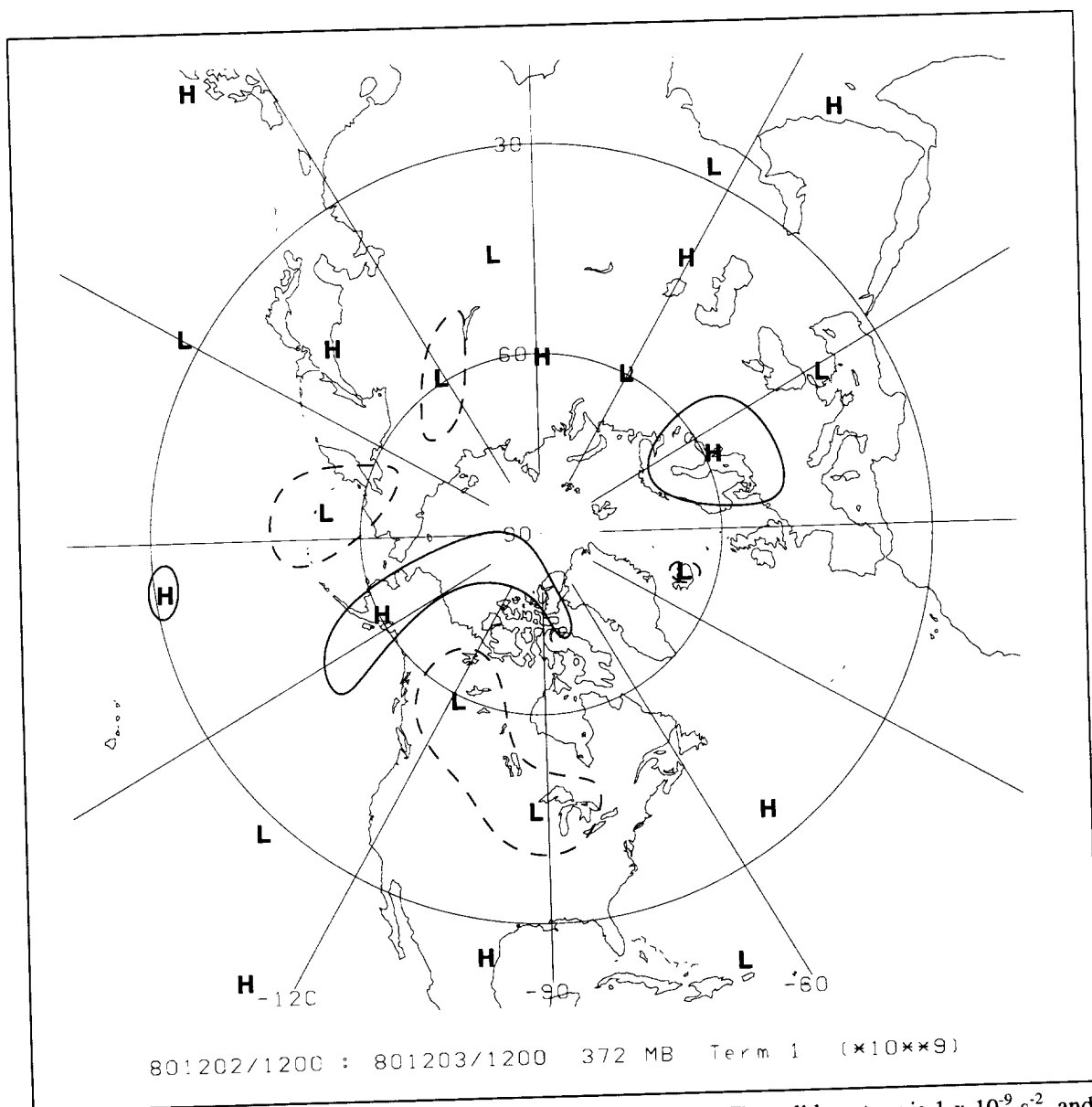


Fig. 4.18. Term 1 valid at 0000 UTC 3 December 1980 at 372 mb. The solid contour is  $1 \times 10^{-9} \text{ s}^{-2}$ , and the dashed contour is  $-1 \times 10^{-9} \text{ s}^{-2}$ . The zero contour is not drawn.

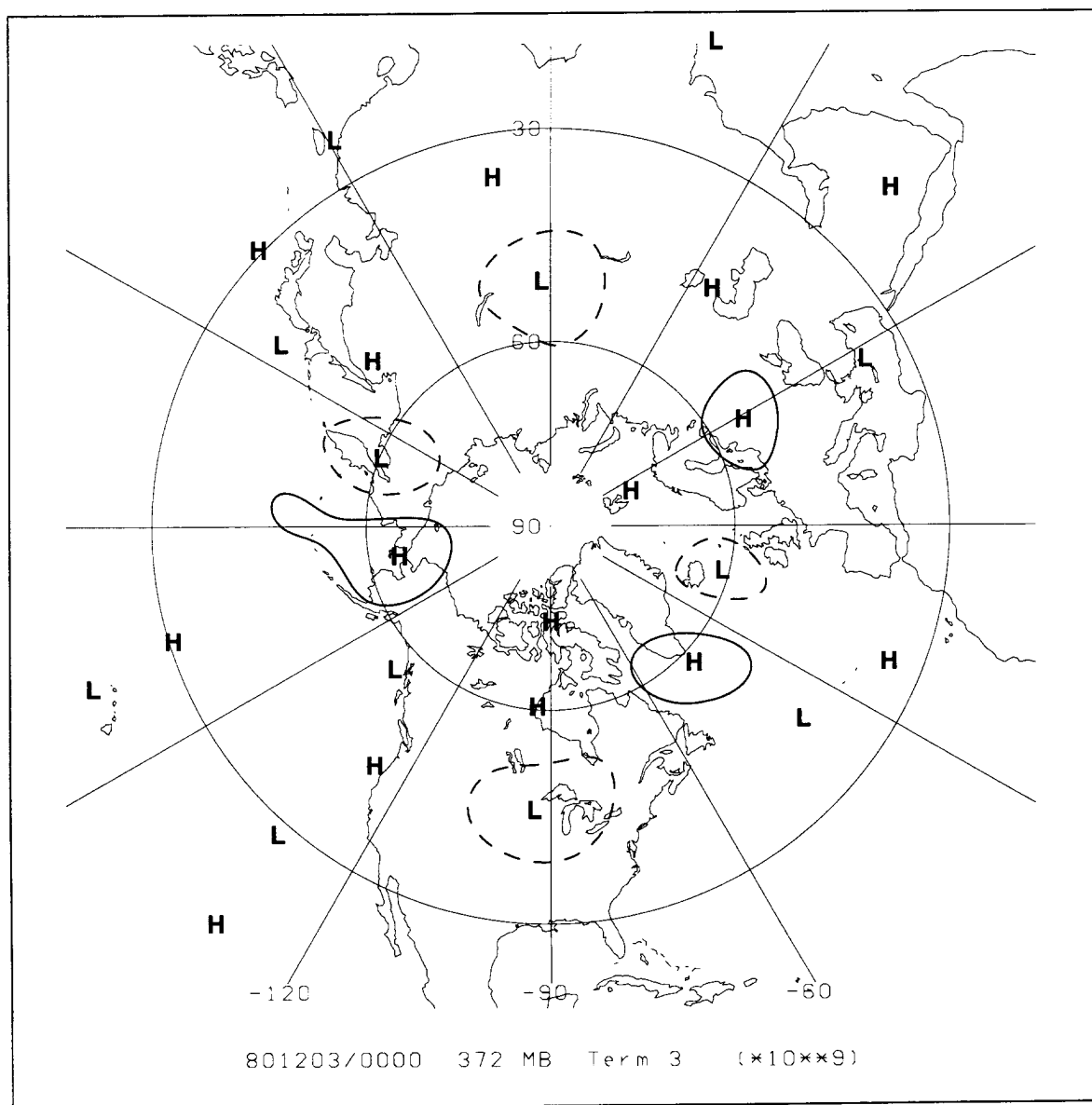


Fig. 4.19. Term 3 valid at 0000 UTC 3 December 1980 at 372 mb. The solid contour is  $1 \times 10^{-9} \text{ s}^{-2}$ , and the dashed contour is  $-1 \times 10^{-9} \text{ s}^{-2}$ . The zero contour is not drawn.

The relationship between the four remaining terms on the left hand side of (4.39) is given by Figs. 4.20 through 4.23. The temporal finite difference of the total QGPV field (not shown) is almost completely dominated by Term 2 (Fig. 4.20). The pattern of positive and negative  $q'$  tendency in Fig. 4.20 is consistent with the geopotential height field shown in Fig. 4.15 (e.g. positive potential vorticity tendency ahead of troughs).

The contours in Figs 4.21 and 4.22 are consistent with the concepts of Rossby wave advection (Term 4) and propagation (Term 5). Term 4 in (4.39) is the advection of small-scale QGPV by the large-scale flow. In Rossby-wave dynamics the waves are advected downstream by the large-scale flow. This downstream advection of the mobile trough over the Great Lakes (positive maximum of  $q'$  in Fig. 4.14) produces a positive area downstream of the Great Lakes in Term 4 (Fig. 4.21), and a negative area upstream. Term 5 in (4.39) is the advection of large-scale QGPV by the small-scale flow. The deformation of the large-scale QGPV is due to the propagation of the mobile trough. According to Rossby-wave dynamics the propagation of Rossby waves is upstream. The concept of Rossby-wave propagation is consistent with Term 5 and Fig. 4.22. The mobile trough is propagating upstream and produces areas of positive advection west of the Great Lakes, and negative areas east of the Great Lakes.

The maximum amplitude, in an absolute sense, of Term 4 (Fig. 4.21) is approximately two or three times greater than Term 5 (Fig. 4.22). This observation suggests the downstream advection of the mobile trough is greater than the upstream propagation. Again, this observation is consistent with the concept of short Rossby-waves (mobile troughs) having a positive overall phase speed.

Term 6 (Fig. 4.23) describes the advection of small-scale QGPV by the small-scale flow. This term is useful in diagnosing the trough-merger mechanism described in Chapter III, but doesn't have a conceptual analog using Rossby-wave dynamics. The discussion of this term will be postponed until the next section in this chapter.

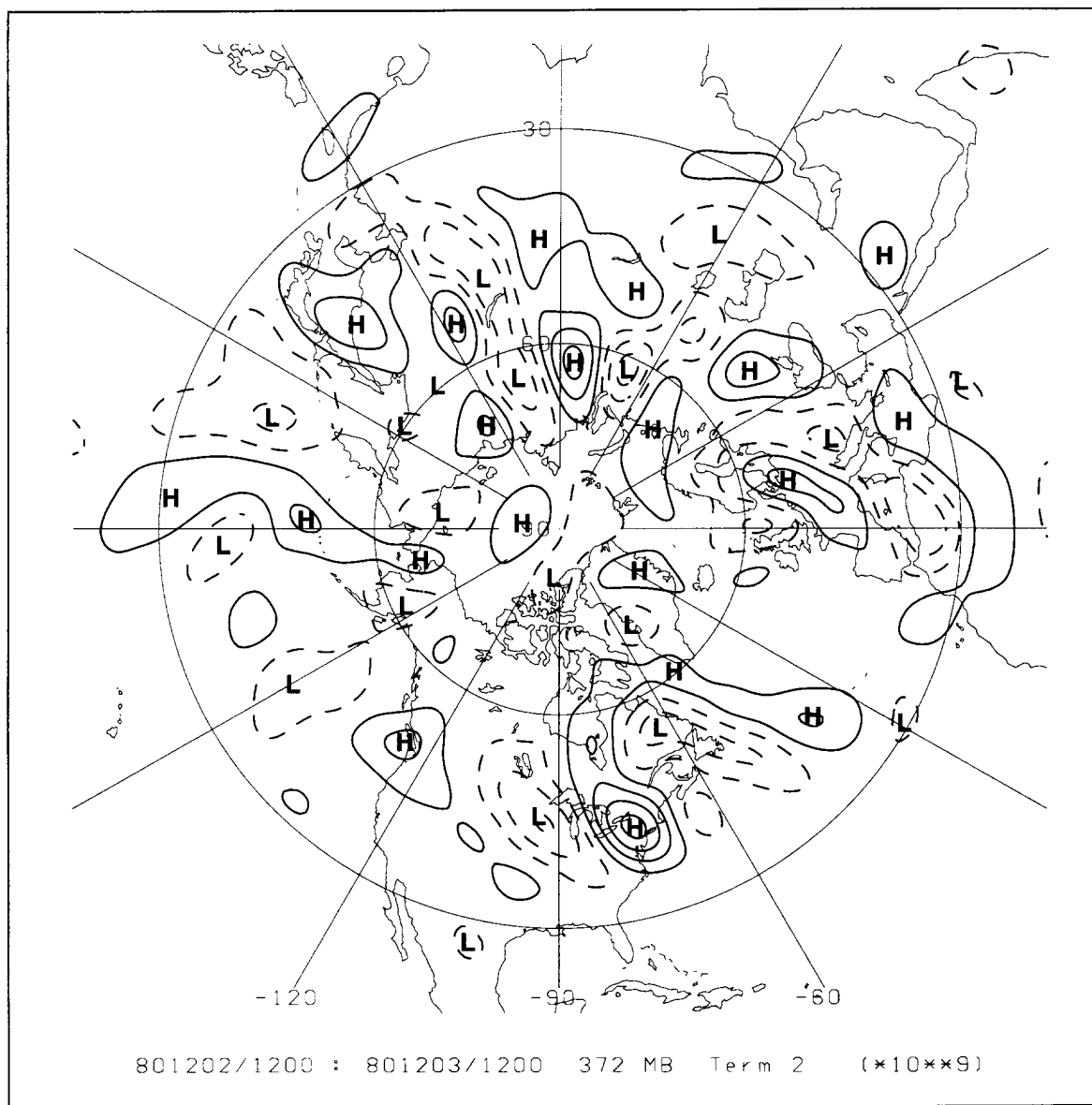


Fig. 4.20. Term 2 valid at 0000 UTC 3 December 1980 at 372 mb. The contour interval is  $2 \times 10^{-9} \text{ s}^{-2}$ . The negative contours are dashed. The zero contour is not drawn.

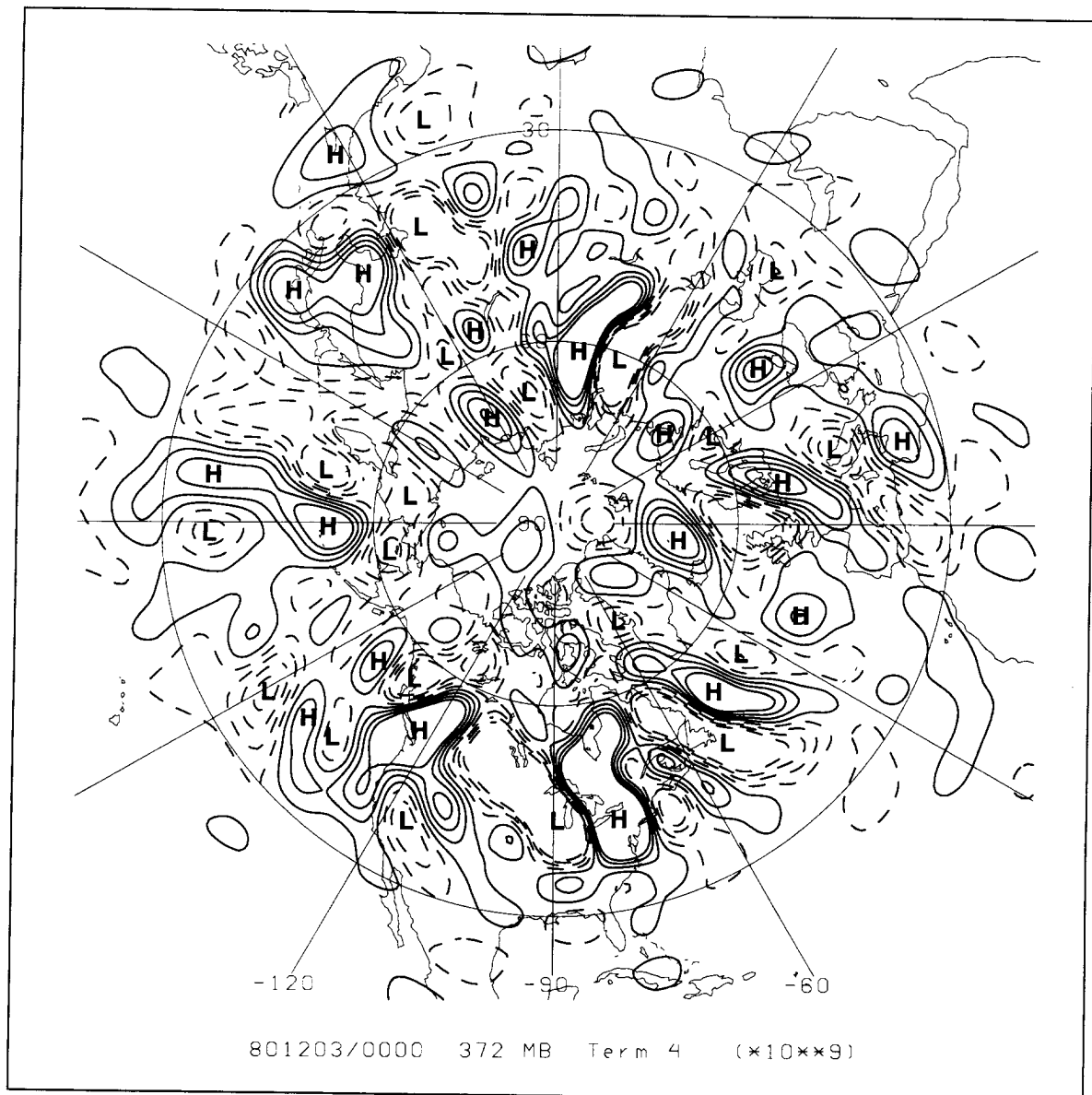


Fig. 4.21. Term 4 valid at 0000 UTC 3 December 1980 at 372 mb. The contour interval is  $2 \times 10^{-9} \text{ s}^{-2}$ . The negative contours are dashed. The zero contour is not drawn.



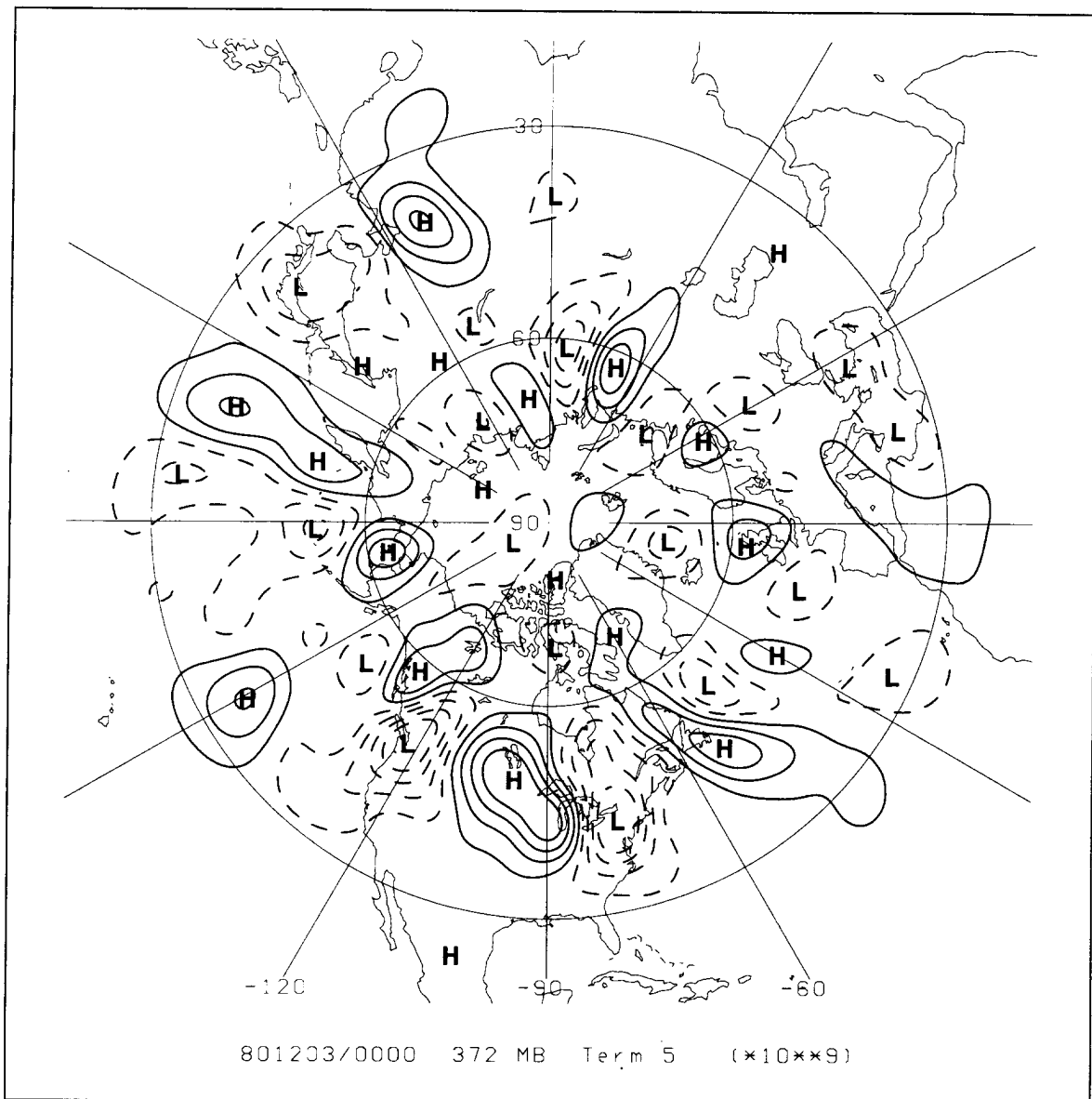


Fig. 4.22. Term 5 valid at 0000 UTC 3 December 1980 at 372 mb. The contour interval is  $2 \times 10^{-9} \text{ s}^{-2}$ . The negative contours are dashed. The zero contour is not drawn.

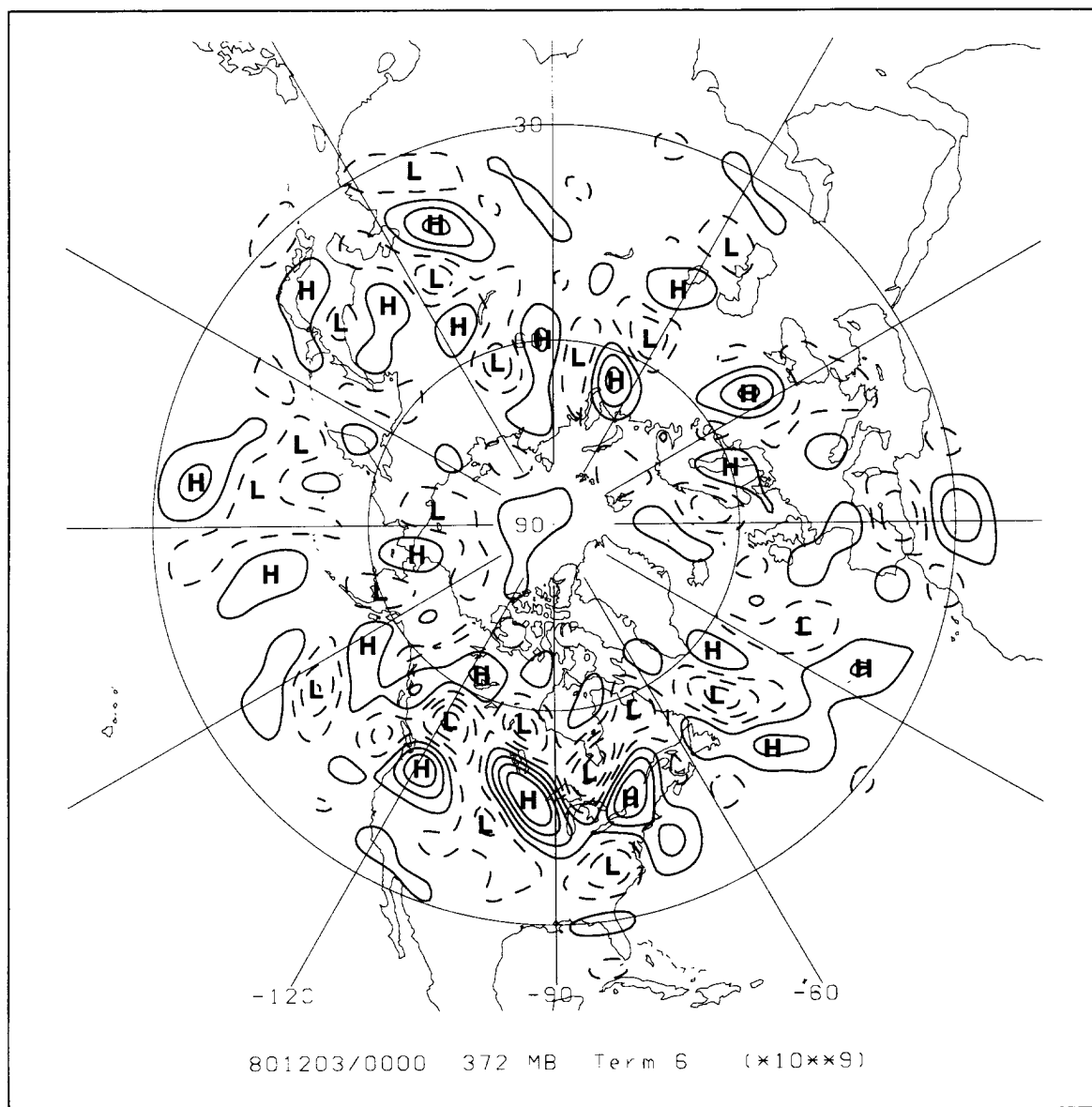


Fig. 4.23. Term 6 valid at 0000 UTC 3 December 1980 at 372 mb. The contour interval is  $2 \times 10^{-9} \text{ s}^{-2}$ . The negative contours are dashed. The zero contour is not drawn.

## 7. Interpretation of the QGPV height tendency equation

The QGPV height tendency equation as discussed in Chapter III is written

$$\frac{g}{f_0} \nabla^2 \left( \frac{\partial z}{\partial t} \right) + g f_0 \frac{\partial}{\partial p} \left( \frac{1}{\sigma} \frac{\partial}{\partial p} \left( \frac{\partial z}{\partial t} \right) \right) = -\mathbf{V}_g \cdot \nabla q \quad (4.40)$$

or,

$$\mathbf{L} \left( \frac{\partial z}{\partial t} \right) = -\mathbf{V}_g \cdot \nabla q \quad (4.41)$$

where the linear operator ( $\mathbf{L}$ ) on the left hand side of (4.41) is defined by

$$\mathbf{L}(\ ) \equiv \frac{g}{f_0} \nabla^2(\ ) + g f_0 \frac{\partial}{\partial p} \left( \frac{1}{\sigma} \frac{\partial}{\partial p}(\ ) \right) \quad (4.42)$$

The linear operator (4.42) is the same as the QGPV operator in (4.20). Therefore, the same inversion technique ( $\mathbf{L}^{-1}$ ) used to compute the geopotential height from the QGPV can be applied to (4.40) to obtain the geopotential height tendency.

The boundary conditions used to invert (4.40) were determined by the appropriate advection of the 922 mb and 122 mb vertical height gradient (equivalent to the temperature advection at the bottom and top). They are incorporated in the inversion as in (4.29) and (4.34), except the  $q$ 's are replaced by the appropriate  $-\mathbf{V}_g \cdot \nabla q$  and the vertical gradients of geopotential height are replaced by the corresponding advection of the vertical gradient of geopotential height. The boundary conditions are valid if the boundary temperature is conserved, which means the vertical motion at the boundaries equals zero (Bell and Bosart 1993).

How does the inversion of the QGPV advection term compare with the temporal finite difference of the geopotential height field? The 12-hour finite difference field and 24-hour finite difference field including or centered about 1200 UTC 3 December 1980 are presented in Figs. 4.24 and 4.25, respectively. The 1200 UTC 3 December 1980 geopotential height tendency at 372 mb is presented in Fig. 4.26. The main centers of height tendency are captured by the inversion of QGPV advection. The positions are

slightly different, but this is likely due to the 12 or 24-hour time steps. The magnitudes are comparable. This comparison provides confidence in the inversion method.

The inverse operator ( $\mathbf{L}^{-1}$ ) of (4.42) and appropriate boundary conditions can be applied to the four remaining terms in (4.39) after neglecting the Terms 1 and 3, yielding

$$\frac{\partial z'}{\partial t} = \mathbf{L}^{-1}(-\bar{\mathbf{V}}_g \bullet \nabla q') + \mathbf{L}^{-1}(-\mathbf{V}'_g \bullet \nabla \bar{q}) + \mathbf{L}^{-1}(-\mathbf{V}'_g \bullet \nabla q') \quad (4.43)$$

The left hand side of (4.43) is the small-scale geopotential height tendency, and will be used to determine midtropospheric mobile trough intensification or decay. Since the nonlinear advections in Terms 7, 8 and 9 will produce some large-scale patterns, each advection term in 4.43 was filtered using the high-pass filter described earlier in this chapter. This additional filtering ensures the geopotential height tendency associated with mobile troughs is truly small-scale.

The first term on the right hand side of (4.43), Term 7, is the mobile trough intensification due to the advection of small-scale QGPV by the large-scale geostrophic wind. Term 7 is used to determine the deformation (superposition) mechanisms described in Chapter III (and Appendix 3). The second term on the right hand side of (4.43), Term 8, is the mobile trough intensification due to the advection of large-scale QGPV by the small-scale geostrophic wind. It is used to determine the baroclinic, barotropic and group velocity processes. The last term on the right hand side of (4.43), Term 9, is the mobile trough intensification due to the advection of small-scale QGPV by the small-scale geostrophic wind. It is used to determine the trough-merger process. The application of each term in (4.43) will be described in detail in Chapter V.

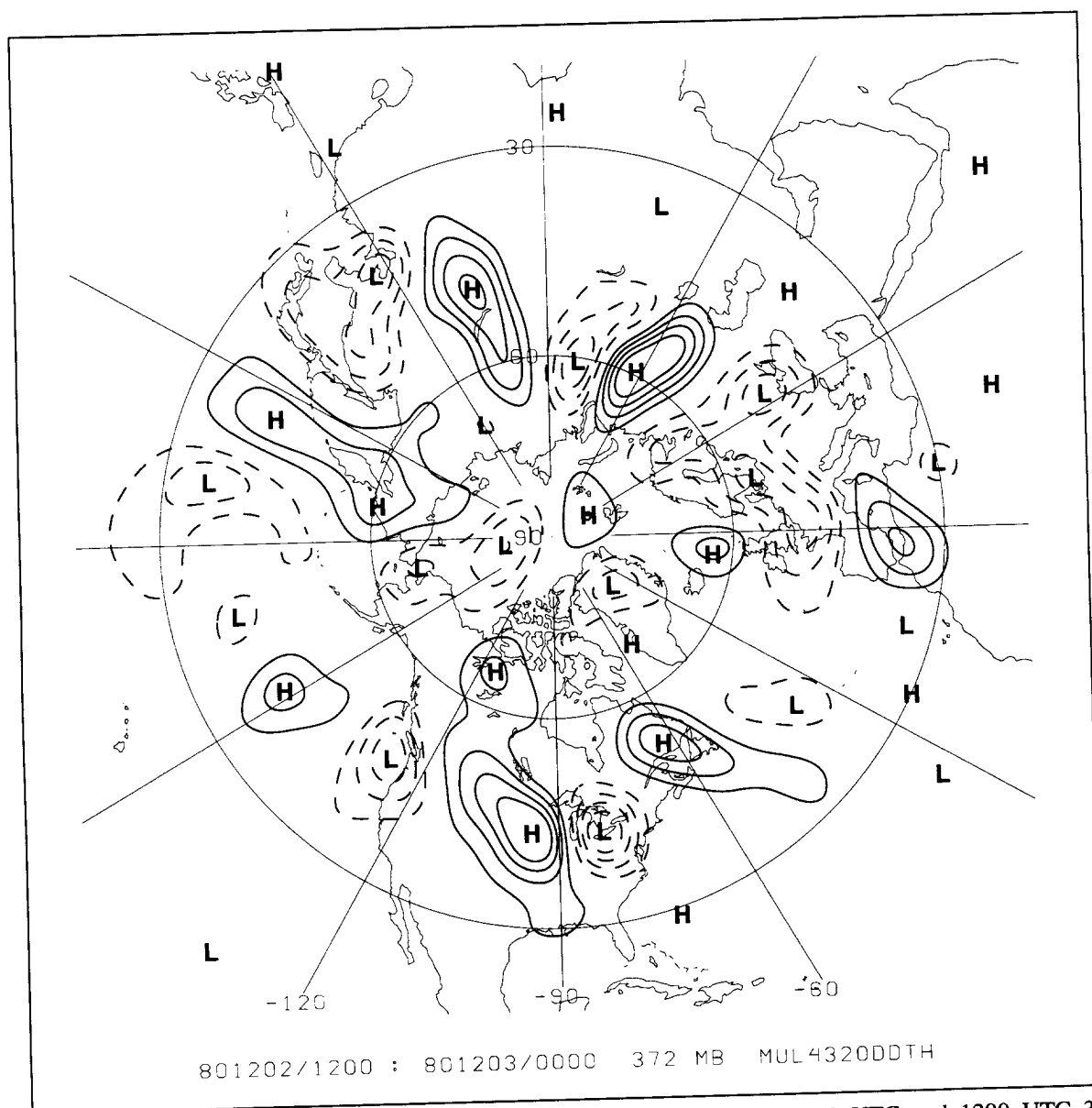


Fig. 4.24. The 12-hour temporal finite difference at 372 mb using the 0000 UTC and 1200 UTC 3 December 1980 geopotential height fields. The contour interval is 5 dam per 12 hours. The zero contour is not drawn.

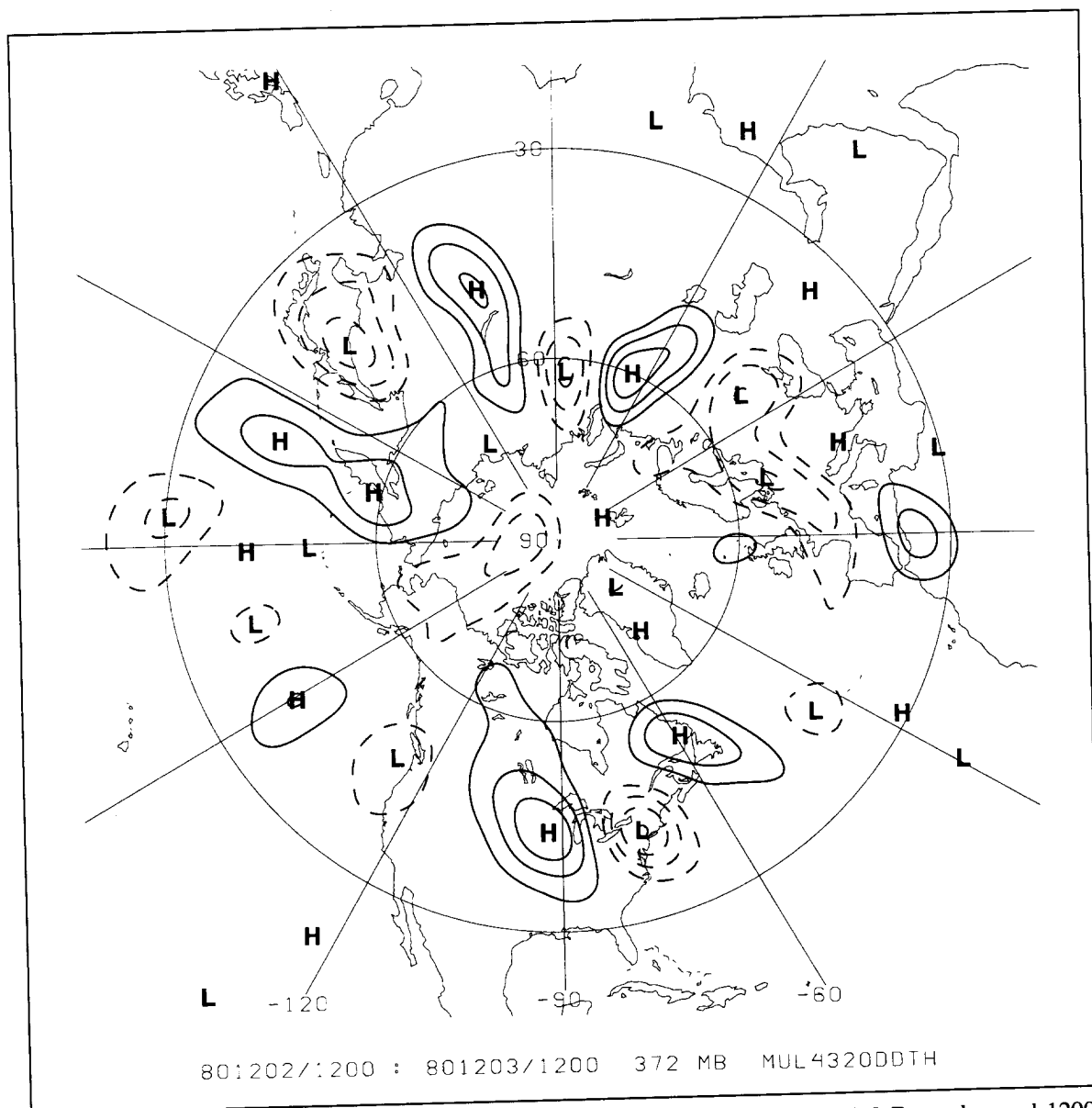


Fig. 4.25. The 24-hour temporal finite difference at 372 mb using the 1200 UTC 2 December and 1200 UTC 3 December 1980 geopotential height fields. The contour interval is 5 dam per 12 hours. The zero contour is not drawn.

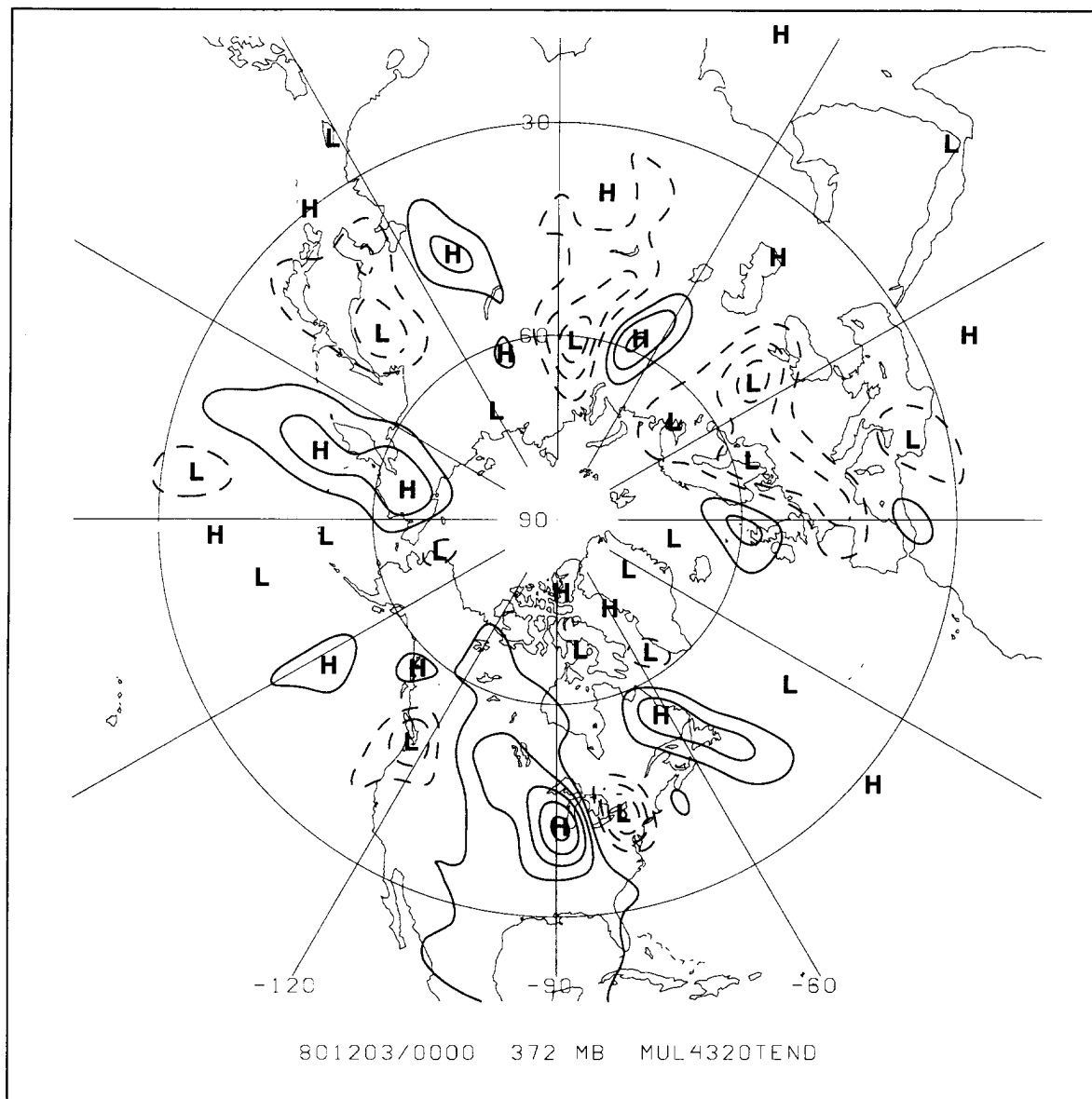


Fig. 4.26. The 372 mb geopotential height tendency field using the linear inversion of the 0000 UTC 3 December 1980 QGPV advection field. The contour interval is 10 dam per 12 hours. The zero contour is not drawn.

## 8. Summary

The large-scale background QGPV field used in this research is based on the spherical harmonic filtering of the total QGPV field. Zonal wavenumbers less than or equal six are considered to be large-scale, and zonal wavenumbers greater than six are considered small-scale, or perturbations on the large-scale. The choice of large-scale is justified for the analysis of mobile troughs. The objectively identified mobile troughs occur, for the most part, in the perturbation field, not the large-scale field. The break between large-scale and small-scale has been confirmed by other authors.

The linear inversion of the total QGPV fields and the piecewise inversion of the vertically partitioned QGPV fields is robust. The inversion of the total height field recovers all the geopotential height signal. The sum of the pieces in the piecewise inversion is almost identical to the original geopotential height field.

The linear inversion of the advection of QGPV by the geostrophic wind yields the geopotential height tendency. This geopotential height tendency resembles the 12 and 24-hour temporal finite difference of the corresponding geopotential height fields.

The piecewise inversion of the individual terms in the QGPV geopotential height tendency equation is straightforward in a mathematical sense. The application of the inversion results to mobile trough intensification will be demonstrated in detail in Chapter V.



## **CHAPTER V**

### **CASE STUDY OF MOBILE TROUGH DEVELOPMENT**

The purpose of this chapter is to apply the quasigeostrophic potential vorticity (QGPV) diagnostic technique as described in Chapter IV to an example of midtropospheric mobile trough genesis and intensification. The mobile trough selected for the case study was identified by the objective trough tracking method described in Chapter II. Three of the prominent development mechanisms described in Chapter III will be studied in detail using the QGPV diagnostics.

#### **1. Selecting the mobile trough**

The mobile trough used in this case study was one of 27,469 mobile troughs identified and tracked during the 20-year trough climatology. The first criterion to narrow the possible trough candidates was to select a trough that formed and remained over the data-rich land areas within the midlatitudes. For this reason, the search for a candidate was limited to the troughs forming in the region near the west coast of North America (Fig. 2.9). This trough genesis area accounted for 385 mobile troughs.

The average lifespan of mobile troughs forming in this chosen area was 5.7 days, compared to the overall average of 5.3 days. The maximum life span was 21 days. A terse overview of many of the troughs forming in this area reveals two predominant flow patterns that spawned mobile troughs.

The first pattern typically produced mobile troughs during the late-Fall through Spring months. It was associated with a broad, large-scale trough near the west coast of North America. A large-scale, blocking ridge evident in the middle and upper troposphere often occurred upstream of the large-scale trough. Sometimes, but not always, the large-scale trough was associated with a cutoff low pressure center in the upper troposphere.

The mobile troughs would generally begin as small perturbations in the belt of maximum winds near the base of the 500 mb large-scale troughs in the geopotential height field. The flow was typically zonal across the United States in the middle and upper troposphere. The mobile troughs would amplify as they left the large-scale trough and

progress steadily across the United States in the zonal large-scale flow. If the mobile troughs gained a significant amplitude, they typically produced a cutoff low pressure center in the middle troposphere near the east coast of North America.

The second pattern produced mobile troughs in a fairly zonal flow over the central and southern United States. This flow pattern occurred most often during the summer months. The mobile troughs typically formed over southern California, distant from the cutoff low pressure centered over western Canada.

The trough selected to demonstrate the functionality of the QGPV height tendency diagnostic technique formed in a large-scale pattern similar to the first pattern described above. The trough lasted 21 days according to the objective tracking technique. This trough was one of the two most long-lived troughs forming in this area. It was chosen because it developed, moved across the United States, and formed a cutoff low pressure area off the east coast of the United States all within a few days from its birth. The objective tracking of this trough followed it through the quasi-stationary cutoff low phase at the end of the first ten days, and began moving it again over the north Atlantic Ocean and Europe for an additional 11 days. Only the first ten days of this trough's lifespan will be studied here.

## **2. Life history of the trough at 500 mb**

The objective identification and tracking portion of this research initiated a mobile trough from within a large-scale trough in the 500 mb geopotential height field (Fig. 5.1). The large-scale trough extended from central Canada toward the west coast of North America. A pronounced, large amplitude geopotential height ridge was located directly upstream of the large-scale trough. The overall pattern present during the genesis of this mobile trough was similar to the midtropospheric pattern studied by Reed et al. (1992).

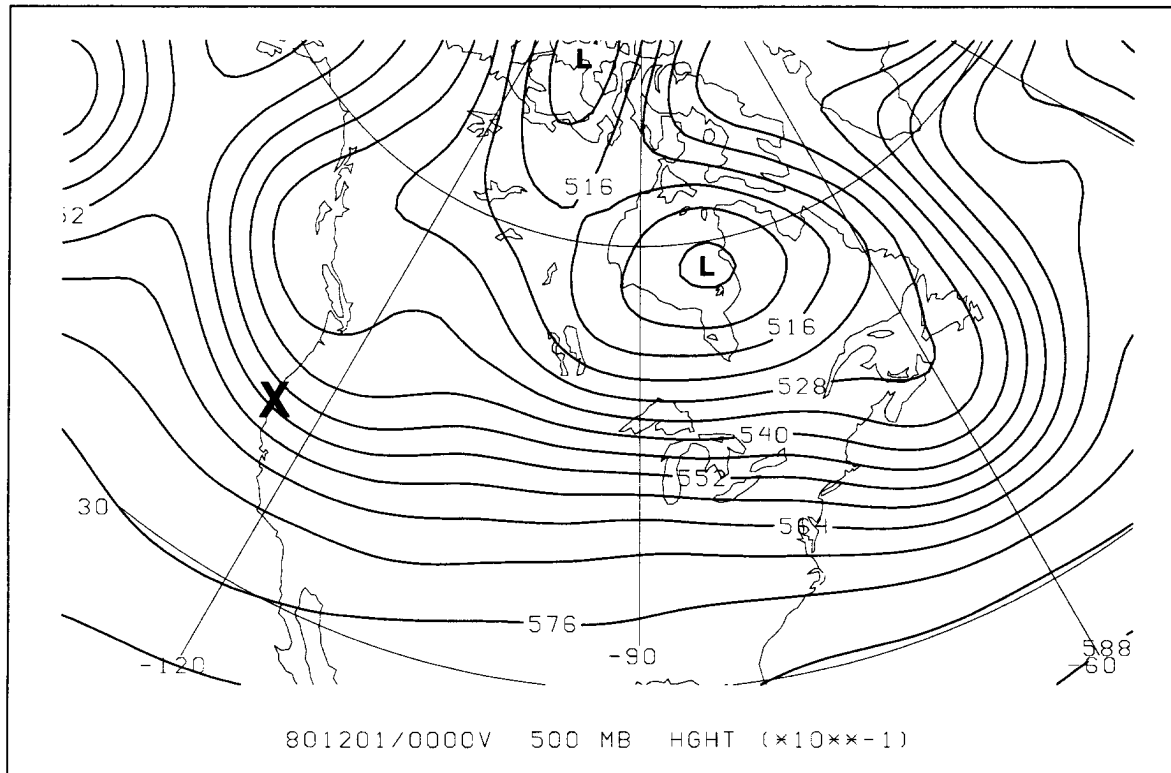


Fig. 5.1. A 500 mb geopotential height analysis for 0000 UTC 1 December 1980. The contour interval is 6 dam. The mobile trough is marked with an X.

One could argue the small-scale trough identified by the objective method could have continued from a small-scale trough which originated off the east coast of North America on 16 November 1980 (not shown), and eventually developed into the large-scale ridge-trough pattern over the eastern Pacific Ocean in Fig. 5.1. However, the small-scale trough dispersed from the large-scale trough on 1 December 1980 as evidenced by its location at 0000 UTC 3 December 1980 (Fig. 5.2). The objective method initiated this trough on 1 December 1980 and produced an acceptable scenario. Therefore, the initial analysis of the small scale trough development used in this portion of the study was on 1200 UTC 30 November 1980, the time step immediately preceding the trough genesis. However, all the data presented will begin on 0000 UTC 1 December 1980. The time prior to this was used for continuity in the temporal finite difference tendency calculations.

The small-scale trough in the 500 mb geopotential height field moved across central North America and continued to amplify. By 0000 UTC 3 December it was centered over the Ohio Valley with significant amplitude (Fig. 5.2). By 0000 UTC 5 December it almost formed a complete cutoff low at 500 mb off the east coast of North America. The low remained quasi-stationary for the next 72 hours. The objective tracking technique continued to follow a small-scale trough around the main "cutoff" low. On 0000 UTC 10 December the small-scale mobile trough began moving steadily across the north-central Atlantic Ocean (Fig. 5.3).

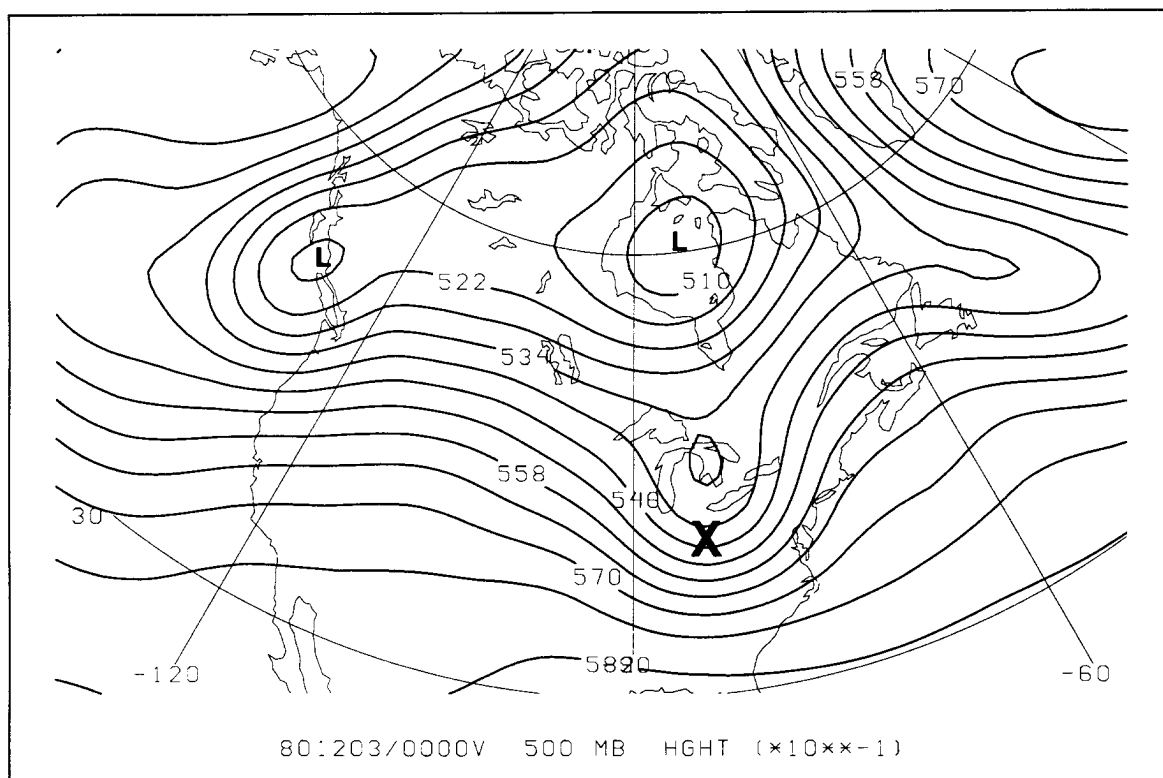


Fig. 5.2. A 500 mb geopotential height analysis for 0000 UTC 3 December 1980. The contour interval is 6 dam. The trough near the Great Lakes originated from the cutoff low off the west coast of North America on 0000 UTC 1 December 1980. The mobile trough is marked with an X.

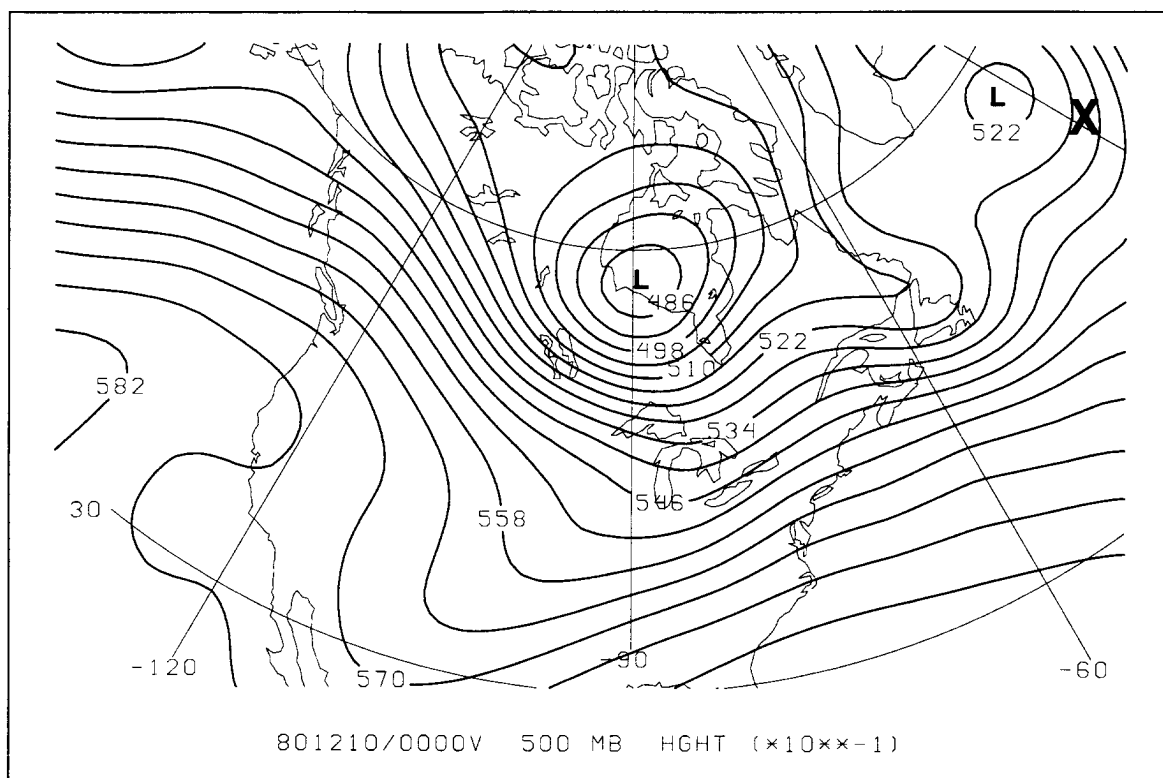


Fig. 5.3. A 500 mb geopotential height analysis for 0000 UTC 10 December 1980. The contour interval is 6 dam. The mobile trough is marked with an X.

The small-scale mobile trough continued across northern Europe and central Asia (not shown). It eventually disappeared in nearly zonal flow across southwest Asia. The objective tracking method terminated this trough near Taiwan on 0000 UTC 19 December 1980 (not shown).

The QGPV diagnostics were used to analyze the formation of the small-scale trough near the west coast of North America, the amplification of it over the mainland, and its maturation to a near cutoff low off the east coast of North America. Even though the second half of this trough's life cycle from the cutoff low to its termination off of east Asia would be interesting, the first ten days of its lifespan provide ample information to demonstrate the application of the diagnostic technique.

While the midtropospheric mobile trough was beginning on 0000 UTC 1 December, the surface (taken as 922 mb) low in the geopotential height field was also developing over the central United States (Fig. 5.4). At this time it is difficult to conclude that the surface low present over the central United States was associated with the midtropospheric trough forming near the west coast of Canada.

The surface low center, however, does eventually couple with the midtropospheric trough during the subsequent 24 hours as it moves into the Ohio Valley. It continued to move toward the northeast and developed into a fairly intense system by 0000 UTC 5 December (Fig. 5.5). It remained quasi-barotropic with the midtropospheric trough and began to fill during the next 72 hours. As the midtropospheric trough began its second stage, the surface low began to deepen again and move also.

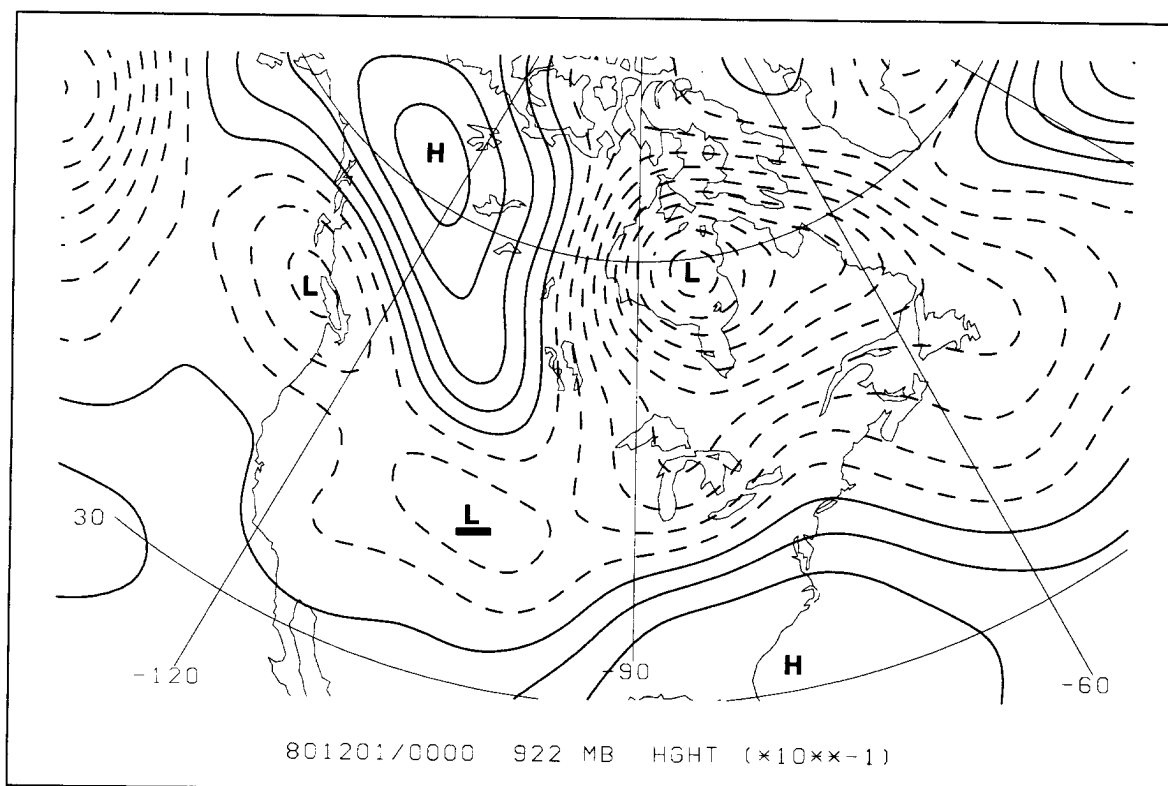


Fig. 5.4. A 922 mb geopotential height analysis on 0000 UTC 1 December 1980. The contour interval is 3 dam. The first solid contour is equal to zero. The low pressure center taken to be the start of the surface low is underlined.



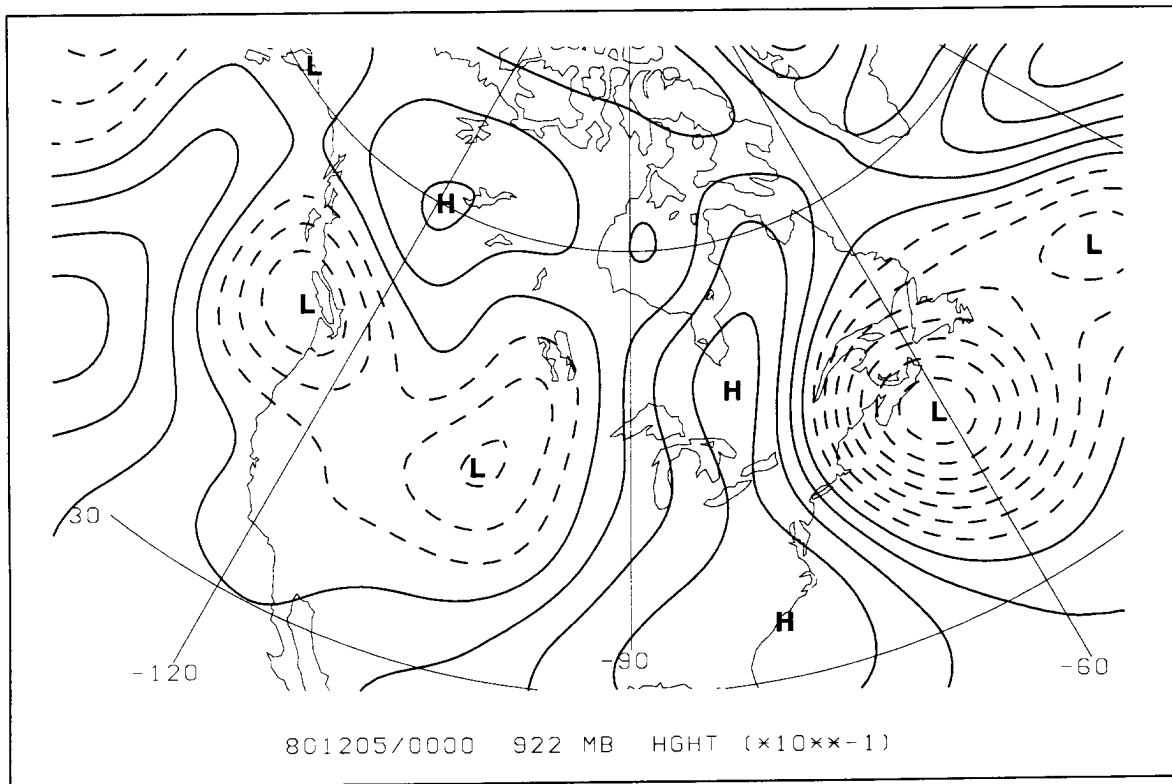


Fig. 5.5. A 922 mb geopotential height analysis on 0000 UTC 5 December 1980. The contour interval is 3 dam. The first solid contour is equal to zero.

Until now, the midtropospheric mobile trough and surface low center have been discussed using the full geopotential height fields and the objectively identified trough locations. However, it will be more enlightening to track the small-scale perturbation geopotential and QGPV anomalies as produced by the spherical harmonic filtered fields. The small-scale and large-scale fields are described in Chapters IV.

The small-scale perturbation centers are typically found between the objectively-tracked trough positions and the low geopotential height center using the full (unfiltered) fields (Fig. 5.6). This positioning is due to the filtering technique. The largest perturbations will occur within the trough, but not necessarily within the maximum wind belt of the objective method. The maximum perturbation will not typically occur with the low center of the full field because the perturbation is generally embedded within a large-scale height gradient.

The negative geopotential height centers and positive QGPV centers move consistently with the trough positions identified using the objective method. Development of the midtropospheric mobile trough is defined by the magnitude and sign of the small-scale perturbation geopotential height centers. The troughs or low level centers intensify when the small-scale centers have negative height tendency, and decay when the tendency is positive. Recall from Chapter IV the intensification or height tendency determination results from the inversion of the QGPV form of the geopotential height tendency equation.

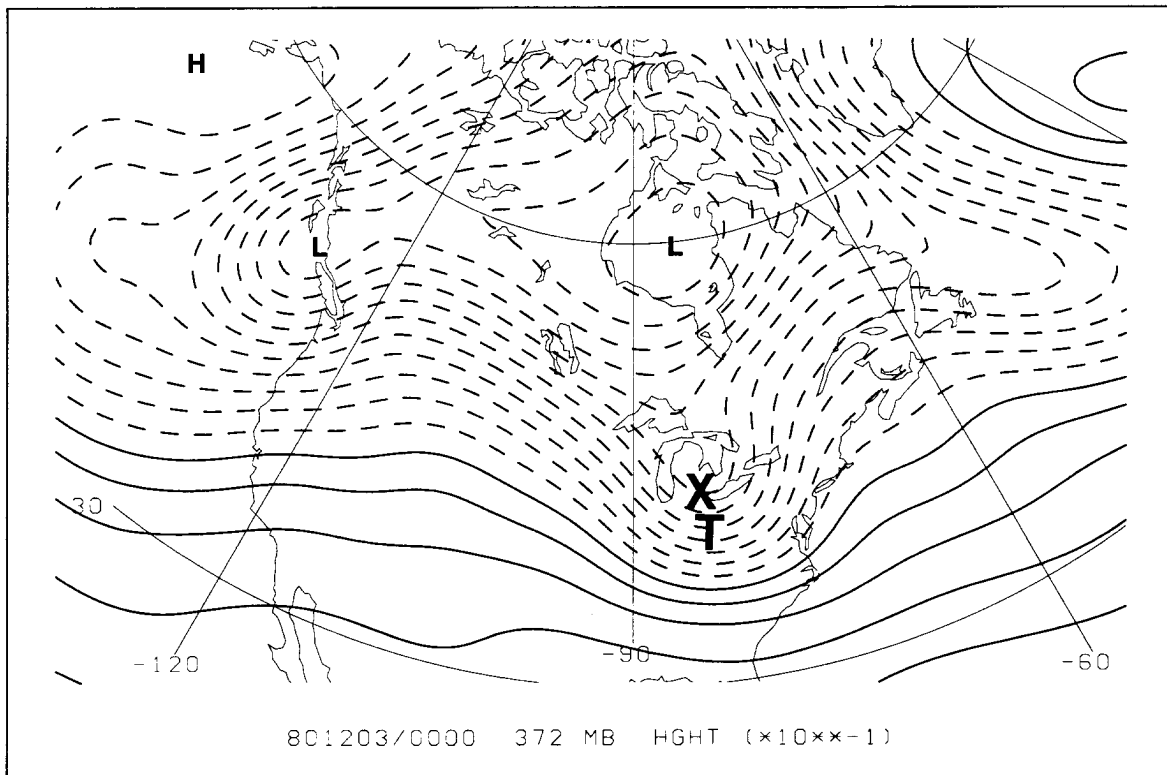


Fig. 5.6. A 372 mb analysis of the geopotential height field for 0000 UTC 3 December 1980. The contour interval is 6 dam. The first solid contour is equal to zero. The "T" marks the position of the 500 mb trough as identified by the objective tracking method. The "X" marks the position of the 372 mb small-scale perturbation center.

### 3. Diagnosing the trough development mechanisms

The trough development diagnosis is based on the large-scale and small-scale wind (height) and QGPV fields for the upper and lower troposphere. Table 5.1 describes the acronyms used to simplify the discussion of the advection components in Terms 7, 8 and 9 of (4.43). The first two letters identify the wind field used to advect the QGPV. The first letter (L, U, or F) identifies the geopotential height (geostrophic wind) field resulting from the lower, upper, or full (all) levels of the piecewise QGPV inversion. The second letter (B or P) represents the height (geostrophic wind) field resulting from the inversion of the large-scale (bar) or small-scale (prime) QGPV. The third and fourth letters represent the QGPV gradient being advected by the wind described using the first two letters. The third letter (L, U, or F) represents the lower, upper, or full QGPV gradient. The fourth letter (B or P) represents the large-scale (bar) or small-scale (prime) QGPV gradient. The last letter (T) represents the geopotential height tendency.

The reconstruction of the full geostrophic height tendency from the component pieces results from the purely linear QGPV operator described in Chapter IV. The time series of the geopotential height (Figs. 5.7 top) and geopotential height tendency (Figs. 5.7 bottom), filtered to identify only the small-scale effects, demonstrates the legitimacy of using the QGPV diagnostic technique. The initial development from 0000 UTC 1 December through 0000 UTC 3 December and the decay from 0000 UTC 3 December through 0000 UTC 5 December are captured fairly well. After 0000 UTC 5 December the mobile trough cycled through periods of weak intensification and decay, but predominantly decayed.

Table 5.1. The definition of the acronyms used to describe the intensification processes.

Acronym	Tendency Due to QGPV Advection
Term 7	
FBLPT	Wind from all levels, large scale QGPV inversion advecting lower-level, small-scale QGPV
FBUPT	Wind from all levels, large scale QGPV inversion advecting upper-level, small-scale QGPV
Term 8	
LPLBT	Wind from lower level, small scale QGPV inversion advecting lower-level, large-scale QGPV
LPUBT	Wind from lower level, small scale QGPV inversion advecting upper-level, large-scale QGPV
UPLBT	Wind from upper level, small scale QGPV inversion advecting lower-level, large-scale QGPV
UPUBT	Wind from upper level, small scale QGPV inversion advecting upper-level, large-scale QGPV
Term 9	
FPFPT	Wind from all levels, small scale QGPV inversion advecting all-levels, small-scale QGPV

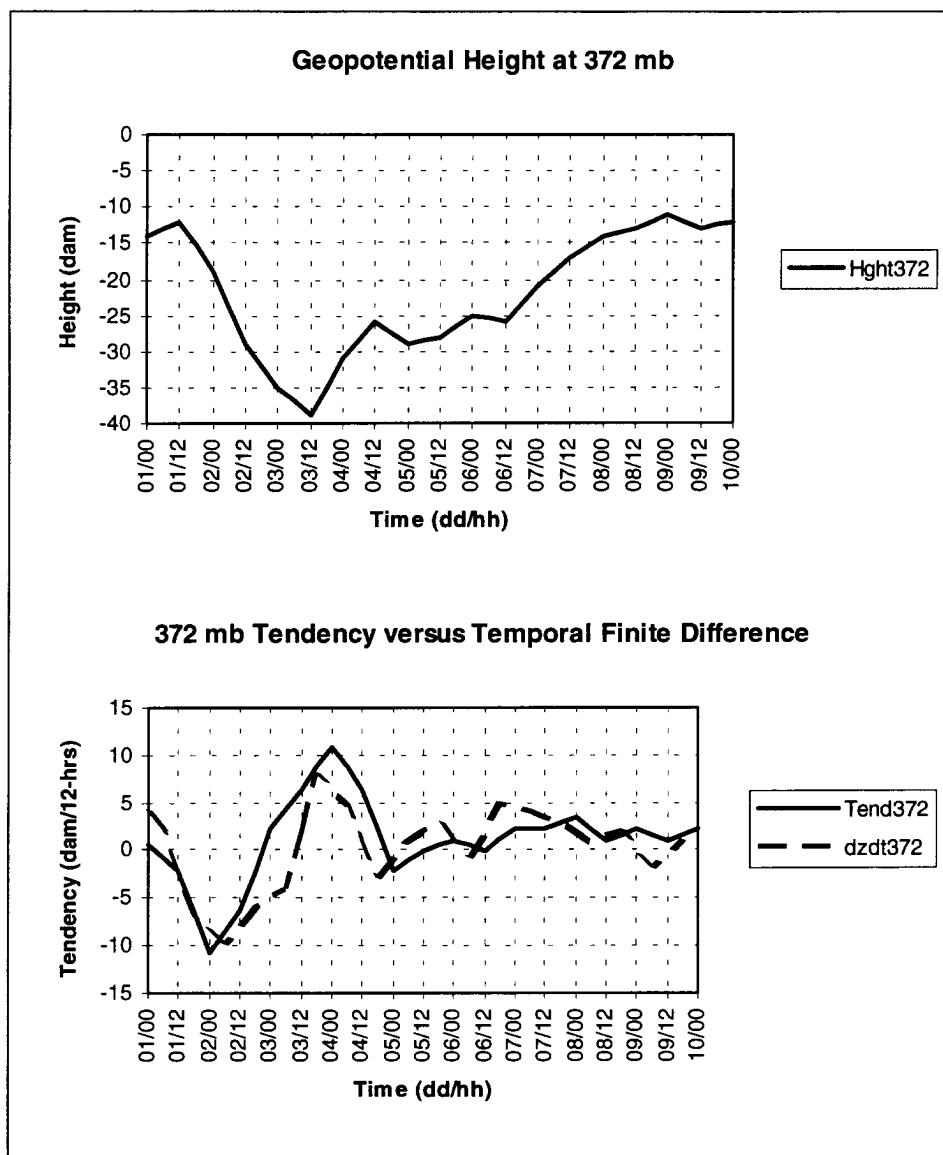


Fig. 5.7. Time series of geopotential height and geopotential height tendency at 372 mb. The upper chart shows geopotential height (dam) at the trough position. The lower chart shows geopotential height tendency (dam/12-hrs). The solid line is the geopotential height tendency calculated by the QGPV equation at the position of the 372 mb trough location. The dashed line is the temporal finite difference geopotential height tendency at 372 mb.

As mentioned in Chapter IV, temporal finite difference geopotential height tendency calculated from 12-hourly geopotential height analyses differs from the geopotential tendency calculated by the QGPV form of the geopotential height tendency equation (Figs. 5.7 and 5.8). Chapter III described some of the possible errors using the QG assumptions. A large portion of the error is likely due to the 12-hour finite difference. The QGPV form of the height tendency calculations will be used as the “standard” to diagnose the development of the midtropospheric mobile trough.

The initial intensification (0000 UTC 1 December through 1200 UTC 1 December) occurred when the mobile trough formed west of the Rocky Mountains. The trough intensified, but not significantly. The most rapid intensification occurred at 0000 UTC 2 December. The trough was east of the Rockies and entering the central plains of the United States. After this time the mobile trough continued to intensify, but at a slower rate. After approximately 1800 UTC 2 December the trough began to weaken. The most intense decay occurred at 0000 UTC 4 December. By 0000 UTC 5 December the trough was situated off the New England coast and weakening.

The time series for the surface low center geopotential height and geopotential height tendency for this case are not shown, because the tendency calculations were only performed for the interior levels. However, the 872 mb level, the lowest interior level, is only 50 mb above the 922 mb surface, and is assumed to be representative of the surface development. The time series of geopotential height (Fig. 5.8 top) and geopotential height tendency (Fig. 5.8 bottom) shows the surface low center developed during the time when the mobile trough developed.

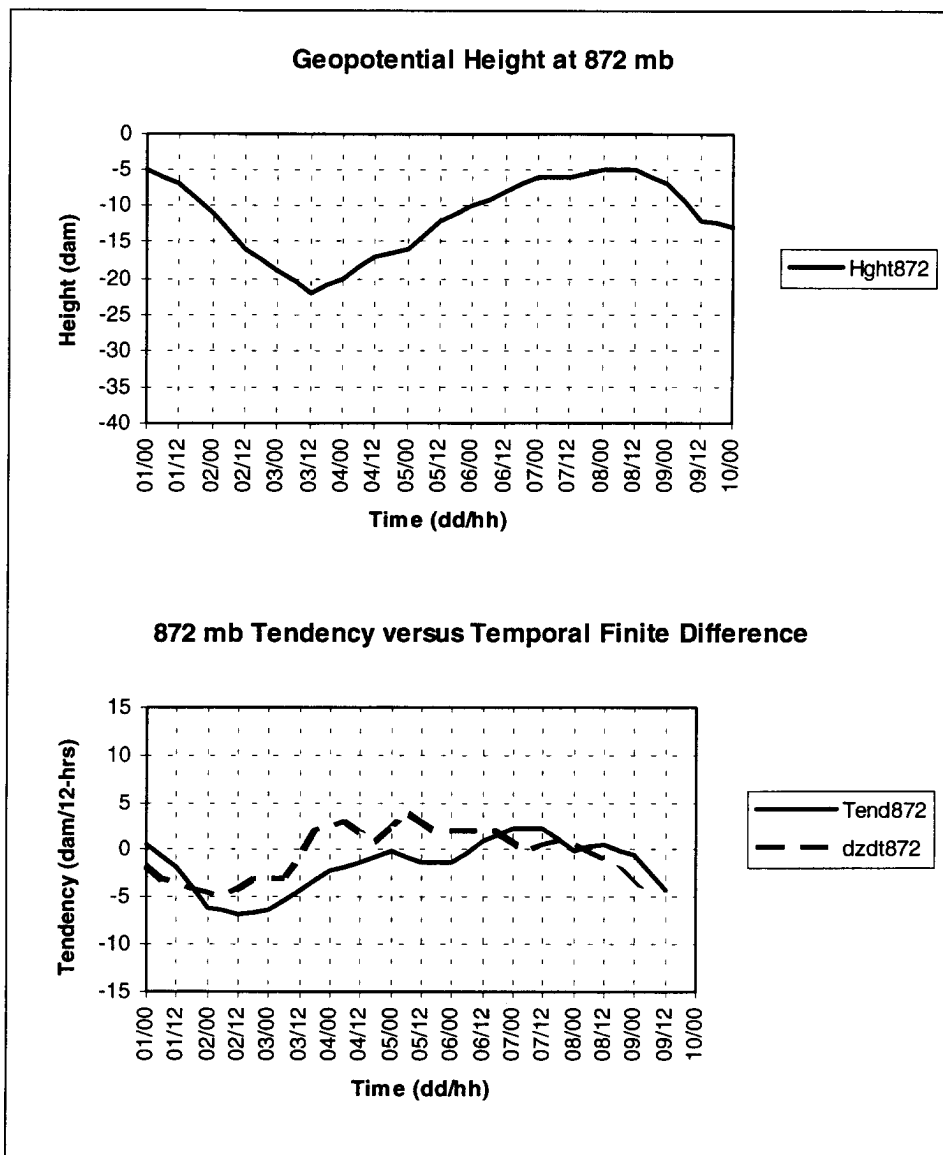


Fig. 5.8. Time series of geopotential height and geopotential height tendency at 872 mb. The upper chart shows geopotential height (dam) at the trough position. The lower chart shows geopotential height tendency (dam/12-hrs). The solid line is the geopotential height tendency calculated by the QGPV equation at the position of the 872 mb trough location. The dashed line is the temporal finite difference geopotential height tendency at 872 mb.



The surface intensification was not as intense as the mobile trough development, but lasted for a longer time. The surface low center initially developed with the mobile trough until 1800 UTC 2 December. When the mobile trough began to decay, the surface low center continued to intensify. The intensification of the surface low did not subside until 0000 UTC 5 December, when the mobile trough's intense decay slowed. After 0000 UTC 5 December the surface low cycled through weak periods of intensification and decay. In general, this cyclic period at the surface corresponded to weak decay of the mobile trough.

The series of analyses in Figs. 5.9 through 5.12 show the large and small-scale geopotential height and QGPV fields at one upper tropospheric level (372 mb). The analyses in Figs. 5.13 and 5.14 show the corresponding large and small-scale geopotential height fields at the surface (922 mb). The lower level QGPV is not shown. Instead, the negative of the vertical geopotential height gradient at the surface (proportional to the surface temperature) is presented in Figs. 5.15 and 5.16.

The QGPV field has an influence on the geopotential height fields at every level. Setting the upper or lower QGPV fields equal to zero and inverting the QGPV to get geopotential height results in nonzero geopotential height fields at all levels. Since the strongest effect of small-scale QGPV is fairly localized to the level with the QGPV (Davis and Emanuel 1991, Davis 1992a), the small-scale height fields at 372 mb and 872 mb due to piecewise inversion of the UP and LP QGPV fields, respectively, resemble the full small-scale geopotential height fields at 372 mb and 872 mb. However, the large-scale geopotential height fields due to piecewise inversion (for example, setting the vertical gradient of geopotential height equal to zero at the surface and inverting the upper-level large-scale QGPV) results in an unrealistically intense north-south gradient of geopotential height, or geostrophic wind (not shown).

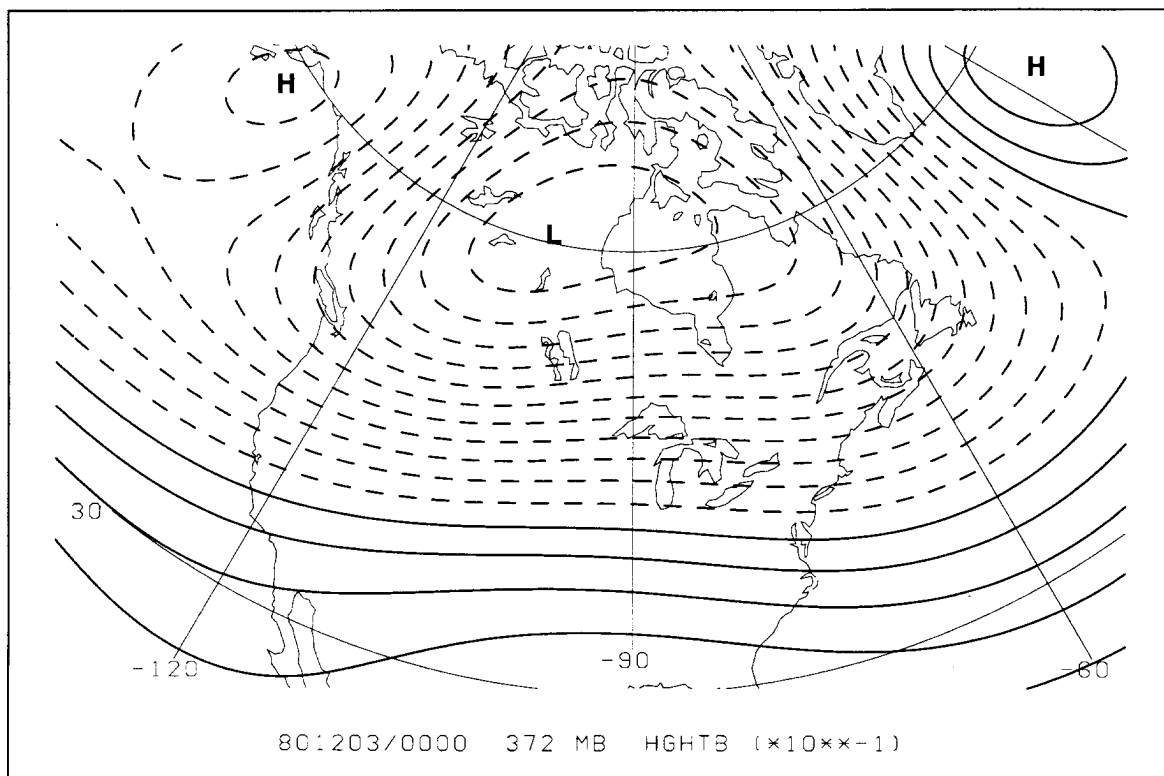


Fig. 5.9. The large-scale geopotential height field at 372 mb on 0000 UTC 3 December 1980. The contour interval is 6 dam. The first solid contour is equal to zero.

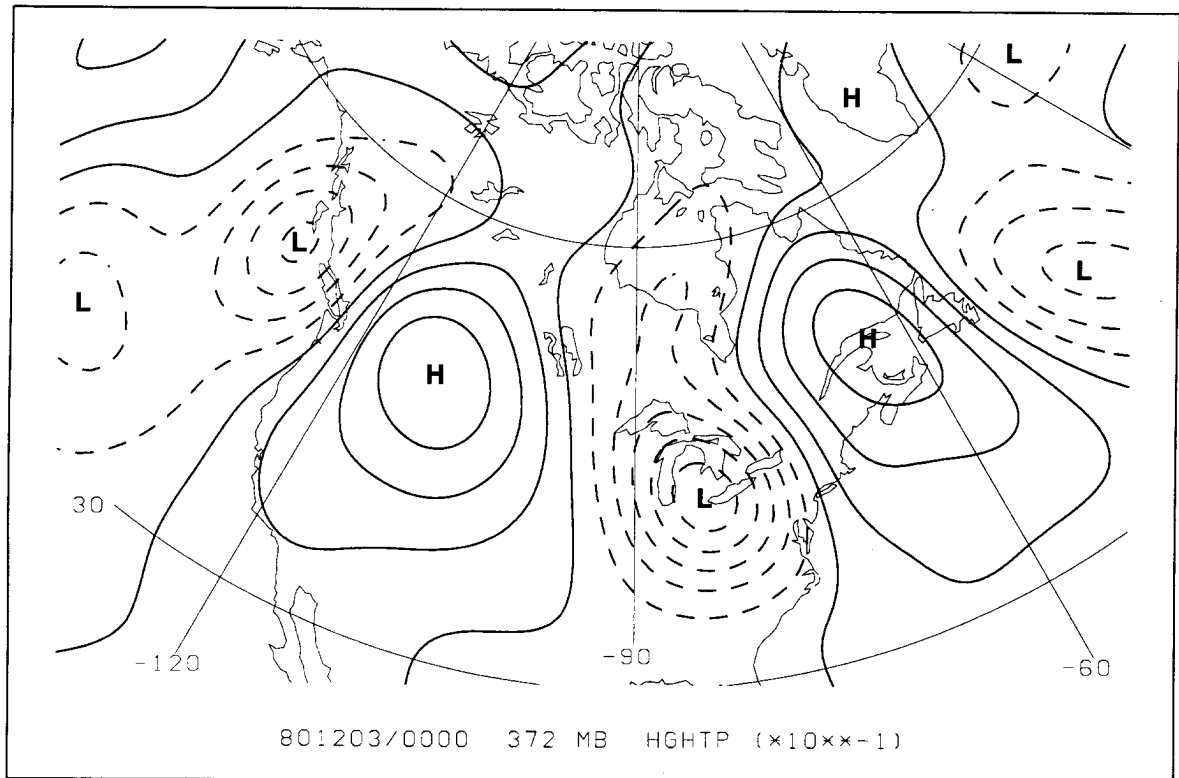


Fig. 5.10. The small-scale geopotential height field at 372 mb on 0000 UTC 3 December 1980. The contour interval is 6 dam. The first solid contour is equal to zero.

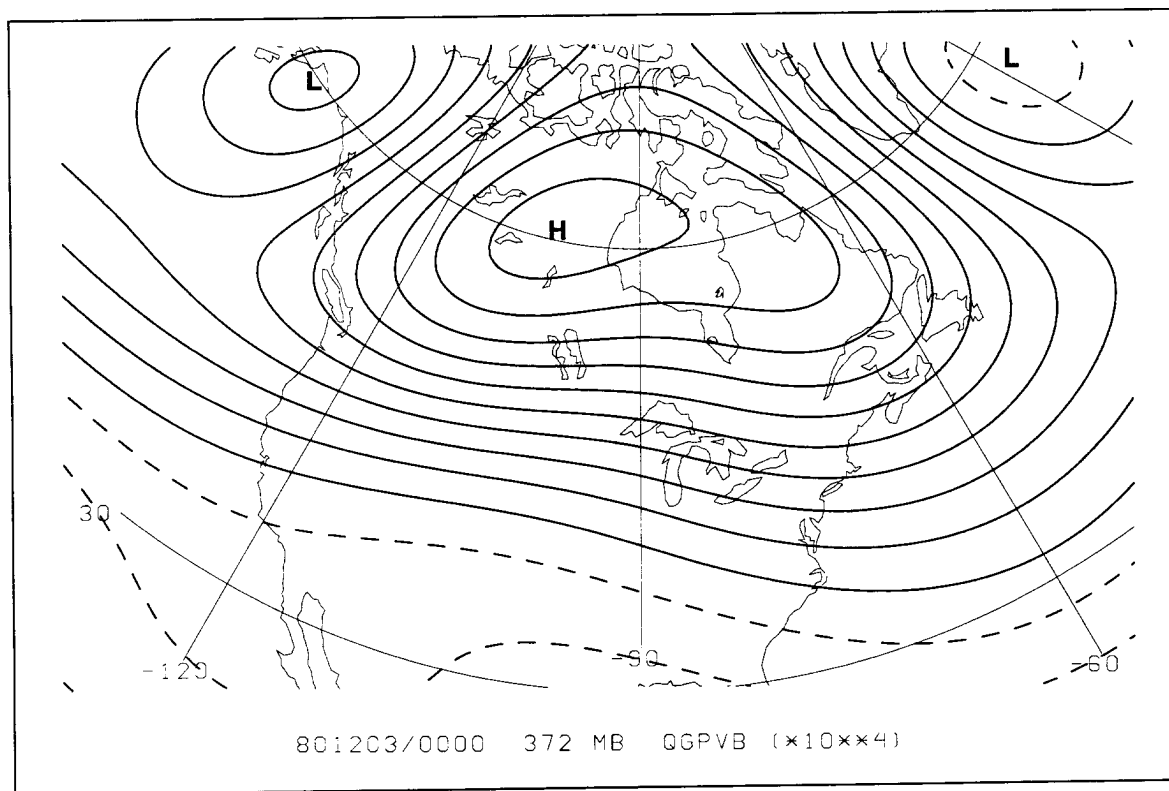


Fig. 5.11. The large-scale QGPV field at 372 mb on 0000 UTC 3 December 1980. The contour interval is  $0.5 \times 10^{-4} \text{ s}^{-1}$ . The first solid contour is equal to zero.

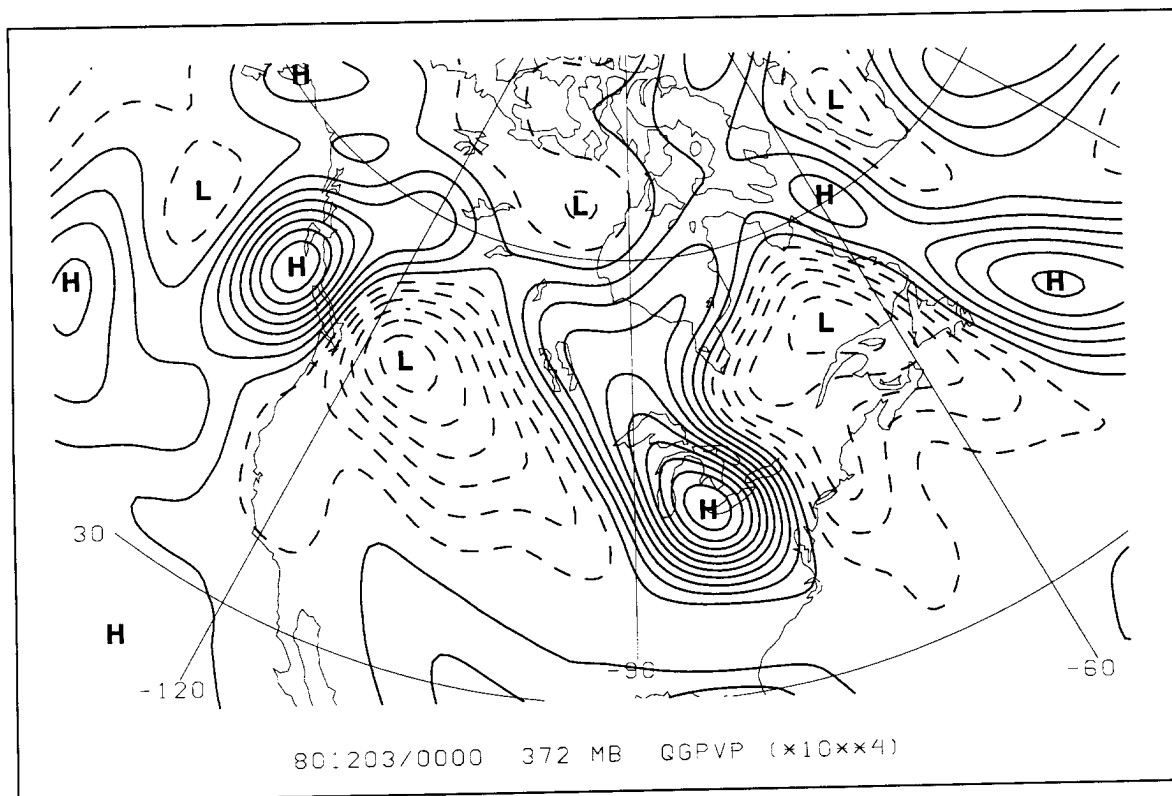


Fig. 5.12. The small-scale QGPV field at 372 mb on 0000 UTC 3 December 1980. The contour interval is  $0.5 \times 10^{-4} \text{ s}^{-1}$ . The first solid contour is equal to zero.

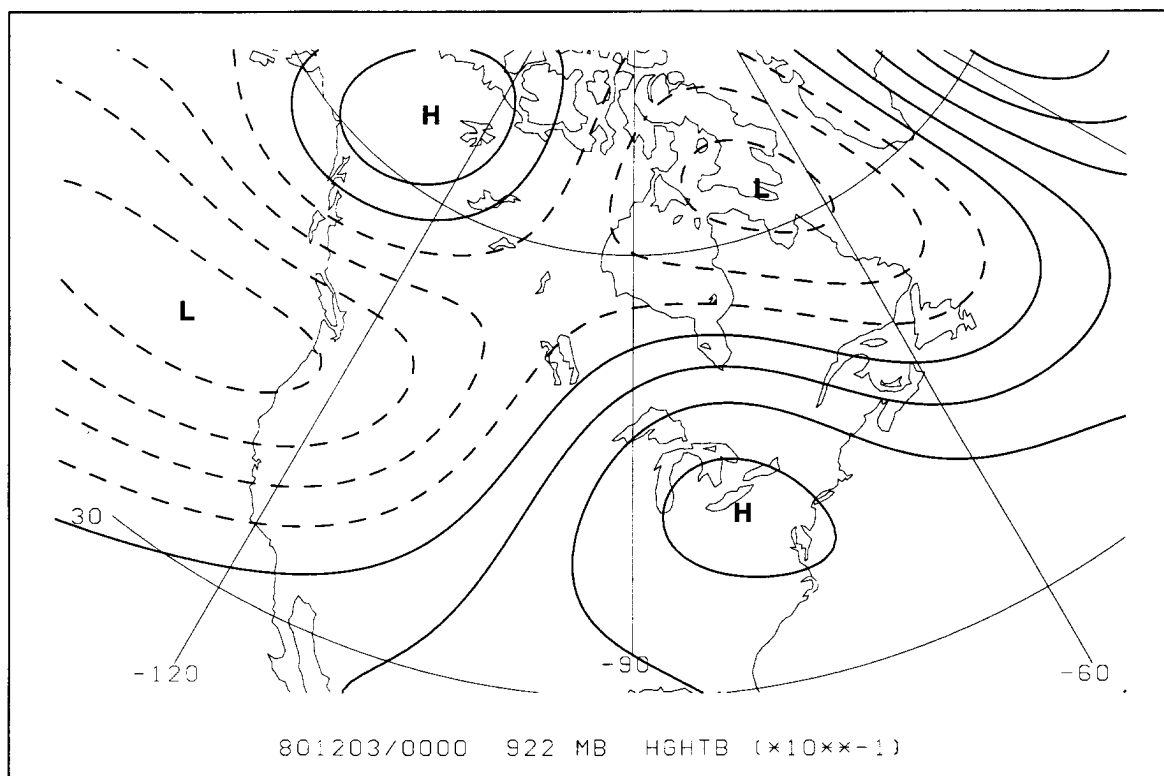


Fig. 5.13. The large-scale geopotential height field at 922 mb on 0000 UTC 3 December 1980. The contour interval is 3 dam. The first solid contour is equal to zero.

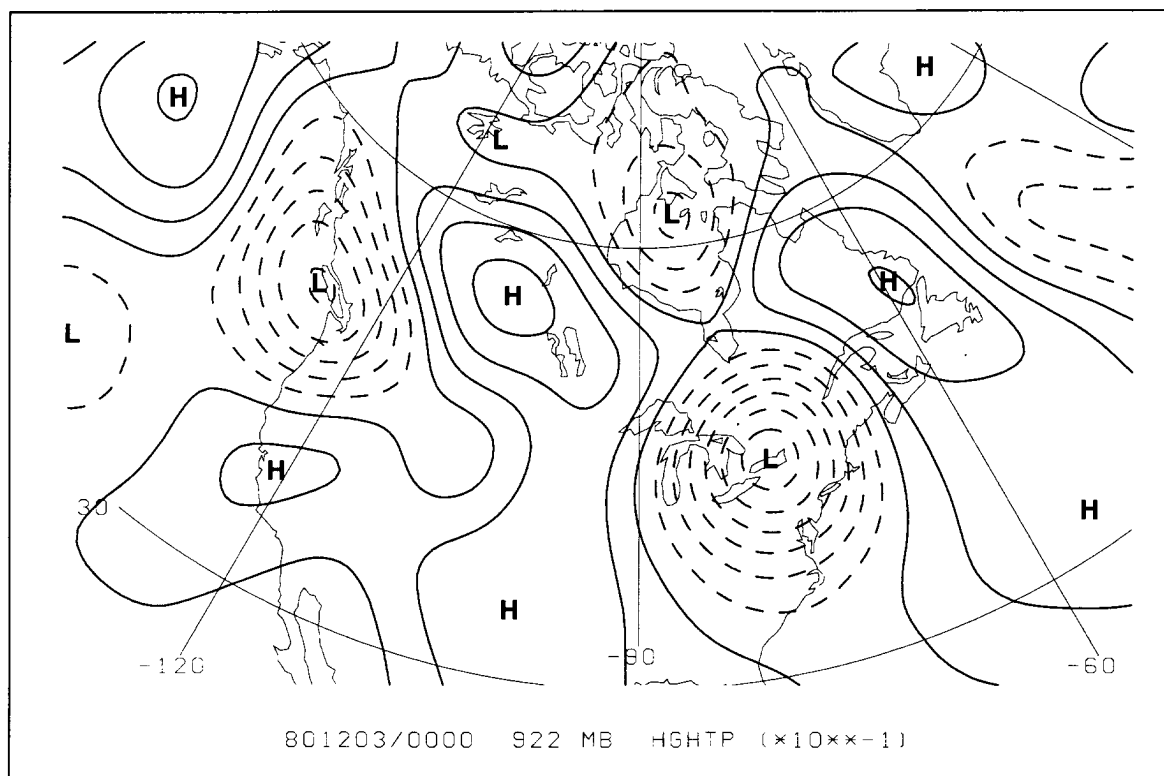


Fig. 5.14. The small-scale geopotential height field at 922 mb on 0000 UTC 3 December 1980. The contour interval is 3 dam. The first solid contour is equal to zero.

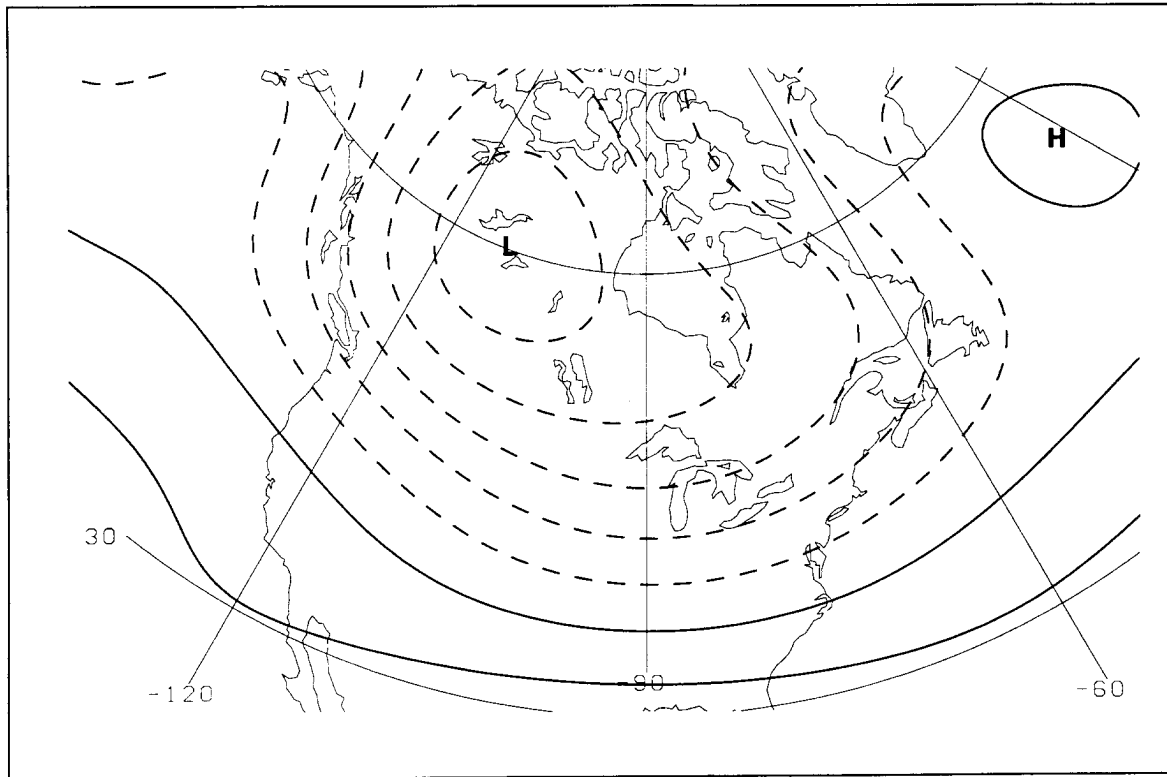


Fig. 5.15. The large-scale vertical gradient geopotential height at 922 mb on 0000 UTC 3 December 1980. The gradient has been multiplied by  $-1.0$  to make it proportional to the surface potential temperature field. The contour interval is  $2 \times 10^{-3} \text{ m mb}^{-1}$ . The first solid contour is equal to zero.



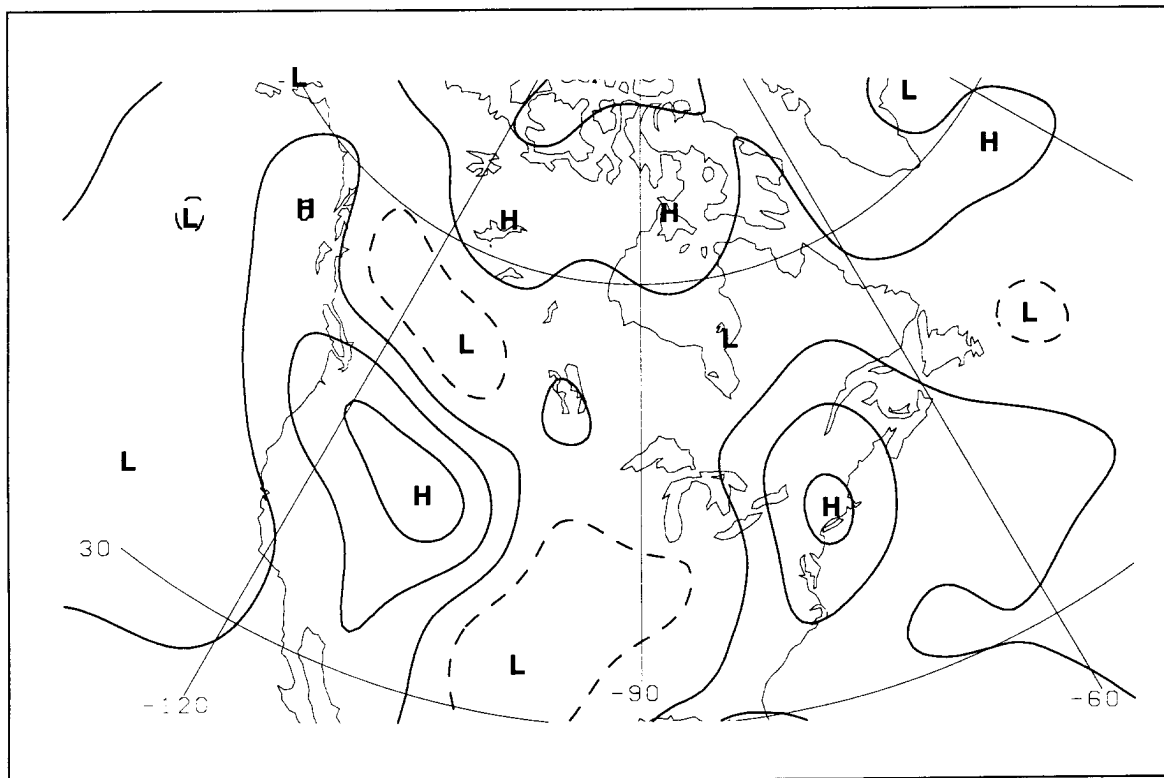


Fig. 5.16. The small-scale vertical gradient geopotential height at 922 mb on 0000 UTC 3 December 1980. The gradient has been multiplied by -1.0 to make it proportional to the surface potential temperature field. The contour interval is  $2 \times 10^{-3} \text{ m mb}^{-1}$ . The first solid contour is equal to zero.

This result agrees with those by Holopainen and Kaurola (1991 and 1993) and Davis (1993). It occurs because the piecewise inversion of the large-scale QGPV removes the critical “near-cancellation” between the boundary and interior QGPV. For a complete discussion of this cancellation see Holopainen and Kaurola, or Davis. The full large-scale (FB) geopotential height fields were used to advect the QGPV in the appropriate terms of (4.43).

The purpose of the previous eight figures (Figs. 5.9 through 5.16) was to provide a point of reference for the discussion of the QGPV advection and tendency to follow. The time selected for these figures, 0000 UTC 3 December 1980, was after the peak development, early in the life cycle of the midtropospheric mobile trough.

The 372 mb large-scale geopotential height field (Fig. 5.9) was typical of the large-scale height field throughout the life cycle. The field was fairly zonal across North America with negative geopotential heights toward the north (recall the hemispheric mean has been removed from all analyses). Later in the life cycle a large-scale wave pattern with two complete ridges and troughs within the map domain occurred, but the same basic height gradient was present.

The 372 mb small-scale geopotential height field (Fig. 5.10) shows the well-developed perturbation over the Great Lakes region. The center of this perturbation corresponds exactly with the midtropospheric mobile trough at this time. Strong northerly perturbation geostrophic wind was present upstream from the low center, and strong southerly winds occurred downstream.

The 372 mb large-scale QGPV field (Fig. 5.11) has the same general shape as the large-scale geopotential height field, except the sign of the gradient is opposite. The large positive QGPV values occurred toward the north.

Likewise, the 372 mb small-scale QGPV field (Fig. 5.12) has a similar shape, but opposite sign, to the upper level small-scale geopotential height field. The small-scale QGPV has more small-scale structure than the corresponding geopotential height field, consistent with the inversion of the elliptical operator.

The large-scale surface geopotential height field (Fig. 5.13) shows a smooth pattern with lower heights toward the north. A ridge is apparent over the Great Lakes where the upper tropospheric trough is positioned.

The small-scale surface geopotential height field (Fig. 5.14) shows a low center near the Great Lakes region. The position of the surface low center is displaced slightly toward the east compared to the upper tropospheric low center. The tilt between these low centers continued to decrease with time as the tropospheric cyclone became equivalent barotropic near New England a few days later.

In general, the pattern of large-scale vertical height gradient at the surface (Fig. 5.15) resembles the pattern of the upper tropospheric large-scale QGPV, but is opposite in sign. These patterns imply an equivalent barotropic nature of the large-scale troposphere over the northern hemisphere in winter. The thickness maximum near the east coast of the United States is displaced eastward in relation to the upper level small-scale QGPV center (Fig. 5.16). This configuration is typical of baroclinically growing systems.

#### *a. Baroclinic process*

The first dynamical mechanism of mobile trough genesis and development to investigate will be the baroclinic process. Recall from Chapter IV that baroclinic mechanism occurs when there is mutual amplification (two one-way intensification processes) by the lower level acting upon the upper level and vice versa. If the lower level and upper level waves (defined as negative geopotential height anomalies) are both deepening while this mutual amplification is occurring the process is termed baroclinic instability. Bleck (1990) graphically depicts the three dimensional nature of potential vorticity within the baroclinic process. Using the tendency terminology defined in Table 5.1, baroclinic processes can be diagnosed using the UPLBT (representing the lower-on-upper effects) and the LPUBT (representing the upper-on-lower effects) fields (Fig. 5.17). The UPLBT tendency, however, is most apparent in the lower troposphere and the LPUBT tendency is most apparent in the upper troposphere (not shown).

The schematic diagram in Fig. 5.17 shows both the UPLBT and LPUBT mechanisms. We will initially focus on the upper diagram and describe the one-way intensification, LPUBT, at the position of the mobile trough (the dot in Fig. 5.17). The thick, straight lines represent the large-scale horizontal QGPV gradient present in the middle and upper troposphere. The geostrophic wind associated with lower level QGPV anomalies are represented by the straight arrows (LP). The wind will advect the large-scale gradient at the positive anomaly in such a way as to increase the magnitude of the positive anomaly. The increased magnitude of the positive anomaly will be associated with negative geopotential height tendency at the trough (dot), mobile trough intensification. This mechanism is called one-way intensification.

The baroclinic amplification mechanism is completed by including the surface effects (UPLBT in this case) as presented in Fig. 5.17. The lower level effects form the another one-way intensification. The straight arrows on the temperature gradient in the lower diagram represent the geostrophic wind associated with the upper layer anomalies. In this case the wind is such that the positive temperature anomaly at the surface is increasing. The increased warm anomaly is manifest as a negative geopotential height tendency above (vertically) the warm anomaly, including height falls at the position of the mobile trough. The quantitative effect of the two one-way mechanisms described in Fig. 5.17 is used to diagnose the baroclinic process in this research.

The 372 mb level represents the upper troposphere, and the 872 mb level represents the lower troposphere in this research. A time series plot of these components at the upper and lower levels shows that the baroclinic process was present throughout the development of this mobile trough (Fig. 5.18).

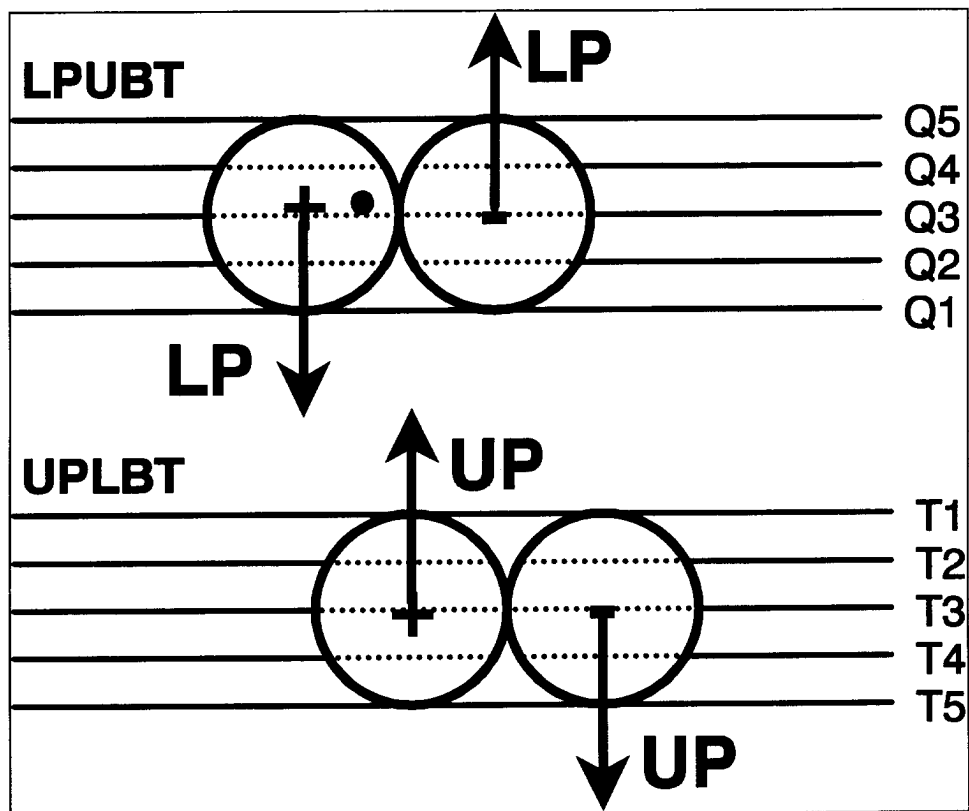


Fig. 5.17. A schematic diagram of the baroclinic process. The upper diagram is a horizontal depiction of the large-scale QGPV gradient in the upper troposphere. The arrows in the upper diagram are the winds associated with the small-scale temperature anomalies at the surface. The lower diagram is a horizontal depiction of the large-scale temperature gradient at the surface. The arrows in the lower diagram are the winds associated with the small-scale QGPV anomalies in the upper troposphere. The upper and lower positive anomalies are optimally positioned to produce mutual intensification at the position of the mobile trough in the upper troposphere as indicated by the dot near the center of the positive anomaly.

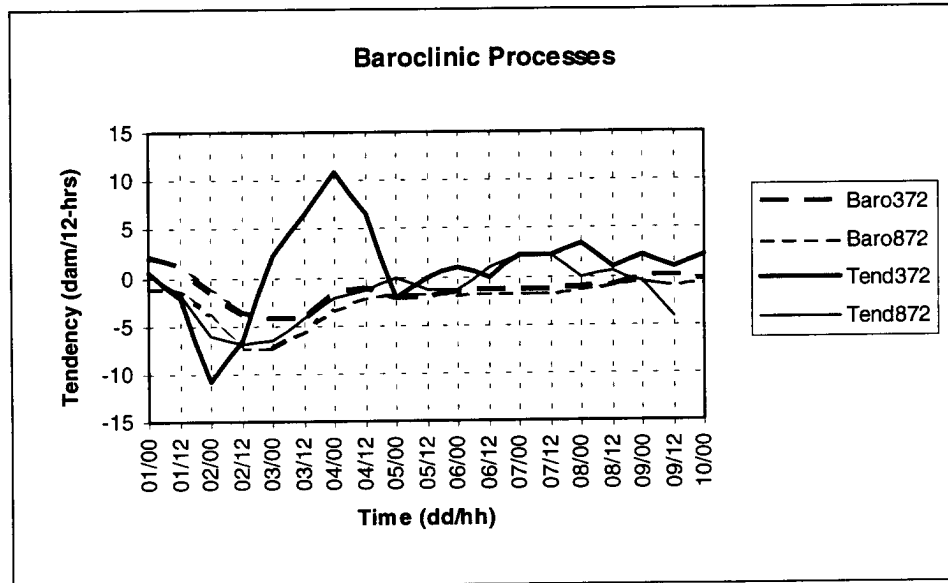


Fig. 5.18. Time series of geopotential height tendency describing the baroclinic process. The thick solid line is the geopotential height tendency at 372 mb centered at the trough position. The thin solid line is similar to the thick solid line but for the 872 mb level. The thick dashed line is the baroclinic tendency at 372 mb. The thin dashed line is the baroclinic tendency at 872 mb.

The two one-way processes composing the baroclinic intensification are given by the dashed lines. During the first 12 hours of trough development the baroclinic processes did not contribute to the development. In fact, the baroclinic processes may have been a detriment. From 1200 UTC 1 December through 0000 UTC 3 December the mobile trough at 372 mb and the 872 mb low center both developed along with the two one-way components. During this period baroclinic processes, specifically baroclinic instability, contributed to the development of the mobile trough. After 0000 UTC 3 December the mobile trough began to weaken, but the baroclinic effects remained a player (not baroclinic instability). The baroclinic process remained in effect for the entire period, but were only significant until 0000 UTC 4 December. Using QGPV thinking, it is possible to determine how the baroclinic processes affected the mobile trough development.

Figs. 5.19 through 5.22 show the 372 mb large-scale (UB) QGPV field and the associated small-scale geostrophic wind vectors due to the piecewise inversion of the lower QGPV (LP) for selected times in the baroclinic development. The thick gray contours and bold letters identify the trough and ridge pattern as defined by the small-scale QGPV at 372 mb. Using these component analyses, it is possible to determine the phase relationships responsible for intensification or decay due to baroclinic processes.

At 1200 UTC 1 December the mobile trough is west of the Rockies (bold H in Fig. 5.19). From Fig. 5.18 we know the trough was not intensifying by baroclinic processes at this time. The arrows near the H are not oriented significantly perpendicular to the QGPV gradient. In fact, the advection due to the lower level QGPV was contributing to decay at this time. Downstream of this trough, however, the arrows point down the QGPV gradient. During this period, the advection pattern is nearly stationary, so as the trough moves into this region it is expected to intensify.

At 0000 UTC 2 December (Fig. 5.20) the trough did indeed move into the area of cross contour flow and began to develop (Fig. 5.18). The upstream ridge was also developing due to baroclinic processes. The downgradient advection was even greater downstream of the trough at this time.

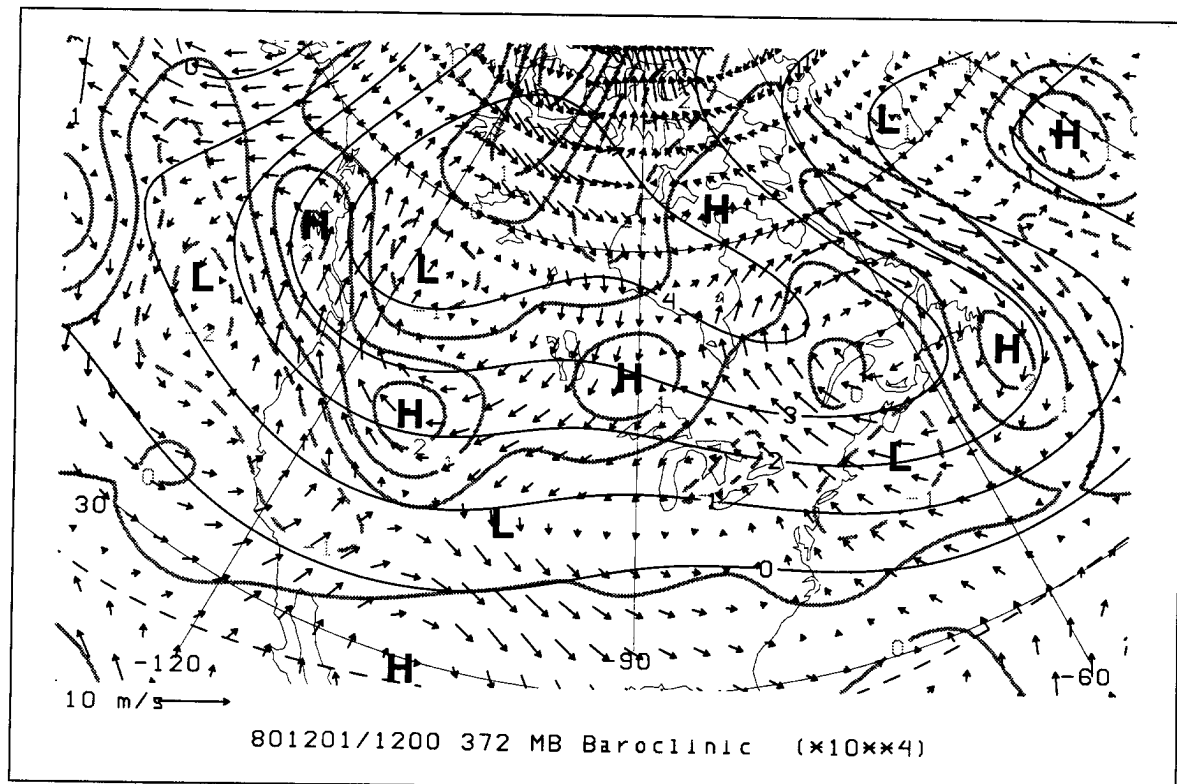


Fig. 5.19. The 372 mb baroclinic component analysis at 1200 UTC 1 December 1980. The dark contours are the large-scale QGPV (contour interval is  $1 \times 10^{-4} \text{ s}^{-1}$ ). The negative contours are dashed. The thick gray contours are the small-scale QGPV (contour interval is  $1 \times 10^{-4} \text{ s}^{-1}$ ). The bold letters show the small-scale positive (H) and negative (L) QGPV centers. The vectors represent the geostrophic wind associated with the piecewise inversion of the small-scale QGPV in the lower levels. The  $10 \text{ m s}^{-1}$  representative wind vector is in the lower left of the figure.



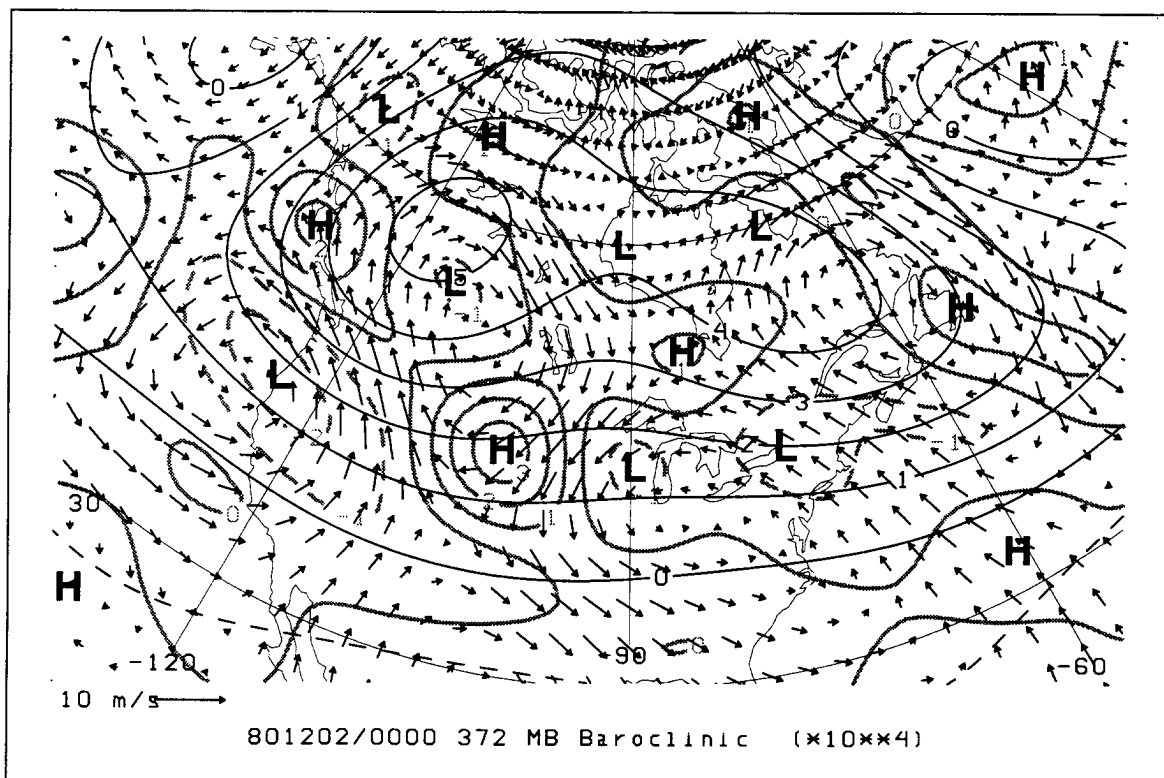


Fig. 5.20. The 372 mb baroclinic component analysis at 0000 UTC 2 December 1980. The dark contours are the large-scale QGPV (contour interval is  $1 \times 10^{-4} \text{ s}^{-1}$ ). The negative contours are dashed. The thick gray contours are the small-scale QGPV (contour interval is  $1 \times 10^{-4} \text{ s}^{-1}$ ). The bold letters show the small-scale positive (H) and negative (L) QGPV centers. The vectors represent the geostrophic wind associated with the piecewise inversion of the small-scale QGPV in the lower levels. The  $10 \text{ m s}^{-1}$  representative wind vector is in the lower left of the figure.

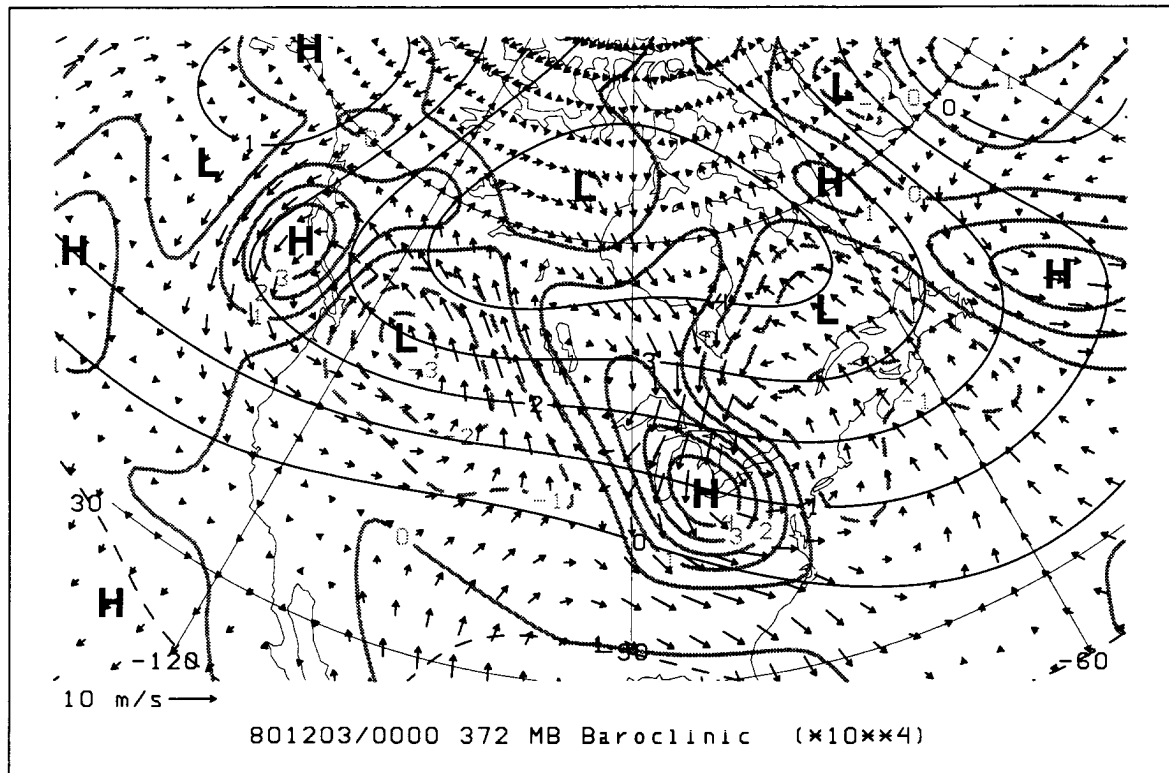


Fig. 5.21. The 372 mb baroclinic component analysis at 0000 UTC 3 December 1980. The dark contours are the large-scale QGPV (contour interval is  $1 \times 10^{-4} \text{ s}^{-1}$ ). The negative contours are dashed. The thick gray contours are the small-scale QGPV (contour interval is  $1 \times 10^{-4} \text{ s}^{-1}$ ). The bold letters show the small-scale positive (H) and negative (L) QGPV centers. The vectors represent the geostrophic wind associated with the piecewise inversion of the small-scale QGPV in the lower levels. The  $10 \text{ m s}^{-1}$  representative wind vector is in the lower left of the figure.

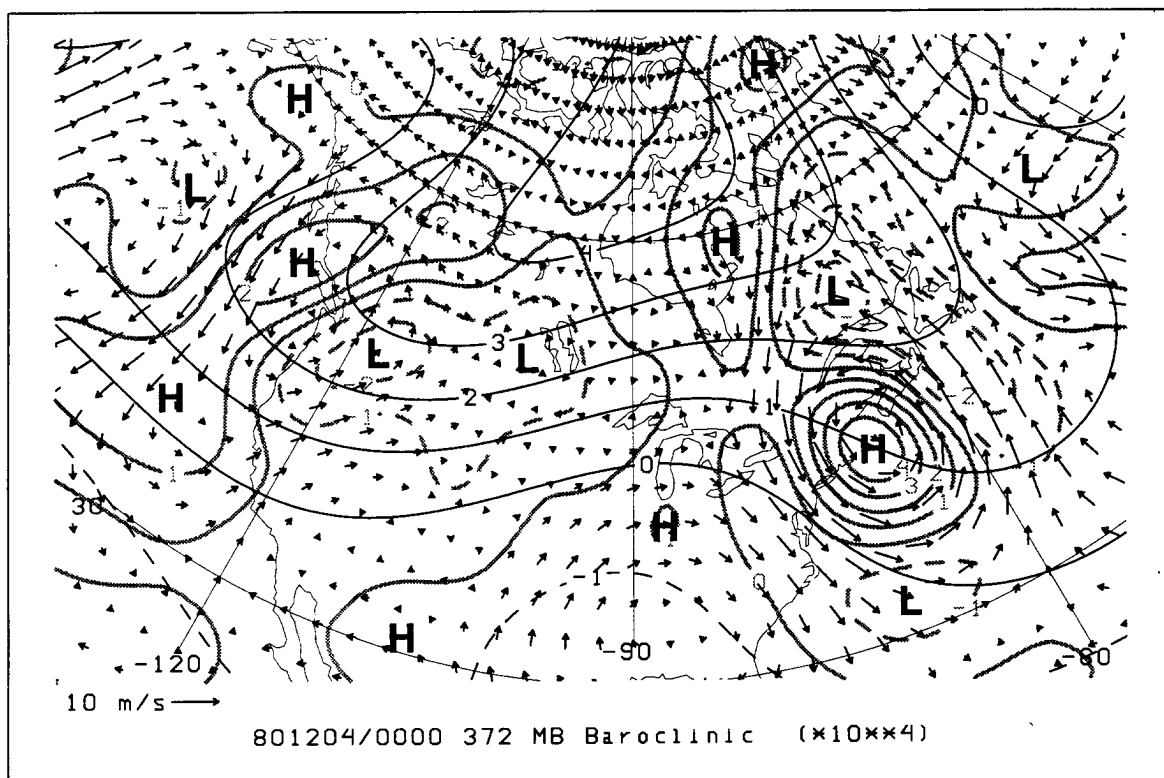


Fig. 5.22. The 372 mb baroclinic component analysis at 0000 UTC 4 December 1980. The dark contours are the large-scale QGPV (contour interval is  $1 \times 10^{-4} \text{ s}^{-1}$ ). The negative contours are dashed. The thick gray contours are the small-scale QGPV (contour interval is  $1 \times 10^{-4} \text{ s}^{-1}$ ). The bold letters show the small-scale positive (H) and negative (L) QGPV centers. The vectors represent the geostrophic wind associated with the piecewise inversion of the small-scale QGPV in the lower levels. The  $10 \text{ m s}^{-1}$  representative wind vector is in the lower left of the figure.

At 0000 UTC 3 December the geostrophic flow is perpendicular to the QGPV contours at the location of the trough near the Great Lakes. The baroclinic intensification as depicted in Fig. 5.18 is also maximized at this time. The upper level trough and surface low center were approximately  $90^\circ$  out of phase. The flanking ridges had favorable advection for their development. The advection patterns at this time are partially due to the intensification of the surface low center (shown later), and are ideally configured for mobile trough amplification. After this time, the surface anomaly will continue to intensify, but the favorable tilt (phase) between the upper and lower advection patterns will decrease. This decrease in tilt will contribute to the decay of the mobile trough.

At 0000 UTC 4 December the flow at the center of the trough was weak (Fig. 5.22). The strong cyclonic flow surrounding the mobile trough is evidence of the equivalent barotropic nature of the cyclone. The baroclinic intensification was weaker, if present at all.

Figs. 5.23 and 5.24 show the 922 mb large-scale vertical geopotential height gradient (multiplied by minus one to make it proportional to the temperature) and the associated small-scale geostrophic wind vectors at 872 mb due to the piecewise inversion of the upper QGPV (UP). The thick gray contours and bold letters identify the surface warm and cold anomalies (H and L, respectively). These figures are used to determine the influence of the mobile trough on the surface development. Figs. 5.19 through 5.24 provide the component analyses of the two-way intensification used to define baroclinic development.

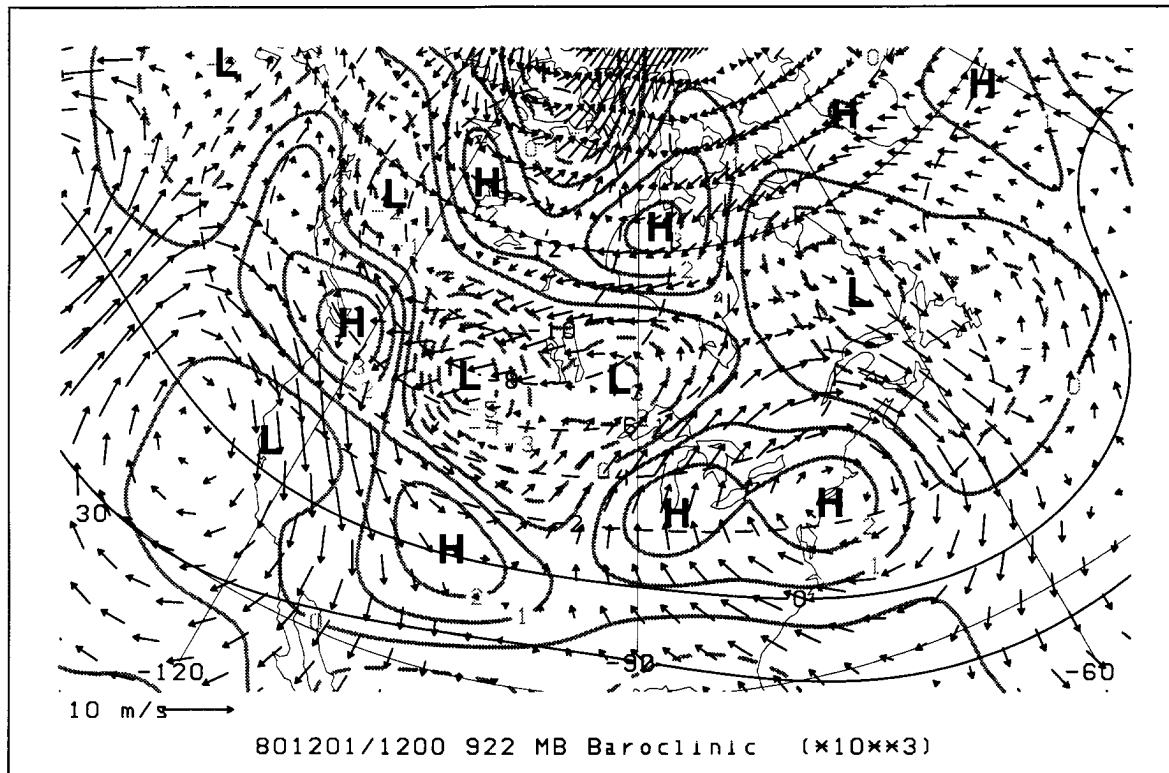


Fig. 5.23. The 922 mb baroclinic component analysis at 1200 UTC 1 December 1980. The dark contours are the large-scale vertical geopotential height gradient multiplied by minus one (contour interval is  $2 \times 10^{-3} \text{ m mb}^{-1}$ ). The negative contours are dashed. The thick gray contours are the small-scale vertical geopotential height gradient multiplied by minus one (contour interval is  $2 \times 10^{-3} \text{ m mb}^{-1}$ ). The bold letters show the small-scale warm (H) and cold (L) temperature centers. The vectors represent the geostrophic wind associated with the piecewise inversion of the small-scale QGPV in the upper levels. The  $10 \text{ m s}^{-1}$  representative wind vector is in the lower left of the figure.

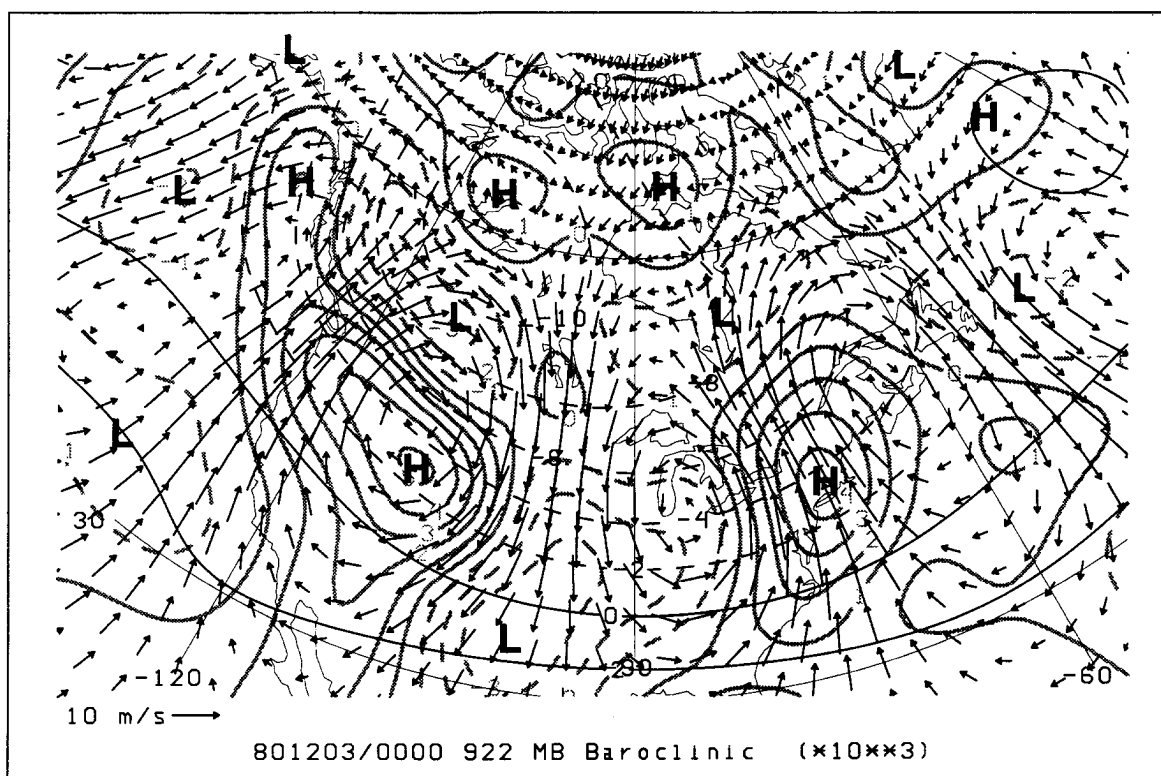


Fig. 5.24. The 922 mb baroclinic component analysis at 0000 UTC 3 December 1980. The dark contours are the large-scale vertical geopotential height gradient multiplied by minus one (contour interval is  $2 \times 10^{-3} \text{ m mb}^{-1}$ ). The negative contours are dashed. The thick gray contours are the small-scale vertical geopotential height gradient multiplied by minus one (contour interval is  $2 \times 10^{-3} \text{ m mb}^{-1}$ ). The bold letters show the small-scale warm (H) and cold (L) temperature centers. The vectors represent the geostrophic wind associated with the piecewise inversion of the small-scale QGPV in the upper levels. The  $10 \text{ m s}^{-1}$  representative wind vector is in the lower left of the figure.

At 1200 UTC 1 December the surface warm center (H in the central plains of Fig. 5.23 associated with the surface cyclone) was not in an area of significant warm advection. It appears the strongest warm advection is to the northeast of the surface cyclone at this time. The surface warm anomaly did track toward the northeast over the Great Lakes (not shown). By 0000 UTC 3 December the warm anomaly was located over the east coast of the United States (Fig. 5.24). It is in an area of strong warm advection. This warm advection corresponds to the maximum intensification shown in Fig. 5.18 at this time. In addition to being optimally configured, the surface cyclone and mobile trough had the same horizontal scale. The lower level and upper level curves in Fig. 5.18 track with each other during this period of optimal advection, resulting in rapid intensification due to the baroclinic process.

*b. Deformation process*

The next intensification process to describe is the deformation process associated with QGPV superposition. In Chapter IV the deformation process was separated into three components: horizontal shearing deformation, horizontal stretching deformation, and vertical shearing deformation. It was not possible to devise a clear and concise method to delineate the three subprocesses. However, a “quasi-qualitative” means to describe the deformation due to vertical wind shear was developed. The difference between this vertical deformation component and the overall deformation, along with a qualitative assessment of the horizontal deformation component, provides an adequate analysis of the deformation process. The overall deformation process can be described by the FBUPV tendency at 372 mb.

A first attempt at describing the deformation field using the FBUPV field yielded a large amplitude positive-negative dipole centered at the position of the mobile trough. The deformation affect was masked by the simple translation of small-scale QGPV by the large-scale geostrophic wind. To avoid this translation-effect and to isolate the deformation effects, the large-scale velocity at the center of the three-dimensional small-scale QGPV perturbation (defined by a 5-point average at 372 mb) was used to compute a

“non-deformational advection” field. The geopotential height tendency due to this advection of the small-scale QGPV was subtracted from the FBUPV field.

An example of the horizontal deformation mechanism is presented in Fig. 5.25. The large-scale horizontal wind shear (FB) deforms the small-scale QGPV anomaly (UP). As the QGPV anomaly gets stretched diagonally, the centers of negative potential vorticity advection (NVA), initially in quadrants two and four, remain closer to the mobile trough at the center (+). The geopotential height tendency at the mobile trough increases (the trough weakens) because the NVA dominates. If the QGPV anomaly was initially distorted and the horizontal shear produced a more compact (spherical) anomaly, then the positive potential vorticity advection (PVA) would likely dominate and the mobile trough would be intensifying. The vertical deformation mechanism could be described likewise if the ordinate in Fig. 5.25 was oriented vertically.

The FBUPV field at 372 mb that results after subtracting the effects of the non-deformation tendency (call this new field FBUPV also) is meaningless far away from the mobile trough. If the three-dimensional field was approximately devoid of any horizontal or vertical shear the new FBUPV field would be exactly zero at the trough position. The time series of the FBUPV field at the location of the mobile trough is given by the dashed line in Fig. 5.26. Like the baroclinic processes, the deformation processes did not contribute to the initial growth of the mobile trough. The deformation processes only contributed to trough intensification from 1800 UTC 1 December through 0000 UTC 3 December. The magnitude of the deformation influence was comparable to the magnitude of the baroclinic influence. However, the deformation process played a significant role in the decay of the mobile trough that followed after 0000 UTC 3 December. This result is not surprising since the only way for the deformation process to intensify a trough would be if the deformation field forced the QGPV anomaly into a spherical shape. Any other influence would weaken the trough due to QGPV superposition.



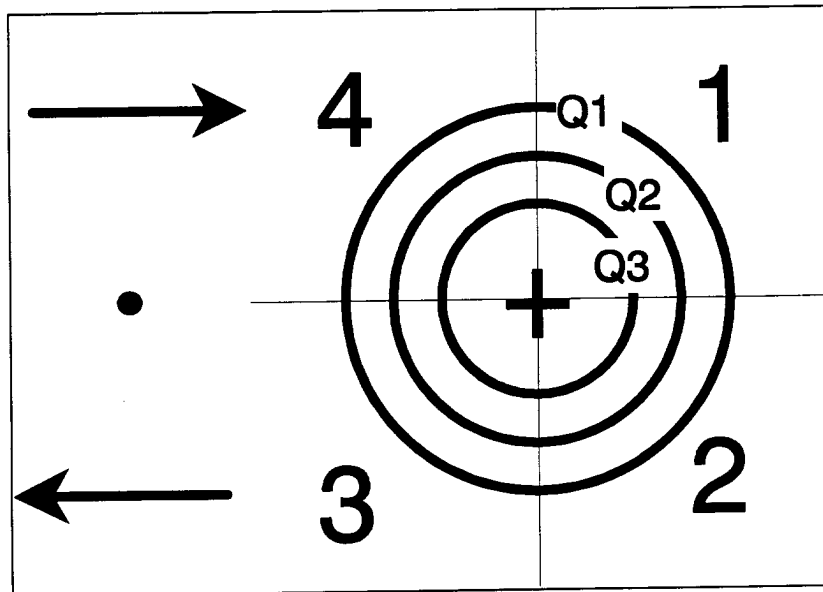


Fig. 5.25. A schematic diagram of the horizontal deformation process. The diagram is a horizontal depiction of a positive QGPV anomaly (UP) embedded within the large-scale flow (straight arrows representing the FB wind). The non-deformation geostrophic wind has been subtracted from the overall large-scale flow (the reason for the zero wind in the middle). The thin solid lines separate the area into four quadrants. The QGPV advection is positive in quadrants one and three, and negative in quadrants two and four.

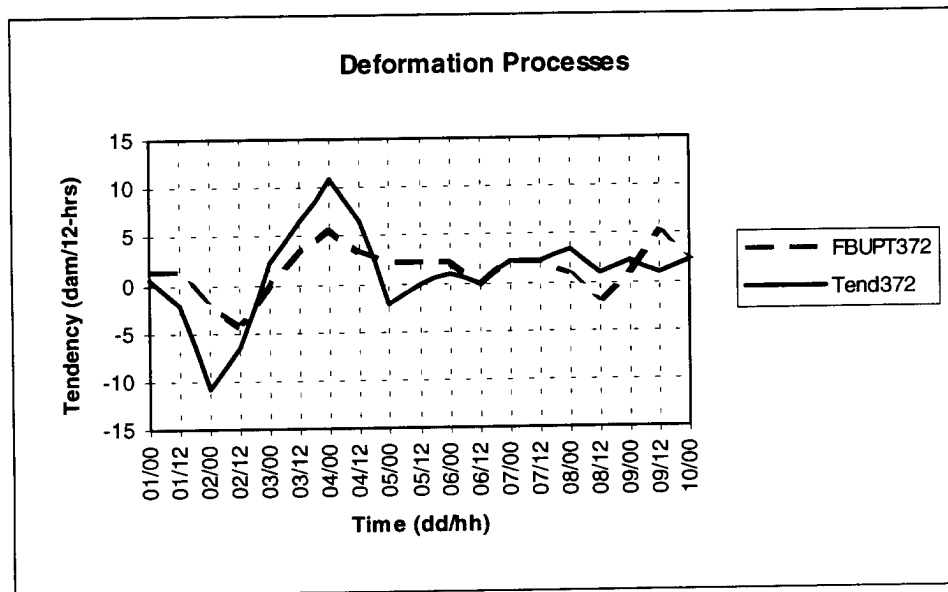


Fig. 5.26. Time series of geopotential height tendency describing the deformation process. The thick solid line is the geopotential height tendency at 372 mb centered at the trough position. The thick dashed line is the FBUPT tendency at 372 mb.

Figs. 5.27 through 5.29 show the 372 mb small-scale QGPV anomaly (UP) and the associated large-scale geostrophic wind vectors, less the non-deformation wind. As stated earlier, the wind vectors over most of the field are meaningless. However, the vectors near the center of the mobile trough describe the horizontal deformation of the QGPV anomaly. In every case the vector at the center of the QGPV anomaly is near zero (as it should be, because this is the position and level used to get the non-deformation wind).

At 1200 UTC 1 December the wind vectors are fairly parallel to the QGPV contours near the mobile trough (H near the Rocky Mountains in Fig. 5.27). There may be a slight deformation effect due to the stretching over the southwest quadrant, and a contraction along the southeast quadrant of the anomaly. This deformation would reduce the intensity of the trough.

At 1200 UTC 2 December the deformation process was a maximum (Fig. 5.26), but the horizontal deformation component did not appear to contribute (Fig. 5.28). The mobile trough was west of the Great Lakes. The vectors are oriented, for the most part, parallel to the contours. There may have been a slight shearing affect in the northwest quadrant.

At 0000 UTC 4 December the deformation process was contributing to the decay of the mobile trough (Fig. 5.28). The horizontal deformation component appears to play a significant role in this decay. The mobile trough was located off the east coast of the United States, in a flow characterized by strong stretching deformation (Fig. 5.29).

The relationship between the position of the mobile trough at 372 mb and the center of the negative geopotential height anomaly associated with the piecewise inversion of the lower level QGPV anomaly (LP) was used to determine the component of vertical shear deformation. If the mobile trough at 372 mb and the LP height anomaly remain in the same position relative to each other over time, the intensification component due to vertical deformation would be zero (e.g. there was no vertical shear to change the relative position of the anomalies). However, if the relative position changed with time, the geopotential tendency associated with this change would be diagnosed as a vertical superposition process.

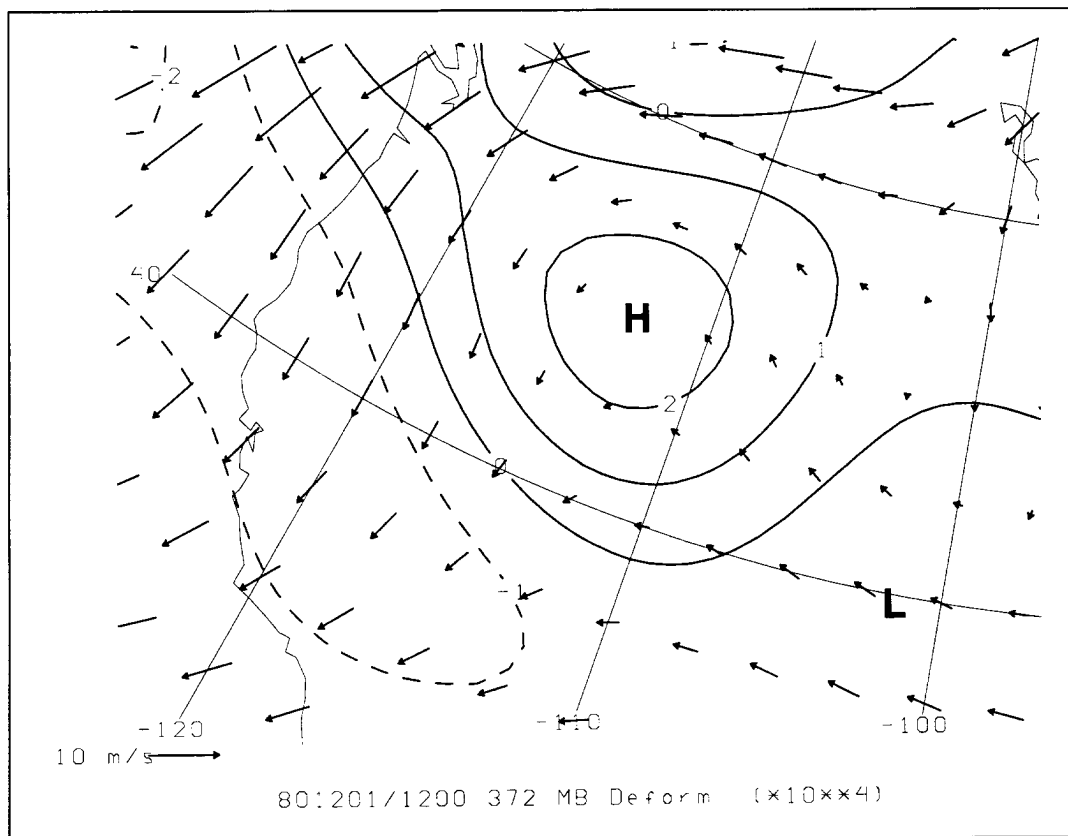


Fig. 5.27. The 372 mb horizontal deformation component analysis at 1200 UTC 1 December 1980. The thick contours are the small-scale QGPV (contour interval is  $1 \times 10^{-4} \text{ s}^{-1}$ ). The negative contours are dashed. The vectors represent the large-scale geostrophic wind minus the non-deformation wind representing the large-scale geostrophic wind at the center of the mobile trough. The  $10 \text{ m s}^{-1}$  representative wind vector is in the lower left of the figure.

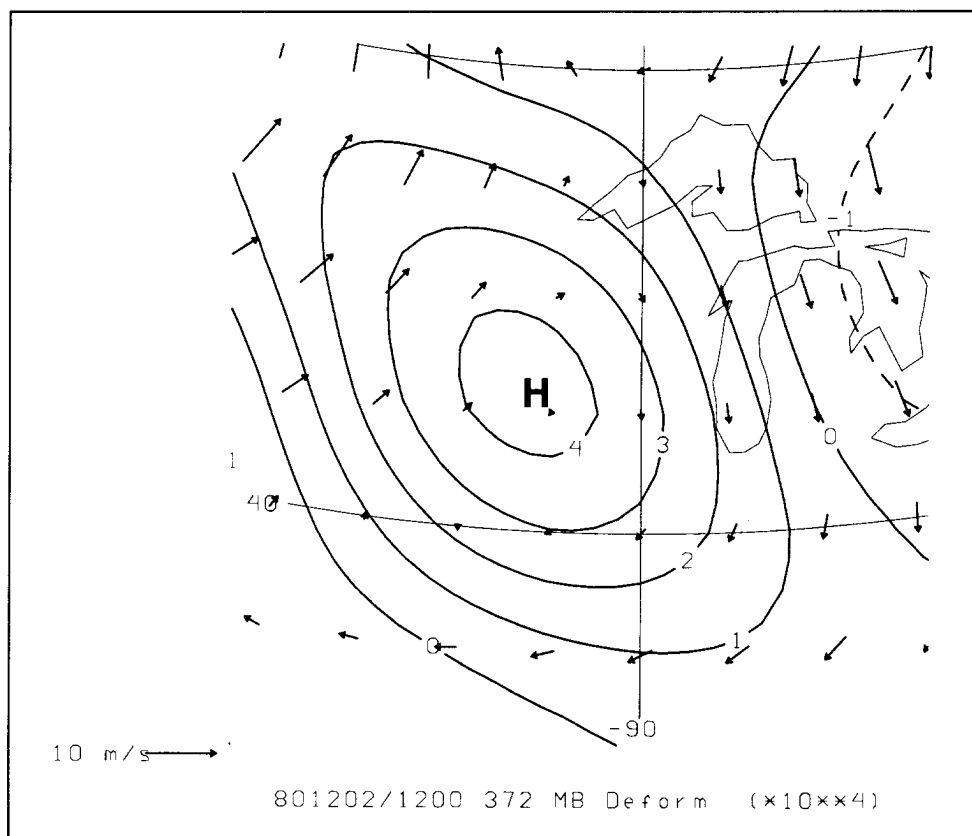


Fig. 5.28. The 372 mb horizontal deformation component analysis at 1200 UTC 2 December 1980. The thick contours are the small-scale QGPV (contour interval is  $1 \times 10^{-4} \text{ s}^{-1}$ ). The negative contours are dashed. The vectors represent the large-scale geostrophic wind minus the non-deformation wind taken as the large-scale geostrophic wind at the center of the mobile trough. The  $10 \text{ m s}^{-1}$  representative wind vector is in the lower left of the figure.

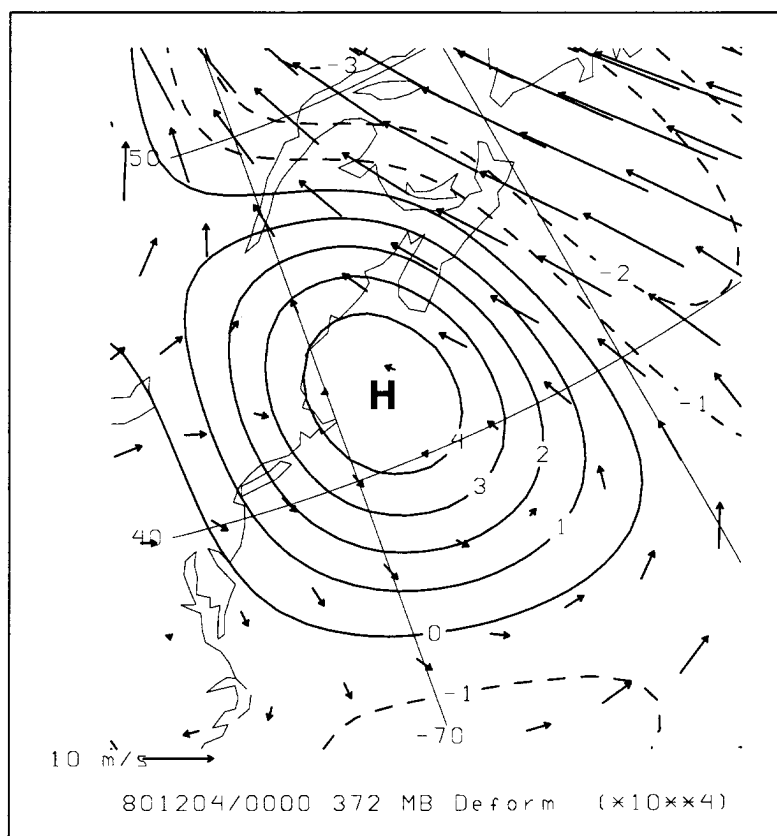


Fig. 5.29. The 372 mb horizontal deformation component analysis at 0000 UTC 4 December 1980. The thick contours are the small-scale QGPV (contour interval is  $1 \times 10^{-4} \text{ s}^{-1}$ ). The negative contours are dashed. The vectors represent the large-scale geostrophic wind minus the non-deformation wind taken as the large-scale geostrophic wind at the center of the mobile trough. The  $10 \text{ m s}^{-1}$  representative wind vector is in the lower left of the figure.

The procedure used to determine the vertical shearing deformation was based on the ratio between the magnitude of the geopotential height anomaly due to the piecewise inversion of the low level small-scale QGPV (LP) at the position of the mobile trough and the magnitude of the center of the LP anomaly at 372 mb. The temporal variation (centered finite difference) of this ratio multiplied by the magnitude of the LP anomaly gives the intensification due to vertical deformation (the lightly shaded columns in Fig. 5.30).

During the first two days in the mobile trough's life cycle it was located upstream of the surface low center. The westerly vertical shear present as the mobile trough progressed toward the east likely decreased the phase difference between the mobile trough and surface low center. This decrease in tilt was manifest as a vertical superposition between the lower and upper QGPV anomalies, and a significant contribution of the vertical shear component to the overall deformation (Fig. 5.30). As had been suggested by Fig. 5.28, the horizontal deformation process did not play a significant role during this time. The vertical shear deformation component often accounted for more than 50% of the overall deformation. However, at 0000 UTC 4 December the mobile trough and surface cyclone were almost vertically stacked. The vertical shear deformation did not have a significant role in the deformation, but the horizontal stretching appeared to dominate.

*c. Downstream development process*

The third intensification process to describe is that due to energy transport or group velocity tendency. This effect will be described by the sum of the UPUBT and LPLBT fields at 372 mb. Downstream development (DD) and downstream baroclinic development (DBD) fall into this intensification category as well (Orlanski and Sheldon 1993, Chang 1993, Chang and Orlanski 1993, Orlanski and Chang 1993, Orlanski and Katzfey 1991).

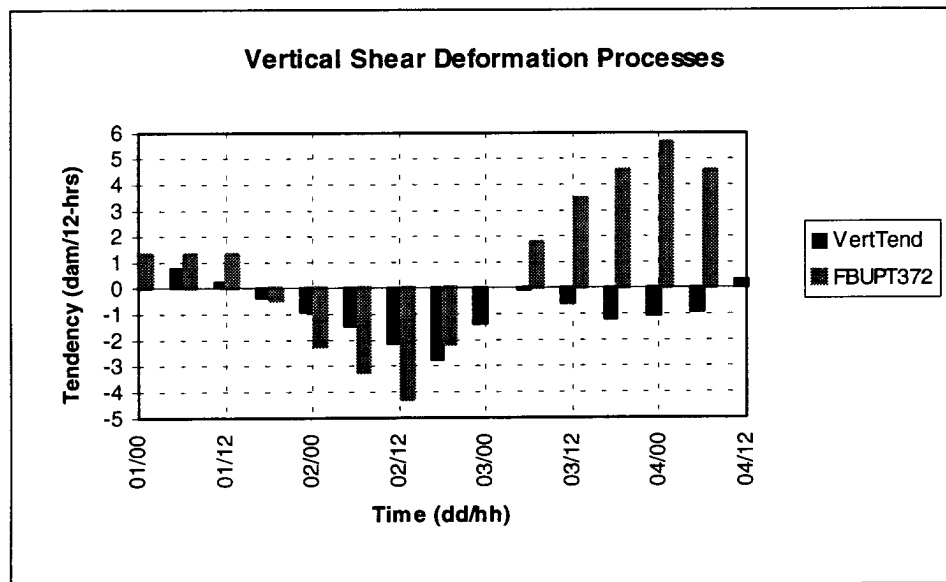


Fig. 5.30 Time series of vertical shear deformation process. The lightly shaded columns are the overall deformation geopotential tendency. The dark columns are the vertical shear component.



The schematic diagram in Fig. 5.31 represents one part, the UPUBT part, of the downstream development process. The geostrophic wind at the mobile trough (positive QGPV anomaly at the right) associated with both the upstream trough (positive QGPV at the left) and the ridge (negative QGPV anomaly in the center) is oriented down the large-scale QGPV gradient. The wind is downgradient because the effect of the negative anomaly closer to the mobile trough is stronger than the upstream positive anomaly. The positive potential vorticity advection (PVA) at the mobile trough will result in geopotential height falls, or mobile trough intensification. The negative potential vorticity advection (NVA) at the upstream trough (the positive anomaly at the left) will result in geopotential height rises, or weakening. Thus, the mobile trough intensifies at the expense of the upstream trough. A similar process may also occur in the lower layer (LPLBT), and if optimally positioned, will also contribute to intensification of the mobile trough. However, the LPLBT effect is significantly weaker than the UPUBT effect at upper levels.

The time series of the downstream development tendency at the trough location is given by the dashed line in Fig. 5.32. The initial development of the mobile seems to be due to the downstream development process. The DD process contributes to the intensification of the trough through 0000 UTC 2 December. After this initial development, the DD process actually weakens the trough until 1800 UTC 8 December. This result is consistent with Orlanski's work if one assumes the trough initially develops by the convergence of ageostrophic geopotential flux or eddy kinetic energy at the location of the trough. As the trough matures it radiates its eddy kinetic energy downstream and begins to decay.

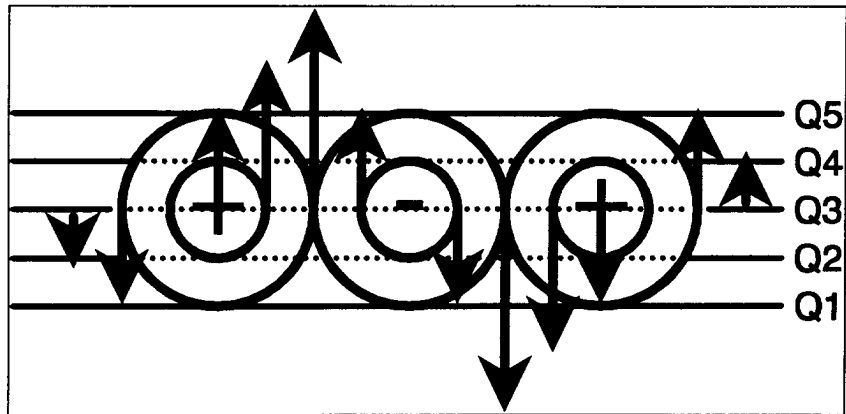


Fig. 5.31. A schematic diagram of the downstream development process (UPUBT). The diagram represents a horizontal section at the level of the mobile trough. The left anomaly is positive (+) and represents an upstream trough. The middle anomaly is negative (-) and represents an upstream ridge. The right anomaly is positive (+) and represents the mobile trough of interest. The thin lines represent the large-scale QGPV gradient. The arrows represent the net geostrophic flow associated with the three anomalies.

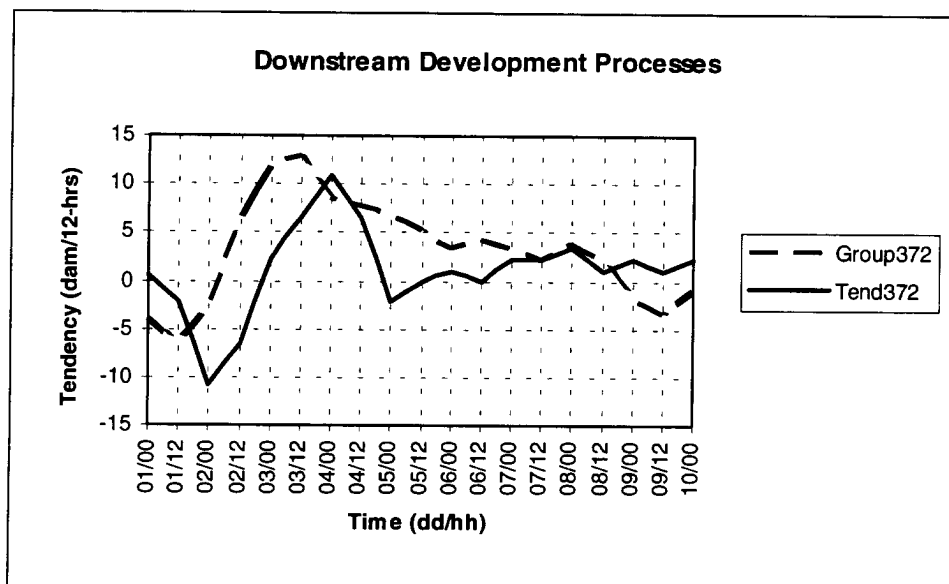


Fig. 5.32. Time series of geopotential height tendency describing the downstream development process. The thick solid line is the geopotential height tendency at 372 mb centered at the trough position. The thick dashed line is the sum of the UPUBT and LPLBT tendency at 372 mb.

The assumption that the UPUBT and LPLBT fields are related to Orlanski's downstream development mechanism may be a leap of faith. The only way to know for certain if these two results are related would be to calculate the ageostrophic geopotential flux for this case. Such calculations were not completed for this research. However, a qualitative assessment is possible by observing the magnitude and position of the flanking ridges (positive small-scale geopotential height centers) on both sides of the mobile trough during its development (Table 5.2).

At 0000 UTC 1 December the upstream ridge is stronger and closer to the trough than the downstream ridge. In this case the amplifying affect of the upstream ridge upon the trough should be greater than the decaying effect of the downstream ridge--energy should be transported into the trough. At 1200 UTC 1 December the ridge intensities are equal, but the upstream ridge is closer to the trough--the upstream amplification affect should predominate again. At 0000 UTC 2 December the upstream ridge is more intense and closer to the trough, therefore, it should have an intensification affect. At 1200 UTC 2 December the upstream ridge is more intense than the downstream ridge, but farther away than the downstream ridge. A qualitative assessment is difficult, but according to the deformation analysis the intensification by the upstream ridge "wins the battle." At 0000 UTC 3 December the upstream ridge is again stronger, but much farther away from the trough. This time the closeness of the downstream ridge prevails and the trough weakens due to superposition of the ridge--a net energy loss for the trough. On 1200 UTC 3 December the downstream ridge dominates in both the ridge-intensity and proximity categories.

Table 5.2. Intensity and distance comparison for flanking ridges.

<b>Time (dd/hh)</b>	<b>Upstream ridge intensity (meters)</b>	<b>Downstream ridge intensity (meters)</b>	<b>Distance from upstream ridge to trough (degrees latitude)</b>	<b>Distance from downstream ridge to trough (degrees latitude)</b>
01/00	14	8	13	32
01/12	12	12	16	34
02/00	15	13	16	23
02/12	20	18	19	18
03/00	23	22	21	16
03/12	17	24	25	15

Another method used to assess the contribution of the downstream development process in mobile trough development is to analyze the components of the deformation advection at 372 mb (only the UPUBT components are shown). At 0000 UTC 1 December the mobile trough was located near the west coast of North America (H within the thin QGPV contours in Fig. 5.33). The geostrophic wind vectors associated with the piecewise inversion of the upper level QGPV anomaly are oriented almost exactly parallel to the QGPV anomaly (as expected since these anomalies produce this geostrophic wind).

Downstream development, as conceptualized in Chapter III and Appendix 3, occurs when the large-amplitude trough located upstream (near  $150^{\circ}$  W in Fig. 5.34) of the mobile trough transfers energy into the mobile trough at  $120^{\circ}$  W. The induced geostrophic wind due to this large-amplitude, small-scale trough and ridge upstream of the mobile trough in Fig. 5.33 produced downgradient advection of large-scale QGPV near the mobile trough. This positive advection of QGPV is what initially developed the mobile trough.

At 1200 UTC 1 December the strong favorable advection upstream and weak unfavorable advection downstream of the mobile trough continued to intensify it by the downstream development process (Fig. 5.35 and Fig. 5.33). At 0000 UTC 3 December the unfavorable advection downstream of the trough over the Great Lakes dominated the favorable upstream advection (Fig. 5.36). As discussed earlier, the downstream ridge's destructive effect dominated the weakening of the mobile trough.

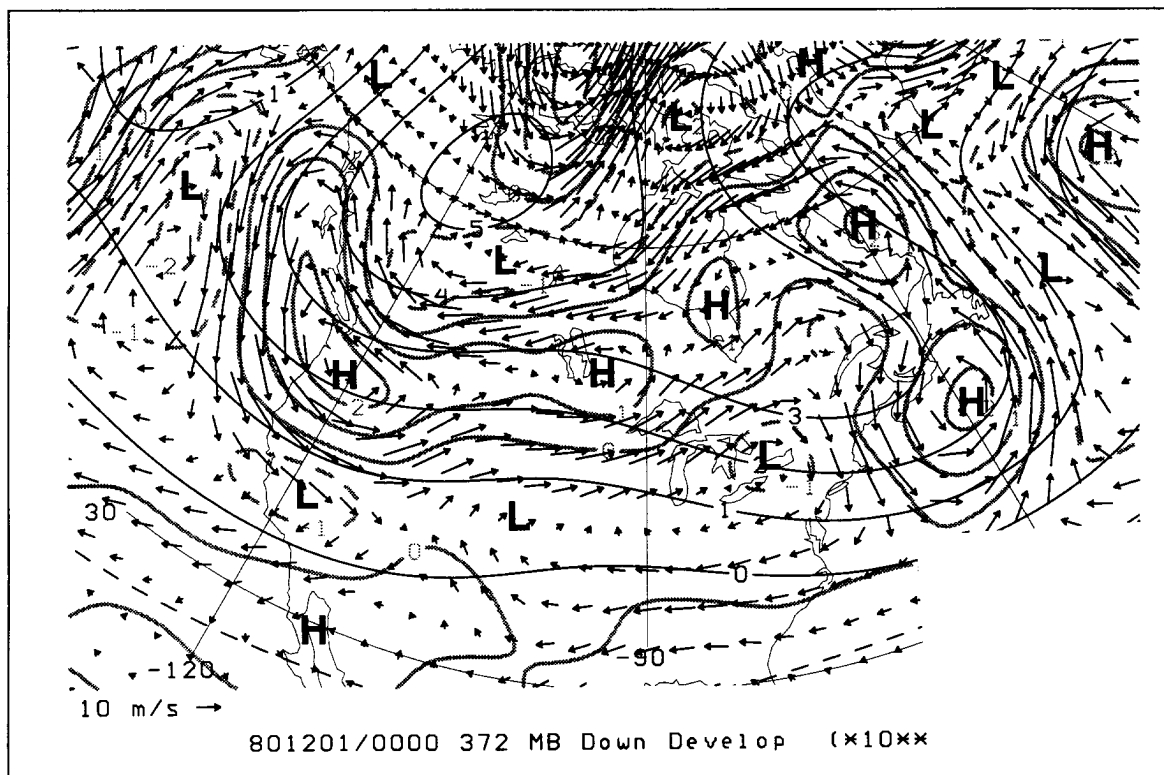


Fig. 5.33. The 372 mb downstream development component analysis at 0000 UTC 1 December 1980. The dark contours are the large-scale QGPV (contour interval is  $1 \times 10^{-4} \text{ s}^{-1}$ ). The negative contours are dashed. The thick gray contours are the small-scale QGPV (contour interval is  $1 \times 10^{-4} \text{ s}^{-1}$ ). The bold letters show the small-scale positive (H) and negative (L) QGPV centers. The vectors represent the geostrophic wind associated with the piecewise inversion of the small-scale QGPV in the upper levels. The  $10 \text{ m s}^{-1}$  representative wind vector is in the lower left of the figure.

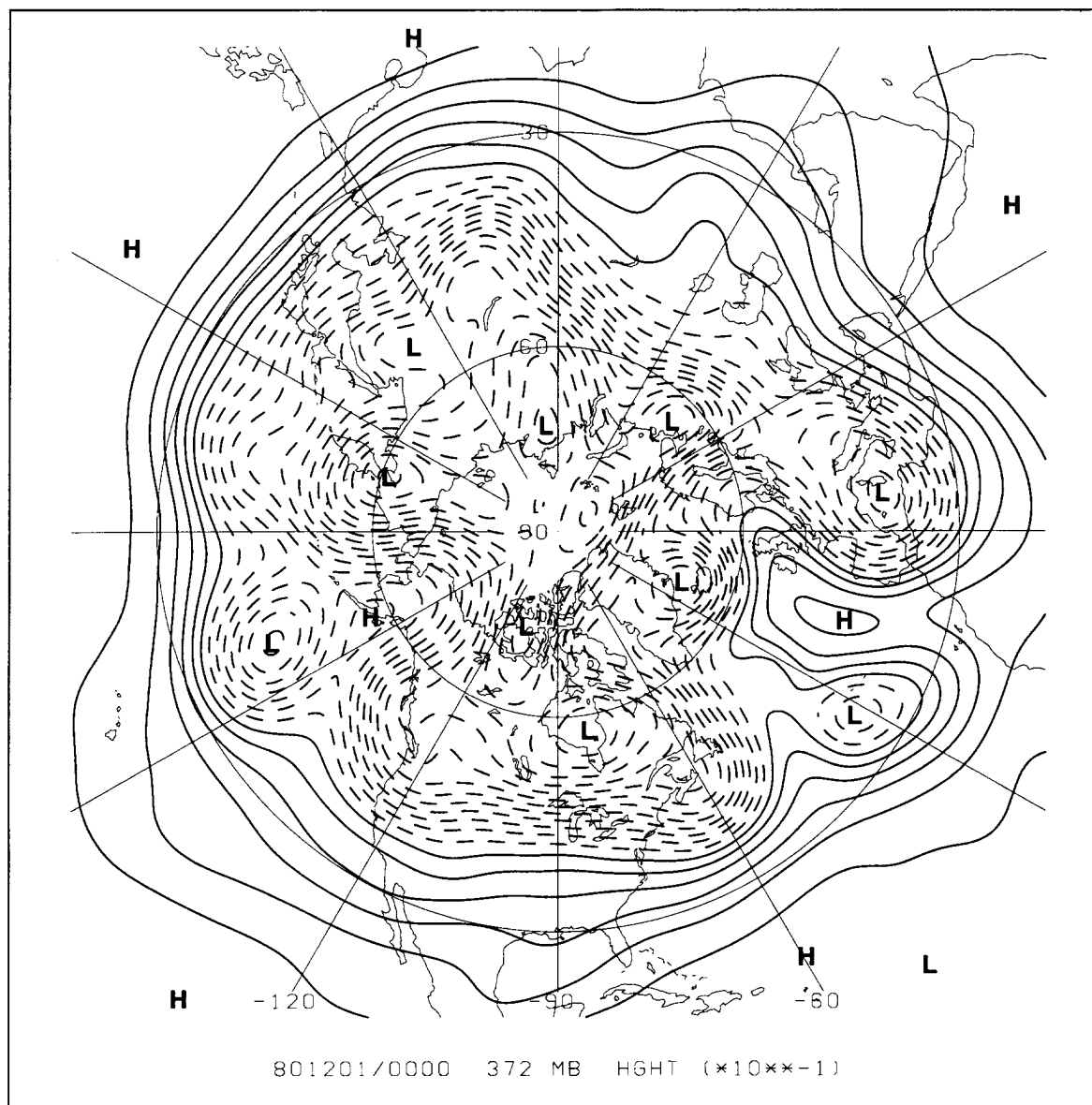


Fig. 5.34. A 372 mb hemispheric geopotential height analysis valid at 0000 UTC 1 December 1980. The contour interval is 6 dam. Negative contours are dashed. The first solid contour is equal to zero. The locally high (H) and low (L) centers are labeled.



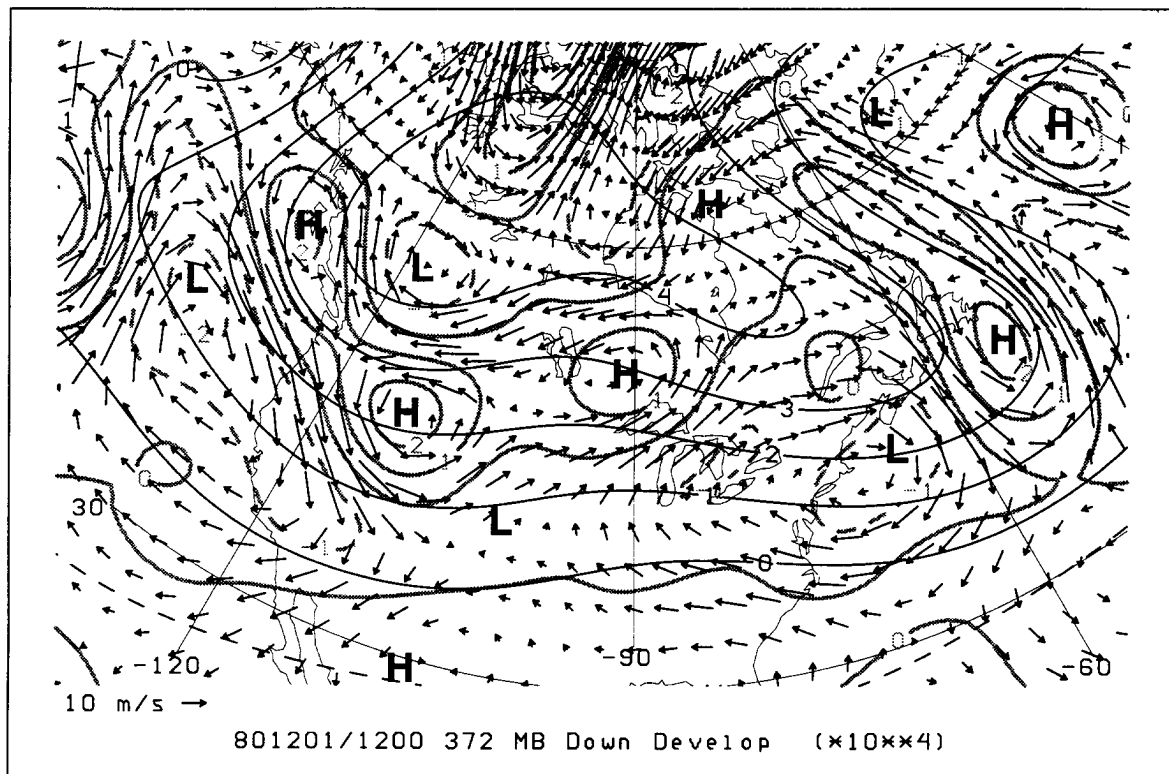


Fig. 5.35. The 372 mb downstream development component analysis at 1200 UTC 1 December 1980. The dark contours are the large-scale QGPV (contour interval is  $1 \times 10^{-4} \text{ s}^{-1}$ ). The negative contours are dashed. The thick gray contours are the small-scale QGPV (contour interval is  $1 \times 10^{-4} \text{ s}^{-1}$ ). The bold letters show the small-scale positive (H) and negative (L) QGPV centers. The vectors represent the geostrophic wind associated with the piecewise inversion of the small-scale QGPV in the upper levels. The  $10 \text{ m s}^{-1}$  representative wind vector is in the lower left of the figure.

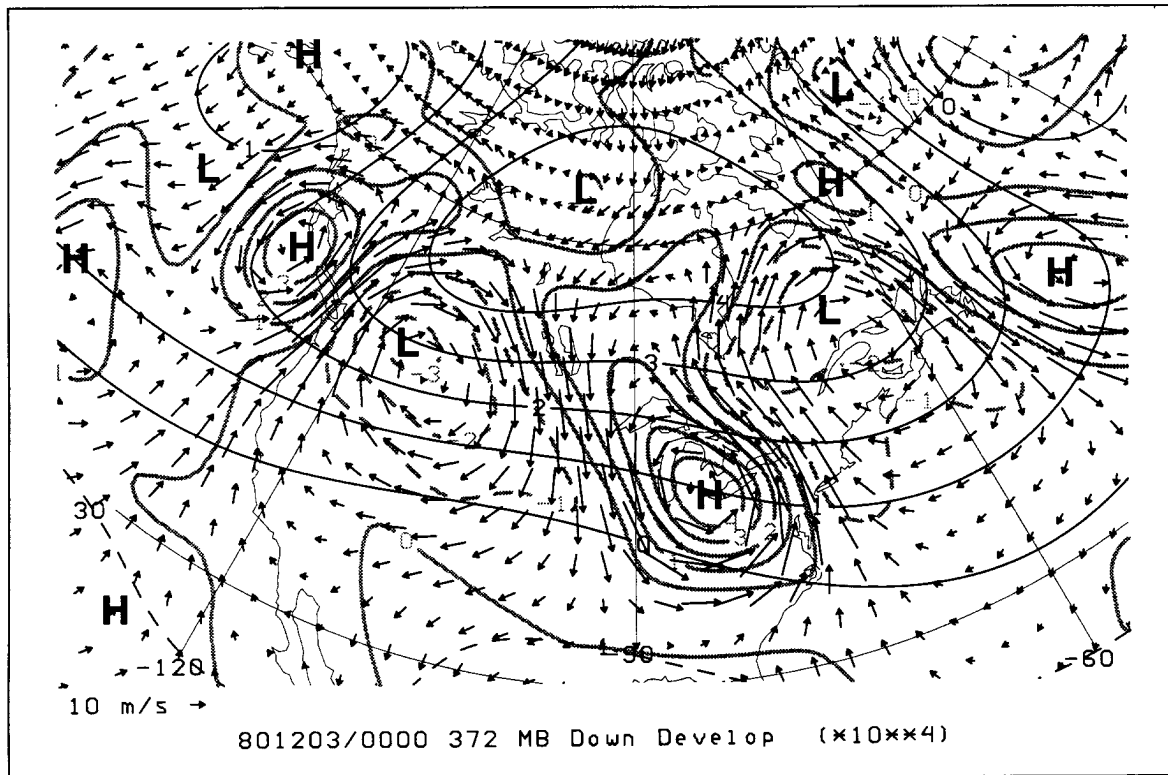


Fig. 5.36. The 372 mb downstream development component analysis at 0000 UTC 3 December 1980. The dark contours are the large-scale QGPV (contour interval is  $1 \times 10^{-4} \text{ s}^{-1}$ ). The negative contours are dashed. The thick gray contours are the small-scale QGPV (contour interval is  $1 \times 10^{-4} \text{ s}^{-1}$ ). The bold letters show the small-scale positive (H) and negative (L) QGPV centers. The vectors represent the geostrophic wind associated with the piecewise inversion of the small-scale QGPV in the upper levels. The  $10 \text{ m s}^{-1}$  representative wind vector is in the lower left of the figure.

*d. Trough-merger process*

The trough-merger process as described in Chapter III and Appendix 3 was examined, but it did not contribute significantly to the overall development of the mobile trough in this case (not shown). The FPFPT tendency fluctuated near zero for the entire life cycle. The fluctuations were likely due to the occasional superposition effects (horizontal and vertical) associated with two or more anomalies passing through the large-scale flow. The other anomalies did not appear to come sufficiently close to the mobile trough to affect the diagnosis.

*e. Combination of processes*

The three processes described above work together to produce the overall development of the midtropospheric mobile trough. The sum of the three processes (dashed line) are compared to the overall geostrophic geopotential height tendency (solid line) in Fig. 5.37. The overall shape between the geostrophic tendency and the sum of the three processes is comparable. However, the summation occasionally differs by a large margin during the life cycle of this trough. The combination of the processes underestimates the tendency during the time of maximum intensification.

The residual process, not included in the three main processes described above, is composed of the large-scale effect (Term 3 as discussed in Chapter IV), the trough-merger process (Term 6), and the tendency due to the large-scale advection of the lower troposphere small-scale QGPV. The residual process did not contribute significantly to the geopotential tendency (Fig. 5.38). This result is not surprising since the focus of the diagnostic technique is only on the small-scale, and merging of troughs was not present.

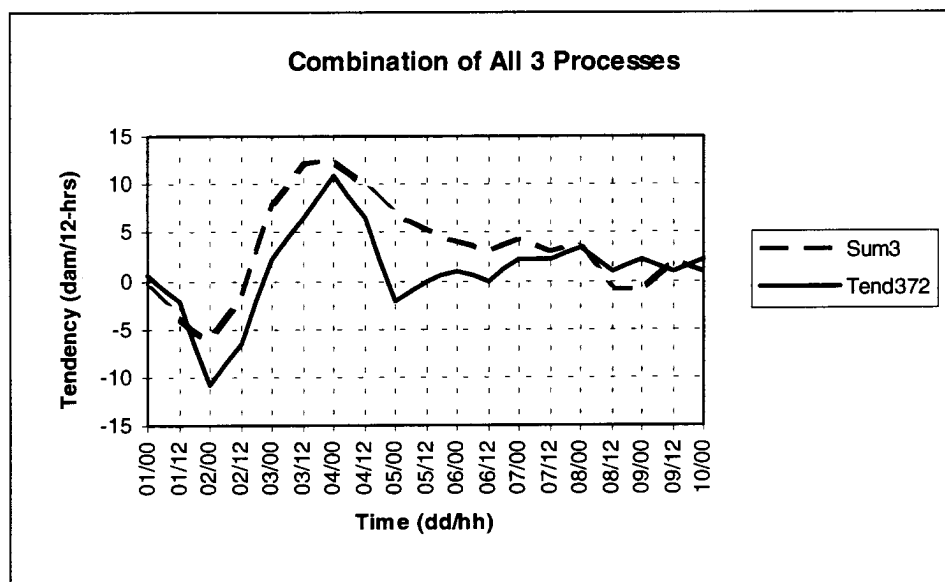


Fig. 5.37. Time series of geopotential height tendency due to the combination of the baroclinic, deformation and downstream development processes. The thick solid line is the geopotential height tendency at 372 mb centered at the trough position. The thick dashed line is the tendency due to the sum of the three processes at 372 mb.

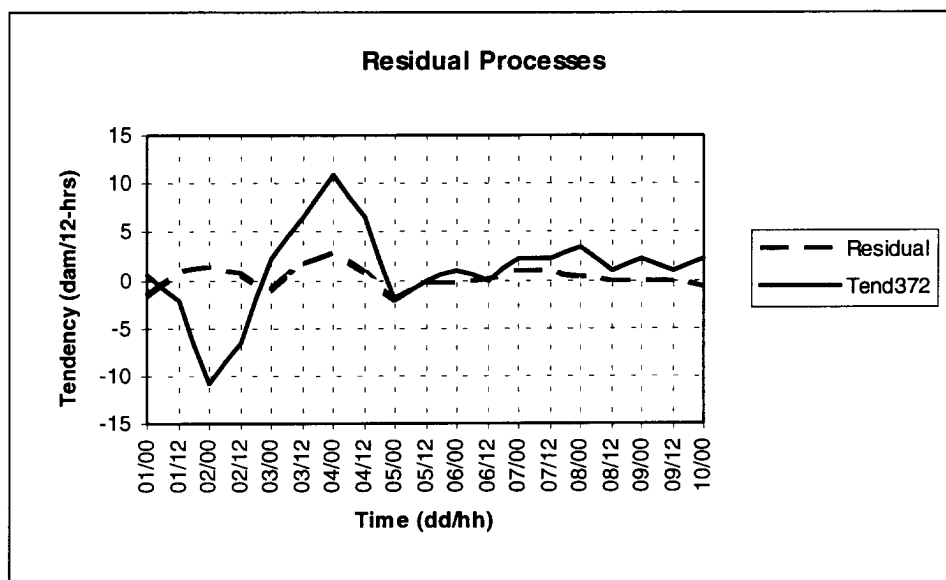


Fig. 5.38. Time series of geopotential height tendency due to the residual process. The components of this process are described in the text. The thick solid line is the geopotential height tendency at 372 mb centered at the trough position. The thick dashed line is the tendency due to the residual process at 372 mb.

The primary factor contributing to the discrepancy between the actual geopotential tendency and the tendency due to the combination of the three main processes (the difference between the lines in Fig. 5.37) was the tendency due to the non-deformation wind used to diagnose the deformation process (Fig. 5.39). In general, the non-deformation tendency accounted for a 5 dam  $12\text{-hrs}^{-1}$  intensification (negative tendency) of the trough. The negative tendency results from the method used to determine the deformation process.

The position of the trough was determined by the center of the small-scale negative geopotential height anomaly at 372 mb associated with the full (all levels) inversion of the small-scale QGPV. During the first half of this trough's life cycle, the surface warm anomaly was east of the mobile trough. Therefore, the center of the upper tropospheric negative geopotential height anomaly was actually east of the small-scale QGPV at 372 mb. Given a westerly large-scale flow, the center of the height anomaly was in an area of positive QGPV advection. The positive advection results in an intensification (negative tendency) of the trough.

The discrepancy between the small-scale geopotential height tendency and the tendency due to the combination of the three main processes (Figs. 5.37 and 5.39) is largely due to the relationship between QGPV anomalies in the upper and lower layers (vertical superposition). Since the focus of this study was on the upper level mobile trough, and to minimize the discrepancy in Fig. 5.37, the effects from the advection of lower level, large-scale QGPV were left out of the three main mechanisms (Fig. 5.40). In essence, the two-way intensification mechanisms are now only one-way (only the LPUBT and UPUBT were used). The non-deformation tendency was equal to zero at the center of the small-scale geopotential height anomaly since the advective effects of the lower level QGPV were not included. The tendency (temporal finite difference) due to the superposition of the lower level anomalies was included with the three one-way processes in Fig. 5.40.

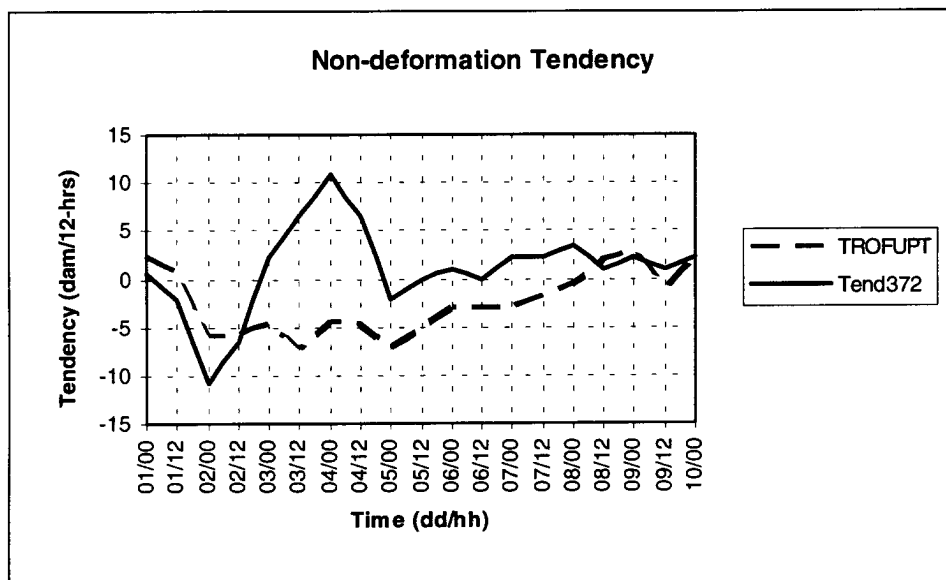


Fig. 5.39. Time series of geopotential height tendency due to the non-deformation advection. The components of this process are described in the text. The thick solid line is the geopotential height tendency at 372 mb centered at the trough position. The thick dashed line is the tendency due to the non-deformation process at 372 mb.

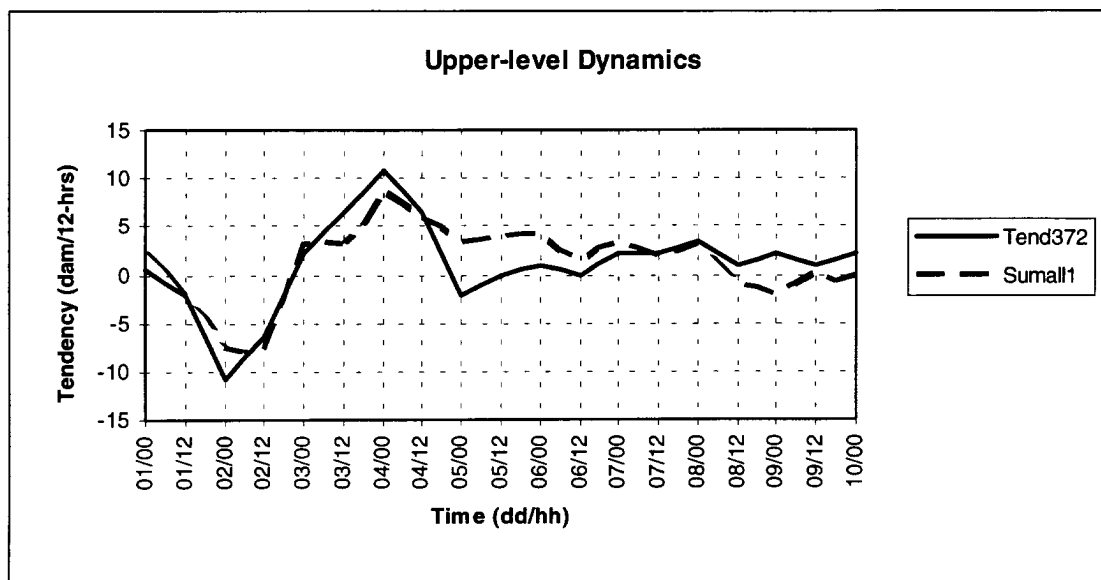


Fig. 5.40 Times series of geopotential height tendency due to the combination of three one-way processes. The dashed line is the geopotential height tendency at 372 mb centered at the trough position after adding the three one-way processes and the geopotential height due to the lower level small-scale QGPV. The solid line is the small-scale geopotential height tendency at 372 mb at the center of the small-scale height anomaly associated with only the upper level small-scale QGPV.



The overall conclusion based on the individual processes combined to form the solid line in Fig. 5.40 was the same as the two-way conclusion; the downstream development process was responsible for the initial trough development and the deformation and baroclinic processes played a secondary role. However, the combination of the three processes and the lower level superposition (solid line in Fig. 5.40) resulted in a tendency more consistent with the overall 372 mb geopotential height tendency (dashed curve in Fig. 5.40). The discrepancy between the lines in Fig. 5.40 is likely due to the temporal finite difference of the 372 mb geopotential height field associated with the lower level QGPV.

#### 4. Sensitivity to the selection of the large-scale

The sensitivity due to the choice of the large-scale partition was tested using two additional truncation schemes. First, the large-scale was defined using zonal wavenumbers 0 through 7 and total wavenumbers 0 through 9 (e.g.  $m=7$ , and  $n-m=9$ ), like Fig. 4.5. The mobile trough signature was present in the large-scale, so the intensification as measured by the geopotential height tendency of the small-scale was minimal. In fact, the observed intensification and decay present during the first 4 days in Fig. 5.32 was completely missed using this large-scale partition.

The second test was performed using large-scale zonal wavenumbers 0 through 6, and total wavenumbers 0 through 6 (e.g.  $m=6$ , and  $n-m=6$ ), like Fig. 4.7. This large-scale was similar to the one used in the case study ( $m=6$ , and  $n-m=9$ ), except the north-south geopotential height gradient was more diffuse. The entire mobile trough was partitioned in the small-scale, like in the case study.

The overall diagnosis using the combination of the three mechanisms (baroclinic, deformation, and downstream development) was equally robust as in the case study, but slightly different (not shown). The discrepancy between the geostrophic height tendency and the QGPV-determined height tendency in this case study (Fig. 5.37) was reduced using this second truncation. This difference is likely due to the position of the center of the geopotential height anomaly and the center of the small-scale QGPV at 372 mb. In

general, the contribution of the individual processes were similar between the case study and this second partition. Qualitatively, the conclusion about which process was dominant during a specific stage of development was the same.

## 5. Summary

In summary, the intensification of the midtropospheric mobile trough, as diagnosed by the QGPV form of the geostrophic geopotential height tendency equation, involved at least three processes. The initial genesis and development of the trough was primarily due to the downstream development process. As soon as the surface low center began to develop, the baroclinic process participated in the overall trough development. The deformation affect had a hand in the development at about the same time as the baroclinic process. The decay of the mobile trough was primarily due to the downstream development (the transport of energy away from the trough) and the deformation processes. The baroclinic process continued to develop the trough even when it was weakening. These results corroborate the qualitative trough assessment by Nielsen-Gammon (1995) for a different case of trough development.

The diagnostic technique, including the component analyses, is sufficiently robust, provided the break between large and small-scale partitions the mobile trough with the small-scale. If the large-scale partition includes a significant portion of the energy associated with the mobile trough it is likely this method will misdiagnose the trough development.

The trough-merger mechanism did not contribute significantly to the development of the mobile trough. This result is in contrast to the development of a midtropospheric cutoff circulation that occurred on 18 and 19 January 1986 (Bell and Bosart 1993). Bell and Bosart used the full QGPV height tendency equation to diagnose the presence of a short-wave-jet-streak feature as it propagated into the base of a larger scale trough. They did not refer to this process as a trough-merger, but the merging of the two troughs (QGPV anomalies) would be classified as such in this research.

## CHAPTER VI

### CONCLUSION

The purpose of this research was to develop and apply a quantitative method to describe the dynamics of the midtropospheric mobile trough life cycle. A logical first step toward the assessment of the development mechanisms was to determine where the mobile troughs develop. The objective trough identification and tracking technique used to compile the 20-year trough climatology fit the bill. This objective technique was based on the relationship between midtropospheric mobile troughs and the maximum transport of geostrophic curvature vorticity, or Eulerian Centripetal Acceleration (ECA).

The mean lifespan of troughs over the 20-year dataset was 5.3 days and the maximum lifespan was 44 days. The geographical shape of trough genesis and termination regions are associated with orography. The three preferred genesis regions are southeast Asia, north-central North America, and the Mediterranean Sea. The three preferred termination regions are southwest Asia, the extreme eastern Pacific Ocean, and the Mediterranean Sea. Trough genesis regions tend to be well upstream of major areas of wintertime surface cyclogenesis.

The quantitative technique used to diagnose the dynamical mechanisms responsible for mobile troughs was based on the quasigeostrophic potential vorticity (QGPV) geopotential height tendency equation. The piecewise inversion of QGPV and QGPV advection to recover the associated height and tendency is referred to as "QGPV thinking." QGPV thinking is based on inverting QGPV anomalies superimposed on a basic state flow. The basic state, or large-scale as used in this research, was defined by low-pass filtering the spherical harmonic representation of QGPV. The QGPV anomalies, or small-scale, were defined using the high-pass harmonic coefficients.

The QGPV technique is somewhat sensitive to the choice of the large-scale truncation. If the large-scale flow includes a significant portion of the energy associated with the mobile trough, the QGPV method fails to diagnose the trough development. However, this failure is not a reflection of the diagnostic technique as much as it is a reflection of the

reasoning behind choosing the large-scale flow. As long as the large-scale is void of the mobile trough, the QGPV diagnostic is technique sufficiently robust.

The QGPV technique was applied to one of the mobile troughs identified and tracked by the objective method. It may seem logical to choose a sample trough from one of the three preferred genesis regions. However, these three genesis regions likely produced troughs progressing over areas of questionable meteorological data density (e.g. over the oceans). Instead, a trough specimen from one of the secondary genesis centers near the west coast of the United States was chosen to demonstrate the applicability of the diagnostic technique.

The selected trough lived for 21 days, but only the first 10 days of its life cycle were studied because during this time it remained over or near North America. The mobile trough deepened from 0000 UTC 1 December 1980 through 0000 UTC 3 December 1980. After this time it decayed, with the most rapid decay occurring between 1200 UTC 3 December 1980 and 1200 UTC 4 December 1980.

The trough initially developed due to the transport of kinetic energy from upstream disturbances. This mechanism is commonly referred to as downstream development. Baroclinic processes, as usually attributed to trough initiation, were not present during the birth of this trough. The baroclinic mechanism played an equal role with downstream development approximately 24 hours into the overall trough intensification. A third mechanism, superposition of QGPV due to deformation, was also dormant during the first 24 hours of trough development. At the 24-hour point, however, it too contributed equally to the intensification of the trough.

The decay of this trough was primarily due to the downstream development process transporting kinetic energy away from the mobile trough. The horizontal deformation process also contributed to the decay. The baroclinic process, however, continued to act to maintain the trough, but with reduced intensity.

A fourth intensification mechanism, trough-merger, was investigated, but did not contribute significantly to the development or decay of this trough. It was not included in the assessment of the trough diagnostic technique.

The combination of the three main intensification processes mentioned above were responsible for the genesis of the sample mobile trough. A discrepancy between the QGPV geopotential height tendency and the combination of the three processes occurred during the first half of the life cycle. The residual process composed of the mechanisms not included in the combination of the processes contributed minimally to the intensification of the mobile trough. The discrepancy was primarily due to the non-deformation advection of the small-scale QGPV used to diagnose the deformation process. When only the upper layer advection was used in the diagnosis the discrepancy was decreased significantly.

The QGPV diagnostic tool developed in this research worked well. The error in the technique was likely due to the geostrophic approximation used to compute potential vorticity. The application of this technique using a higher-order balanced flow, such as used by Davis (1992b), may improve the assessment of mobile trough development (David Gold, personal communication). However, an improved balance which includes nonlinear terms comes with a cost. The potential vorticity inversion is no longer strictly linear.

The QGPV diagnostic technique was only applied to one of the 27,469 mobile troughs identified by the objective tracking technique. This leaves 27,468 troughs ripe for analysis. Is there a difference in development mechanisms between troughs developing over oceans and land? What development mechanism dominates in troughs forming in the lee of mountain ranges?

Other possibilities for further research include a comparison between the QGPV diagnostic technique and traditional energy conversion calculations, especially using simplified global models instead of actual observed atmospheric data. A comparison between these results and results using the ageostrophic flux of kinetic energy would prove interesting (Orlanski and Chang 1993, Orlanski and Sheldon 1993).

## REFERENCES

- Alpert, P., B. U. Neeman, and Y. Shay-el, 1990: Climatological analysis of Mediterranean cyclones using ECMWF data. *Tellus*, **42A**, 65-77.
- Bell, G. D., and L. F. Bosart, 1989: A 15-year climatology of northern hemisphere 500 mb closed cyclone and anticyclone centers. *Mon. Wea. Rev.*, **117**, 2142-2163.
- , and D. Keyser, 1993: Shear and curvature vorticity and potential-vorticity interchanges: interpretation and application to a cutoff cyclone event. *Mon. Wea. Rev.*, **121**, 76-102.
- , and L. F. Bosart, 1993: A case study diagnosis of the formation of an upper-level cutoff cyclonic circulation over the eastern United States. *Mon. Wea. Rev.*, **121**, 1635-1655.
- Bishop, C. H., and A. J. Thorpe, 1994: Potential vorticity and the electrostatics analogy: Quasi-geostrophic theory. *Quart. J. Roy. Meteor. Soc.*, **120**, 713-731.
- Black, R. X., and R. M. Dole, 1993: The dynamics of large-scale cyclogenesis over the North Pacific Ocean. *J. Atmos. Sci.*, **50**, 421-442.
- Blackmon, M. L., 1976: A climatological spectral study of the 500 mb geopotential height of the Northern Hemisphere. *J. Atmos. Sci.*, **33**, 1607-1623.
- , N. C. Lau, and S. L. Mullen, 1977: An observational study of the northern hemisphere wintertime circulation. *J. Atmos. Sci.*, **34**, 1040-1053.
- Bleck, R., 1990: Depiction of upper/lower vortex interaction associated with extratropical cyclogenesis. *Mon. Wea. Rev.*, **118**, 573-585.
- Bluestein, H. B., 1992: *Synoptic-Dynamic Meteorology in Midlatitudes. Vol. I: Principles of Kinematics and Dynamics*. Oxford University Press, 431 pp.
- , 1993: *Synoptic-Dynamic Meteorology in Midlatitudes. Vol. II: Observations and Theory of Weather Systems*. Oxford University Press, 594 pp.
- Bretherton, F. P., 1966: Critical layer instability in baroclinic flows. *Quart. J. Roy. Meteor. Soc.*, **92**, 325-334.
- Carlson, T. N., 1991: *Mid-latitude Weather Systems*. Harper Collins, 507 pp.
- Chang, E. K. M., and I. Orlanski, 1993: On the dynamics of a storm track. *J. Atmos. Sci.*, **50**, 999-1015.
- , 1993: Downstream development of baroclinic waves as inferred from regression analysis. *J. Atmos. Sci.*, **50**, 2038-2053.
- Charney, J. G., 1947: The dynamics of long waves in a baroclinic westerly current. *J. Meteor.*, **4**, 135-162.

- , and M. E. Stern, 1962: On the stability of internal baroclinic jets in a rotating atmosphere. *J. Atmos. Sci.*, **19**, 159-172.
- Chen, S. J., Y. H. Kuo, P. Z. Zhang, and Q. F. Bai, 1991: Synoptic climatology of cyclogenesis over East Asia, 1958-1987. *Mon. Wea. Rev.*, **119**, 1407-1418.
- Davis, C. A., and K. A. Emanuel, 1991: Potential vorticity diagnostics of cyclogenesis. *Mon. Wea. Rev.*, **119**, 1929-1953.
- , 1992a: Piecewise potential vorticity inversion. *J. Atmos. Sci.*, **49**, 1397-1411.
- , 1992b: A potential-vorticity diagnosis of the importance of initial structure and condensational heating in observed extratropical cyclogenesis. *Mon. Wea. Rev.*, **120**, 2409-2428.
- , 1993: Comments on "Decomposing the atmospheric flow using potential vorticity framework". *J. Atmos. Sci.*, **50**, 2065-2067.
- Dean, D., 1993: A northern hemisphere climatology of 500 hPa trough merger and fracture. M.S. Thesis, State University of New York at Albany, 234 pp.
- Dey, C. H., 1989: The evolution of objective analysis methodology at the National Meteorological Center. *Wea. Forecasting*, **4**, 297-312.
- Dole, R. M. and R. X. Black, 1990: Life cycles of persistent anomalies. Part II: The development of persistent negative height anomalies over the North Pacific Ocean. *Mon. Wea. Rev.*, **118**, 824-826.
- Eady, E. T., 1949: Long waves and cyclone waves. *Tellus*, **1**, 33-52.
- Egger, J., 1990: Some aspects of potential vorticity inversion. *J. Atmos. Sci.*, **47**, 1269-1275.
- Eliassen, E., and B. Machenhauer, 1965: A study of the fluctuations of the atmospheric planetary flow patterns represented by spherical harmonics. *Tellus*, **17**, 220-239.
- , and B. Machenhauer, 1969: On the observed large-scale atmospheric wave motions. *Tellus*, **21**, 149-165.
- Eliassen, A., 1984: Geostrophy. *Quart. J. Roy. Meteor. Soc.*, **110**, 1-12.
- Farrell, B. F., 1982: The initial growth of disturbances in a baroclinic flow. *J. Atmos. Sci.*, **39**, 1663-1686.
- , 1989: Optimal excitation of baroclinic waves. *J. Atmos. Sci.*, **46**, 1193-1206.
- Gall, R., 1976: Structural changes of growing baroclinic waves. *J. Atmos. Sci.*, **33**, 374-390.
- Haltiner, G. J., and R. T. Williams, 1980: *Numerical Prediction and Dynamic Meteorology*. John Wiley & Sons, 477 pp.
- Holopainen, E., and J. Kaurola, 1993: Reply. *J. Atmos. Sci.*, **50**, 2068-2069.

- , and J. Kaurola, 1991: Decomposing the atmospheric flow using potential vorticity framework. *J. Atmos. Sci.*, **48**, 2614-2625.
- Holton, J. R., 1992: *An Introduction to Dynamic Meteorology*. Academic Press, 511 pp.
- Hoskins, B. J., I. Draghici, and H. C. Davies, 1978: A new look at the  $\omega$ -equation. *Quart. J. Roy. Meteor. Soc.*, **104**, 31-38.
- , M. E. McIntyre, and A. W. Robertson, 1985: On the use and significance of isentropic potential vorticity maps. *Quart. J. Roy. Meteor. Soc.*, **111**, 877-946.
- , 1991: Towards a PV- $\theta$  view of the general circulation. *Tellus*, **43AB**, 27-35.
- Kanamitsu, M., 1989: Description of the NMC global data assimilation and forecast system. *Wea. Forecasting*, **4**, 335-342.
- , J. C. Alpert, K. A. Campana, P. M. Caplan, D. G. Deaven, M. Iredell, B. Katz, H.-L. Pan, J. Sela, and G. H. White, 1991: Recent changes implemented into the global forecast system at NMC. *Wea. Forecasting*, **6**, 425-435.
- Klein, W. H., 1957: Principal tracks and frequencies of cyclones and anticyclones in the northern hemisphere. Research Paper No. 40, U. S. Weather Bureau, 60 pp.
- Kuo, Y. H., M. A. Shapiro, and E. G. Donall, 1991: The interaction between baroclinic and diabatic processes in a numerical simulation of a rapidly intensifying extratropical marine cyclone. *Mon. Wea. Rev.*, **119**, 368-384.
- Lefevre, R. J., and J. W. Nielsen-Gammon, 1995: An objective climatology of mobile troughs in the northern hemisphere. Submitted to *Tellus*.
- Mass, C. F., H. J. Edman, H. J. Friedman, N. R. Cheney, and E. E. Recker, 1987: The use of compact discs for the storage of large meteorological and oceanographic data sets. *Bull. Amer. Met. Soc.*, **68**, 1556-1558.
- Nielsen-Gammon, J. W., 1995: Dynamical conceptual models of upper-level mobile trough formation: Comparison and application. Submitted to *Tellus*.
- Orlanski, I., and J. Katzfey, 1991: The life cycle of a cyclone wave in the Southern Hemisphere. Part I: Eddy energy budget. *J. Atmos. Sci.*, **48**, 1972-1998.
- , and E. K. M. Chang, 1993: Ageostrophic geopotential fluxes in downstream and upstream development of baroclinic waves. *J. Atmos. Sci.*, **50**, 212-225.
- , and J. Sheldon, 1993: A case of downstream baroclinic development over western North America. *Mon. Wea. Rev.*, **121**, 2929-2950.
- Palmen, E., and C. W. Newton, 1969: *Atmospheric Circulation Systems*. Academic Press, 603 pp.
- Petterssen, S., 1955: A general survey of factors influencing development at sea level. *J. Meteor.*, **12**, 36-42.



- , 1956: *Weather Analysis and Forecasting. Vol. 1: Motion and Motion Systems*. McGraw-Hill, 428 pp.
- , and S. J. Smebye, 1971: On the development of extratropical cyclones. *Quart. J. Roy. Meteor. Soc.*, **97**, 457-482.
- Plumb, R. A., 1983: A new look at the energy cycle. *J. Atmos. Sci.*, **40**, 1669-1688.
- Pratt, R. W., 1976: The interpretation of space-time spectral quantities. *J. Atmos. Sci.*, **33**, 1060-1066.
- Press, W. H., S. A. Teukolsky, W. T. Vetterling, and B. P. Flannery, 1992: *Numerical Recipes in Fortran The Art of Scientific Computing*. Cambridge University Press, 963 pp.
- Reed, R. J., M. T. Stoelinga, and Y. H. Kuo, 1992: A model-aided study of the origin and evolution of the anomalously high potential vorticity in the inner region of a rapidly deepening cyclone. *Mon. Wea. Rev.*, **120**, 893-913.
- Rivest, C., C. A. Davis, and B. F. Farrell, 1992: Upper-tropospheric synoptic-scale waves. Part I: maintenance as Eady normal modes. *J. Atmos. Sci.*, **49**, 2108-2119.
- , and C. A. Davis, 1992: Upper-tropospheric synoptic-scale waves. Part II: maintenance and excitation of quasi modes. *J. Atmos. Sci.*, **49**, 2120-2138.
- Robinson, W. A., 1989: On the structure of potential vorticity in baroclinic instability. *Tellus*, **41A**, 275-284.
- Rossby, C.-G., 1945: On the propagation of frequencies and energy in certain types of oceanic and atmospheric waves. *J. Meteor.*, **2**, 187-204.
- Sanders, F., 1986: Explosive cyclogenesis over the west-central North Atlantic Ocean, 1981-1984. Part I: Composite structure and mean behavior. *Mon. Wea. Rev.*, **114**, 1781-1794.
- , 1988: Life history of mobile troughs in the upper westerlies. *Mon. Wea. Rev.*, **116**, 2629-2648.
- Shuman, F. G., 1989: History of numerical weather prediction at the National Meteorological Center. *Wea. Forecasting*, **4**, 286-296.
- Sinclair, M. R., 1994: An objective cyclone climatology for the southern hemisphere. *Mon. Wea. Rev.*, **122**, 2239-2256.
- Snyder, C. M. and R. S. Lindzen, 1988: Upper-level baroclinic instability. *J. Atmos. Sci.*, **45**, 2445-2459.
- Staley, D. O., 1988: Baroclinic instability in the upper troposphere. *J. Atmos. Sci.*, **45**, 3298-3304.
- Sutcliffe, R. C., 1947: A contribution to the problem of development. *Quart. J. Roy. Meteor. Soc.*, **73**, 370-383.

- Thorncroft, C. D., B. J. Hoskins, and M. E. McIntyre, 1993: Two paradigms of baroclinic-wave life-cycle behaviour. *Quart. J. Roy. Meteor. Soc.*, **119**, 17-55.
- Thorpe, A. J., 1985: Diagnosis of balanced vortex structure using potential vorticity. *J. Atmos. Sci.*, **42**, 397-406.
- , 1986: Synoptic scale disturbances with circular symmetry. *Mon. Wea. Rev.*, **114**, 1384-1389.
- Trenberth, K. E., 1978: On the interpretation of the diagnostic quasi-geostrophic omega equation. *Mon. Wea. Rev.*, **106**, 131-137.
- Wallace, J. M., G. H. Lim, and M. L. Blackmon, 1988: Relationship between cyclone tracks, anticyclone tracks and baroclinic waveguides. *J. Atmos. Sci.*, **45**, 439-462.
- Wash, C. H., J. E. Peak, W. E. Calland, and W. A. Cook, 1988: Diagnostic study of explosive cyclogenesis during FGGE. *Mon. Wea. Rev.*, **116**, 431-451.
- Washington, W. M., and C. L. Parkinson, 1986: *An Introduction to Three-Dimensional Climate Modeling*. University Press, 422 pp.
- Whitaker, L. M., and L. H. Horn, 1984: Northern hemisphere extratropical cyclone activity for four mid-season months. *J. Climatol.*, **4**, 297-310.
- , and A. Barcilon, 1992a: Type B cyclogenesis in a zonally varying flow. *J. Atmos. Sci.*, **49**, 1877-1892.
- , and A. Barcilon, 1992b: Genesis of mobile troughs in the upper westerlies. *J. Atmos. Sci.*, **49**, 2097-2107.
- Zishka, K. M., and P. J. Smith, 1980: The climatology of cyclones and anticyclones over North America and surrounding ocean environs for January and July, 1950-77. *Mon. Wea. Rev.*, **108**, 387-401.

## APPENDIX 1

## TELLUS RELEASE LETTER

## TEXAS A&amp;M UNIVERSITY

Department of Meteorology  
College Station, Texas, 77843-3150

Phone: (409) 845-~~1680~~ 1680

FAX: (409) 862-4466

E-mail rlefevre@tamu.edu

TO Tellus Editor FAX 468 16 5778  
No. Pages 1  
(including this page)

FROM: Randy Lefevre DATE 16 Feb 95

## MESSAGE:

Dear Editor,

I would like to include the manuscript you approved for publication in my dissertation at Texas A&M Univ. The title of the manuscript is "An objective climatology of mobile troughs in the northern hemisphere" and it will appear in the Tellus Special Issue on Extratropical Cyclones, Bergen Norway. Texas A&M requires an approval letter from the publisher stating the reproduction has been granted.

If approved, please mail or fax a letter to me. Please tell me exactly how you require the citation of the manuscript. Thank you for your consideration. This fax is a follow-up to an early e-mail message.

*Randy J. Lefevre*

Permission granted.

Please feel free to quote "An objective climatology....." Tellus A (in press).

or "An objective climatology....." to appear in Tellus A.

or "An objective climatology....." Accepted for

publication in Tellus A.

17 February 1995

*Marianne Skärman*  
Marianne Skärman

Managing Editor Tellus

## APPENDIX 2

### QGPV DERIVATION

Since there are so many papers related to potential vorticity, and each uses one of many forms of potential vorticity, it is appropriate to give a detailed derivation of the specific form used in this research. The (x,y,p,t) coordinate system was chosen to simplify the density calculations. The first four assumptions used in computing quasigeostrophic potential vorticity (QGPV) are:

- 1) The atmosphere is hydrostatic, which means the vertical wind acceleration is eliminated.
- 2) The curvature of the earth is small so spherical coordinates are not required.
- 3) The advection of planetary vorticity by the vertical component of the wind is neglected.
- 4) The frictional forces are neglected.

The full set of equations of motion and thermodynamic equations under the four assumptions (the “primitive” equations without friction) are given by,

$$\frac{d}{dt}(u_g + u_{ag}) = f v_{ag} \quad (\text{A2.1})$$

$$\frac{d}{dt}(v_g + v_{ag}) = -f u_{ag} \quad (\text{A2.2})$$

$$\frac{d\theta_T}{dt} = \dot{\theta}_T \quad (\text{A2.3})$$

$$\frac{\partial \phi_T}{\partial p} = -\frac{1}{\rho} = -\frac{RT}{p} = -\frac{R}{p} \left( \frac{p}{p_0} \right)^{\kappa} = -f \theta_T \quad (\text{A2.4})$$

$$u_g = -\frac{1}{f} \frac{d\phi_T}{dy} \quad (\text{A2.5})$$

$$v_g = \frac{1}{f} \frac{\partial \phi_T}{\partial x} \quad (\text{A2.6})$$

$$\frac{\partial}{\partial x}(u_g + u_{ag}) + \frac{\partial}{\partial y}(v_g + v_{ag}) + \frac{\partial \omega}{\partial p} = 0 \quad (\text{A2.7})$$

The following list describes the variables used throughout the equations in this section:

$x$  is the west-to-east displacement

$y$  is the south-to-north displacement

$u$  is the west-to-east component of the observed wind

$v$  is the south-to-north component of the observed wind

$u_g$  is the geostrophic wind in the west-to-east direction

$u_{ag} = u - u_g$ , is the ageostrophic wind in the west-to-east direction

$v_g$  is the geostrophic wind in the south-to-north direction

$v_{vg} = v - v_g$ , is the ageostrophic wind in the south-to-north direction

$\omega$  is the vertical velocity in pressure coordinates

$f = \mathbf{k} \bullet 2\mathbf{\Omega} \times \mathbf{V}$ , is the Coriolis parameter

$f_0 = 10^{-4} \text{ s}^{-1}$

$\mathbf{\Omega}$  is the rotation rate of the earth

$\mathbf{V}$  is the three-dimensional wind vector

$\theta_T(x, y, p, t) = \theta_s(p) + \theta(x, y, p, t)$ , is the total potential temperature

$\theta_s(p)$  is the basic state potential temperature. It is based on the spatial average  $\theta_T$  at each vertical pressure level.

$\theta(x, y, p, t)$  is the deviation of the potential temperature from the basic state

$\phi = gz_T$ , is the total geopotential

$z_T = z_s(p) + z(x, y, p, t)$ , is the total geopotential height of the pressure surface

$z_s(p)$  is the basic state geopotential height. In this study  $z_s(p)$  is the mean northern hemisphere geopotential height at each vertical pressure level.

$z(x, y, p, t)$  is the deviation of the geopotential height from the basic state

$R = 287.04 \text{ J K}^{-1} \text{ kg}^{-1}$ , the gas constant for dry air

$T$  is the temperature (K)

$p$  is the pressure

$\rho$  is the density

$$p_0 = 1000 \text{ mb}$$

$$\gamma = \frac{R}{f p} \left( \frac{p}{p_0} \right)^\kappa$$

$$\kappa = \frac{R}{c_p} = 1 - \frac{c_v}{c_p}$$

$$c_p = 1004 \text{ J K}^{-1} \text{ kg}^{-1}, \text{ the specific heat of dry air at constant pressure}$$

$$c_v = 717 \text{ J K}^{-1} \text{ kg}^{-1}, \text{ the specific heat of dry air at constant volume}$$

$$\frac{d}{dt} = \frac{\partial}{\partial t} + u \frac{\partial}{\partial x} + v \frac{\partial}{\partial y} + \omega \frac{\partial}{\partial p} \text{ is the total derivative.}$$

Three additional assumptions consistent with quasigeostrophic scaling arguments are,:

- 5)  $V_{ag} \ll V_g$  due to the smallness of the Rossby number ( $R_o = U/fL \approx 0.1$ )
- 6) The vertical gradients of the basic state potential temperature and geopotential height are only a function of pressure and approximately constant.
- 7) The variation of the Coriolis parameter,  $f$ , is small and can be replaced by  $f_0$ , except when involved in the meridional derivative.

After applying the three assumptions to the full equations, (A2.1) through (A2.7) become,

$$\frac{d_g u_g}{dt} = f_0 v_{ag} \quad (\text{A2.8})$$

$$\frac{d_g v_g}{dt} = -f_0 u_{ag} \quad (\text{A2.9})$$

$$u_g = -\frac{1}{f_0} \frac{\partial \phi_T}{\partial y} \quad (\text{A2.10})$$

$$v_g = \frac{1}{f_0} \frac{\partial \phi_T}{\partial x} \quad (\text{A2.11})$$

$$\frac{d_g \theta_T}{dt} = -\omega \frac{\partial \theta_s}{\partial p} + \dot{\theta}_T = \frac{\sigma}{f_0 \gamma_0} \omega + \dot{\theta}_T \quad (\text{A2.12})$$

$$\frac{\partial \phi_T}{\partial p} = -\frac{1}{\rho} = -\frac{RT}{p} = -\frac{R}{p} \left( \frac{p}{p_0} \right)^\kappa = -f_0 \gamma_0 \theta_T \quad (\text{A2.13})$$

$$\frac{\partial u_g}{\partial x} + \frac{\partial v_g}{\partial y} = 0 \quad (\text{A2.14})$$

$$\frac{\partial u_{ag}}{\partial x} + \frac{\partial v_{ag}}{\partial y} + \frac{\partial \omega}{\partial p} - \frac{v_g}{f_0} \frac{\partial f}{\partial y} = 0 \quad (\text{A2.15})$$

where

$\frac{d_g}{dt} = \frac{\partial}{\partial t} + u_g \frac{\partial}{\partial x} + v_g \frac{\partial}{\partial y}$  is the total geostrophic derivative,

$\sigma(p) = -f_0 \gamma_0 \frac{d\theta_s}{dp}$  is the static stability of the basic state, and

$$\gamma_0 = \frac{R}{f_0 p} \left( \frac{p}{p_0} \right)^\kappa$$

The thermal wind equations are given by

$$\frac{\partial u_g}{\partial p} = \gamma_0 \frac{\partial \theta_r}{\partial y} \quad (\text{A2.16})$$

$$\frac{\partial v_g}{\partial p} = -\gamma_0 \frac{\partial \theta_r}{\partial x} \quad (\text{A2.17})$$

If  $\partial/\partial y$ (A2.8) is subtracted from  $\partial/\partial x$ (A2.9), the result is

$$\frac{d_g}{dt} \left( \frac{\partial v_g}{\partial x} - \frac{\partial u_g}{\partial y} \right) = -f_0 \left( \frac{\partial u_{ag}}{\partial x} + \frac{\partial v_{ag}}{\partial y} \right) \quad (\text{A2.18})$$

The right hand side of (A2.18) will be modified by (A2.15), yielding

$$\frac{d_g}{dt} \left( \frac{\partial v_g}{\partial x} - \frac{\partial u_g}{\partial y} \right) = f_0 \frac{\partial \omega}{\partial p} - v_g \frac{\partial f}{\partial y} \quad (\text{A2.19})$$

However, the second term on the right hand side of (A2.19) can be rewritten using

$$\frac{d_g f}{dt} = \frac{\partial f}{\partial t} + u_g \frac{\partial f}{\partial x} + v_g \frac{\partial f}{\partial y} = v_g \frac{\partial f}{\partial y} \quad (\text{A2.20})$$

and moved to the left hand side of (A2.19) yielding the quasigeostrophic vorticity equation,

$$\frac{d_g}{dt}(\zeta_g + f) = f_0 \frac{\partial \omega}{\partial p} \quad (\text{A2.21})$$

where the geostrophic relative vorticity ( $\zeta_g$ ) is defined as

$$\zeta_g \equiv \frac{\partial v_g}{\partial x} - \frac{\partial u_g}{\partial y} = \frac{1}{f_0} \nabla^2 \phi_T \quad (\text{A2.22})$$

and  $\nabla^2$  is the two-dimensional Laplacian operator. The absolute vorticity, as defined by the planetary vorticity,  $f$ , plus the geostrophic relative vorticity,  $\zeta_g$ , can only change by vortex tube stretching or contraction by vertical motion.

If the diabatic effects are neglected from the quasigeostrophic thermodynamic equation, (A2.12) (this is assumption 8), and  $\sigma(p)$  and  $\gamma_0(p)$  are moved into the total geostrophic derivative, (A2.12) becomes,

$$\frac{d_g}{dt} \left( \frac{\theta_T f_0 \gamma_0}{\sigma} \right) = \omega \quad (\text{A2.23})$$

If the total geostrophic derivative on the left hand side of (A2.23) is expanded and the whole equation is differentiated by  $\partial/\partial p$  the result is,

$$\frac{d_g}{dt} \left( f_0^2 \frac{\partial}{\partial p} \left( \frac{\theta \gamma_0}{\sigma} \right) \right) = f_0 \frac{\partial \omega}{\partial p} \quad (\text{A2.24})$$

after two terms were canceled using the thermal wind relationship, (A2.16) and (A2.17), and the whole equation was multiplied by  $f_0$ . The total potential temperature ( $\theta_T$ ) in (A2.23) was replaced by  $\theta$  in (A2.24) because the vertical gradient of total potential temperature is replaced by the vertical derivative of basic state potential temperature (recall assumption 6), and the geostrophic time derivative does not have a local pressure derivative.

The left hand side of (A2.24) describes the stratification changes following the motion of a parcel being advected by the geostrophic wind. Stratification, as used in this study, is related to vertical stretching but includes the basic state static stability; therefore, its tendency will be opposite in sign to the vertical stretching. Like the vorticity equation, (A2.21), the stratification will change in response to vortex tube stretching or contraction.



For example, increasing upward vertical motion with elevation (stretching) will decrease the stratification.

Since the right hand side of (A2.21) and (A2.24) are equal, the combination of these equations yields

$$\frac{d_g q}{dt} = 0 \quad (\text{A2.25})$$

where the quasigeostrophic potential vorticity (QGPV) is defined by

$$q \equiv \zeta_g + f - f_0^2 \frac{\partial}{\partial p} \left( \frac{\theta \gamma_0}{\sigma} \right) \quad (\text{A2.26})$$

Since the QGPV diagnostics used in this research will be concerned with the variation in geopotential height of pressure surfaces, (A2.26) is transformed to a single variable,  $\phi$ , yielding

$$q \equiv \frac{1}{f_0} \nabla^2 \phi + f + f_0 \frac{\partial}{\partial p} \left( \frac{1}{\sigma} \left( \frac{\partial \phi}{\partial p} \right) \right) \quad (\text{A2.27})$$

by using the hydrostatic equation, (A2.13), along with the geostrophic wind definitions, (A2.10) and (A2.11). For the same reasons  $\theta$  replaced  $\theta_r$  in deriving (A2.24),  $\phi$  replaces  $\phi_r$  when deriving (A2.27). Finally, the static stability,  $\sigma(p)$  in (A2.27), is modified to

$$\sigma(p) = -\frac{R}{p_0} \left( \frac{p_0}{p} \right)^{\frac{c_v}{c_p}} \frac{d\theta_s}{dp} \quad (\text{A2.28})$$

by using an alternate form of  $\kappa$  (i.e.  $1 - c_v/c_p$ ). Therefore, the QGPV used in this research is defined by

$$q \equiv \frac{g}{f_0} \nabla^2 z + f + g f_0 \frac{\partial}{\partial p} \left( \frac{1}{\sigma} \frac{\partial z}{\partial p} \right) \quad (\text{A2.29})$$

It is important to stress a few key aspects of (A2.29). First, the QGPV is conserved following geostrophic motion. Second, the change in stratification by the vertical motion exactly cancels the change in vorticity due to vertical motion. The vertical motion present is only available to maintain thermal wind balance, it doesn't advect any QGPV.

Hoskins et al. (1985) and Charney and Stern (1962) give the relationship between Ertel's potential vorticity and QGPV (Hoskins et al. Eqns. 39a and 39b) as follows,

$$\left. \frac{\partial P}{\partial t} \right|_s \approx -g \frac{d\theta_s}{dp} \left( \left. \frac{\partial q}{\partial t} \right|_p \right) \quad (\text{A2.30})$$

$$\nabla_\theta P \approx -g \frac{d\theta_s}{dp} \nabla_p q \quad (\text{A2.31})$$

Therefore, the rate of change of Ertel's potential vorticity following an air parcel moving on an isentropic surface is approximately proportional to the rate of change of QGPV following a parcel moving on a pressure surface. The Lagrangian behavior of Ertel's potential vorticity is in the same sense as the Lagrangian behavior of QGPV since the basic state atmosphere is stably stratified (the vertical potential temperature gradient is negative).

## APPENDIX 3

### UNPUBLISHED MANUSCRIPT BY NIELSEN-GAMMON (1994)

The text and figures in this appendix were **extracted** directly from an unpublished manuscript written by John. W. Nielsen-Gammon, Department of Meteorology, Texas A&M University (1994). Some of the ideas in this manuscript were later submitted to *Tellus* for publication. The figures and specific description of each figure, however, remain unpublished at the time of this dissertation. The reference section was edited to only list the cited papers.

The "basic state" shall be regarded as a straight westerly jet (Fig. 1). Using the terminology of Hoskins et al. (1985), any departure of the PV contour from its position in Fig. 1 produces a PV anomaly: a region of anomalously high or low values of potential vorticity relative to the basic state or relative to adjacent areas within the same isentropic layer. Associated with these departures of PV from the basic state are variations in wind and temperature which, while strongest near the anomaly, are not confined to the anomaly itself. As discussed in Eliassen and Kleinschmidt (1957), positive PV anomalies, which correspond to equatorward displacements of the PV contour, are associated with positive relative vorticity and a cyclonic circulation, and shall be referred to as troughs. Similarly, poleward displacements correspond to ridges.

Of particular interest is the cross-contour flow associated with the anomalies, for it is this advective flow which affects the motion of the PV contour, thereby altering the future configuration of the balanced winds and temperatures. In a frame of reference moving with the large-scale westerly flow, the associated wind is poleward between a trough and its downstream ridge, for example, which acts to advect the PV contour poleward. We shall ignore the non-linear easterly component of the flow associated with the fact that the locations of positive anomalies are necessarily south of the locations of negative anomalies, and focus on the north-south displacement of the contour. The remainder of the three-dimensional flow field away from the contour does not affect the potential

vorticity distribution and therefore has no significance for the quasi-balanced, adiabatic, inviscid dynamics.

As an example, Fig. 2a shows the instantaneous position of the PV contour and associated north-south advective winds for a periodic one-dimensional Rossby wave. To the east of any given trough, or positive PV anomaly (represented by a '+'), the flow is acting to advect low PV air northwards, while to the west, the flow is acting to advect high PV air southwards. At the peaks of the troughs and ridges, the north-south flow is exactly zero. The net result of these advections is that the entire pattern is moving westward without change of amplitude. This is the familiar Rossby wave propagation, westward relative to the mean zonal flow.

Similar arguments apply to a surface potential temperature gradient. High values of potential temperature at the ground are associated with similar wind and temperature fields as high values of potential vorticity in the free atmosphere (Thorpe 1986). Since surface temperature gradients are often concentrated in frontal regions, a similar diagram can be used to describe "Rossby edge waves" (Fig. 2b). The single contour then represents the surface frontal position, except that the sign of the effective PV gradient is reversed to correspond to the typical configuration of warm air equatorward and cold air poleward. Thus, cyclonic vorticity corresponds to poleward displacements of the front, and the sense of the associated circulation centers is similarly reversed. The edge wave pattern propagates to the east rather than to the west.

Propagation can also proceed across PV contours. Imagine a configuration in which there are two like-signed PV gradients at different horizontal or vertical locations. If there is a wave along one of the gradients, its associated winds will excite a wave along the other gradient. In Fig. 2c, the wave along the southern gradient is acting to amplify the wave along the northern gradient. However, the new wave is configured in such a way as to cause the reduction in amplitude of the old wave. By this process wave energy moves from one PV gradient to another. The previous examples dealt with the motion of lines of constant phase rather than energy, and their motion was governed by the phase speed rather than the group velocity.

The first mechanism to be considered is baroclinic instability (Charney 1947; Eady 1949), which would produce an upper-level wave and a surface cyclone simultaneously in a form of development which Petterssen called Type A (Petterssen and Smebye 1971). Baroclinic instability requires opposite-signed gradients of potential vorticity, or its surrogate, at different isentropic levels (Charney and Stern 1962; Bretherton 1966), which is represented here (Fig. 3) as an upper-level jet stream (black line) overlying a surface frontal zone (gray line). With the proper phase shift, the winds associated with the Rossby edge wave along the frontal zone can produce PV advections in the base of the upper-level troughs and ridges which act to amplify the wave. These winds decay with height above the surface frontal zone, but can still be of significant strength at jet level if the wavelength is sufficiently long and the stratification is sufficiently weak. The same phase tilt allows the winds associated with the upper-level Rossby wave to amplify the wave along the surface frontal zone.

The phase shift need not be exactly  $90^\circ$  as shown. As discussed by Hoskins et al. (1985), the waves will phase-lock at whatever tilt is necessary to maintain a constant phase shift against the combined effects of advection and propagation. If there were large vertical wind shear, for example, a decreased tilt between the upper and lower positive anomalies would increase the westward propagation of the upper wave and the eastward propagation of the lower, counterbalancing the advective effects of the shear.

Since most cyclones are unambiguously associated with a preexisting upper trough, some investigators have suggested that some forms of baroclinic instability can lead to a prominent upper-level disturbance with a weaker low-level or surface signal. Most recently, Whitaker and Barcilon (1992) considered basic states with weak baroclinicity at low levels and investigated the effects of a shallow stable layer at the surface and enhanced surface friction. Both effects produced the largest wave amplitudes at upper levels, with the upper-level PV gradient interacting either with the weak surface temperature gradient or with a negative PV gradient at the top of the stable layer. Other studies of baroclinic instability with energy concentrated at upper levels have been performed by Snyder and Lindzen (1988) and Staley (1988).

Barotropic instability was proposed by Kuo (1949) as a mechanism for the generation of mobile troughs, although the synoptic example he gives is unconvincing. Although barotropic instability is easily distinguished from baroclinic instability on the basis of energetics, the basic mechanism of mutually-reinforcing counter-propagating Rossby waves is the same. A reversal of the PV gradient within a given isentropic layer is required, and the resulting disturbance would be confined to the upper troposphere. The schematic of Fig. 3 applies if the gray line is taken to mark the southern boundary of a region of low PV whose northern boundary is marked by the solid black line.

Farrell and coworkers have argued against the significance of modal instability in the atmosphere. They observe that the most unstable wavelengths tend to be too large and that a suitable initial disturbance whose spatial structure is allowed to vary is capable of growing much more rapidly than the most unstable mode for a finite period of time. Indeed, the basic-state flow need not be barotropically or baroclinically unstable.

Rivest and Farrell (1992) describe initial conditions which lead to the rapid transient intensification of upper-level mobile troughs. Although their solutions involve a continuous distribution of potential vorticity, the basic mechanism can be illustrated by a series of line vortices located at upper levels beneath the tropopause. In Fig. 4, each symbol represents a north-south line of vortices located beneath the tropopause and which are unaffected by the north-south component of the wind. Initially, the vorticity field tilts upshear. Because the vortices are not embedded within a potential vorticity gradient, they cannot propagate or intensify, and are simply advected downstream. However, the winds associated with each vortex are felt at the level of the PV gradient, and the associated advections induce a wave. As time goes on, the vertical shear of the basic state causes the tilt between the line vortices at different levels to decrease and eventually move past vertical to downshear. Meanwhile, the associated winds have remained in phase with the developing upper-level wave, which continues to amplify. Furthermore, the westward propagation of this upper-level Rossby wave allows it to keep in step with the vortices just beneath it, prolonging the amplification.

While it seems unlikely that a train of three-dimensional vortices in the atmosphere would randomly align themselves with the proper horizontal and vertical displacements and be able to maintain their structure against horizontal deformation, the mechanism discussed by Rivest and Farrell is a two-dimensional, periodic extension of the somewhat simpler problem of a vortex interacting with a PV gradient. The process, which we call the trough-merger mechanism, is shown in Fig. 5. An isolated vortex, initially far south of the PV gradient, is drawn northward toward the jet by some process such as large-scale deformation or beta-gyre propagation. The vortex could be an upper-level cutoff cyclone or a tropical cyclone. As the vortex gets close to the PV gradient, its associated winds produce a wave along the jet, which grows more and more rapidly as the vortex is drawn closer. An additional interaction not present in the Rivest-Farrell model is due to the resulting position of the vortex between the trough and downstream ridge. The southerlies associated with the developing wave accelerate the vortex northward toward the gradient, allowing even stronger cross-gradient advections but speeding the eventual incorporation of the vortex into the westerlies.

A somewhat different problem arises if a disturbance originates along the potential vorticity gradient (Fig. 6). After the initial wave formation, additional wave crests and troughs appear downstream, but not upstream, because of the eastward group velocity of Rossby waves (Rossby 1945). This is the mechanism proposed by Yeh (1949) to explain observed wave development downstream of developing cyclones (e.g., Cressman 1948). The group velocity mechanism, as presented, seems to have been directed toward explaining the downstream propagation of long waves, as opposed to mobile troughs, and considerable observational evidence has confirmed that downstream development is common for long waves. Nonetheless, the same dynamical mechanism can in principle produce downstream development of mobile troughs as well.

A closely related theory, explicitly focused on the development of cyclone-scale mobile troughs, has been dubbed downstream baroclinic development, or DBD, by Orlanski and collaborators. Idealized examples are found in Simmons and Hoskins (1979) and Orlanski and Chang (1993), and case studies are reported in Orlanski and Katzfey

(1991) and Orlanski and Sheldon (1993). As with the group velocity mechanism, wave energy propagates downstream at upper levels, but the source of the energy is the unstable baroclinic growth of an initial disturbance (Fig. 7). Eventually, successive disturbances continue to extract energy from the unstable basic state while continuing to spawn further downstream development. For the initial formation of a particular upper-level mobile trough, the main difference between the mechanisms in Figs. 6 and 7 is quantitative: in the former, the energy flux from upstream is fixed; in the latter, it is growing.

The last two mechanisms to be considered here do not so much involve an increase in the perturbation potential vorticity as an increase in the associated circulation resulting from a change in the configuration of the potential vorticity. Farrell (1989) pointed out that a suitably configured disturbance in a deformation flow can undergo energy growth as well as changes in shape. For a wave on a localized PV gradient, the situation corresponds to Fig. 8. An initially elongated, small-amplitude disturbance is embedded in diffluence, causing the wavelength to decrease while the north-south extent of the wave increases. Although the total area covered by the PV anomalies does not change, the anomalous PV becomes more compact, allowing the circulations associated with the PV to become superimposed and resulting in an increase in the kinetic energy associated with the wave. If the diffluence continues, the wave becomes increasingly elongated in the north-south direction and the kinetic energy weakens. The same sort of mechanism can operate in confluence, in which case the initial disturbance must be elongated in the cross-flow direction.

The final mechanism, which may be called digging, is directly related to the observed tendency for mobile troughs to intensify when they enter long-wave troughs or possess a jet streak on their upstream side. To illustrate this mechanism, consider a long-wave pattern on the PV gradient associated with the subtropical jet and a mobile trough on the PV gradient associated with the polar jet (Fig. 9). The gradients are like-signed, so no barotropic or baroclinic instability is possible in this example. Initially (Fig. 9a), the mobile trough may possess little or no positive relative vorticity, since it is embedded within an environment with large-scale negative relative vorticity. As it moves eastward



from the large-scale ridge to the large-scale trough, the environmental (and total) vorticity in the base of the mobile trough increases (Fig. 9b). In addition, the winds associated with the large-scale wave preferentially advect the high potential vorticity in the base of the mobile trough southward, further enhancing the strength of the trough. Both processes continue until the mobile trough reaches maximum amplitude at the base of the long-wave trough (Fig. 9c). The signature of a strong (digging) upstream jet is present as the mobile trough descends the long-wave trough, since the two PV gradients are superimposed on the upstream side of the mobile trough.

## REFERENCES

- Bretherton, F. P. 1966. Critical layer instability in baroclinic flows. *Q. J. R. Meteorol. Soc.* **92**, 325-334.
- Charney, J. G. 1947. The dynamics of long waves in a baroclinic westerly current. *J. Meteor.* **4**, 135-163.
- Charney, J. G., and Stern, M. E. 1962. On the stability of internal baroclinic jets in a rotating atmosphere. *J. Atmos. Sci.* **19**, 159-172.
- Cressman, G. P. 1948. On the forecasting of long waves in the upper westerlies. *J. Meteor.* **5**, 44-57.
- Eady, E. T. 1949. Long waves and cyclone waves. *Tellus* **1**(2), 33-52.
- Eliassen, A., and Kleinschmidt, E. 1957. Dynamic meteorology. *Handbuck der Physik* **48**, 1-154.
- Farrell, B. F. 1989. Transient development in confluent and diffluent flow. *J. Atmos. Sci.* **46**, 3279-3288.
- Hoskins, B. J., McIntyre, M. E., and Robertson, A. W. 1985. On the use and significance of isentropic potential vorticity maps. *Q. J. R. Meteorol. Soc.* **111**, 877-946.
- Kuo, H.-L. 1949. Dynamic instability of two-dimensional nondivergent flow in a barotropic atmosphere. *J. Meteor.* **6**, 105-122.
- Orlanski, I., and Chang, E. K. M. 1993. Ageostrophic geopotential fluxes in downstream and upstream development of baroclinic waves. *J. Atmos. Sci.* **50**, 212-225.
- Orlanski, I., and Katzfey, J. 1991. The life cycle of a cyclone wave in the Southern Hemisphere. Part I: Eddy energy budget. *J. Atmos. Sci.* **48**, 1972-1998.
- Orlanski, I., and Sheldon, J. 1993. A case of downstream baroclinic development over western North America. *Mon. Wea. Rev.* **121**, 2929-2950.
- Petterssen, S., and Smebye, S. J. 1971. On the development of extratropical cyclones. *Q. J. R. Meteorol. Soc.* **97**, 457-482.
- Rivest, C., and Farrell, B. F. 1992. Upper-tropospheric synoptic-scale waves. Part II: Maintenance and excitation of quasi modes. *J. Atmos. Sci.* **49**, 2120-2138.
- Rossby, C.-G. 1945. On the propagation of frequencies and energy in certain types of oceanic and atmospheric waves. *J. Meteor.* **2**, 187-204.
- Simmons, A. J., and Hoskins, B. J. 1979. The downstream and upstream development of unstable baroclinic waves. *J. Atmos. Sci.* **36**, 1239-1254.
- Snyder, C., and Lindzen, R. S. 1988. Upper-level baroclinic instability. *J. Atmos. Sci.* **45**, 2445-2459.
- Staley, D. O. 1988. Baroclinic instability in the upper troposphere. *J. Atmos. Sci.* **45**, 3298-3304.

- Thorpe, A. J. 1986. Synoptic scale disturbances with circular symmetry. *Mon. Wea. Rev.* **114**, 1384-1389.
- Whitaker, J. S., and Barcilon, A. 1992. Genesis of mobile troughs in the upper westerlies. *J. Atmos. Sci.* **49**, 2097-2107.
- Yeh, T.-C. 1949. On energy dispersion in the atmosphere. *J. Meteor.* **6**, 1-16.

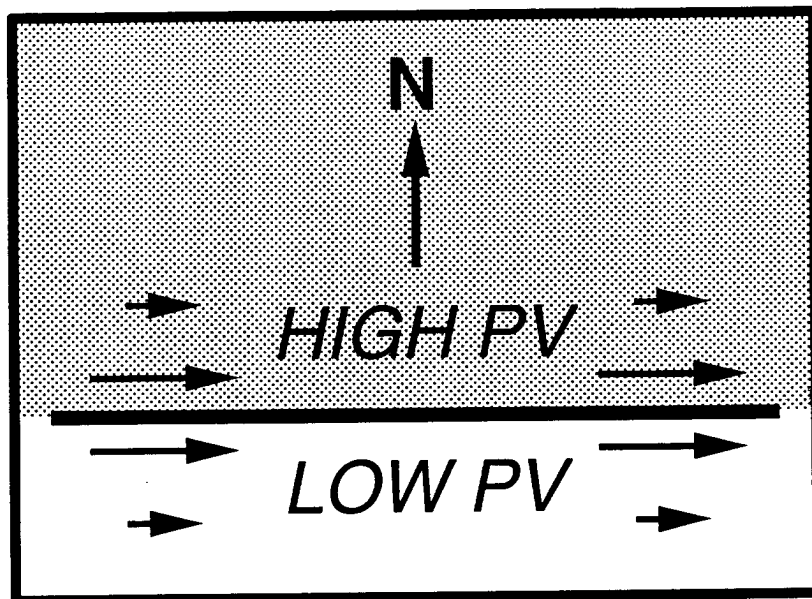


Fig. 1. Schematic diagram of basic-state configuration of potential vorticity and wind (arrows) on an isentropic surface intersecting the tropopause. The thick line denotes the tropopause, assumed to be essentially vertical near the jet core, and separates the high potential vorticity stratospheric air to the north from the low potential vorticity tropospheric air to the south.

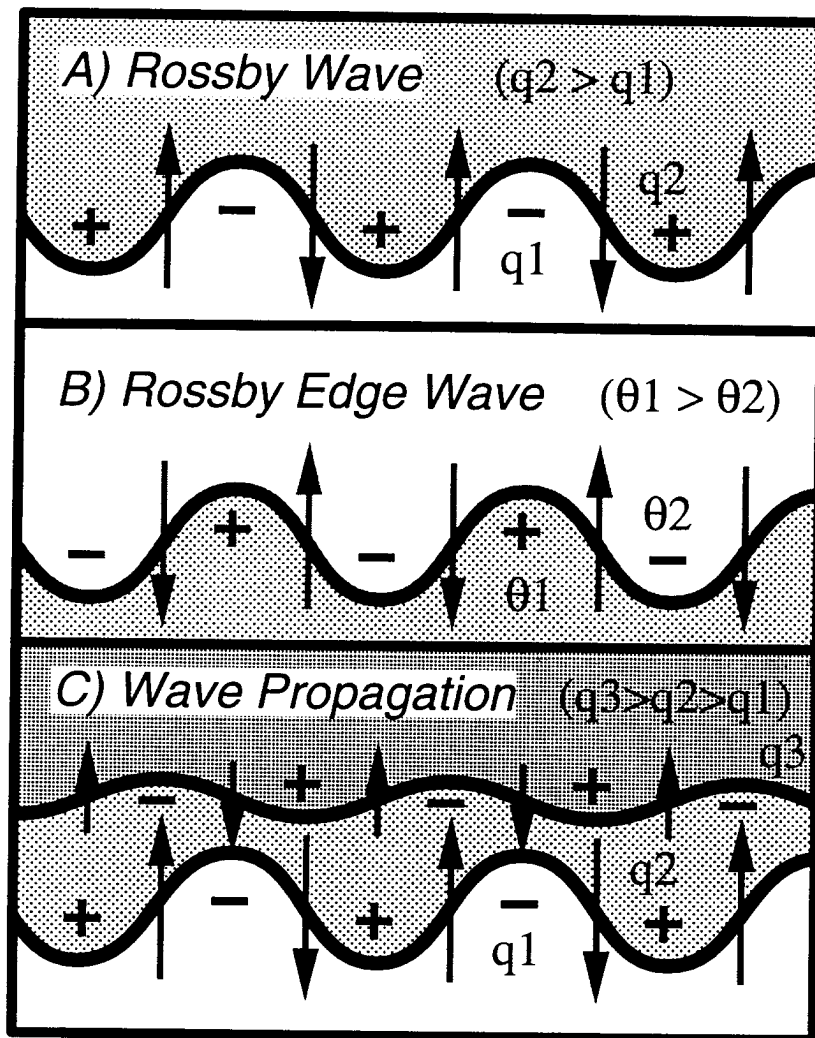


Fig. 2. a) Diagram illustrating Rossby wave phase propagation. Troughs and ridges (positive and negative PV anomalies) are denoted by '+' and '-', respectively. Potential vorticity values on either side of the tropopause are denoted by  $q_1$  and  $q_2$ . Arrows indicate sense and magnitude of north-south wind associated with the anomalies. b) Diagram illustrating Rossby edge wave propagation along a surface front. Potential temperature values on either side of the front are denoted by  $\theta_1$  and  $\theta_2$ . c) Diagram illustrating Rossby wave energy propagation. The two solid lines represent the position of the tropopause on two neighboring isentropic surfaces. North-south winds are plotted along the tropopause whose undulations give rise to them; the winds are to be understood to extend to the neighboring tropopause and produce potential vorticity advection there. As configured, the winds associated with the southern tropopause contour would amplify the waves on the northern contour, while winds associated with the northern contour would weaken the waves on the southern contour. This wave is propagating from south to north.

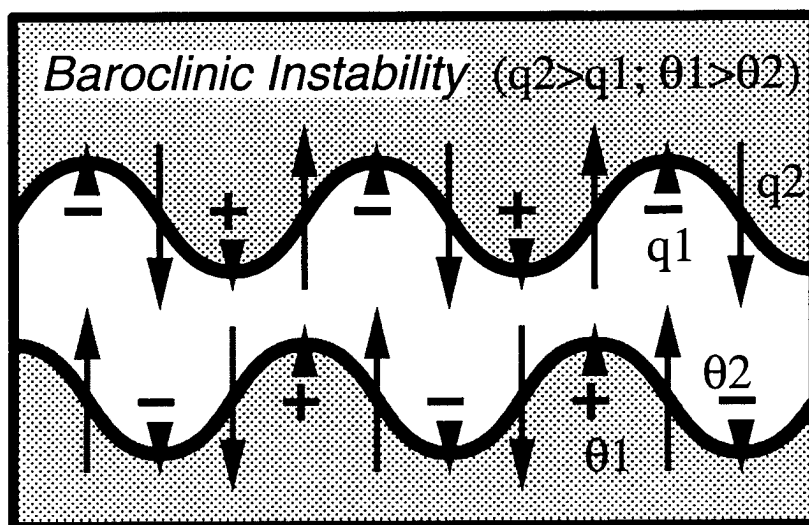


Fig. 3. Diagram showing basic mechanism for baroclinic instability. Upper contour (black) shows horizontal configuration of tropopause along isentropic surface at jet level; lower contour (gray) shows horizontal configuration of surface front. Surface front is drawn south of jet position for clarity, and should be understood to lie directly beneath it. Winds associated with the waves along the tropopause and surface front are shown in black and gray, respectively. The winds associated with the waves along one contour are configured so as to amplify the wave along the other contour, and vice versa. A basic-state vertical shear, consistent with the presence of a jet and frontal zone, is presumed to exist and to help maintain the positions of wave crests against the tendency for them to propagate in opposite directions at the two levels.

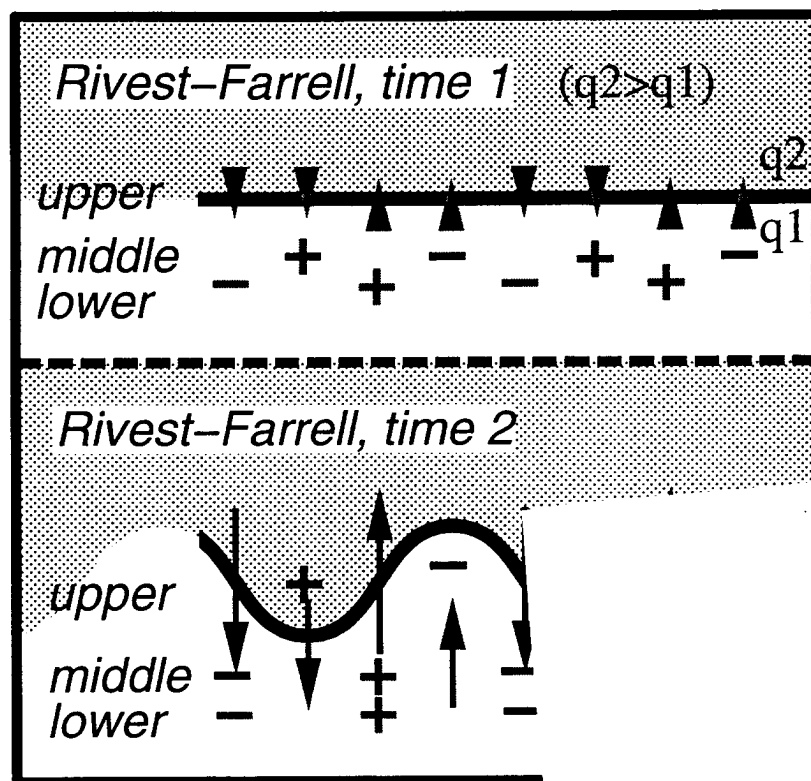


Fig. 4. Diagram illustrating the mechanism of Rivest and Farrell (1992). Line vortices, oriented north-south and indicated by '+' and '-', are located beneath the tropopause. Their east-west position is as shown and their height is given by the shading, with the darker vortices closer to the tropopause and the lighter vortices farther from the tropopause. Horizontal winds associated with the vortices are shown along the tropopause. The winds induce a wave along the tropopause, while the background vertical shear decreases the vertical tilt of the vortices.

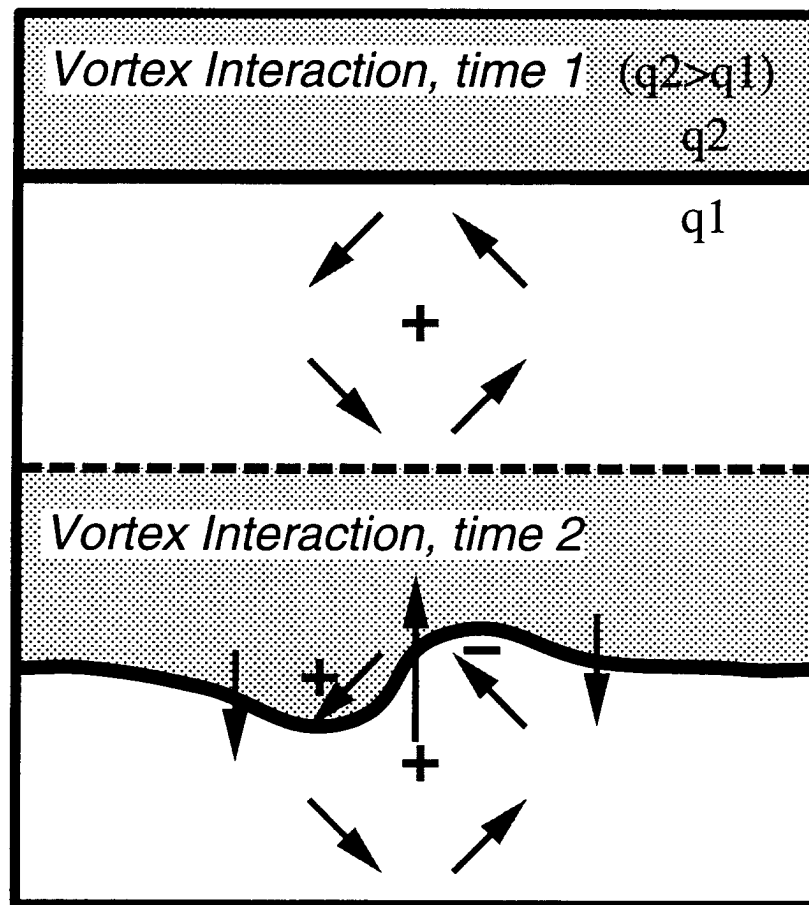


Fig. 5. Diagram illustrating the interaction between a potential vorticity discontinuity and an approaching vortex. The vortex produces a wave along the tropopause, whose associated winds act to draw the vortex northward.



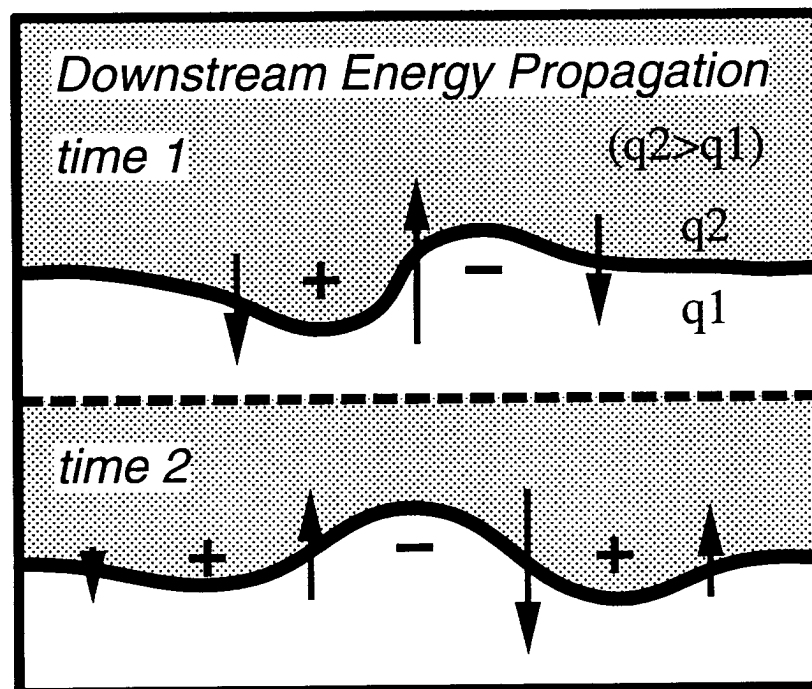


Fig. 6. Diagram showing the generation of a wave trough downstream of an initial disturbance along the tropopause. At later times, a succession of ridges and troughs will continue to form toward the east and dissipate toward the west, as long as the wave energy is confined to this tropopause.

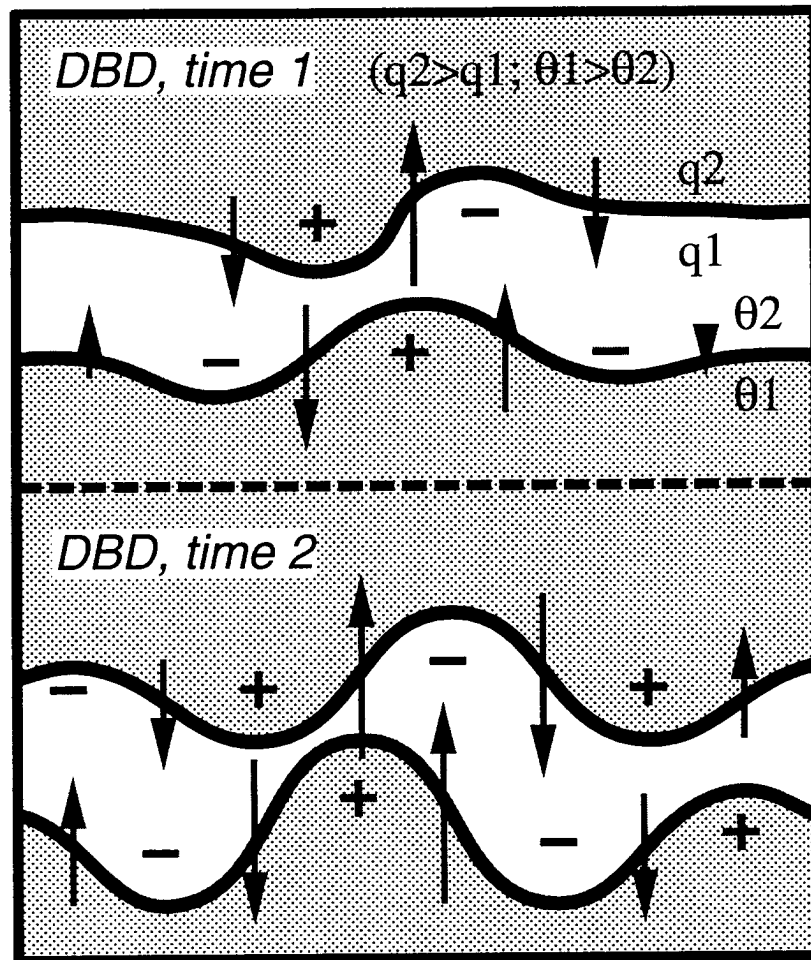


Fig. 7. Illustration of downstream baroclinic development, essentially a combination of Figs. 3 and 6. The phase difference between the surface frontal waves and waves along the tropopause produces amplification, while energy propagates toward the east along the tropopause and toward the west along the surface.

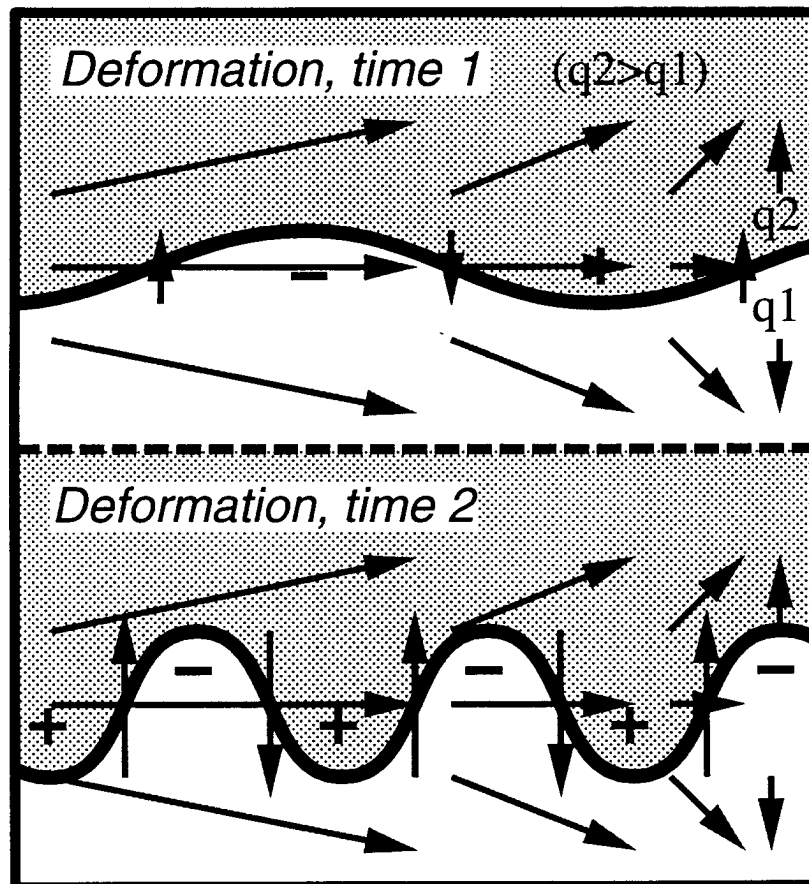


Fig. 8. Illustration of the effect of diffusive deformation on a small-amplitude wave at the tropopause. Wave crests and troughs extend farther north and south, while the east-west wavelength decreases. Maximum kinetic energy is attained near time 2, when the east-west and north-south scales of the PV anomalies are most similar.

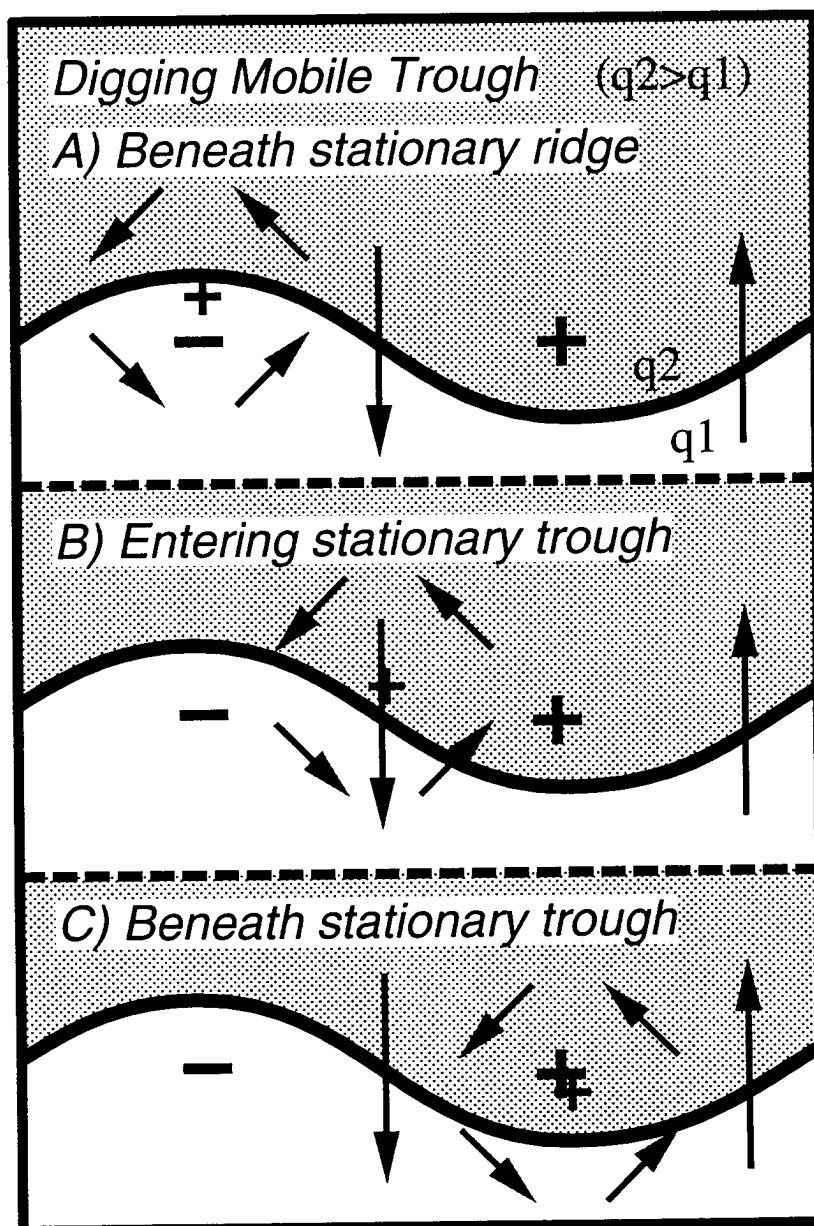


Fig. 9. Example of a mobile trough (gray) traveling along a stationary long wave (black). As the mobile trough moves eastward, its circulation becomes increasingly superposed with that of the stationary wave, and the mobile trough is drawn southward. In the middle diagram, the northwesterly wind SW of the mobile trough would superpose with the large-scale northwesterly flow, producing a "digging" jet streak on the west side of the long-wave trough.

## VITA

Randy Joseph Lefevre was awarded a Bachelor of Arts degree in Biology in 1982 from Sonoma State University, California. After graduating he worked as an environmental biologist for one and a half years before entering the United States Air Force (USAF). He was commissioned a Second Lieutenant on 13 December 1983 and attended the one year USAF Basic Meteorology Program at Texas A&M University.

Lieutenant Lefevre's first operational assignment was at Travis AFB, California. During this time he provided worldwide weather support for Army and Air Force operations. In 1987 he left Travis AFB to attend the Naval Postgraduate School (NPGS), California.

Captain Lefevre's research at NPGS was focused on numerical weather prediction and the dynamics of East Asian cold surges. He graduated from NPGS in March 1989 with a Master of Science degree in Meteorology. His next USAF assignment was to Wright-Patterson AFB (WPAFB), Ohio.

Captain Lefevre worked as a staff meteorologist at WPAFB for three and a half years. During this time he helped scientist and engineers develop new weapon systems for the USAF. His area of specialty was aircraft icing and its effect on aerodynamic performance.

Captain Lefevre moved to College Station, Texas in August 1992 and entered the doctoral program in the Department of Meteorology at Texas A&M University. Captain Lefevre was selected for promotion to Major in August 1994. He can be reached through the Department of Meteorology, Texas A&M University, College Station, TX 77843-3150. His e-mail address is: [rlfevre@tamu.edu](mailto:rlfevre@tamu.edu).